Hydrogen Induced Cracking in Energy Pipelines and Its Monitoring with Acoustic Emission

A thesis submitted for the degree of Doctor of Philosophy by:

Dandan Liu

Department of Mechanical and Aerospace Engineering

Brunel University London

London

United Kingdom

Abstract

This research investigated the development of Hydrogen Introduced Cracks (HIC) on steel plates monitored with Acoustic Emission (AE) technology in detail. The work focuses on identifying and clustering HIC signals from mixed signals with different experimental setups, as well as describing HIC development in the light of signals' characteristics.

Electrochemical hydrogen charging (ECHC) method was applied to generate HIC on A516 steel plates with mixed solution of 0.5mol/L H_2SO_4 and 0.5g/L $NaAsO_2$. Four defect mechanisms were found to generate elastic waves during a test, which were H_2 evolution, HIC, crevice corrosion and uniform corrosion. An experimental procedure was designed for pattern recognition of these mixed signals. Short-time tests with or without current were carried out using only 0.5mol/L H_2SO_4 solution for identifying non-HIC signals separately. The energy proportions in the frequency range of 0-100kHz (PE1) and 100-200kHz (PE2) in the energy spectrum as well as the parameters in the time domain of the Duration, the Energy and the Counts are the main characteristics used for pattern recognition. These characters were the basic parameters for signals identification, irrespective of the profile of the plate, the value of applied current, the locations of the sensors.

Due to the large amount of data, manual classification would be extensively time-consuming. In this study, a two-step Gaussian Mixed Model (GMM) clustering method was proposed for automatically clustering the mixed signals, in which the parameters of PE1 and PE2 obtained from the frequency domain were used for identifying signals from corrosions, and the Duration, the Counts and the Energy were then used to distinguish signals between H_2 evolution and HIC. The effectiveness of this method was verified by experiments with different setup parameters.

For the two types of sensors (Nano30 and VS150-RSC) used in this study, it was found that more components of the signals acquired by VS150-RSC were concentrated at 150kHz compared with those by Nano30 sensors. Therefore, the accurate rate of the proposed automatic clustering method was lower due to the scattering frequency distribution among the critical signals. However, sensor VS150-RSC is more suitable for HIC monitoring in situations of a low signal-to-noise ratio or over a long distance between the event and the sensor. For the different thickness of the specimen (5mm,

10mm and 20mm), it was found that the HIC signals acquired by VS150-RSC had components between 160-190kHz when the thicknesses of specimens were 10mm or 20mm. For the test with a complex structural profile including a hole and a seam of the same size, it was found that the seam heavily influenced the frequency distribution of HIC signals while a hole only influenced the characteristics of signals in the time domain.

This research also investigated the source localisation of HIC events under different experimental setups, including the specifications of specimens and the type of sensors. The Simplex method was used to calculate the location based on the parallelogram sensor array. The onset time of each signal was determined by the Akaike Information Criterion (AIC) method to improve the accuracy. This method located HIC events well on simple plates with different setups but not on complex structures, such as a structure with holes, seams, welds, flanges and others. The delta-T mapping method was then investigated to localise HIC events on the complex plate with a hole and a seam. A FE model was also built by Abaqus to simulate the delta-T maps for each pair of sensors under this setup. Compared to the location results calculated by the Simplex method, the accuracy of localisation obtained by overlapping the simulated delta-T maps was greatly improved.

Acknowledgement

First and foremost, I would like to extend my sincere gratitude to my academic supervisor, Dr. Bin Wang and my industrial supervisor, Dr. Stephen Grigg for their continuous supervision and support. Their patient guidance, professional knowledge and rich experience encourage me in all the time through my PhD study. I would also like to thank my previous industrial supervisor, Dr. Ryan Marks for his suggestions and encouragement, and my industrial mentor, Dr. Yikun Wang, for her support on my studies.

I would like to offer my special thanks to Dr. Han Yang, Dr. Jialin Tang and Dr. Linghao Zhou for their support throughout my years of study, as well as their help in my life. I also thank to Ms. Catherine Leahy, Dr. Qing Lu, Dr. Channa Nageswaran, Ms. Lu Zhao and my colleagues at TWI for the assistance in my experiments.

My appreciation also goes out to Lloyd's Register Foundation, Brunel University London and the National Structural Integrity Research Centre (NSIRC) for providing funding for this study.

I am very grateful to my landlord, Ms. Chuxi Zhao and her family for their help in my life, especially during the difficult period of the epidemic.

Thanks to all the people who helped and cared about me.

Last but not the least, I would like to thank my parents and my boyfriend for their unwavering support and belief in me.

Declaration

The candidate confirms that the work submitted is her own and that appropriate credit has been given where reference has been made to the work of others.

This copy has been supplied on the understanding that it is copyright material and that no quotation from the thesis may be published without proper acknowledgement.

The right of Dandan Liu to be identified as the author of this work has been asserted by her in accordance with the Copyright, Designs and Patents Act 1988.

Some parts of the work have been published in the following article:

1. **Liu, D.**; Wang, B.; Yang, H.; Grigg, S. A Comparison of Two Types of Acoustic Emission Sensors for the Characterization of Hydrogen-Induced Cracking. *Sensors* 2023, *23*, 3018. https://doi.org/10.3390/s23063018

2. **Liu, D.**, Yang, H., Wang, B., & Grigg, S. Hydrogen induced cracks monitored with Acoustic Emission under the laboratory condition. 2023. *35th European and 10th International conference on Acoustic Emission testing, EWGAE & ICAE 10.*

List of Abbreviations

Abbreviations	Meaning
AD	Amplitude Difference
AE	Acoustic Emission
AIC	Akaike Information Criterion
CNTs	Counts
CoV	Coefficient of Variance
DIC	Digital Image Correlation
DPC	Density Peaks Cluster
ECHC	Electrochemical Hydrogen Charging
FE(M)	Finite Element (Method)
FFT	Fast Fourier Transform
GMM	Gaussian Mixed Model
HE	Hydrogen Embrittlement
HEDE	Hydrogen-enhanced decohesion model
HIC	Hydrogen Induced Cracks
HPT	Hydrogen Pressure Theory
IFFT	Inverse Fast Fourier Transform
KNN	k-Nearest Neighbours
LEFM	Linear Elastic Fracture Mechanics
ML	Machine Learning
NACE	National Association of Corrosion Engineers
NDT	Non-Destructive Testing
OM	Optical Microscope
PCA	Principle Component Analysis
PE1	Energy proportion of Part 1 (Frequency range in 0-100kHz)
PE2	Energy proportion of Part 2 (Frequency range in 100-200kHz)
PE3	Energy proportion of Part 3 (Frequency range in 200-300kHz)
PE4	Energy proportion of Part 4 (Frequency range in 300-400kHz)
PLB	Pencil Lead Break
PZT	Lead zirconate titanate
RT	Rise Time
SA	Simplex Algorithm
SCC	Stress Corrosion Cracks
SHM	Structure Health Monitoring
SNR	Signal-to-Noise Ration
SOM	Self-Organized Mapping
TDOA	Time Difference of Arrivals
TOA	Time of Arrival
UT	Ultrasonic Testing
WT	wavelet transform

List of tables

List of figures

Contents

1 Introduction

1.1 Background

Hydrogen Induced Cracking (HIC), a type of Hydrogen Embrittlement (HE), is a widespread failure phenomenon in metal and alloy materials. It is a brittle fracture caused by the infiltration and diffusion of hydrogen atoms or hydrogen ions in the internal structure of a material. The phenomenon that occluded hydrogen will influence the properties of iron or steel when exposed to acid environment was first identified by W. H. Johnson in 1875 [1], and was confirmed by Reynolds [2]. The intrusion of hydrogen severely degrades the mechanical properties of metal materials. This results in a significant shortening of the material's fatigue life and a significant reduction in impact toughness values. However, the mechanism of hydrogen assisted degradation was not clear. In the 1940s, Andrew et al. [3] discovered the principle of HE in steel when investigating the fracture of the main shaft of an aircraft engine. Numerous theories have been suggested due to the complicated nature of HE [4–8]. In addition, ways of removing hydrogen from steel and preventing the failures from HE have also been widely studied [9–13].

Nevertheless, HIC is still found to occur in steel structures in long-term service, which has caused through thickness cracks, resulting in serious equipment damage and casualties. In 2013, the catastrophic failure of bolts and anchor rods of San Francisco Bay Bridge was found after only two weeks of service [14], leading to $25 million for repair. In an oil refinery in Chicago, USA, 1975, a 15cm stainless steel pipe suddenly burst, causing an explosion and fire, resulting in a long-term shutdown [15]. In 2014, Sarawak, eastern Malaysia, experienced a powerful explosion because of a ruptured natural gas pipeline [16]. This incident caused a loss of nearly £900 million to Malaysia's National Petroleum Corporation. In the aforementioned cases, HE had been identified as the cause of crack formation. Cumulative damage in the oil and gas industry due to HIC induced failure is estimated to be more than $1 billion annually [17]. At the same time, revenue losses due to repair operations exceed $10 billion annually [18]. Generally, the average annual cost for pipeline maintenance and repair tools is between $5000 and $20000 [19]. In addition to the oil and gas industries, due to the emerging application of hydrogen energy at present, the problems of HE in the

storage tank or transportation pipelines of hydrogen fuel are attracting increasing attention [20-21].

It is impossible to completely isolate contact with hydrogen during the preparation and use of steel. However, HIC cannot be eliminated once it starts in a material, thus after HIC occurs, the state and development of the crack needs to be detected to judge the integrity of the structure and monitored regularly to understand the updated status for the remaining service life of the structure to prevent sudden failures.

1.1.1 Hydrogen Induced Cracking

Hydrogen cannot enter the internal material in the form of its diatomic molecule (H_2) because of the big size, but it will break down into hydrogen atoms when the environment temperature is high. The decomposed hydrogen atoms are adsorbed on the metal outer surface. After passing through the surface into the material, hydrogen atoms will dissolve into the lattice and can jump to other lattices in any direction. Another common way that hydrogen enters materials is in the case of wet environments. In the presence of water, hydronium ions (H^+H_2O) are formed by the ionized hydrogen ion. They gain electrons when they migrate to the metal surface. Hydrogen atoms are then adsorbed on the metal outer surface and then pass through into the inner layers. Figure 1.1 shows these two processes of hydrogen atoms entering the interior of the structure. There exist many defects in materials that can trap hydrogen atoms, collectively called hydrogen traps, such as crystal defects (vacancy, dislocation, grain boundary, etc.), the second phase, micro-pores, etc. [22].

Since the strain field energy caused by external loading interacts with the hydrogen strain field around the hydrogen trap, it attracts hydrogen atoms and some will gather inside the traps to rebind together into the gas format as H_2. The process continues and the pressure of H_2 increases, leading to the initiation of micro-cracks and their subsequent propagation under the combined action of hydrogen pressure and plastic deformation.
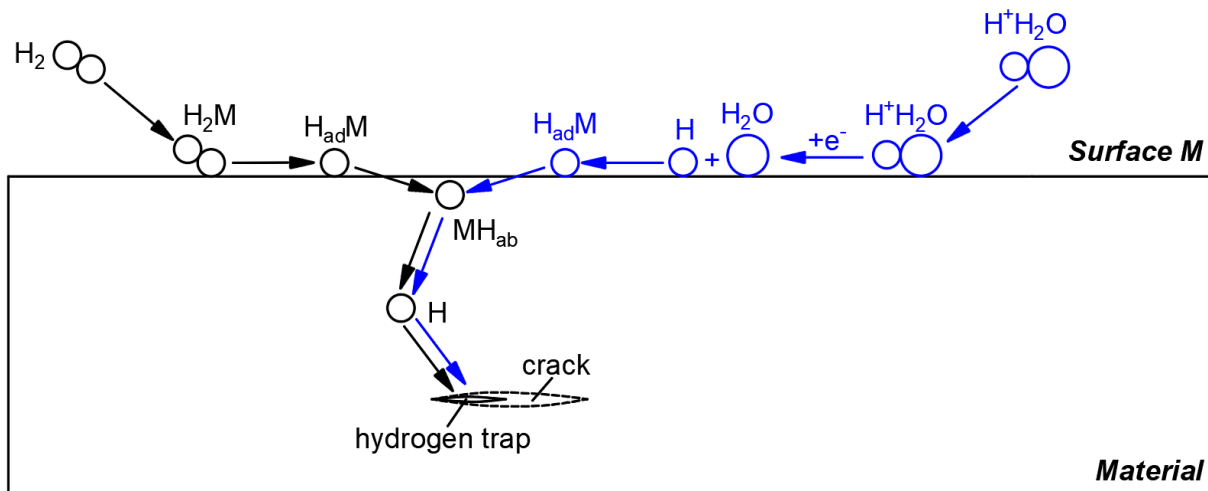
Figure 1.1 The generation of Hydrogen Induced Crack

The sources of hydrogen in steels can be divided into two categories: hydrogen absorbed during manufacture and hydrogen absorbed during service. Specific circumstances that steels may absorb hydrogen can be derived from one or more of the situations as follows [23]:

(1) During the manufacture of steel, hydrogen can be absorbed to varying degrees in the processes, like smelting, pickling, electroplating, welding (especially with the wet electrodes in Manual Metal Arc Welding), etc.

(2) Cathodic protection is often used to inhibit corrosion during the service of steels. However, over-protection, caused by improper cathodic protection, or induced current can lead to excessive atomic hydrogen formation at the cathode.

(3) Direct contact in service with hydrogen gas (H_2), or hydrogen sulfide (H_2S) such as exist in oil and gas pipelines, liquid hydrogen storage vessels, etc. leading to the absorption shown in Figure 1.1.

A series of precautions have been proposed aiming to reduce the hydrogen ingress during the manufacturing and heat treatment processes of steels. For example, corrosion inhibitors are added to hinder discharges of hydronium ions during pickling; dehydrogenation treatments are applied for plating parts to remove most of the hydrogen inside the material [24]. As for in-service steels, especially steels used as energy pipelines in the petroleum refining industry, they are inevitably in contact with hydrogen. Measures have been taken to improve the HIC-resistance of steels to mitigate the potential dangers of crack development. For instance, relieving residual stresses by heat treatment to reduce the number of hydrogen traps in the steel or

coating the steel surface with low hydrogen solubility to reduce hydrogen infiltration [25].

Generally speaking, there are three stages of HIC development according to the different degrees of damage, which is displayed in Figure 1.2 [26]. When the hydrogen-filled cavity is close to the surface, plastic deformation is observed on the surface, resulting in hydrogen blisters. Then, with the hydrogen pressure gradually increasing, multiple relatively straight cracks are formed inside material, or under the large blisters, whose direction is generally parallel to the metal surface. Finally, the interconnection of adjacent HIC on different layers will produce stepwise cracks along the thickness direction. This is the worst situation, which will reduce the effective thickness, potentially resulting in the equipment failure.
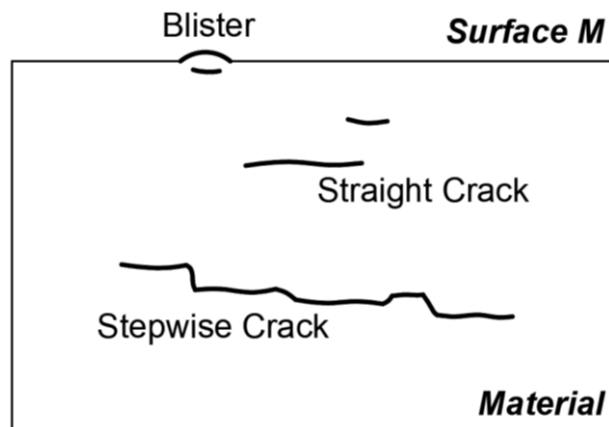
Figure 1.2 Three kinds of Hydrogen Induced Cracks

Most of the material used for energy pipelines is currently low-alloy high-strength steel (although the polymer alternatives are being explored). As with this type of material, the common failure modes include stress corrosion, corrosion fatigue and HIC. Among these failures, HIC leads to a drastic reduction of the steel pipes' life span. Moreover, it has been found that some HIC can also occur under low stress scenarios [27].

1.1.2 Structure Health Monitoring

In additional to energy pipelines, there are many infrastructures that are closely related to our lives, such as railways, bridges, airplanes, buildings and others. When these facilities are built, engineers will predict their approximate lifetimes. However, during this time, a variety of situations can occur to damage the structure to reduce their lifetime, like strong winds, acid rain, earthquakes etc. If the damage is ignored, they would deteriorate and ultimately could cause major accidents and threat to personal

safety. For example, in 1995, a department store building in South Korea collapsed into the ground within 20 seconds. It was a major casualty accident that caused 502 deaths and nearly 1,000 injuries [28]. In 2007, the Mississippi River Bridge in the United States collapsed suddenly due to severe corrosion, causing at least 8 deaths and dozens of injuries [29]. In addition, in other industrial fields, there are many serious consequences or great economic losses caused by infrastructure or equipment disrepair. Thus, assessing the real-time status of these facilities has been the focus of many industrial and academic studies. Damage is inevitable during long-time use-cases and often it cannot be entirely eliminated, so the most effective way is prevention. For large in-service structures, regular inspections should ideally be carried out without affecting its normal operation, which otherwise will be costly and time-wasting.

Non-Destructive Testing (NDT) methods inspect and test the performance, status and defects of the internal and surface of the specimen through analysing the changes of heat, sound, light, electricity and magnetism caused by abnormal internal structure or the existence of defects with modern technology and equipment. There are many NDT methods that have been applied for inspecting structures for damage, such as Ultrasonic Testing (UT), Radiographic Testing, Magnetic Particle Testing, Penetrant Testing, Eddy current Testing, etc. Among them, UT is a well-established way to detect damages of large structures without the restrictions of surface smoothness, structural complexity, location of defect, material conductivity and others. It is typically applied for getting the information about the changing properties of the structure by detecting and analysing ultrasonic waves. The way to get the information by detecting ultrasonic waves can be divided to two categories: active and passive [30]. Conventional UT is an active system – ultrasonic probe is adopted to transmit ultrasonic pulses and measuring the response. On the contrary, passive systems, such as Acoustic Emission (AE), don't require external inputs but the structure itself needs some changes, like the propagation of a crack which in turn produces an ultrasonic wave. Both techniques have been used in oil and gas pipeline damage detection cases. However, conventional UT methods are often used for regular or intermittent testing, which requires setting up equipment every time. This is not only time-consuming but may also miss the occurrence of damage. Ultrasonic probes can be left in-suit on structures theoretically, but it will cost a lot which is not suitable for long-term monitoring. Moreover, it is difficult to carry out UT on specimens with complex shapes

or irregular shapes, and the location, orientation and shape of defects will have a certain impact on the detection results.

In order to apply continuous monitoring and to identify damage early to ensure safety and cost reductions, Structural Health Monitoring (SHM) is used. SHM system can be interpreted by analogy with the physical examination of human body. For humans, if we feel unwell somewhere, the nervous system is capable of alerting the area of concerns. This enables the doctor to test our body by medical equipment, like stethoscope, B-ultrasound, etc. to find the place where the problem exactly is, and give us suggestions. Similarly, the SHM system is a special engineering examination developed for the health of the structure which is a process of testing, diagnosing and evaluating structural integrity. With SHM, a warning of serious problems can be obtained by assessing the information collected and pre-cautions can be subsequently implemented. For instance, traffic will be restricted to avoid over-heavy loads if it is detected that the safe bearing capacity of a bridge decreases. Besides, the lifetime of the structure can be predicted and maintained accurately based on its condition. As for the economic level, cost can be saved by avoiding large maintenance operations. SHM has been used for bridge monitoring since the 1980s, and more and more large structures have been equipped with SHM systems in the world, such as Stonecutters Bridge in Hong Kong, the offshore oil platform in the Danish North Sea [31], "Lakhta Center" tower in St. Petersburg, France [32].

The goal of SHM is incipient damage detection in real-time which also can be divided into four levels from easy to difficult:

(1) Identifying the existence of damage: the occurrence of damage can be confirmed.
(2) Identifying the location of the damage: the accurate locations of damage can be circled.
(3) Identifying the extent of the damage: the classification and the development of damage can be determined.
(4) Analysing the impact of the damage on the structure: the operating requirements and the residual life of structure can be deduced.

However, the approximate location of the damage is not known in advance before testing the structure. In addition, the application objects of SHM system are generally

large structures, which cannot be disassembled into small parts for separate inspection. In order to achieve the regular inspection, the operation of the system can be roughly designed as the following four processes:

(1) Periodic sampling by Non-Destructive Technology for structural response
(2) Extraction of damage sensitive indicators
(3) Statistical analysis of damage sensitive indicators
(4) Determining current structural health and providing suggestions

For the surveillance and detection of structural damage, the collection of data carrying damage information is the first and crucial step. Some Non-Destructive Technologies can be used in SHM system, such as Acoustic Emission, vibration analysis, strain gauging and others.

In this study, for monitoring of energy pipelines, AE technology was chosen for the SHM system. AE is the phenomenon of radiation of acoustic (elastic) waves in solids that occurs when a material undergoes irreversible changes in its internal structure, such as crack growth. These energy-carrying waves propagate through the structure to be captured by the AE sensor system. The sensors do not measure damage directly, instead converting the waves into electrical signals, then the damage information can be obtained by analysing the features of captured signals.

The AE test process is shown in Figure 1.3. There will generate acoustic wave when the damage inside develops, which will be captured by AE sensors during propagating. It is then converted into an electrical signal by the piezoelectric crystal in the sensor and an amplifier. The electric signal is sent to AE equipment to be conditioned, analysed and evaluated.
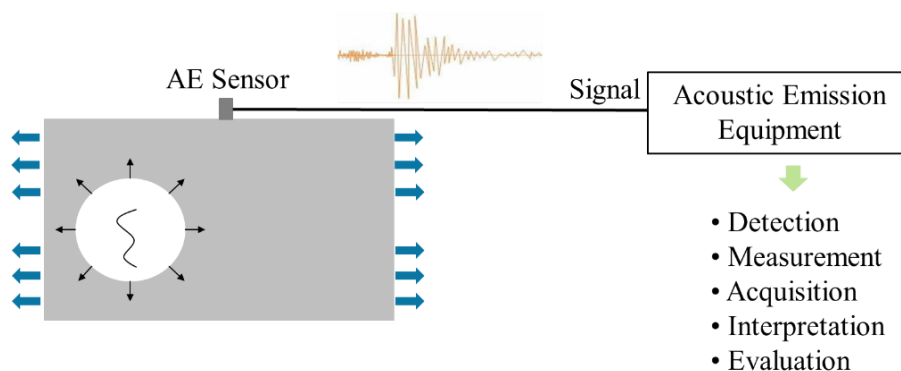
Figure 1.3 Simple schematic of AE technology

Other methods, such as vibration and strain measurement, can only be used to simply flag issues and track the overall changes in structures. Compared with other methods, the reasons why AE technology was chosen for this study are as follows [33]:

(1) Global monitoring

AE can not only detect damage within the local area but whole structures with a distributed sensor array even if the structure is very large, such as an airplane, bridges, etc. Moreover, it has been demonstrated that monitoring using AE is not significantly limited when used on complex geometries. With favourable conditions, only a handful of sensors are required to capture and monitor the AE activity of a structure under loading without scanning point by point (as would be the case with a more conventional NDT method).

(2) Continue dynamic monitoring

AE only requires specific sensors to test the condition of structure. Besides, AE requires less power and therefore this technology is able and suitable for continuous monitoring. In addition, because the captured elastic waves were developed by the damage itself, the whole damage processes in materials can be observed through continuous monitoring.

(3) Locating the damage

Because AE is related to the dynamic processes or sudden changes inside a material, the active area of damage can be highlighted in the acquired signals. Therefore, by using sensor arrays it is possible to locate the source of the AE event and hence the location of the damage.

(4) Identifying the damage

As different damage mechanisms emit AE signals with different characteristics, the types of damage can be characterised by clustering signals with similar features.

Although AE technology has made great progress in recent years, there are still some difficulties and limitations in SHM systems which use AE technology to collect information:

(1) The noises such as those caused by fluid-structure interactions, friction or machinery may influence the result of AE signal, for instance, taken as signals of damage by misidentification.

(2) The amount of data taken would be huge with continuous real-time monitoring, and every data is unique resulting from the irreversible propagation of crack. Therefore, there is a data management issue.

(3) Wave propagation would be affected as the waves propagate through layers of materials with varying properties, and signal detections at the surface of the structure are altered by the use of piezoelectric sensors.

During the development of AE, some countermeasures for these problems have been proposed, such as minimizing environmental noise, using AE sensors that are not sensitive to background noise signals, reducing the storage data by statistical measure, and so on [33-35]. All in all, AE is important in monitoring the strength and integrity of large structures as the unique sensitivity to defect initiation and expansion and the unique function of dynamic detection intensity. In this study, AE technology has been chosen to monitor HIC damage, aiming for application in energy pipeline assets, such as tanks, reservoirs, commonly used oil and gas pipelines, etc. Due to the small curvature of these structures, waves can be regarded as propagating on the plate structures. Therefore, this investigation was carried out on plates to obtain the basic understanding of HIC occurrence and development. Through the analysis of AE data, the characteristics of signal emitted by HIC propagation and the source locations can be investigated with different experimental parameters, such as the specification of the specimen, the position of the sensor relative to the AE event source, the type of AE sensors, etc.

1.2 Aims and Objectives

The aim of this work is to investigate HIC behaviour in energy pipeline material monitored with AE technology.

The main objectives of this research are as follows:

• To design an experimental procedure which can identify the HIC signals from others, such as signals from H_2 evolution, uniform corrosion and crevice corrosion.

• To better understand the signal propagation in specimens with different geometric profiles and specifications, as well as the influence on signal recognition and source location.

• To investigate an automatic unsupervised cluster method for signal clustering under this experimental setup.

• To verify the universal applicability of the proposed automatic cluster method by different experimental parameters, such as increasing external hydrogen concentration, increasing the number of non-HIC signals.

• To investigate the influence of specimen's thickness on signal propagation and expression.

• To investigate the influence of different types of sensors on the expression of signals.

• To simulate the HIC signals on complex structures and build a Finite Elements Model for more accurate source localisations.

1.3 Novelty Statement

The novelty of this work is given as,

• The way to identify HIC signals from noise-mixed signals accurately. The characteristics of the signals in the Time/Frequency domains were summarised under the experimental setup of this study.

• A new reliable two-step GMM cluster method with the input of signals' energy spectrum for signal clustering. It is suitable for clustering signals with different frequency distributions.

• A new investigation on the influence of nano30 and VS150-RSC sensors on the expression of signals. This provided suggestions on the selection of sensor types for practical application based on different purposes.

• An overall description about the effect of specimen's thickness on the signal types and signal propagation.

• Comparison of HIC signals propagating in simple and complex structures.

• The feasibility of source localisation with simulated delta-T mapping with real AE damage events.

1.4 Thesis Organisation

This thesis was devised in seven chapters.

Chapter 1 introduced the background information about Hydrogen Induced Cracking phenomenon and Structural Health Monitoring technology. The significance and objectives of investigating HIC by Acoustic Emission were explained.

Chapter 2 provided the relevant theory about the occurrence of HIC and waves propagation. It gave an emphasis on research done so far on signal processing, such as pattern recognition and signal clustering methods. In addition, the experimental method for generating HIC under laboratory conditions was covered as well.

Chapter 3 presented the procedures of ECHC-HIC tests in details to identify signals from various damage mechanism and extract the characteristics from Time/Frequency domain of HIC signals. Besides, the fundamental understanding about signal propagation and source localisation of HIC events on carbon steel plates with different 2D specification was provided.

Chapter 4 investigated methods to cluster mixed signals automatically. A two-step GMM cluster method was proposed with inputs of energy spectrum and duration, energy and counts. The universal applicability of this method was verified with tests' results by changing experimental parameters, i.e. the external hydrogen concentration, the amount of noise signals.

Chapter 5 discussed the influence of specimens' thickness on the wave propagation. Two types of sensors, Nano 30 and VS150-RSC were placed on a specimen simultaneously for observing the difference of signal expression. Subsequently, signal characteristics and source localisations were analysed and compared carefully. In addition, Ultrasonic Testing technology was applied for valuing the analysis results given by AE technology.

Chapter 6 investigated the ECHC-HIC test on a plate with a hole and a seam. The expressions of HIC signals propagating through a hole and a seam were compared to that through a homogeneous way. In addition, FE model for simulating a delta-T mapping was carried out to prove the better source localisations. The model for simulating signals from HIC was established and was then verified with experimental results.

Chapter 7 gave the conclusions of this work and some suggestions for future work.

2 Literature Review

2.1 Theory of Elastic Waves

An elastic wave, a kind of stress wave, is a transfer form of stress and strain caused by disturbance or external force in an elastic medium. There is an interactive elastic force between the particles in the elastic medium. After a certain mass point leaves the equilibrium position due to disturbance or external force, the elastic restoring force causes the mass point to vibrate, which causes displacement and vibration of surrounding mass points, so the vibration propagates in the elastic medium and is accompanied by energy transfer.

Acoustic Emission (AE) technique detects the elastic waves. In engineering materials, some common sources of AE are initiation and growth of cracks, yielding and others in metals, as well as fibre failure, failure of bonds, and pull-out in composites [36]. In complex situations, AE sources may come from a combination of multiple mechanisms. In a broad sense, the elastic waves generated by mechanical damages have the same properties as the elastic waves generated by rock crack propagation and earthquakes [37]. The initial AE source model concept was derived from seismology as seismic waves are detected by seismographs when they spread through the earth [38]. Similarly, it is worth to note that the elastic waves can only be emitted by active or growing cracks.

The waves detected in Structure Health Monitoring (SHM) applications are generally ultrasonic waves, which have a frequency higher than 20kHz. Ultrasonic waves can be divided into Bulk Waves and Surface Waves according to the different propagation medium.

2.1.1 Bulk Waves

A bulk wave is an elastic wave in an elastic medium which propagates in the bulk on the material where there are limited or no influences of the boundaries. It can therefore be thought of as propagating in an infinite medium. According to the relationship between the propagation direction and the particle vibration direction, the bulk wave can be divided into longitudinal waves and transverse waves as shown in Figure 2.1[39]. Longitudinal waves (Figure 2.1(a)) are pressure waves, in which the vibration direction of the particle is parallel to the wave propagation direction. It is also called

Primary wave (P-wave) because they travel faster than other waves. Transverse waves (Figure 2.1(b)) are shear waves, also called Secondary waves (S-waves), in which the vibration direction of the particle is perpendicular to the wave propagation direction. S-waves only exist in solids, as fluids (liquids and gases) do not support shear stresses.
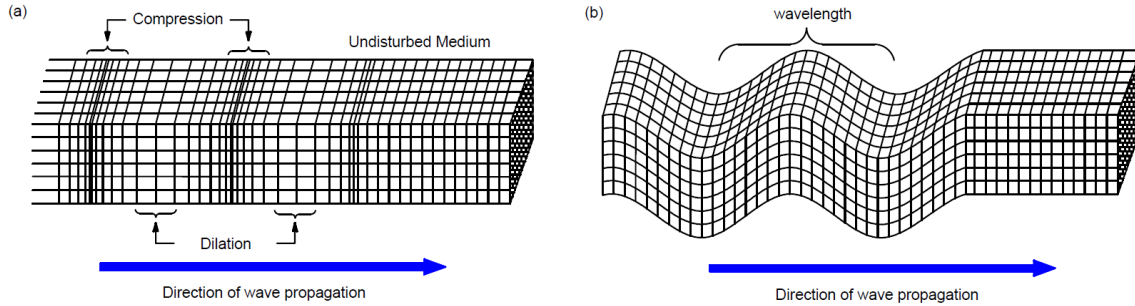
Figure 2.1 The schematic diagram of bulk waves (a) Longitudinal waves (b) Transverse waves [18]

The relation of the velocity for longitudinal waves in a solid is shown in Equation (2.1) [40].

$$c = \sqrt{\frac{E}{\rho}} \tag{2.1}$$

Where E is the Young's modulus and ρ is density of the material.

However, it is only suitable for the waves propagating axially in a thin rod, where the thin means that the diameter of the rod is smaller than the wavelength [41]. As for the waves propagating in isotropic and homogeneous solids, it is basically derived from the characteristics of elastic medium.

It is known from Hooke's law that the stress is linearly related to the strain in the linear elastic range of a medium. When a medium is under the 3D stress, the stress-strain relation is shown in Equation (2.2).

$$\sigma_{ij} = \sum_{k=1}^{3} \sum_{l=1}^{3} c_{ijkl}\, \varepsilon_{kl}, i, j = 1,2,3 \tag{2.2}$$

Where σ is the stress tensor, ε is the strain tensor, and c is a fourth-order elastic tensor.

However, this equation represents the general stress-strain relation for a heterogeneous anisotropic medium. For an isotropic elastic medium, the elastic tensor is shown in Equation (2.3).

$$c_{ijkl} = \lambda\delta_{ij}\delta_{kl} + \mu(\delta_{ik}\delta_{jl} + \delta_{il}\delta_{jk}) \tag{2.3}$$

Where δ is the Kronecker delta, λ and μ are the Lamé constants, which are related to the Poisson's ratio ν and Young's modulus E. The relation among them are shown in Equations (2.4) and (2.5).

$$\nu = \frac{\lambda}{2(\lambda + \mu)} \tag{2.4}$$

$$E = \frac{\mu(3\lambda + 2\mu)}{\lambda + \mu} \tag{2.5}$$

Substituting the Equation (2.3) into the Equation (2.2), the stress-strain relation for an isotropic elastic medium can be obtained, as expressed in Equation (2.6).

$$\sigma_{ij} = \lambda(\nabla \cdot \boldsymbol{u})\delta_{ij} + 2\mu\varepsilon_{ij}, i, j = 1,2,3 \tag{2.6}$$

Where **u** is the displacement vector, ∇ is the Hamiltonian.

In addition, according to Newton's second law of motion, *the total force = mass × acceleration*, the equation of motion of a volume or the dynamic force equilibrium equation is expressed by Equation (2.7). Note that the *force* is consisted of both the traction **T** (stresses) and the body forces.

$$\sum_{j=1}^{3} \frac{\partial \sigma_{ij}}{\partial x_j} + f_i = \rho \frac{\partial^2 u_i}{\partial t^2}, i = 1,2,3 \tag{2.7}$$

Where x is the position of an element of volume, $\frac{\partial^2 u_i}{\partial t^2}$ is the acceleration, f_i is the body force. Therefore, if the Equation (2.6) is substituted into the Equation (2.7), and disregarding the body forces, the equation of motion for an isotropic elastic medium can be written as Equation (2.8) in vector form.

$$(\lambda + \mu)\nabla(\nabla \cdot \boldsymbol{u}) + \mu\nabla^2\boldsymbol{u} = \rho \frac{\partial^2 \boldsymbol{u}}{\partial t^2} \tag{2.8}$$

2.1.2 Surface Waves

In SHM technology, surface waves are typically used rather than bulk waves since structures monitored with SHM are not infinitely thick in practice. Surface waves are elastic wave which propagates along the surface of an elastic medium or on the

interface of two different elastic mediums. It only exists on the surface or near the interface. The biggest different between surface waves and bulk waves is the boundary conditions of the former. The wave equation governing surface waves is the same set of partial differential wave equation governing Bulk waves, which is also Equation (2.8). Based on the study of bulk waves, the wave solutions at the boundaries of surface waves can be derived.

2.1.2.1 Rayleigh Waves

Rayleigh wave is a common surface wave and widely used in SHM for characterizing materials, like the presence of cracks and the status of structures. It travels on a free surface of a semi-infinite solid, such as geotechnical, mine, highway, and so on. The schematic diagram of Rayleigh waves shown as Figure 2.2 [42]. It can be seen that Rayleigh waves include both longitudinal and transverse motions. Besides, the particle disturbance amplitude decays rapidly as the distance between the particle and the interface increases, this is also a feature of surface waves.

Partial Motion

Direction of wave propagation
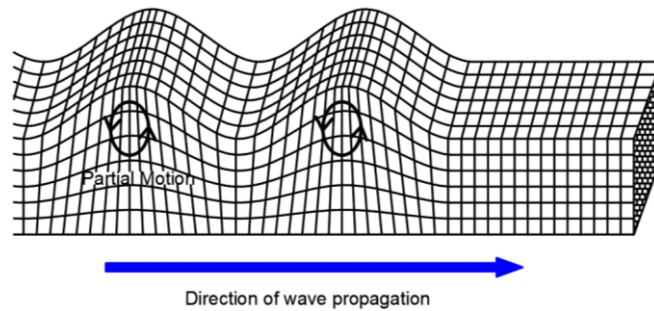
Figure 2.2 The schematic diagram of Rayleigh waves [42]

Based on the Helmholtz decomposition, the displacement vector **u** can be regarded as the sum of an irrotational vector field ϕ and a solenoidal vector field $\boldsymbol{\psi}$:

$$\boldsymbol{u} = \nabla\phi + \nabla \times \boldsymbol{\psi} \tag{2.9}$$

By substituting Equation (2.9) into Equation (2.8), an equation can be obtained and then simplified as Equation (2.10).

$$\nabla\left[(\lambda + 2\mu)\nabla^2\phi - \rho\frac{\partial^2\phi}{\partial t^2}\right] + \nabla \times \left[\mu\nabla^2\boldsymbol{\psi} - \rho\frac{\partial^2\boldsymbol{\psi}}{\partial t^2}\right] = 0 \tag{2.10}$$

Two simple wave equations can be separated from Equation (2.10), which are for longitudinal waves (Equation (2.11)) and transverse waves (Equation (2.12)).

$$\frac{\partial^2 \phi}{\partial t^2} = c_L^2 \nabla^2 \phi \tag{2.11}$$

$$\frac{\partial^2 \boldsymbol{\psi}}{\partial t^2} = c_T^2 \nabla^2 \boldsymbol{\psi} \tag{2.12}$$

Where c_L and c_T are the velocities of longitudinal waves and transverse waves travelling in the infinite elastic medium which are given by Equations (2.13) and (2.14), respectively [43].

$$c_L = \sqrt{\frac{\lambda + 2\mu}{\rho}} = \sqrt{\frac{E(1-v)}{\rho(1+v)(1-2v)}} \tag{2.13}$$

$$c_T = \sqrt{\frac{\mu}{\rho}} = \sqrt{\frac{E}{2\rho(1+v)}} \tag{2.14}$$

Rayleigh waves have a speed slightly less than shear waves by a factor dependent on the elastic constants of the material. The value of its velocity is $0.919c_T$ [44] in a semi-infinite elastic medium.

2.1.2.2 Lamb Waves

If the wavelength of a Rayleigh wave is bigger than the thickness of a plate, then Lamb waves forms. Lamb waves were first analysed and described by Horace Lamb in 1917 [45]. Lamb waves are special elastic waves which also consist of longitudinal and transverse waves that only travel in the horizontal direction. According to the different distribution patterns of particle vibration displacement, there are two kinds of modes of Lamb waves: symmetrical Lamb waves (S mode) and anti-symmetric Lamb waves (A mode), as shown in Figure 2.3. It can be regarded as a wave which propagates horizontally on a solid plate whose thickness is 2d and both surfaces are considered traction free.

With different plate thicknesses and excitation frequencies, Lamb waves show different propagation modes. The velocity of Lamb waves depends on the frequency is termed velocity dispersion. There are different orders for modes of Lamb waves, which are usually represented by S_0, S_1, S_2... for symmetrical Lamb waves, and A_0, A_1, A_2... for antisymmetric Lamb waves. This phenomenon is called the multimodality of Lamb waves [46]. Therefore, when using ultrasonic Lamb wave technology for

detection, the appropriate Lamb wave mode must be selected based on the dispersion curve.

The propagation characteristics of Lamb wave can be described by the phase and group velocities, respectively. The phase velocity is defined as the propagation velocity of a certain phase of the waveform, while the group velocity can be understood as the propagation velocity of the wave envelope. Both characteristics have their own dispersion curves in specific propagation media.
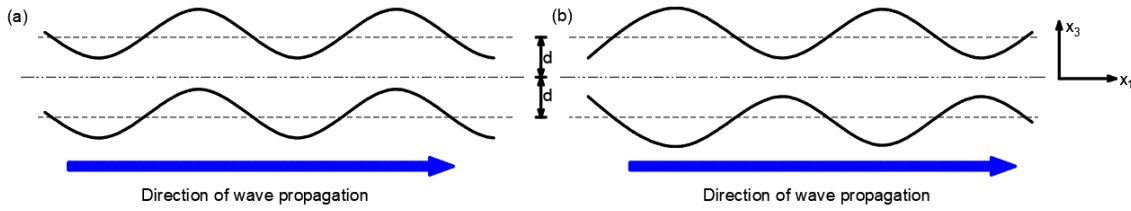
Figure 2.3 Modes of Lamb Waves (a) Anti-symmetric Lamb Waves (A mode) (b) Symmetrical Lamb Waves (S mode)

Longitudinal and transverse wave equations for plane strain can be obtained which is analogous to the derivation of the Rayleigh wave equations [47]:

$$\frac{\partial^2 \phi}{\partial x_1^2} + \frac{\partial^2 \phi}{\partial x_3^2} = \frac{1}{c_L^2} \frac{\partial^2 \phi}{\partial t^2}, \qquad longitudinal\ waves \qquad (2.15)$$

$$\frac{\partial^2 \boldsymbol{\psi}}{\partial x_1^2} + \frac{\partial^2 \boldsymbol{\psi}}{\partial x_3^2} = \frac{1}{c_T^2} \frac{\partial^2 \boldsymbol{\psi}}{\partial t^2}, \qquad transverse\ waves \qquad (2.16)$$

By the method of Potentials, the solutions to these equations for displacement were found with symmetric and antisymmetric modes. At the same time, by applying the boundary conditions [47]:

$$\sigma_{31} = \sigma_{33} \equiv 0\ at\ x_3 = \pm d \qquad (2.17)$$

the dispersion equations can be obtained for symmetric and antisymmetric mode as Equations (2.18) and (2.19) [47]:

$$\frac{tan(qd)}{tan(pd)} = -\frac{4k^2 pq}{(q^2 - k^2)^2}, \qquad for\ symmetric\ mode \qquad (2.18)$$

$$\frac{tan(qd)}{tan(pd)} = -\frac{(q^2 - k^2)^2}{4k^2 pq}, \qquad for\ antisymmetric\ mode \qquad (2.19)$$

Where p and q are given by [47]:

$$p^2 = \frac{\omega^2}{c_L^2} - k^2 \text{ and } q^2 = \frac{\omega^2}{c_T^2} - k^2$$

Where ω is the circular frequency, and k is wavenumber which is defined as the number of wave cycles per unit length in the direction of wave propagation. According to the relationship between phase velocity c_p and k, i.e., $k = \frac{\omega}{c_p} = \frac{2\pi f}{c_p}$, the phase velocity relationship curve can be depicted with $f \cdot d$ and c_p.

As for the group velocity c_g, it can be derived from c_p and the result is shown in Equation (2.20).

$$c_g = c_p^2 \left[c_p - (fd) \frac{dc_p}{d(fd)} \right]^{-1} \tag{2.20}$$

Where f is the frequency.

For steel plate - tanks, pressure vessels, pipes and other structures that can be regarded as infinite plates, Lamb wave theory is the prime theory for explaining the signal forms and propagation velocities that are observed when conducting AE testing.

2.2 Signal Acquisition

A sensor is a device that produces an output signal for the purpose of sensing a physical phenomenon. It will respond to input quantities and convert them into an output signals which can be read by instruments. For the surface wave that causes the dynamic motion in this study, the output signal is typically an electric signal produced by a piezo-electric element installed in an AE Sensor. However, due to the weak signals, there are normally pre-amplifier and main amplifier applied which improve the Signal-to-Noise Ratio (SNR). In the acoustic emission system, the pre-amplifier plays an important role, in which the noise of the entire system is determined by the performance of the pre-amplifier. The pre-amplifier can be an integral part of the sensor or an external device connected to the sensor. In addition, the irrelevant background or environment noise should be removed as much as possible. Therefore, after amplifying the signals, a filter is necessary to raise the SNR. After that, the signals are acquired and recorded in the software through the acquisition system and the host computer.

In a set of monitoring system with AE technology, the performance of the sensor fundamentally and directly influences the acquired signals. An AE sensor is typically composed of the following parts: wear plate, piezoelectric element, connector and a case, which is shown in Figure 2.4.
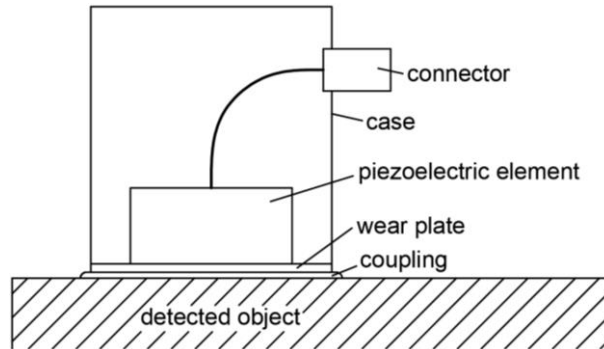
Figure 2.4 Schematic of an AE sensor

Piezoelectric element is the core part of an AE sensor, and plays a crucial role in the motion-electric signal conversion process. Piezo-electricity is a characteristic of certain solid materials, such as crystals, ceramics, animal bones, etc., that can generate a voltage between its two ends when pressure is applied. This is called the piezoelectric effect. Lead zirconate titanate (PZT) piezoelectric ceramic is a common choice because of its low cost, high sensitivity and selective frequency responses [48]. The relation of the resonant frequency f and the thickness d of a piezoelectric element is expressed by: $fd = \frac{v}{2}$, where v is the longitudinal velocity in the medium [49].

An AE sensor that is sensitive to signals in a certain frequency band is called a resonant AE sensor. Generally, a sensor with the resonant frequency at 150kHz is typical for monitoring the damage in metal structures. However, the thickness of the material and its type may change this. In the case of multiple sources or unclear source-related mechanical mechanisms, a broadband AE sensor may be used to better acquire signals over a wider frequency range, which is closer to the real signals. To achieve this, damping material (also called backing) is applied to broaden the frequency response width of the sensor by loading the piezoelectric element to make it less resonant [50]. The acoustic impedance of the damping material should be well matched to the piezoelectric element. Nevertheless, broadband AE sensors often lack the sensitivity due to the energy absorption by the damping material, when compared with resonant AE sensors [49].

To prevent the piezoelectric element from mechanical damage in service, a wear plate is widely used by adhering it to the piezoelectric element. In addition to its role for protection, a wear plate can promote the transfer of energy between the element and the test surface. Better transmission can be achieved when the following two conditions are satisfied [51]:

(1) The thickness of the wear plate is $\frac{\lambda}{4}$, where λ is the wavelength at interested frequency;

(2) The acoustic impedance of the wear plate is between that of piezoelectric element and the test object.

Acoustic impedance refers to the resistance that the medium needs to overcome when the medium deviates from the equilibrium state when the sound wave is transmitted. The greater the difference in acoustic impedance between two media, the more energy will be reflected at the boundary. For example, at a boundary between a metal and air, there is almost total reflection, whereas between metal and water about 90% is reflected. Several materials can be chosen to fabricate the wear plate for different monitoring purposes and test objects, such as steel, quartz, resin, ceramic. The wear plate can adhere to the piezoelectric element through several ways. Some can be glued together with epoxy-resin–based and certain heat-resistant glues. Others, such as the resins with a filler powder can be applied on the surface of the piezoelectric element, and then polymerized as a protective layer, which can be ground to the ideal thickness [52].

The other side of the wear plate is in contact with the surface of test object. An ultrasound couplant is applied to enable acoustic coupling which can reduce the acoustic impedance mismatch between them for better transmission. The couplant is generally a liquid or gel, such as propriety ultrasound gels used in medical scanners, silicones and even honey (for shear wave sensors).

For PZT AE sensors used in industrial applications, three characteristics of the sensor should be considered: frequency response width, resonant frequency and amplitude sensitivity. These can be affected by the following:

(1) The shape, size, elasticity and piezoelectric constant of the piezoelectric element;

(2) The method of damping the element.

(3) The coupling method used.

Therefore, suitable AE sensors can be selected to monitor damage with different mechanisms in different objects.

2.3 Signal Processing

As discussed in Chapter 1, the aim of SHM is to determine the presence, location, type and extent of the damage in a structure. After signals acquisition, extracting useful and accurate parameters from data is fundamental to understand the damage status. According to these parameters, signals can be recognized whether they derived from the same damage mechanism and individual events can be located.

2.3.1 Signal Features

Figure 2.5 shows a simplified AE waveform. Generally, the important features extracted from it are [53]:

(1) Threshold (T): A threshold amplitude needs to be set to filter the background noise. Only the AE signals with the amplitude higher than the threshold are recorded by the AE system.

(2) Amplitude (A): The maximum voltage of the signal.

(3) Duration (D): The time interval between the first and the last threshold crossings.

(4) Rise time (R): The time interval between the first threshold crossing and the maximum amplitude.

(5) Counts (N): The number of times that the AE signal exceeds the threshold within the waveform's duration.

(6) Energy (E): The area beneath the envelope of the rectified linear voltage-time signal from the sensor within the waveform's duration.

Except for the features from time domain, some features from frequency domain are shown in Figure 2.6:

(1) Peak Frequency: The frequency of maximum power in frequency spectrum.

(2) Frequency Gravity: The frequency at which the spectrum has its centre of gravity, which is also called spectral centroid.
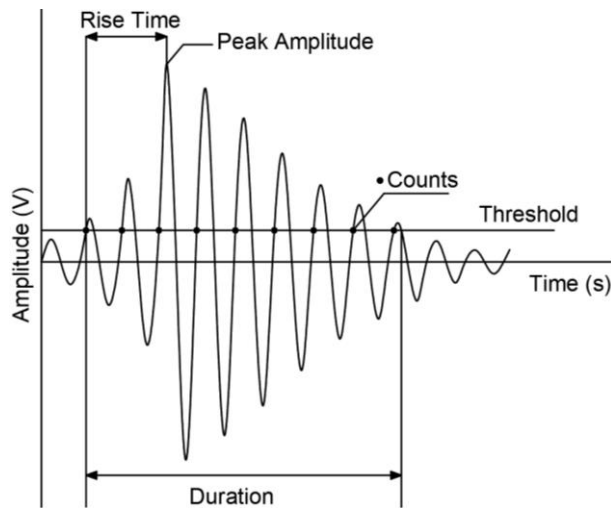
Figure 2.5 A typical AE waveform
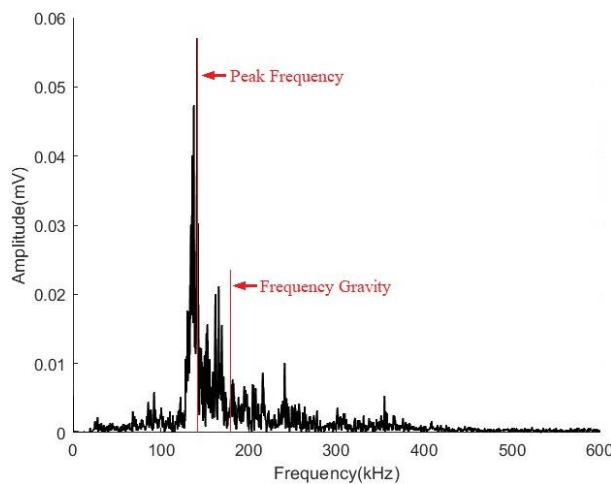
Figure 2.6 Frequency Domain of a signal

2.3.2 Pattern Recognition and Signal Classification

In practical AE monitoring, there is likely to be some noise mixed with the signals, even though a threshold has been set above general background noise. In addition, multiple damage mechanisms may present during the test, resulting in complex signal results. Moreover, there may be multiple reflections of the same AE pulse before it reaches the sensor, leading to superposition of one signal over another. Therefore, it is vital to identify the signal that is generated directly by the damage, before any understanding of the damage mechanism can be achieved. Signals derived from the same mechanism in a defined setup exhibit some similar characteristics, which is the basis for pattern recognition. The selection of features varies with different identification requirements and experimental setup.

Generally, one or more features mentioned in Section 2.3.1 are used, combined with a test parameter, for example pressure during a vessel proof test in order to determine the damage mechanism. Ramirez-Jimenez et al. [54] used glass/polypropylene composite test pieces in tensile tests and found that the stages of tensile fracture could be divided by their AE peak frequency ranges. Similarly, Aggelis et al. [55] subjected a hybrid concrete beam to a four-point bending test monitored by AE and Digital Image Correlation (DIC) methods. They found that the AE signals from matrix cracking had high frequency content, while those from delamination had a lower frequency and longer duration. Both studies revealed that the progress of fracture can be described by AE characterization resulting in a prediction of failure mode. In these cases, the fracture mechanisms were clearly different and with high SNR. Therefore, analysis of only a few AE features was enough for pattern recognition. However, for the mixed damage from corrosion, leakage, frictions and others with low SNR, more features would be required.

Hwang et al. [56] divided the progress of Stress Corrosion Cracks (SCC) on 304 stainless steel into four stages by the cumulative AE counts and compared the characteristics of AE energy, amplitude and rise time within each stage. In the work of Rivera et al [57], the crack growth in a mooring chain was monitored by AE for about four months to investigate the SCC initiation and development. They considered energy and counts as the main parameters for discriminating different stages of SCC, with auxiliary features of hits, peak amplitude, rise time and duration. Toubal et al. [58] revealed three mechanisms during the tensile test of hydrogen-embrittled test coupons mainly based on peak amplitude, hits, duration and frequency.

Except for the basic AE features that can be obtained directly from signal's waveform and spectrum, other new AE parameters have been developed for classification requirements. For example, a tensile crack and shear crack can be discriminated using Average Frequency (AF) and RA values, where the AF is counts divided by duration and RA is the rise time divided by peak amplitude [59], [60]. Moreover, for the case when AE amplitude is much weaker than the background noise, Yang Zhensheng et al. [61] proposed a new feature representation method based on similarity of probability distributions from raw AE waveforms. The Bhattacharyya coefficient was used to measure two forms of similarity, instantaneous similarity and relative similarity. These were proposed as a way of identifying abnormal signals based on their

probability distributions. The method was verified as an alternative feature representation in the experimental results from determining the filament breakage during fused deposition modelling. In addition, Santo et al. [62] proposed a new AE feature based on the unique chaos of each waveform. Here a measure of this chaos was regarded as an AE feature. In effect, this new AE feature was the collective information extracted from the waveform, and was independent of threshold and timing settings. They based this new AE feature on the calculation of Renyi's entropy, and it was verified by tensile and fatigue testing of austenitic stainless steel samples. However, when using this technique, it was still necessary to distinguish noise and consider the impact of attenuation on entropy. According to those studies above, aiming to different monitor situation, the damage mechanisms are identified by individual or multi-variate features extracted from AE signals.

2.3.3 Machine Learning

It is time-consuming to manually cluster a large amount of mixed signals from different damage mechanisms and noise. Machine Learning (ML) algorithms have been introduced to cluster the signals automatically. There are two types of ML for data classification: supervised learning and unsupervised learning methods. A biggest difference between them is whether or not there are labelled input practice samples available. The supervised learning creates a model by training the mixed signals of known mechanism (also called training set), which is then used for classifying the signals of unknown mechanism.

2.3.3.1 Supervised learning

The basic supervised learning algorithms are the k-Nearest Neighbours (KNN) algorithm, and the Decision Tree (DT) algorithm, but there are others in common use.

The idea behind the KNN algorithm is to classify data by measuring the distance between different clusters in the cluster plot. To put it simply, the first step is to calculate the distance between the new input data and the labelled samples sequentially, and then find the k samples with the smallest distance. Finally, the new data can be judged belonging to the cluster with the largest number among these k samples. The KNN algorithm has been widely used for signal classification [63-65] because of its simple principle, mature theory and insensitivity to outliers. However, its calculations are complex and intensive, and the number of labelled samples in

training set of each category needs to be balanced to prevent bias in the results. In addition, the intrinsic meaning of the data cannot be obtained.

The DT algorithm is another simple method for classification within a form of tree structure [66], in which each internal node represents a judgment on a characteristic, and each branch represents the output of that judgment. The core of this algorithm is to decide the basis of node splitting. Different standards have been chosen in different tests [67-68]. This method has low computational complexity and intrinsically clear output results, but is prone to causing model overfitting and ignores the correlation of characteristics in the data set.

2.3.3.2 Unsupervised learning

In the case where no signals of known mechanism can be used for training a model, unsupervised learning methods are applied for signal clustering. Many algorithms have been developed. Representative ones, i.e. k-means, Gaussian Mixed Model (GMM), Self-Organized Mapping (SOM) and Density Peaks Cluster (DPC), are introduced in this study. Note that an n-dimensional sample consists of n characteristics selected from a signal. The essence of these algorithms is a data partition method based on Euclidean distance. Dimensions with large values will have a decisive impact on data clustering, for example in AE testing, the value of energy relative to that of rise time. Therefore, it is important to normalize the raw samples data before applying the unsupervised learning methods.

K-means

It is a simple iterative cluster algorithm whose steps are as follows:

(1) Select initialized k samples as the initial cluster centres;
(2) Calculate the distances from each sample in the data set to k cluster centres;
(3) Classify every sample into the category corresponding to the cluster centre with the smallest distance;
(4) Recalculate the cluster centres for each cluster;
(5) Repeat steps 2-4 until reaches the specified number of iterations or the cluster centres are stable.

The k-means algorithm has the simple principle and fast convergence, but not suitable for non-convex sample data set (Definition of a convex set C: for any x, y ∈ C and θ ∈ R with $0 \leq \theta \leq 1$, there is $\theta x + (1 - \theta)y \in C$).

Gaussian Mixed Model (GMM)

The Gaussian Mixed Model is also a common used algorithm. It assumes that the data is composed of multiple clusters, which all obey Gaussian distributions. Therefore, the mean and variance of each Gaussian distribution are the parameters which should be estimated. Similar to the K-means algorithm, GMM also uses the Expectation Maximization algorithm to estimate parameters with iterative calculation. The difference is that in the GMM algorithm, each data point can belong to any cluster, but the probability of belonging to each cluster is different. Thus, there is another parameter, π_i, to describe each Gaussian model, which is defined as the weight.

The steps for GMM algorithm are as follows:

(1) Select the initial random values for each parameter;
(2) Calculate the probability that each point belongs to each Gaussian model based on the current parameters;
(3) Recalculate the mean, variance and weight of each Gaussian model based on the calculated probability;
(4) Repeat steps (2) and (3) until convergence.

GMM algorithm can model data distributions of arbitrary shapes. However, for high-level data, a large number of data is needed to accurately estimate parameters.

Density Peaks Clustering (DPC)

Density Peaks Clustering was proposed by Alex Rodriguez and Alessandro Laio in 2014 [69]. The concept of local density was introduced in DPC, which is the quantity of samples around one sample that is calculated by a given "cutoff distance". There are two basic assumptions for DPC:

(1) The local density of the cluster centre (density peak point) is greater than that of its neighbours around it;

(2) The distance between different cluster centres is relatively far.

Therefore, the cluster centre, which is picked up automatically in DPC, should have higher local density and relatively farther distance. DPC method is suitable for non-convex data sets and is not affected by dimensions of the data set. However, the decision for the "cutoff distance" will directly influence the clustering results.

Self-organized mapping (SOM)

Self-organized mapping was proposed by Kohonen in 1982, and is therefore also called Kohonen mapping [70]. This method uses competitive learning strategies, which imitate human brain nerve cells, to gradually optimize the network by the competition between neurons to generate a low-dimensional and discrete map. The structure of SOM includes two layers: input layer and output layer (also called competition layer). A two-dimensional structure is generally used as the output layer, using rectangular or hexagonal forms. A simple SOM structure is shown in Figure 2.7 [71]. According to the empirical formula, the number of map units is approximately $5\sqrt{n}$, where n is the number of data samples [72]. The first step for applying SOM is to create a randomly initialized weight matrix, in which each row corresponds to a neuron. When a sample is introduced, the similarities, which are normally measured by Euclidean distance between the sample and each neuron, are calculated. Therefore, the winner, i.e. Best Matching Unit (BMU), is the neuron with the smallest distance. The core idea of this iterative method is that neurons near the BMU will be affected to a certain extent. That is to say, there is a neighbourhood area around the winning neuron, in which the weights are updated changing with the distance. Thus, the topology of the input space is maintained by using the neighbourhood function.
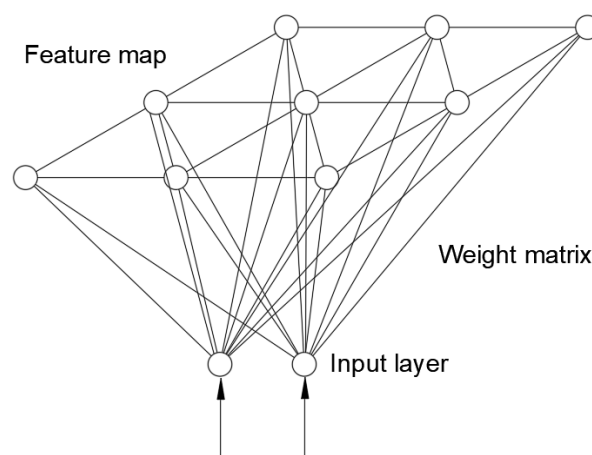
Figure 2.7 Self-Organizing Map structure

Each classification or clustering method has its advantages and disadvantages in applicable situations. Some researchers also combine multiple methods to provide more accurate classification [73-75]. In conclusion, whether it is manual classification or automatic clustering, the sample data set consisting of the characteristics extracted from signals is the basis for implementation. However, some of characteristics are not completely independent of each other. For example, signals with high amplitudes typically have higher durations and counts, which means it is unnecessary to consider durations and counts at the same time. In this case, Pearson correlation coefficient can be used to decide the correlation between two or more parameters. In addition, some characteristics of signals derived from different mechanisms are similar, which will not contribute much to pattern recognition. These redundant data may increase the complexity of classification, and even affect the recognition results. Suitable parameters for classification can be chosen by statistical methods. The Coefficient of Variance (CoV) is a statistic that measures the dispersion of data distribution, and is always used for comparison of variation degrees of multiple parameters [76]. A larger CoV value means that the signal represented by the characteristic is more different. The corresponding characteristic is thus possibly more efficient used for signal discrimination. Through this method, main parameters are picked out and the classification process is simplified, but some information may be missed. Principle Component Analysis (PCA) is a classic dimensionality reduction method that uses orthogonal transformation to transform a series of possibly linearly related variables into a set of linearly uncorrelated new variables. The different between CoV method and PCA is that the former directly discards the characteristic parameters that have little influence on pattern recognition, while the later method changes the high dimensional data into low dimensional data by using as much raw data as possible, even though both will cause the loss of information. If the number of parameters is small, PCA can be used as a cluster method to realize the simple visualisations of the data [77]. Many researchers perform dimensionality reduction before signal clustering [78-79].

2.3.4 Source Location

There are a variety of AE source location procedures dependent of the geometry used in the source location method and the timing of the AE onset.

2.3.4.1 Source Location Methods

Estimating the AE source location is another important characteristic for assessing the integrity of structure. For each AE event, the Time of Arrival (TOA) method is the standard approach [80]. The source location is calculated by the time that AE waves arrive at each sensor. However, there are prerequisites for using this method. First, there is a minimum requirement of the number of sensors that detect signals. Second, the velocity of AE wave propagation in the material is known and is constant. Third, the distances between each sensor are known.

For the simplest situation of one-dimension (1-D), such as rod-like structure, the minimal number of sensors is two. Figure 2.8 shows the setup of 1-D localization by AE.
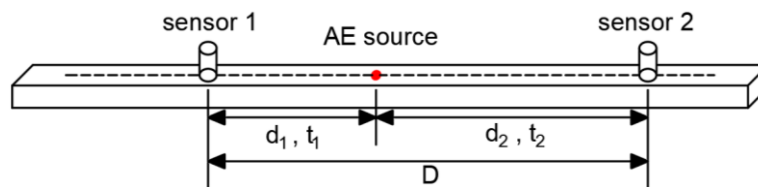
Figure 2.8 The schematic of 1D localization

The damage occurs at the time of t_0 , and waves arrive at sensors 1 and 2 at t_1 and t_2, respectively. The distance between two sensors is D. The distances d_1 and d_2, from each sensor to the AE source are unknown. Because of the hypothesis that the known propagation velocity (v) of waves is constant, the location of AE source can be calculated by Equations (2.21).

$$\begin{cases} d_1 + d_2 = D \\ d_1 = (t_1 - t_0) * v \\ d_2 = (t_2 - t_0) * v \end{cases} \qquad (2.21)$$

For this study, the tested objects are transmission pipelines that can be regarded as 2-D structures. The source location principle is the same as that for 1-D structures. However, the minimal number of sensors is 3, and they should not be placed in a straight line. Figure 2.9 describes the way to calculate the source location with TOA method. A 2D coordinate system is set and the coordinates of Sensors 1, 2 and 3 are (x_1, y_1), (x_2, y_2) and (x_3, y_3). The coordinate of AE source is assumed to be (x, y) and the AE event happens at the time of t_0. The sensors are triggered at the time of t_1, t_2

and t_3, respectively. The distances between each s1-D, the coordinate of AE source can be determined by Equations (2.22).
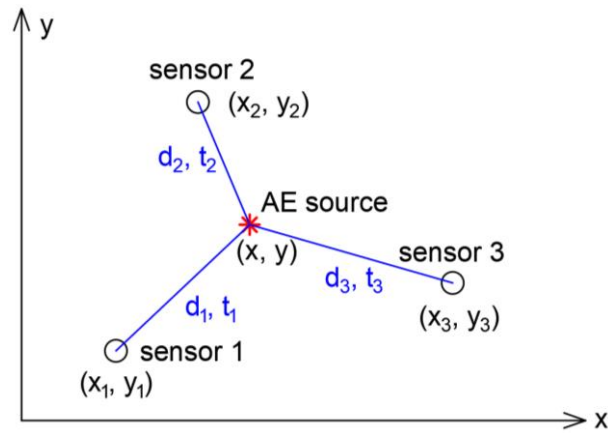
Figure 2.9 Calculation of AE source location in 2D situation

$$\begin{cases} d_1 = \sqrt{(x_1 - x)^2 + (y_1 - y)^2} = (t_1 - t_0) * v \\ d_2 = \sqrt{(x_2 - x)^2 + (y_2 - y)^2} = (t_2 - t_0) * v \\ d_3 = \sqrt{(x_3 - x)^2 + (y_3 - y)^2} = (t_3 - t_0) * v \end{cases} \qquad (2.22)$$

However, the time-synchronization is required between the AE source and triggered sensors in TOA method, and the time t_0 is unknown in practical monitoring implementation. Equations (2.22) is therefore simplified as Equations (2.23) without t_0, which is known as Time Difference of Arrivals (TDOA) method.

$$\begin{cases} d_1 - d_2 = (t_1 - t_2) * v \\ d_1 - d_3 = (t_1 - t_3) * v \end{cases} \qquad (2.23)$$

Nevertheless, in actual engineering, there are always errors in TDOA measurements because different sensors may not be triggered by the same wavefront for an AE event, due to different propagation directions and distances. In addition, the uncertainty of wave velocity is a cause of error when using the TDOA method. It is not easy to find the solution of nonlinear equations with considering errors. Many scholars have investigated the solutions of AE source location based on TOA/TDOA. Generally, there are two kinds of methods: iterative and non-iterative methods.

The Geiger Method [81] is a classical method that laid the foundation for currently used methods. It is a linear iterative method, whose main idea is to make the residual of arrival times reach minimum in the iterative process, by obtaining the corrections with first-order derivation. However, an initial guess of the location is needed, which

requires being sufficiently close to the true source location. Otherwise, the obtained result may be the local minimum rather than global minimum.

With the development of computational tools, non-linear methods can be more realistic in solving the problem. The Simplex Algorithm (SA) was developed by Nelder and Mead [82] to solve the minimization of multivariable functions. In 1988, The SA was introduced for microearthquake location by Prugger and Gendzwill [83] , in which the minimum location error was obtained by an iterative geometric search. Figure 2.10 illustrates the logic of the SA algorithm in the 2-D situation with 3 sensors as an example [84].
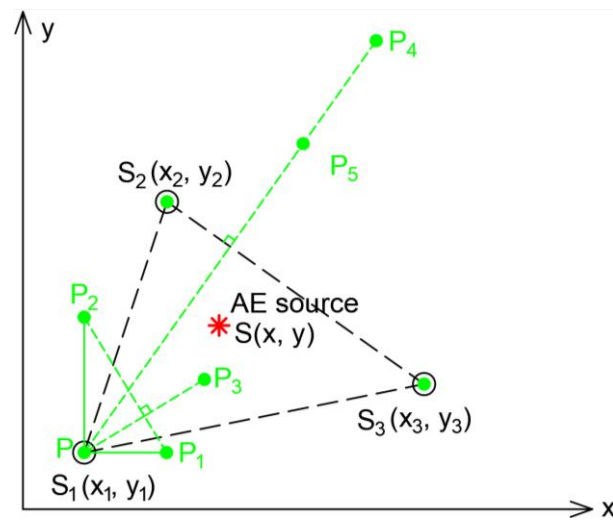
Figure 2.10 Source location by Simplex algorithm in 2D situation

Based on the Equations (2.23), the loss function of location errors yields:

$$\mathfrak{f}(x) = \left((d_1 - d_2) - ((t_1 - t_2) * v)\right)^2 + \left((d_1 - d_3) - ((t_1 - t_3) * v)\right)^2 \qquad (2.24)$$

The purpose is to find a point S (x, y) that can make the value of $\mathfrak{f}(x)$ the minimum or a certain accuracy. The steps are as follows:

   (1) Take 3 points, P (x_P, y_P), $P_1(x_{P_1}, y_{P_1})$, $P_2(x_{P_2}, y_{P_2})$, on the 2D plane as the initial vertices. Generally, the position of one of the sensors is used as point P;
   (2) Calculate the location errors of each vertex $\mathfrak{f}(P)$, $\mathfrak{f}(P_1)$, $\mathfrak{f}(P_2)$ and find the vertex with maximum value of location error (which is vertex P shown in Figure 2.10);
   (3) Mirror vertex P along the line P_1P_2 to obtain P_3 as a new vertex which replace point P;

(4) Use P_1, P_2, P_3 as a new set of vertices to repeat Steps 2 and 3 till find a point S with the minimum location error.

In addition, positions of the three sensors S_1, S_2, S_3 can be chosen as the initial three vertices. As shown in Figure 2.10, the mirrored point of P along the line S_2S_3 is P_4. It can be seen that the location error $f(P_4)$ is still bigger than $f(S_2)$ and $f(S_3)$. In this case, the mirror distance can be shrunk by half to the location of P_5. Therefore, S_2, S_3 and P_5 are used as a new set of vertices to repeat Steps 2 to 4. From the SA process, it can be noted that each iteration is guaranteed to converge before reaching the minimum error or satisfying the artificially set error. Its stability is thus an advantage over derivative-based iterative methods. Moreover, source location can be determined by a fewer number of iterations, and this is a reason for wide use of the SA [85].

Non-iterative methods solve the Equations (2.23) by statistical theory. They do not need to deal with the problems that iterative methods encounter, such as the inappropriate initial source location, iterative divergence, local minimum error obtained, etc. [86]. However, the solution of Equations (2.23) requires finding the intersection of hyperbolic lines. This causes cumbersome computation and difficult error analysis due to the nonlinearity. Schmidt [87] proposed a Plane-intersection (PX) method, which transforms the nonlinear problem into a linear one. The source location is on the major axis of a conic, which passes through a set of three sensors. When the number of sensors exceeds 3, the intersect point of the major axes of several conics is the source location. In this way, straight line equations replace the hyperbolic equations, which alleviates the computational complexity. Nevertheless, some redundant information will be introduced, resulting in inconsistencies [88]. Smith and Abel [89] gave an explicit calculation of the source location estimators, which is called the Spherical-Interpolation (SI) method. It is a closed-form Least-Squares (LS) approximate maximum likelihood method [90]. For the SI method, the localization formula derived from LS "equation error" minimization and the expressions for the variance with noisy TDOA measurements were given. Compared to the PX method, the variance of SI is much lower than that of PX, but with a slightly higher bias. Based on the work of Smith and Abel, Chan and Ho [91] provided a two-staged weighted LS method, which can use the redundant information to improve the source location accuracy when there are more than 3 sensors. An unconstrained LS solution is given by using an extra variable for the first step. The improved source location estimate is then given by a second

weighted LS, which make sure of the constraint between the coordinate of source and that variable.

However, in practice, the source locations are needed to be done on complex inhomogeneous structures, where the methods above are not suitable. In view of this, Baxter et al. [92] proposed the Delta T (ΔT) location method to improve the source location results. There is no assumption about wave paths and wave velocities by using this method. Its steps for application are as follows:

(1) Determine the area of interest: It will be time-consuming if locating the source with this method to cover the complete structure. This method is recommended to be used for improving the source location around the complex part only.

(2) Construct grid: A grid is constructed on the area. To some extent, better location results will be obtained with a higher resolution grid. The relative position of the two sensors is required to locate source, rather than the sensor location.

(3) Conduct source events to obtain time of arrival data: The source events are conducted at each node in the grid for obtaining the Time of Arrival (TOA) of signals acquired by each sensor.

(4) Calculate ΔT maps: For an event, the differences in TOA of each pair of sensors are calculated. A ΔT map of a pair of sensors can be obtained by connecting the nodes with the same difference in TOA.

(5) Locate real source events: For a real event, a line can be chosen on each ΔT map after calculating the time difference of each pair of sensors. The source location is then indicated at the convergence point by overlaying these lines.

This method was proved by Pencil Lead Break (PLB) tests on a complex structure in Baxter's work, in which an aircraft component that contained several thickness changes and a 113mm diameter hole was used. The accuracy of location results was clearly improved in their work. However, the PLB AE sources are simple and repeatable experimental sources, while the sources from actual events are not (e.g. sources from cracks and corrosions). Therefore, the amount of work involved in constructing a ΔT map of real event sources through experiments is huge, and it is difficult to ensure that the experimental conditions at each node are the same. For this situation, numerical method is a promising way to solve this problem, which will be introduced in Section 2.4.

2.3.4.2 Determination of onset time

Form Section 2.3.4.1, it is shown that the source location methods are mostly determined by the Range Difference (RD) measurement, which is based on TDOA between two sensors. The onset time of an AE signal thus plays a crucial role in the accuracy for estimating source location. Generally, the frequency of typical released elastic waves is 10 kHz to 1 MHz. According to this phenomenon, if the threshold is chosen properly, noise with frequencies falling outside of that range will be successfully discriminated. Besides, the onset time of AE signal will be more accurately determined. The threshold-based hit method is suitable when the background noise level is either constant or changing gradually, because there is a big difference between signal and noise. The identification by threshold-crossing point in the AE waveform is shown in Figure 2.11(a). However, the value of threshold is decided on the experience of the test technician in filtering out noise as much as possible. When the Signal-to-Noise Ratio (SNR) is low, a hard-threshold method can't satisfy the requirements because the target signals are inundated with noises. The real onset time will be earlier than the time determined by the threshold-crossing method, which is shown in Figure 2.11.
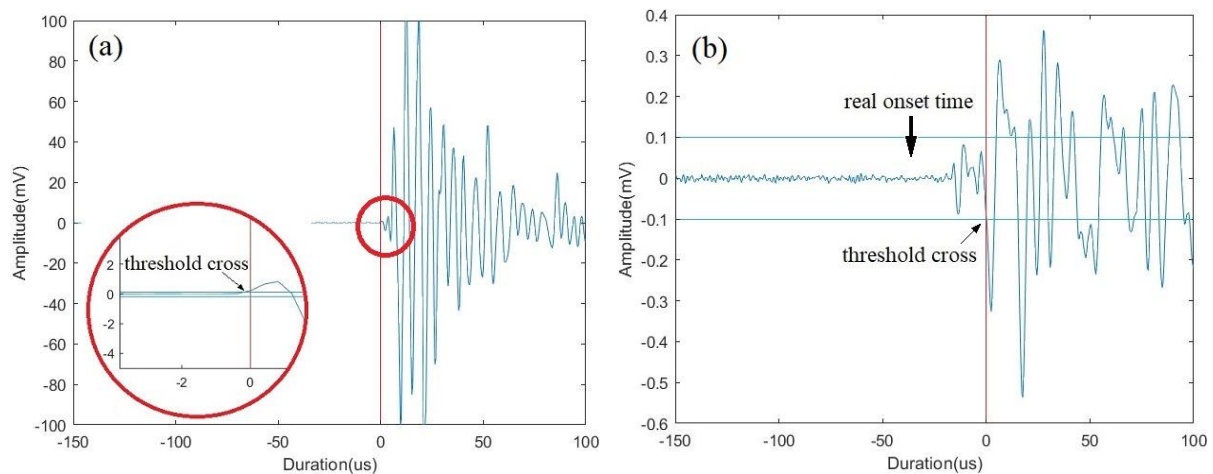
Figure 2.11 Onset time of a signal determined (a) by the Threshold-cross method (b) not suitable by threshold-cross method

For this case, the Akaike Information Criterion (AIC) is a standard to measure the goodness of fit of a statistical model. Based on Autoregressive Process (AP), a common method, AIC picker, is used to pick AE signals in a series of recorded samples [93], whose definition is:

$$AIC = 2k - 2ln(L) \qquad\qquad (2.25)$$

Where k is the number of parameters and L is the Likelihood function for model parameters. The onset point can be identified with the determined separation point of noise and signal by minimized AIC [94], as shown in Figure 2.12.
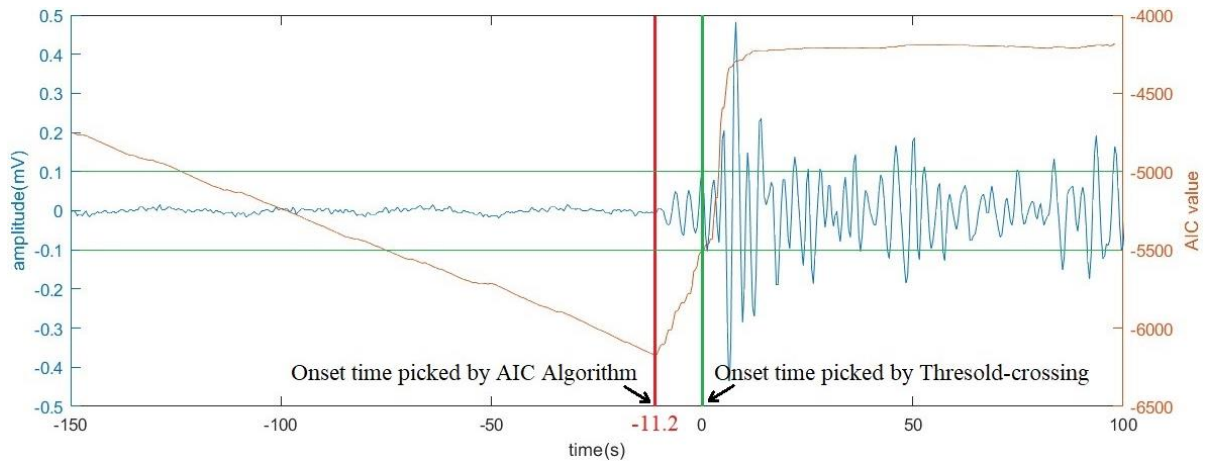
Figure 2.12 Comparison of onset time picked by Threshold-crossing method and AIC algorithm

However, the wrong pick, or multiple minima may happen, because of extremely low SNR and unrecorded arrival. The performance of AIC depends on the characteristic function used for the AE signals. Therefore, it is good to trial different windows on the signal to choose the appropriate time series range for applying AIC. Zhou et al. [95] selected a suitable time series range with the Windowing Lempel-Ziv (WLZ) complexity method and Multi-Scale (MS) theory, before using the AIC method. Sedlak et al. [96] determined an effective limited time window for applying AIC to obtain an accurate onset time by two-step AIC picker. Moreover, Kurz et al. [97] proposed an AIC-based algorithm whose characteristic function is a Hilbert wavelet transform. Its onset time results were compared with an automatic onset detection algorithm based on the Hinkley criterion. The results showed that the proposed AIC picker was reliable for automatic onset detection with improved accuracy for AE with varying SNR. However, misidentify the onset time by AIC is inevitable, when automatically processing thousands of AE signals. An improved AIC-picker method was put forward by Carpinteri et al. [98] where a certainty parameter [99] was introduced to check the validity of obtained onset time.

2.4 Simulation of Acoustic Emission signals

If the experiment cannot be repeated due to the complexity of the experimental process or the unique of the structure, the numerical simulation method is potentially an appropriate way to obtain the desired results.

Finite Element Method (FEM) is a method to simulate real physical systems, such as geometry and load conditions, by using mathematical approximations. Its significance is to calculate the solution of partial differential equations (sets) with specific boundary conditions in mechanics or/and mathematics. It breaks down complex systems into smaller, simpler parts to obtain precise results. This method is traced back to the work of Courant in 1943 [100], but was developed rapidly only from 1970s following computer capacity development.

The feasibility of FEM has already been proven for the simulation of AE signals on plates in the work of Gary [101]. For theoretical description of AE sources, the models are geometrically approximated as point sources based on the work of Aki and Richards [102]. And during the development of crack, there are some step-functions to describe the spatial displacement of the crack surface [103-104]. Here, the source rise time is always an important parameter, which is generally estimated in light of the elastic properties of materials [105]. In Gary's work, influence of the source width, the rise time and the distribution of the stress were investigated on the generated waves. The results predicted by the dynamic finite element model developed are in good agreement with the experimentally measured results from Pencil Lead Break (PLB) tests on an aluminium plate. Nevertheless, the AE sources generated by surface PLB are monopoles, while the practical AE sources are mostly composed of dipoles. Hamstad [106] predicted the AE waveforms developed by buried transient dipole. His work applied two closely connected and simultaneous forces in opposite directions to build the FEM model. It was demonstrated that the maximum source and cell size is relevant to the minimum wavelength, which is calculated with the source rise time. In addition, Hamstad [107] compared the signals developed by monopole and dipole sources through numerical and experimental methods. The step function used in the work was proposed as the 'cosine bell' function, which simulated the applied forces (F) varying with time (t) caused by an PLB source. This function is described by Equation (2.25). The results demonstrated that the FEM method provide good outcomes.

$$F(t) = \begin{cases} 0\ N & ,t \leq 0 \\ 0.5 - 0.5 \times cos\left(\dfrac{\pi \times t}{T}\right)\ N & ,0 < t < T \\ 1\ N & ,t > T(T = 1.5\mu s) \end{cases} \qquad (2.26)$$

Moser et al. [108] investigated the wave propagation in a plate and an annular structure by useing a commercial finite element (FE) code. They studied two essential FE parameters, i.e., mesh density and integration time step, through a known analytical solution on a plate. An optimized model was thus developed, which can be used for the investigation with the annular ring. The numerical results were compared with experimental outcomes, which demonstrated the effectiveness and the potential of FEM to provide the analytical solution with complicated structures.

Sause et al. [109] introduced a new AE source FE model, which used cohesive zone modelling (CZM) approach. The crack development in this model was simulated by the local degradation of the material stiffness, and the dynamic displacement field was calculated. The signal propagation was based on a multi-scale and multi-physics approach. This model was validated by micromechanical experiments. The results demonstrated that the content of amplitude and frequency of simulated signals had a good agreement with those of experimental signals.

Lee et al. [110] proposed a method to generate AE waves by releasing nodes with FEM. Two steps were included for this method, that is, a static load was applied at the beginning, and the nodes on the crack surfaces were then suddenly released to excite AE waves. The high frequency components in the simulated waves were filtered with Gaussian window. However, this model is not suitable for unsymmetrical structures.

2.5 Theory of Hydrogen Induced Cracking

2.5.1 Hydrogen diffusion

Hydrogen generally exists in the interstitial lattice after entering the material. Diffusion by interstitial 'jumps' is the main diffusion mechanism for hydrogen in steel. The chemical potential gradient existing in the crystal makes the hydrogen atoms diffuse from the high position to the low position. This diffusion process is described by Fick's first law [111]:

$$J = -D\frac{\partial c}{\partial x} \qquad (2.27)$$

where J (mol/(cm^2·s)) is diffusion flux (The amount of hydrogen passing through a unit area per unit time); $\frac{\partial c}{\partial x}$ is the concentration gradient of hydrogen present in the crystal, which points in the direction of increasing concentration; D (cm^2/s) is the diffusion coefficient, and can be described by Arrhenius equation that greatly depends on the system and temperature [112]:

$$D = D_0 \exp\left(-\frac{Q}{RT}\right) \qquad (2.28)$$

where D$_0$ (cm^2/s) is the temperature-independent constant; Q (J/mol) is the activation energy; R (8.314 J/(mol·K)) is the gas constant and T (K) is absolute temperature.

The distribution of hydrogen in the material can be derived from the Fick's first law. According to this, there is no net loss or gain of hydrogen atoms, because the rate at which they jump into and out of sites is on average equal to the 1-D form of Fick's second law is [113]:

$$\frac{\partial c}{\partial t} = D\frac{\partial^2 c}{\partial x^2} \qquad (2.29)$$

Fick's second law describes how in ideal metals, the concentration of the hydrogen changes over time at a certain point. However, there are many types of hydrogen traps in metals that could influence the diffusion of hydrogen due to the interaction of strain fields between the trap and hydrogen. Concerning their influence on hydrogen diffusion, researchers have proposed many models for calculating the hydrogen concentration in traps. Oriani [114] proposed a thermodynamic model between the hydrogen situated in the lattice and the traps. Meanwhile, the direct relationship between the equilibrium hydrogen concentration in the lattice (C$_L$) and in the traps (C$_t$) was also obtained:

$$C_t = C_L\frac{N_t}{N_l}\exp\left(\frac{E_b}{R_{gas}T}\right) \qquad (2.30)$$

where N_t and N_l are the total traps and lattice in the material, respectively; E$_b$ is the trap binding energy with hydrogen. Also, under the influence of traps, the effective diffusion coefficient is estimated:

$$D = \frac{D_0\, exp\left(-\frac{Q}{R_{gas}T}\right)}{1 + \frac{N_t}{N_l}\, exp\left(\frac{E_b}{R_{gas}T}\right)} \tag{2.31}$$

where D_0 is the lattice diffusion coefficient factor. Note: this D_0 has been used differently previously.

Although the research of Oriani gave a clearer formula for the relationship between C_L and C_t, kinetic effects and hydrogen interactions with the traps were not considered [115]. However, based on Oriani's theory, Dadfarnia et al. [116] assumed that the occupancy $\theta_T^{(j)}$ of the jth type of trapping sites with a corresponding trap binding energy $E_b^{(j)}$ is related to the normal interstitial lattice sites occupancy θ_L through

$$\frac{\theta_T^{(j)}}{1 - \theta_T^{(j)}} = \frac{\theta_L}{1 - \theta_L} K_T^{(j)}, \quad K_T^{(j)} = exp\left(\frac{E_b^{(j)}}{RT}\right) \tag{2.32}$$

where $K_T^{(j)}$ is the equilibrium constant. In addition, the concentration of hydrogen in the jth type of trapping sites can be stated as Equation (2.33)

$$C_T^{(j)} = \alpha^{(j)} N_T^{(j)} \theta_T^{(j)} \tag{2.33}$$

where $\alpha^{(j)}$ is the number of sites per trap type (j); $N_T^{(j)}$ is the corresponding trap density. The trap density is an important parameter. Besides, Dadfarnia et al. found that the density of carbide or grain boundary traps in a material is constant, while the dislocation trap density changes with the degree of local plastic straining under stress.

With the external force, the stress and strain in a material gradually increase. The diffusion coefficient under stress-induced diffusion can be derived from Fick's law as [117]:

$$D_\sigma = D e^{\sigma_h \bar{V}_H / (RT)} \tag{2.34}$$

where σ_h is hydrostatic stress; $\bar{V}_H$ (cm³/mol) is partial molar volume caused by hydrogen. Diffusion of hydrogen driven by stress can be described as Equation (2.35), also derived from Fick's law [118]:

$$\frac{\partial C}{\partial t} = D\nabla^2 C - \frac{DV_H}{RT}\nabla C \cdot \nabla \sigma_H - \frac{DV_H}{RT} C\nabla^2 \sigma_H \tag{2.35}$$

σ_{xx}, σ_{yy} and σ_{zz} are the passive potential field, which satisfies the Laplace equation, then:

$$\nabla^2 \sigma_h = \frac{\nabla^2 \sigma_{xx} + \nabla^2 \sigma_{yy} + \nabla^2 \sigma_{zz}}{3} = 0 \qquad (2.36)$$

Therefore, Equation (2.34) changes as:

$$\frac{\partial C}{\partial t} = D\nabla^2 C - \frac{DV_H}{RT} C\nabla^2 \sigma_H \qquad (2.37)$$

The numerical solution of this equation has been obtained by Van Leeuwen [119]. Besides, he found that the hydrogen concentration would not rise monotonically, as the tip of the notch or the crack existsin a plastic zone. The hydrogen concentration will be maximum at the edge of the plastic zone, while lower at the crack tip proper, because the hydrogen will be trapped by voids that occur with the intense deformation in the plastic zone. Therefore, where a crack exists crack due to an applied load, the main challenge is to quantify the concentration of hydrogen at the crack tip and around the crack tip, because the diffusion processes need to be considered as well as the micromechanical processes in the fracture zone. Aiming to quantify the hydrogen concentration at the crack tip in the fracture zone, Sofronis et al. [120] proposed a model to simulate the hydrogen distribution in a plastically deformed steel using finite element analysis. This model described interaction between the hydrostatic stress field and the highly strained area at the notch tip. As a result, they found that hydrostatic stress is not as effective in causing hydrogen enrichment as traps caused by plastic deformation. They found a relationship between the number of sites for hydrogen at reversible traps N$_T$ and plastic strain ε_p based on experimental data was given as:

$$logN_T = 23.26 - 2.33e^{-5.5\varepsilon_p} \qquad (2.38)$$

Krom et al. [121]modified this model for the correct hydrogen balance by including a (plastic) strain rate factor. This modified hydrogen transport model predicts that the hydrogen concentration in lattice sites will be strongly dependent on the strain rate, while the hydrogen concentration in trap sites is not affected. If the strain rate is relatively high, the lattice sites can be almost depleted of hydrogen, while the hydrogen distribution is equal to the steady-state, if the strain rate is relatively low.

Taha and Sofronis [122] also demonstrated a hydrogen diffusion model based on the interaction of hydrogen induced strain in the lattice with local material elasto-plasticity following studies by Sofronis [120] and Oriani [114]. Moreover, the hydrogen distribution around the crack tip under small scale yielding conditions was analysed by finite element analysis and observed by experimentation. Olden et al. [123], using the numerical results of Taha's study, proposed a linear correlation between the trapped hydrogen concentration C_T and the plasticity ε_p:

$$C_T = (49.0 \cdot \varepsilon_p + 0.1) \cdot C_L \tag{2.39}$$

Equation (2.38) implies that traps have a major impact on hydrogen concentration, when the plastic strain is larger than 2%. This conclusion is consistent with the results of the work by Krom et al. [119]

The Cohesive Zone Modelling (CZM) approach has been wildly used by researchers for simulating the crack propagation. According to the Traction-Separation Law (TSL), crack propagation is fully described by two parameters: the critical cohesive stress σ_c and critical opening δ_c. (Serebrinsky et al.) [124]. According to this model, combining a stress assisted Fick's law with a cohesive law formulation representative of brittle decohesion gives an expression for the local critical hydrogen dependent cohesive stress $\sigma_c(\theta)$ after giving a constant critical opening [125]:

$$\sigma_c(\theta) = (1 - 1.0467\theta + 0.1687\theta^2)\sigma_c(0) \tag{2.40}$$

Where θ is the hydrogen coverage; $\sigma_c(0)$ is the local critical cohesive stress without hydrogen influence. Hydrogen coverage is defined as a function of the hydrogen concentration and the Gibbs free energy-difference between the interface and the surrounding material, as expressed in the Langmuir–McLean isotherm [126]:

$$\theta = \frac{C}{C + exp\left(-\frac{\Delta g_b^0}{RT}\right)} \tag{2.19}$$

Following Serebrinsky et al.'s work, Olden et al. simulated hydrogen environment assisted cracking of 25% Cr duplex stainless steels in an aqueous environment [123] and of API-5L-X70 steel welds, using a 3-D model [127]. To account for the ductile failure in this class of lower strength steels, the authors introduced a polynomial traction separation law as follows:

$$\sigma(\delta,\theta) = \frac{27}{4}\sigma_c(\theta)\frac{\delta}{\delta_c}\left(1 - \frac{\delta}{\delta_c}\right)^2 \ for \delta < \delta_c, otherwise\ 0 \qquad (2.42)$$

where θ in this equation is calculated by $C_L + C_T$.

Quantifying the diffusion of hydrogen in metals is very complicated, especially with regard to different materials, phases, types and numbers of hydrogen traps, and different loading conditions (different degree of interaction between plastic deformation and hydrogen). Equations that can directly express the diffusion coefficient of hydrogen and the relationship of hydrogen concentration between at the lattice and the traps inside the material do not exist, though deductions from Fick's law theory can be made, most of which are derived through a large amount of experimental data for special materials. Therefore, the quantification of hydrogen diffusion is still a complex and difficult problem.

2.5.2 Fracture theory

Generally speaking, there are three basic types of loading for cracks, as shown in Figure 2.13.
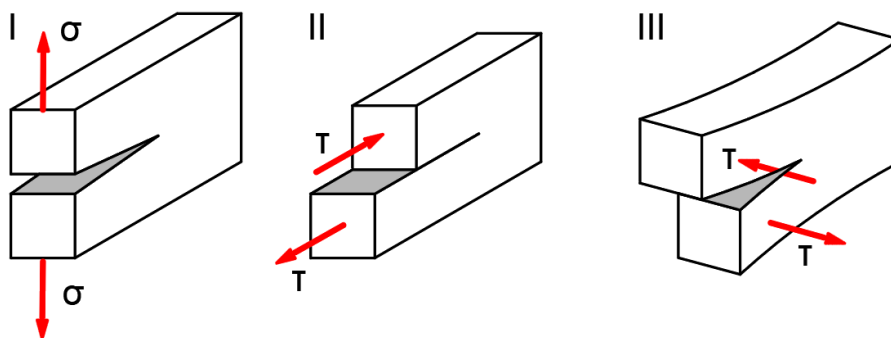
Figure 2.13 Three types of crack: Ⅰ-tensile crack, Ⅱ-shear crack (sliding), Ⅲ-shear crack (tearing)

[128]

Among these three types of crack, type Ⅰ is the most common and harmful in engineering. For subcritical cracking, the stress field near the crack tip is the focus of research. Figure 2.14 shows an infinite flat plate with a penetrating crack of length 2a, which is being loaded with tensile stress σ, perpendicular to the crack surface at both ends. According to Linear Elastic Fracture mechanics (LEFM), the stress field σ_{ij} at any point (r, θ) near the crack tip is:

$$\sigma_{ij} = \frac{K_I}{\sqrt{2\pi r}} \emptyset_{ij}(\theta), K_I = \sigma\sqrt{\pi a} \qquad (2.43)$$

From this a singularity exists, such that as r, the distance from the crack tip, tends toward zero, the stress goes to infinity. Therefore K_I, the stress intensity factor, has been chosen as a parameter which reflects the strength of the crack tip stress field. Assuming elasticity conditions, the existence of the singularity determines that, as long as there is a loading force, the crack will expand. However, the reality is different, due to the plastic deformation around the crack tip. For the high-strength steel used in transportation pipelines, the scale of plastic zone is very small compared to the size of the cracks and LEFM is still applicable. This is called small-scale yield. Besides, LEFM theory predicts that a crack in a metallic component will grow when K_I reaches K_{IC} – the fracture toughness, which is an intrinsic material property obtained by experiment. However, when hydrogen atoms accumulate inside the metal, the onset of crack growth takes place at a lower stress intensity, known as the threshold stress intensity, noted by K$_{TH}$.
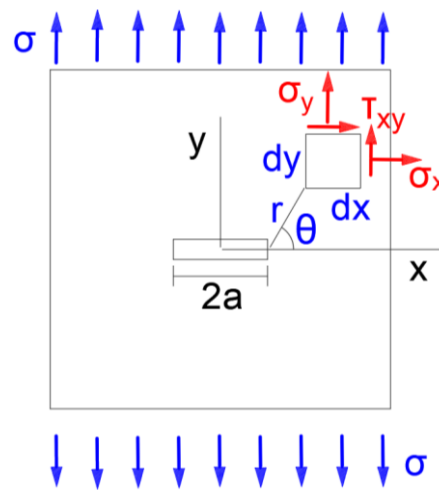
Figure 2.14 Infinite flat plate with penetrating cracks of length 2a loaded by tensile stress σ
perpendicular to the crack surface at both ends

HIC is a complex process, because of the variety and complexity of mechanisms that can lead to embrittlement under different conditions. There are two main types of theory regarding the mechanism of hydrogen embrittlement. The first type of theory believes that the hydrogen induced cracking process does not take plastic deformation as a prerequisite. This includes Hydrogen Pressure Theory (HPT), Hydrogen-Enhanced decohesion model (HEDE), and a theory that Hydrogen adsorption reduces surface energy leading to brittle fracture. The second type of theory believes that the

cracking process of any metal material takes local plastic deformation as a prerequisite. Therefore, hydrogen promotes local plastic deformation, and then causes hydrogen-induced cracking under low stress [129]. The main difference between these two types of theory lies in the consideration of plastic deformation. Fundamentally speaking, different mechanisms are proposed for different types of material, one for brittle materials such as ceramics, the other for ductile materials such as steel.

HPT believes that if there is a cavity inside the material, the atomic hydrogen that enters from the outside during hydrogen charging, or the atomic hydrogen precipitated due to the decrease in solubility during the cooling process, will enter the cavity to recombine to form molecular hydrogen and generate internal pressure. After a bubble of hydrogen is formed in the cavity, the hydrogen concentration in the surrounding lattice will decrease. Then, the difference in concentration will cause hydrogen atoms to diffuse from a distance to the periphery of the bubble. In addition, the pressure in the cavity will produce a stress gradient resulting in the hydrogen atoms enriched near the bubble by stress induced diffusion. Therefore, hydrogen atoms continue to enter the cavity through diffusion, increasing the hydrogen pressure, resulting in higher internal stresses and promoting void growth and coalescence. This in turn will lead to crack propagation. However, many observations of stable crack growth in dry hydrogen gas, as well as in chlorine and other gaseous environments, show that the pressure theory is not always the origin of cracks. For example, HPT cannot explain the mechanism of hysteresis fracture, caused by the continuous formation of low stress cracks through hydrides under constant load [130].

The HEDE theory was first proposed by Troiano (1960) [131] This considers the electron in the 1s orbital of the hydrogen atom entering an unfilled d orbital in the transition metal, thereby increasing the repulsive force between metal atoms and weakening their interatomic bonds. This theory is built on two hypotheses: the first is that crack nucleation and propagation are entirely the result of atomic bonds being broken by normal stress, even without local plastic deformation; the second is that the hydrogen, enriched by stress-induced diffusion, can greatly reduce the atomic bonding force. First-principles calculations [132] and some experiments (hydrogen reduces elastic modulus or ion work function, etc.) provide some evidence for the second hypothesis. Because of the first hypothesis, the HEDE mechanism can well explain the hydrogen hysteresis fracture found in ceramics, since there is no plastic

deformation. In general, the HEDE model was first introduced to explain, on one hand, the load relaxation during the tensile tests and, on the other hand, the inter-granular failure[118].

The Hydrogen Enhanced Local Plasticity (HELP) model was first proposed by Beachem [133] and supported by Birnbaum and Sofronis through observations made in an environmental chamber, with a high voltage electron microscope [134]. The reason why hydrogen can promote local plastic deformation is through its effect on dislocations. This includes

a. facilitating the initiation of dislocations;

b. promoting the proliferation of dislocations;

c. promoting the movement of dislocations.

Moreover, cracks formed when dislocations are created or slipped. Or when multiple edge dislocations of the same number on the same slip surface merge together, a wedge-shaped micro-crack will be formed below. In a word, deformation is concentrated near the crack tip, causing the premature achievement of the critical amount of deformation required to initiate a crack. The mechanism can be described as local plasticity that is macroscopically brittle. A HELP crack will tend to initiate from slip planes at the crack tip.

These several theories have their own applicable scope and conditions. In many cases, several theories may work at the same time. In a word, it is impossible to use just one theory to explain all hydrogen embrittlement phenomena at present. For example, the mechanism of hydrogen induced delayed cracking which commonly occurs after welding can be considered as the combined effect of hydrogen promoting local plastic deformation, hydrogen reducing atomic bonding force and hydrogen pressure. Hydrogen can promote the initiation and movement of dislocations after entering the material. Hydrogen induced local plastic deformation will occur when the enriched hydrogen concentration is over the critical value. As it reaches critical conditions, hydrogen induced cracks begin to form due to the movement of dislocations or the reduction of atomic bonding force. Then, [H] enters the micro-cracks and recombines into H_2, generating hydrogen pressure, which can stabilize the micro-cracks and at the same time assist the stress concentration to make the micro-cracks grow. In the

development of hydrogen embrittlement research, Hydrogen-Enhanced Decohesion model (HEDE) and Hydrogen-Enhanced Local Plasticity (HELP) model (Belonging to the second type of theory) are generally accepted by scholars. Both theories believe that hydrogen embrittlement is the result of a critical combination of stress, strain and hydrogen concentration, but the proposed mechanism of crack initiation and growth is different.

2.6 Hydrogen Induced Cracking generated in laboratory conditions

In industry, the HIC phenomenon in steel commonly occurs in a wet environment containing H_2S. To evaluate the HIC-resistant ability of a steel, an accepted standard has been proposed by National Association of Corrosion Engineers (NACE) [135]. It aims to distinguish the HIC susceptibility of different steels by submerging specimens into a reproducible test environment. Two standard test solutions are provided: one is a solution containing sodium chloride (NaCl) and acetic acid (CH_3COOH) saturated with H_2S at ambient temperature and pressure; the other is a synthetic seawater solution saturated with H_2S at ambient temperature and pressure. Many scholars, including Findley et al [136] have investigated the behaviours of HIC in steel according to the NACE standard [135]. Domizzi et al. [137] submerged eight specimens from different steel plates into the 5% NaCl +0.5% CH_3COOH solution saturated with H_2S for 96h to evaluate their HIC-resistance. They pointed out that the susceptibility to HIC is related to the length and distribution of Sulfide in steels. Huang et al. [138] tested the HIC susceptibility of X120 steels containing different amounts of manganese (Mn) and aluminium (Al) elements, under the environment of 5% NaCl +0.5% CH_3COOH solution saturated with H_2S. It was found that HIC occurs more easily in steels with inclusions and microstructures consisting of granular bainite and martensite/austenite. Zheng et al. [139] investigated the influence of sulfur (S) content on HIC-resistance ability of A350LF2 steel by exposing it to a solution containing 5% NaCl +0.5% CH_3COOH saturated with H_2S. The results demonstrated that the A350LF2 flange steel would be more sensitive with higher S content, especially above 0.02%.

However, H_2S is a colourless and flammable gas with high toxicity. Under laboratory conditions, it requires special health and safety precautions. Moreover, it generally takes more than 96h to generate HIC in steel by exposing it to NACE solutions.

Therefore, the electrochemical hydrogen charging method is often used instead of the way specified by NACE [134] to generate HIC in steel. Figure 2.15 provides the schematic diagram of hydrogen charging by electrolysis of aqueous solution. The steel specimen and platinum (Pt) become the cathode and anode, respectively. The commonly used electrolytes for hydrogen charging are dilute sulfuric acid (H_2SO_4) solution and sodium hydroxide (NaOH) solution. After applying the current, the cathodic reaction is:

$$2H^+ + 2e^- = H_2 \uparrow /2H \tag{2.44}$$

And the anodic reaction is:

$$4OH^- - 4e^- = 2H_2O + O_2 \uparrow \tag{2.45}$$
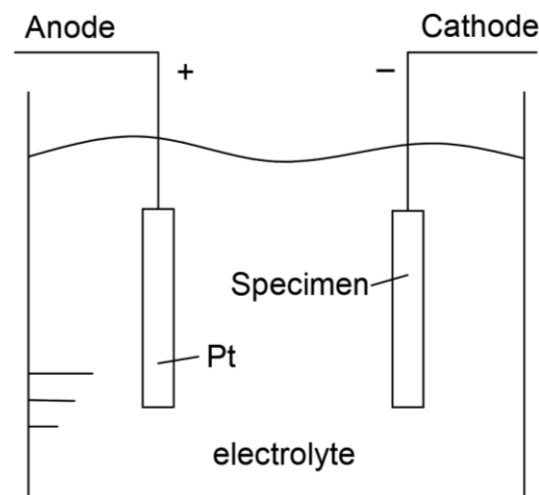
Figure 2.15 The schematic diagram of hydrogen charging by electrolysis of aqueous solution

Nevertheless, most of the hydrogen generated at the cathode will escape as H_2 gas and only a small part will enter the specimen in the atomic form, which is not enough to generate HIC in steel in a short time. As a result, various toxic agents are added to thethe electrolyte for HIC experiments, such as Sodium sulfide (Na_2S), Arsenic trioxide (As_2O_3), Carbon disulphide (CS_2), Sodium arsenite ($NaAsO_2$), Ammonium thiocyanate (NH_4SCN), and Tetrasodium pyrophosphate ($Na_4P_2O_7$). Dunne et al. [140] successfully obtained hydrogen blisters on X70 by hydrogen charging for 2h at 50mA/cm^2 using 0.5N H_2SO_4 and 250mg/L $NaAsO_2$. Banded Ferrite-Pearlite (BFP) microstructure was found to be the more prone to cracking than other microstructures in X70 steel, such as ferrite with granular bainite, equiaxed ferrite-pearlite, and bainitic ferrite laths. Du et al. [141] completed the hydrogen charging of A537 steel plates

using Devanathan's double-electrolytic cell with the electrolyte as 0.2mol/L NaOH and 0.25 g/L As_2O_3 and managed to calculate the effective hydrogen diffusivity. Mohtadi-Bonab et al. [142] applied hydrogen charging on API X70 pipeline steel by electrochemical method with 0.2M H_2SO_4 +3g/L NH_4SCN for different test durations (1h, 3h, 8h, 15h and 24h). They concluded that areas in the steel rich with complex carbonitride provided sites for HIC nucleation and cracks tended to propagate in the direction of the segregation zone containing silicon (Si), carbon (C), Mn, S and other elements. Park et al. [143] evaluated the effects of alloying elements (C, Mo) on hydrogen diffusion behaviour using the electrochemical permeation experiments based on the NACE standard, using NACE + 0.05M Na_2S + 0.3wt.% NH_4SCN with constant cathodic current density of 1mA/cm^2. These studies showed that the electrochemical hydrogen charging can be used as an effective method for rapid assessment of susceptibility of steels to HIC.

For the above publications, HIC susceptibility of the steel was evaluated by observing the cross-section of specimen cut through the thickness after finishing the hydrogen charging. According to NACE-TM0284, there are three ratios that can be used to compare the HIC-resistance ability of steels:

$$Crack\ Sensivity\ Ratio,\quad CSR = \frac{\sum(a \times b)}{(W \times T)} \times 100\% \qquad (2.46)$$

$$Crack\ Length\ Ratio,\quad CLR = \frac{\sum a}{W} \times 100\% \qquad (2.47)$$

$$Crack\ Thickness\ Ratio,\quad CTR = \frac{\sum b}{W} \times 100\% \qquad (2.48)$$

where a and b are the length and width of a single crack, which is defined as a crack separated from other cracks by more than 0.5mm. W and T are the length and width of the observed cross-section area, respectively. The cross-section surface should be polished metallographically to distinguish HIC from inclusions, scratches and other discontinuities. In addition, the early or small cracks are easily missed. In practical detection, it is better to detect the cracks as early as possible.

2.7 AE technology for monitoring HIC

AE technology is needed that can monitor the development of HIC in steel continuously, while being sensitive enough to capture the information from very small cracks.

It was discovered many decades ago that the behaviour of HIC in steel can be analysed from information in AE signals [144-145]. Bhattacharya et al. [146] subjected a hydrogen-charged steel specimen to a three-point bending test at room temperature with AE monitoring. They noted that HIC does not occur without an applied load, because the amount of hydrogen entering into the steel is not enough during the hydrogen charging process alone. Their results showed that the combination of cumulative hits and signal peak amplitudes was able to indicate the "incubation period" of HIC. Soundararajan et al. [147] proved that the analysis of AE spectral-based clusters was reliable in identifying dislocation activities, and the initiation and propagation of cracks of a hydrogen-charged specimen during a tensile test. They also pointed out that the AE signal whose spectral density is dominated by low frequencies could be regarded as a ductile crack. In the work of Shiraiwa et al. [148], the hydrogen-charged HT980 steel specimen was subjected to a Slow Strain-Rate Tensile (SSRT) test. It was concluded that the amount of cracking in a steel specimen can be estimated from the total AE energy, and this clearly correlated with the cracking ratio which was determined in Equation (2.47).

A problem arises because of the high sensitivity of AE testing. During experiments, whether HIC is generated through the NACE standard method, or the electrochemical hydrogen charging method, not only are there signals derived from HIC but also signals from other sources, such as corrosion, hydrogen bubbles, etc. Therefore, signals derived from the HIC need extracting before analysis of HIC activities can begin.

For the purpose of extracting HIC signals, Smanio et al. [149-151] used a Mistras Nano30 resonant sensor with a resonance frequency of 300kHz, for monitoring HIC tests on X65 and C110 steels under the environment with wet H_2S. They found there were 3 mechanisms where signals from, which were HIC, hydrogen charging and FeS film formation processes resulting from the anodic reaction below.

$$Fe^{2+} + S^{2-} \rightarrow FeS \qquad (2.49)$$

Signals from hydrogen charging and FeS film formation were obtained separately by applying the cathodic protection and anodic protection. Two AE parameters, signal energy and signal duration were found, to identify the signals from HIC. For X65 and the buffered solution 50mg/L Sodium chloride (NaCl) and 4mg/L Sodium acetate (CH_3COONa) in distilled water under 1 bar H_2S, they found that the biggest difference between HIC AE signals and other AE signals was the duration of HIC signals, which were found to be longer than 1500us. Many other studies on extracting HIC signals are based on Smanio's work, because of their detailed experimental procedures. However, some investigations have obtained different results.

Merson et al. [152] used the wideband AE sensor MSEA-L2 to monitor HIC activities in 09GSF pipeline steel under experimental conditions using 5% NaCl and 0.4% CH_3COONa solution with H_2S at a partial pressure of 1 bar. They distinguished three types of signal from H_2 evolution, FeS film formation and HIC, respectively, at different stages with different frequency spectra of signals. Shen et al. [153] investigated HIC development in 20R steel using the broadband Vallen AE sensor VS900-RIC, by partially immersing samples in saturated solution. Three clusters of signals from background noise, FeS layer formation and HIC were differentiated, with a classification based mainly on the amplitude and energy of the signal. It was noted that the peak frequency range in each spectrum of signals was very close. In the study of Li et al. [154], on 20R steel exposed to H_2S saturated aqueous solution, results showed that the signal parameter that could be attributed to HIC propagation was the peak amplitude, which was between 72 and 75dB. On the other hand, Smanio's results [149-151] indicated that the peak amplitude of HIC signals was lower than 60dB. These differences highlighted above may be due to different experimental setups, such as the size of specimen, type of material, position of sensors, amplitude threshold, etc.

2.8 Summary

In this chapter, theories about AE technology and the generation of HIC have been reviewed. In addition, the methods of pattern recognition, signal clustering and source location have been introduced for AE analysis. It has been shown that AE technology is a promising method for monitoring the development of HIC in transportation pipelines. The AE signals derived from HIC have been identified in mixed signals

during a variety of different tests. The trends in AE behaviour have been used to indicate the HIC process. However, current studies have been generating HIC with introducing H_2S, which is dangerous, long-lasting and limited by the geometry of the structure. Therefore, this study seeks to develop a safer and more efficient experimental procedure to analyse HIC growth with AE. Moreover, a generally applicable automatic clustering method is investigated to distinguish signals from different damage mechanisms. In addition, few studies have been done about applying Delta-T mapping technique on complex geometric structures with actual damage signals. The numerical simulation technology for actual HIC signals is studied in this work to realize Delta-T mapping to accurately calculate the position of the acoustic emission sources.

3 HIC experiments monitored by AE

It is safer and more efficient to obtain hydrogen induced cracking (HIC) on steels by electrochemical hydrogen charging (ECHC) method than working with H_2S under the laboratory condition. It is well known that there will be multiple phenomena occurring during the hydrogen charging process by the electrochemical method, including H_2 evolution and HIC which defiantly occur, and corrosions that may occur. Therefore, HIC signals need be identified amongst the mixed signals generated in the experiments.

In addition to the damage mechanism, factors such as the material and its dimensions will influence the way in which waveforms form and propagate. The hollow cylinder of an energy pipeline can be regarded as a 2D steel plate where propagation will be influenced by the propagation path, boundary and thickness. The thickness of the plate is an essentially factor influencing the type of wave propagation, i.e. Lamb wave or Rayleigh wave, which is a complex problem and will be explained in a following chapter.

In this chapter, steel specimens with two different specifications on plane dimension were used for HIC tests. A complete experimental procedure was applied for discriminating signals from various damage mechanisms. The characteristics of acquired signals on the two specimens were compared to providing a basic understanding of the HIC signal. In addition, the source location of HIC events were predicted and compared.

3.1 Experimental preparation

3.1.1 Material

3.1.1.1 Materials for ECHC

In order to accelerate the process of hydrogen atoms entering the steel, higher hydrogen concentration is needed. Sulfuric acid (H_2SO_4) solution of 0.5 mol/L was chosen as the main electrolyte to provide the hydrogen source. The H_2SO_4 solution was diluted with the extra pure sulfuric acid (>=95%, CAS-No: 7664-93-9, Fisher Scientific International, Inc.) and deionized water. For the ECHC test, the poison added in the electrolyte is also vital for inhibiting the recombination of hydrogen atoms. In this study, diluted Sodium Arsenite ($NaAsO_2$) solution of 0.05mol/L (CAS-No: 1327-

53-3, Merck Life Science UK Limited,) was selected. The final prepared electrolyte was a mixed solution of 0.5mol/L H_2SO_4 and 0.5g/L $NaAsO_2$ diluted by deionized water.

3.1.1.2 Materials for the steel specimen

HIC-sensitive steels should be considered to ensure that HIC can be obtained. Kane's [155] indicated that HIC susceptibility is high for a carbon steel with high Sulphur content (>0.002%) in as-rolled conditions with MnS inclusions being the main sites of HIC. Dunne et al. [156] investigated the effect of microstructure on HIC with X70 carbon steels and found that the banded ferrite-pearlite is the most suitable microstructure for HIC to occur. In this study, rolled ASTM A516 Grade 65 carbon steel plates were selected with high content of S and Mn (Brown Mcfarlane Ltd.). The chemical compositions of A516 are displayed in Table 3.1. Fig. 3.1 shows the microstructure of the material.

Table 3.1 Chemical Compositions (%) of A516 Grade 65 carbon steel

Composition	C	Mn	Si	P	S	Cr
Content (%)	0.137	1.073	0.169	0.011	0.005	0.015
Composition	Ni	Mo	Cu	Al	Ti	Nb
Content (%)	0.008	0.002	0.016	0.033	0.001	0.014
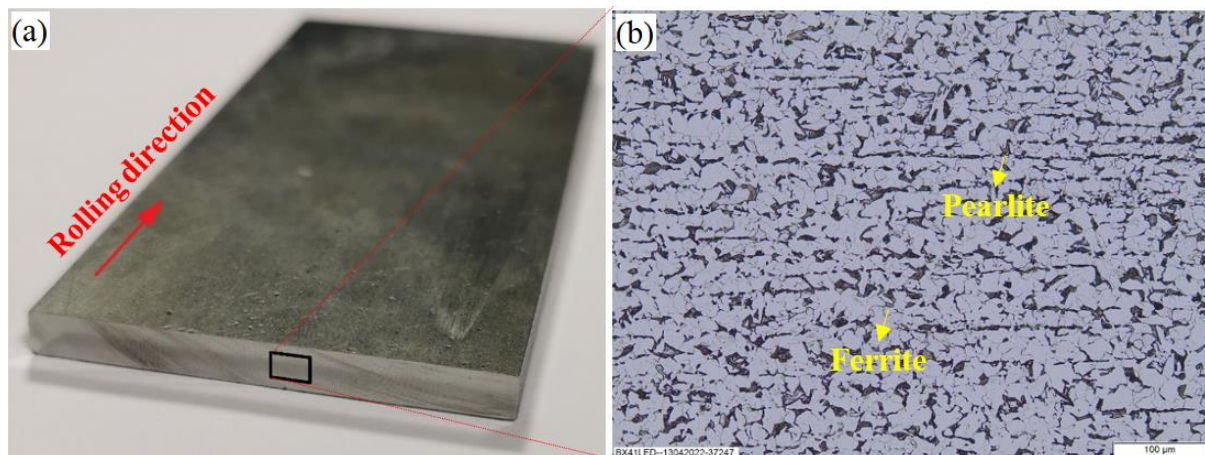
Figure 3.1 (a) Sample plate of A516 carbon steel (b) The banded ferrite-pearlite microstructure

The thickness of specimen was determined as 5mm; therefore, signals with frequency under 1200kHz are propagating in the form of Lamb wave [157]. The specifications of specimens were designed as 200 × 50 × 5mm and 500 × 300 × 5mm. They were ready after polishing the surface to 2500 grit and cleaning with alcohol.

3.1.2 Equipment

A constant electric current for the ECHC method was produced by a Gill AC potentiostat (ACM Instruments Ltd.) shown in Figure 3.2. The applied current was adjusted by the Sequencer supporting software on a computer. The specimen and the platinum mesh were connected with the work electrode (WE) channel and auxiliary electrode (AE) channel of the system separately. Because the specimen should be used as the cathode, the input current value in the system is negative.

Figure 3.2 The potentiostat

Due to the size of the specimen, AE sensors of small size are prioritized. Besides, broadband sensors are good choice for detecting signals of in a test where there is prior knowledge of anticipated signals. Nano30 piezoelectric sensor with a diameter of 8mm (Mistras system) were thus selected for the experiment. Nano30 sensors were connected to a Vallen 4 AE-channels AMSY-6 data acquisition system through the external Vallen AEP4 pre-amplifiers with 34 dB gain (Vallen System GmbH). Electric signals are displayed with basic characteristics on a computer by Vallen software. The response curve from the calibration certificate of Nano30 sensor used in this study is shown in Figure 3.3 [158]. It can be seen that this sensor is a typical broadband sensor with a response frequency of 100-750kHz. It is more sensitive to signals in the frequency range of 150-350kHz, making it very suitable for damage detection in this study.
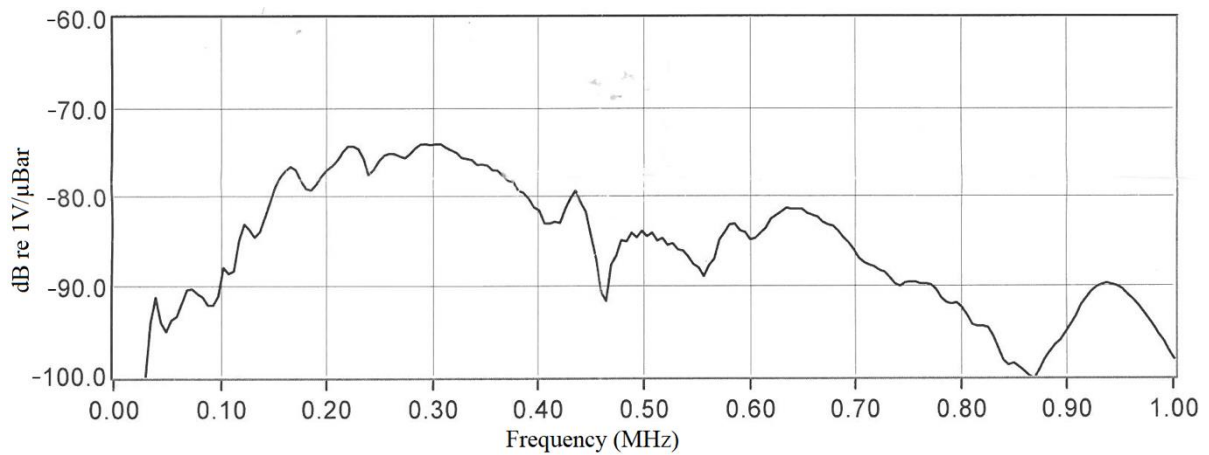
Figure 3.3 Response curves of Nano30 sensor used in this study [158]

3.1.3 Phenomena identification and parameters determination

A pre-test was initially run as a trial to identify suitable settings and to gain basic understanding on ECHC-HIC process. The electrolyte was held in a glass conical funnel-like container that was sealed to the specimen with silicone sealant (Loctite SI 595). The contact surface between electrolyte and specimen surface was circular with a diameter of 30mm. Figure 3.4 shows the four Nano30 sensors fixed on the specimen by silicon as a couplant at selected locations. A piece of high insulation polymer foam was used to separate the specimen from the workbench to prevent acoustical background interference.
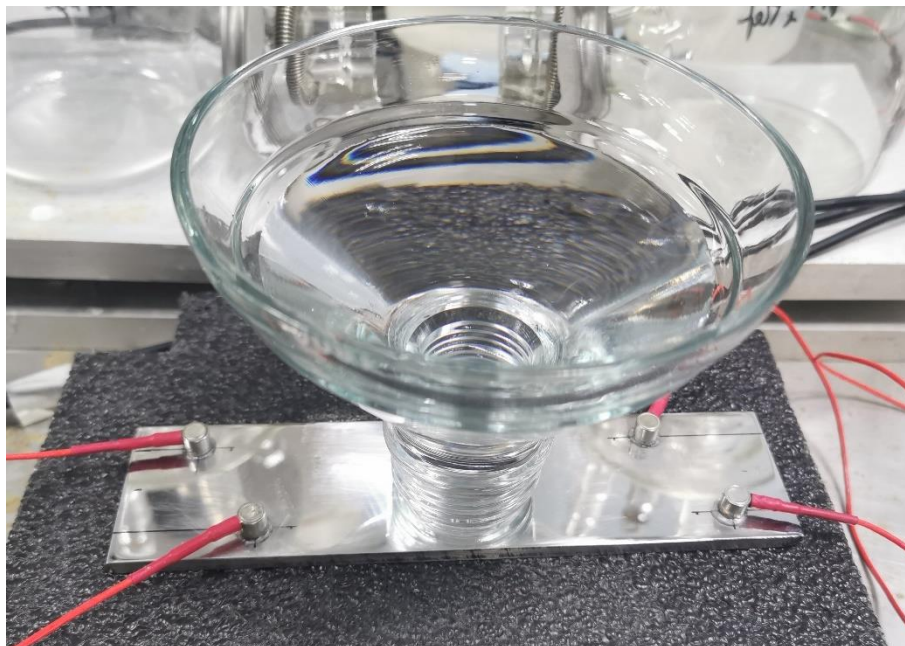
Figure 3.4 Setup of the pre-test

Table 3.2 shows the AE acquisition system setting with a sampling rate at 2.5 MHz.

Table 3.2 Parameter settings of AE acquisition system

Parameters	Threshold (dB)	Rearm Time (us)	Duration Discrimination Time (us)
Values	40	1000	400
Parameters	Pre-trigger Time (us)	Post-duration Time (us)	Pre-amplifier gain (dB)
Values	200	200	34

The applied current was set as 50mA/cm^2 at first, producing numerous signals from H$_2$ evolution. In order to reduce non-HIC signals, the current and the signal threshold were modified to 5mA/cm^2 and 40dB by a trial and error exercise. The test was stopped after 17h and the specimen was cleaned by rinsing with deionized water and alcohol. Figure 3.5(a) shows hydrogen charged specimen's surface which was captured by camera. Figure 3.5(b) shows the polished cross-section of the thickness which was cut along the green line in Figure 3.5(a). The cross-section figure was captured by Optical Microscope (OM). Three phenomena can be observed on the surface in Figure 3.5(a). There are extensive hydrogen blisters, and simultaneously, uniform corrosions and crevice corrosions at the boundary of the contact area. The existences of corrosions are due to the presence of silicone by the sealing used in the experiment. Some generated H$_2$ bubbles stick to the silicone and contacted with the specimen, resulting in the broke circuit in the small contact area. Uniform corrosions were thus generated in wet hydrogen environment. Moreover, due to the low current and the concentration of some Fe^{2+} at the boundary, crevice corrosion also gradually occurred. In addition, HICs under the blisters inside the material can be observed through the thickness in Figure 3.5(b). All these shows the creditable feasibility of the experimental method used in this study.
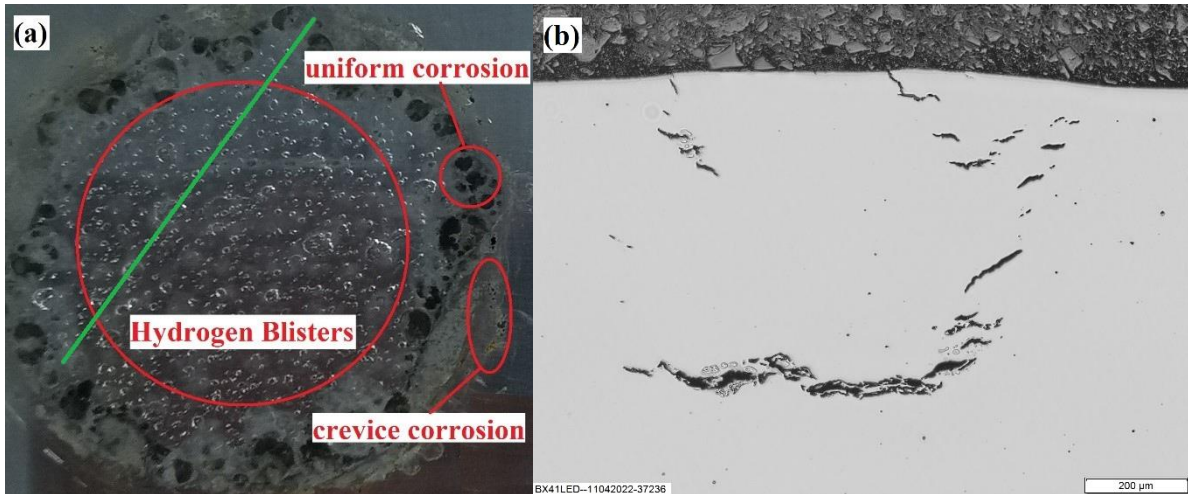
Figure 3.5 (a) hydrogen charged specimen's surface (b) HICs on the cross-section surface

Nevertheless, a large amount of hydrogen was produced in the exposed area, resulting in too many signals from hydrogen evolution. At the same time, it was not easy to evaluate the source locations if there were a lot of HIC events in the big area. Thus, the area was reduced to 1 cm^2 square by covering the rest with Belzona 4311 coating. In addition, to avoid the peel-off of the coating caused by the penetration of electrolyte, the edges of the exposed square area were sealed with silicone. Figure 3.6 exhibits the final area contacted with electrolyte for experiments.
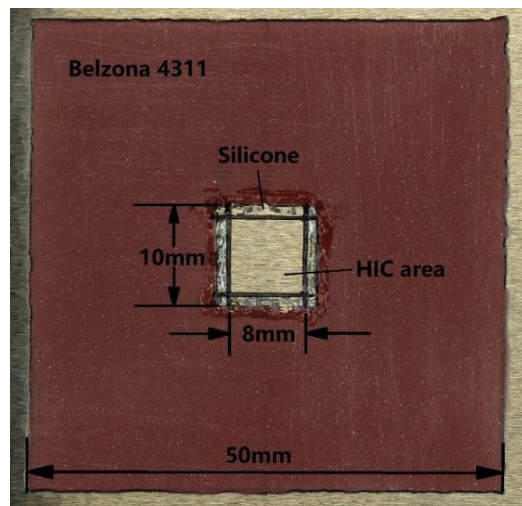
Figure 3.6 Work area on specimen's surface which contacts with electrolyte

3.2 Tests for non-HIC signals identification

Figure 3.5 shows that there are different events occurring at the same location from multiple mechanisms, amongst H_2 evolution, HIC development, uniform corrosion, and crevice corrosion at the boundary. Each of these sources will generate AE signals. As

the aim of this study is to investigate the HIC development monitoring by AE, there is thus a need to discriminate amongst these signals, especially to identify and extract those from HIC accurately. Work was therefore conducted, as detailed in the following sections, to distinguish non-HIC signals at first by tests with varying parameters. HIC signals can thus be obtained out by filtering out the known non-HIC signals.

It is known that uniform corrosion occurs when the steel comes into contact with H_2SO_4, whose reaction is regarded as:

$$\text{Fe} + H_2SO_4 = \text{Fe}SO_4 + H_2 \uparrow$$
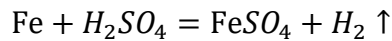
In addition, it was tested that there is no HIC in steel by applying ECHC method with electrolyte only of dilute H_2SO_4 for 24 hours. According to these two phenomena, two tests were designed to generate only uniform corrosions and crevice corrosions in different levels, as introduced below.

3.2.1 Experimental procedure

Two short-time tests (of 2h) were designed for identifying non-HIC signals. Noted that although the phenomena on small and big specimen are similar with the same parameters, signals may differ because of the different propagation path. Thus, two tests were applied on a small and big specimen individually, whose details are shown in Table 3.3. Crevice corrosion always occurs due to the presence of silicone.

Table 3.3 Details for two short-time tests for each specimen

Specimens	Tests	Electrolyte	Current	Theoretically Signal Sources
Small specimen	Test 1	0.5mol/L H_2SO_4	5mA/cm^2	H_2 bubble + crevice corrosion + uniform corrosion (possible)
	Test 2	0.5mol/L H_2SO_4	×	H_2 bubble + crevice corrosion + uniform corrosion (numerous)
Big specimen	Test 3	0.5mol/L H_2SO_4	5mA/cm^2	H_2 bubble + crevice corrosion + uniform corrosion (possible)
	Test 4	0.5mol/L H_2SO_4	×	H_2 bubble + crevice corrosion + uniform corrosion (numerous)

3.2.2 Results

3.2.2.1 Tests 1 and 2 with small specimen

For Test 1, high numbers of H_2 bubbles immediately escaped from the surface of work area after applying the current. At the same time, some bubbles fixed at the boundaries because of the existence of silicon and gradually merged to bigger ones. As for Test 2, the speed of H_2 evolution was much lower than that of Test 1. Only few bubbles were observed on the area at the beginning. After a while, a large number of small bubbles appeared and the surface of work area became darker than other area. Figure 3.7(a) and (b) show the physical phenomena at the beginning of Test 1 and Test 2, respectively.
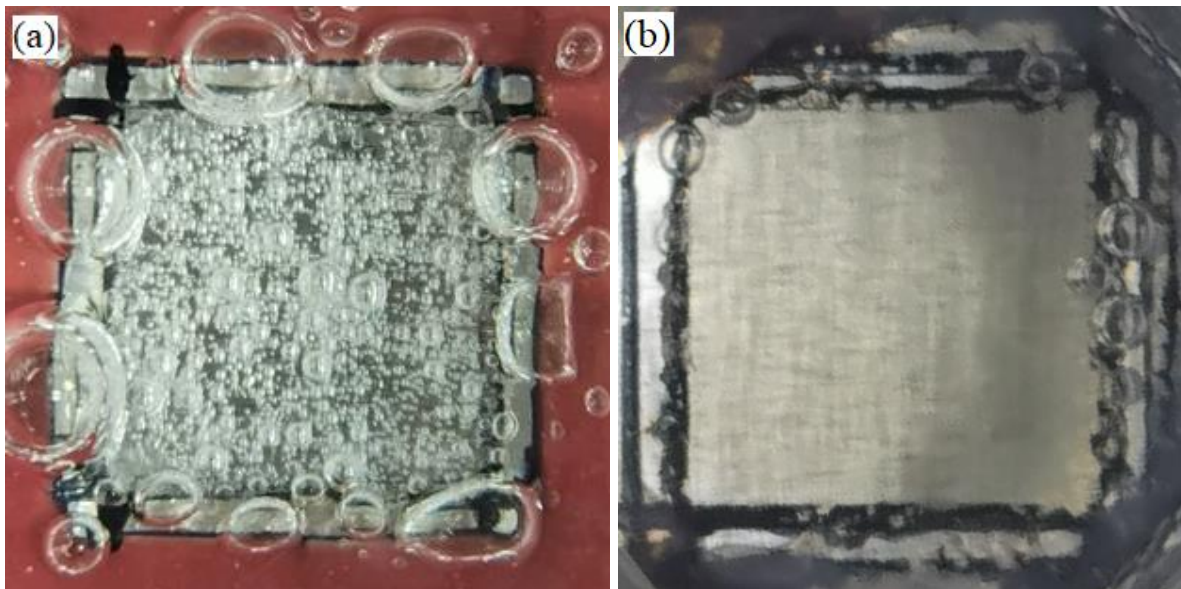
Figure 3.7 The physical phenomena at the beginning of (a) Test 1 and (b) Test 2

Correspondingly, the processes of the two tests were exhibited by AE results. Figure 3.8 shows the representation of the Time-Amplitude graph of signals from Test 1 (Figure 3.8(a)) and Test 2 (Figure 3.8(b)). It can be seen that there are a lot of signals acquired at the beginning of Test 1 while a large amount of signals were obtained from 3600s in Test 2, which demonstrated that signals acquired in late Test 2 are likely to be from uniform corrosion.
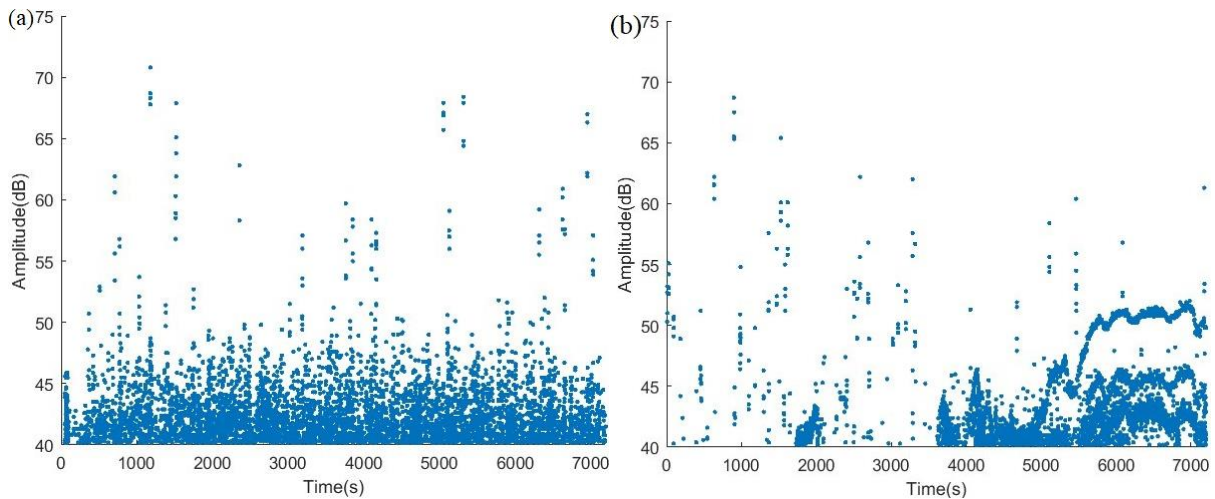
Figure 3.8 Representation about the Time-Amplitude graph of signals from (a) Test 1 (b) Test 2

By manually analysing the signals in Time-domain and Frequency-domain, three types of signals can be identified in both tests. For signals belonging to the same type, they were not the same but shared similar characteristics in their spectrum. Figure 3.9(a), (b) and (c) show the waveforms and frequency spectrums of one typical signal of each type. Compared these three types of signals, their frequency spectrums were clearly different. For signals like Type 1, their peak frequencies generally locate between 120kHz to 160kHz with a narrow band. As for Type 2, the peak frequencies of signals are at around 50kHz or 150kHz but always contain more lower frequency components over a larger spectrum. Similarly, a greater content of higher frequency components existed in signals as Type 3 with peak frequencies at 150kHz or higher than 200kHz. Again, these Type 3 signals have a broad frequency spectrum. From the signal waveforms of these 3 types, the duration, energy and counts of Type 2 and 3 are normally higher than those parameters of Type 1. Based on these characteristics, signals from both tests were divided into 3 clusters. Figure 3.10 exhibits the Time-Amplitude graphs of the three types of signals from Test 1 (Figure 3.10(a)) and Test 2 (Figure 3.10(b)). Additionally, the numbers of signals of each type in both tests are displayed in Table 3.4.
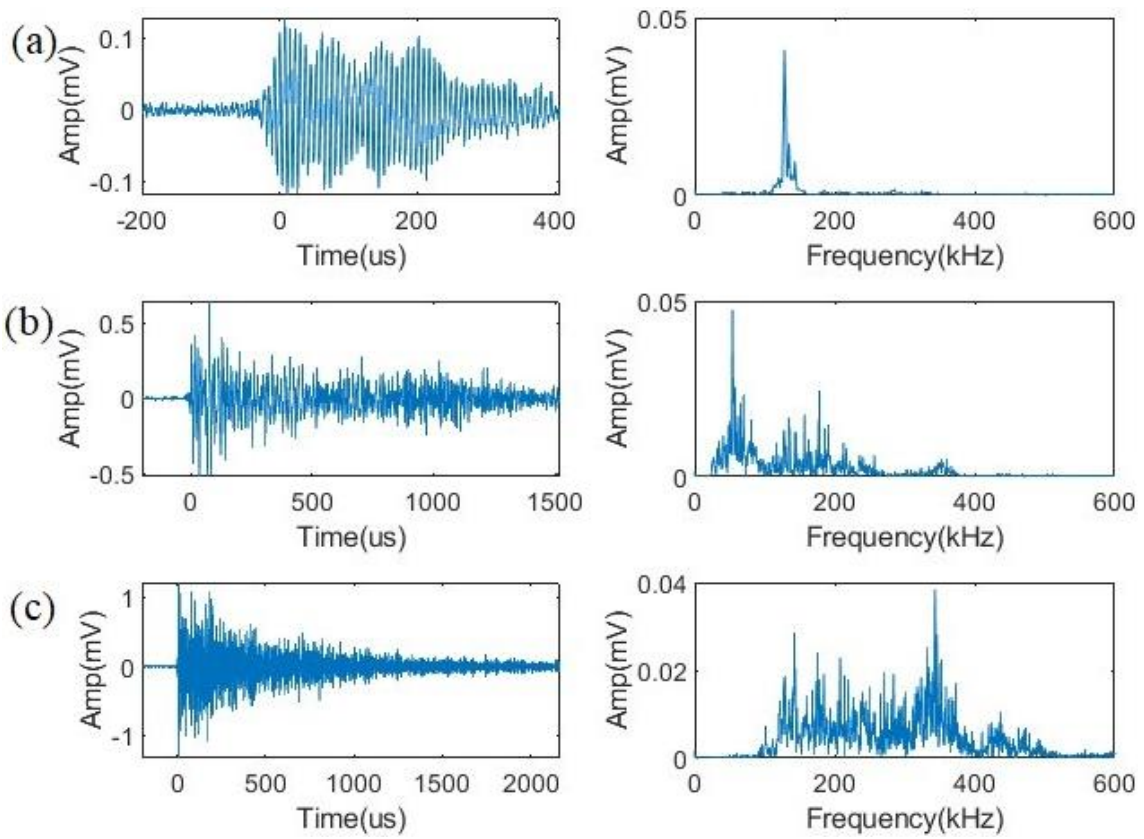
Figure 3.9 Typical waveform and frequency spectrum of signals: (a) Type 1, (b) Type 2, (c) Type 3
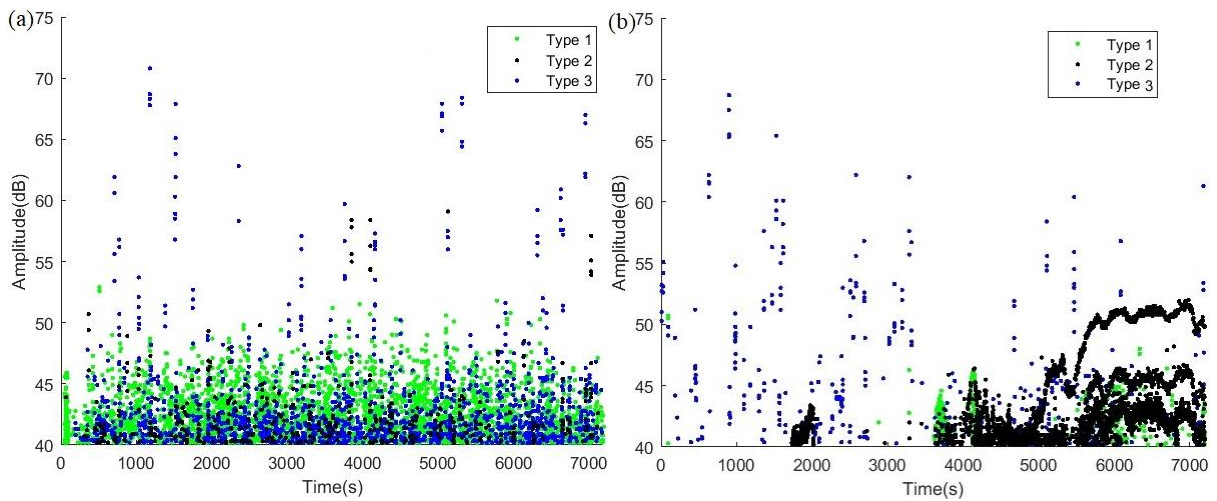
Figure 3.10 Representation about the Time-Amplitude graph of the three types of signals from Test 1 (a) and Test 2 (b)

Table 3.4 Events quantity of each signal type in Tests 1 and 2

Quantity of Events	Type 1	Type 2	Type 3
Test 1	3832	416	1587
Test 2	335	3004	411

By analysing Figure 3.10 and Table 3.4, the phenomenon represented by Type 2 signals was inhibited in Test 1 but dominated in late Test 2. This indicated that the signal looks like Type 2 is likely to be from uniform corrosion. Moreover, others' research [157, 159] indicated the same characteristics of uniform corrosion signals as those represented by Type 2. As for the signals of Types 1 and 3, Type 1 signals were acquired earlier than those of Type 3 in Test 1. This suggested that Type 1 signals are possibly from H_2 evolution because a large quantity of small hydrogen gas bubbles were observed immediately after applying the current. When considering the findings of other researchers [160-163], signals from H_2 evolution were typically observed to consist of lower frequencies. Therefore, signals of Type 1 are likely to be generated by H_2 evolution while those of Type 3 are from crevice corrosion.

3.2.2.2 Tests 3 and 4 with big specimen

The results of Tests 3 and 4 are shown in Figure 3.11 with the representation of signals about the Time-Amplitude graphs. It can be seen that a lot of signals whose amplitudes higher than 50dB were acquired later in Test 4. By observing the numbers of signals, fewer than 100 events were recorded in Test 3, whereas more than 6000 events were in Test 4, which indicated that uniform corrosion was greatly suppressed in Test 3 because of the cathodic protection. Nevertheless, three types of signals still appeared during both tests. Typical waveforms and frequency spectrums of these three types are shown in Figure 3.12(a), Figure 3.12(b), and Figure 3.12(c), respectively. Figure 3.13 exhibits the Time-Amplitude graphs of the three types of signals from Test 3 (Figure 3.13(a)) and Test 4 (Figure 3.13(b)). The quantities of each type are shown in Table 3.5.
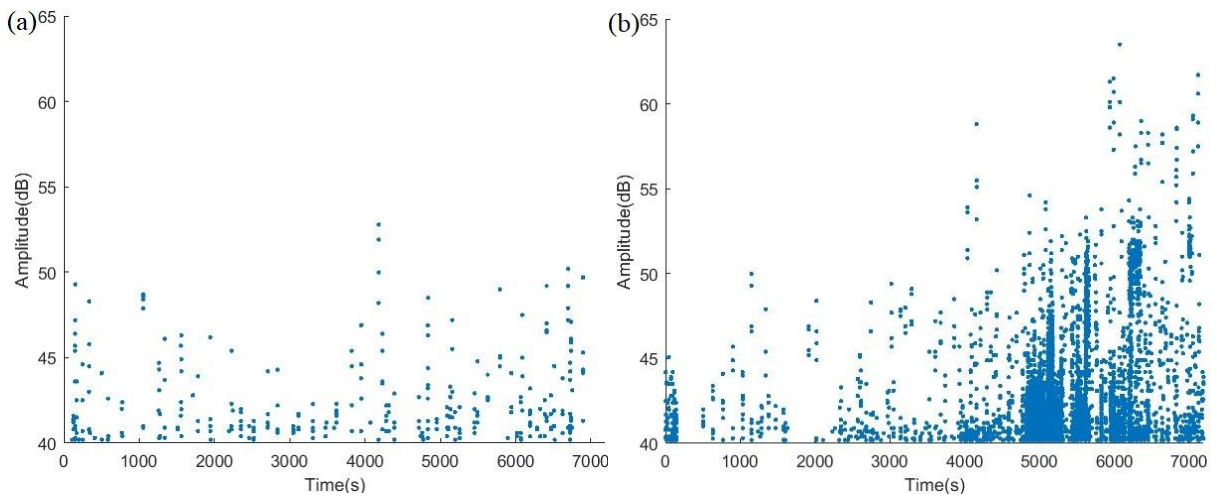
Figure 3.11 Representation about the Time-Amplitude graph of signals from (a) Test 3 (b) Test 4
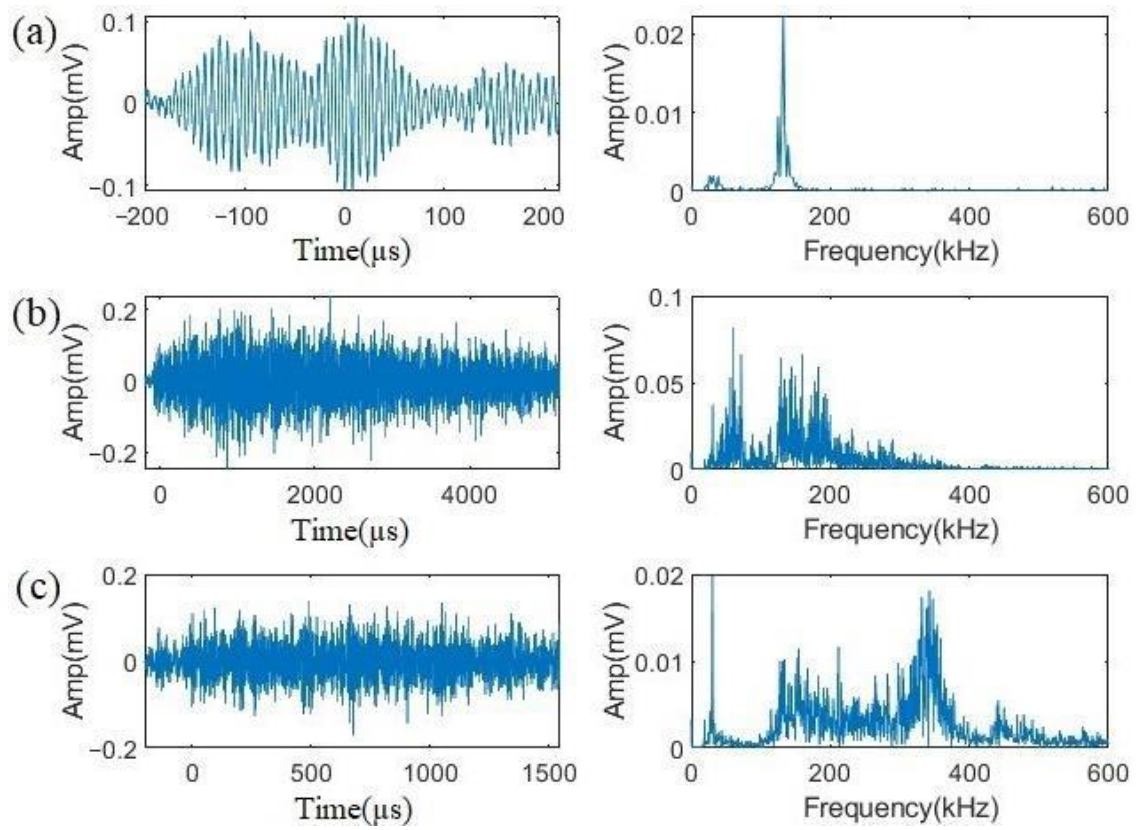
Figure 3.12 Typical waveform and frequency spectrum of signals: (a) Type 1, (b) Type 2, (c) Type 3
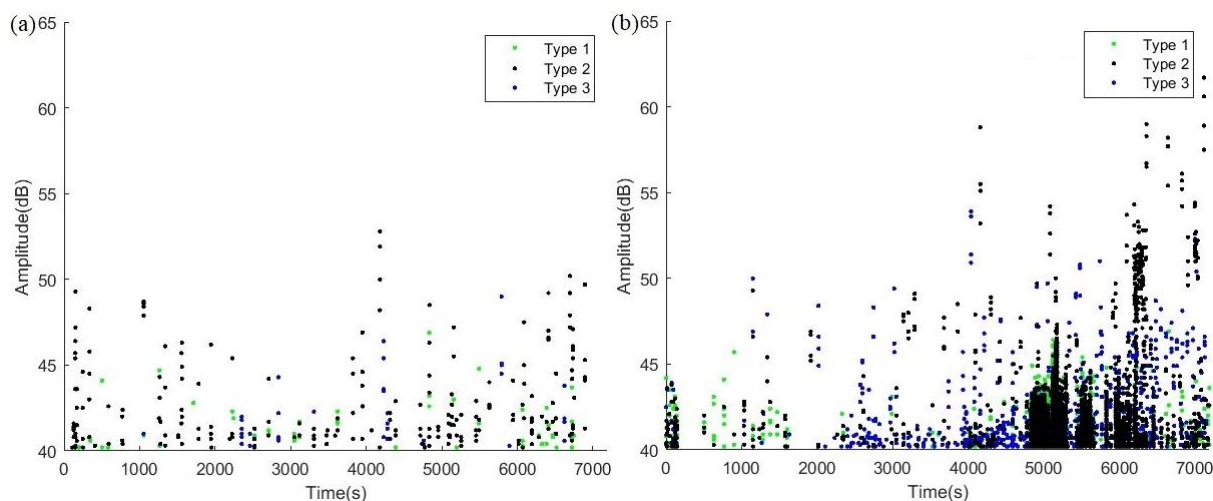
Figure 3.13 Representation about the Time-Amplitude graph of the three types of signals from (a) Test 3 (b) Test 4

Table 3.5 Events quantity of each signal type in Tests 3 and 4

Quantity of Events	Type 1	Type 2	Type 3
Test 3	25	38	19
Test 4	1641	4756	297

Similar to the results of Tests 1 and 2, signals belonging to Type 1 have low amplitudes, short durations, with a narrow peak frequency at about 150 kHz. Type 2 signals differ from Type 1 as they contain significantly more low-frequency content between 50 to 100 kHz, and their peak frequencies spread out up to 200 kHz. Type 3 signals were present in small amounts in both tests with waveforms similar to those of Type 2, but high-frequency components accounted for a large proportion with the peak frequency generally weighted at 350 kHz. As shown in Table 3.2, the most different phenomena between Tests 3 and 4 is that significant uniform corrosions happen in Test 4 while that reaction is largely suppressed in Test 3, which corresponds to the situation of Type 2 signals. Signals of Type 2 accounted for 46.34% in Test 3, but the proportion reached 71.05% in Test 4 where large numbers of signals were obtained after 20 min, indicating uniform corrosion. In the same way as Types 1 and 3 were classified in Tests 1 and 2, signals of Type 1 appeared earlier than those of Type 3 in Test 3. This indicates that Type 1 signals are from H_2 evolution while Type 3 signals are from crevice corrosion.

3.2.3 Discussions

For Test 1 on a small specimen and Test 3 on a big specimen, it was found that three types of signals derived from H_2 evolution, uniform corrosion and crevice corrosion were generated in both tests. In the tests whether with small or big specimens, the distinct difference among the three types of signals is the distributions of the frequency spectrum. Table 3.6 displays the frequency component distribution of signals from the three different mechanisms. It is concluded that all these three types of signals have the components with the frequency between 100-200kHz. Nevertheless, signals of uniform corrosion contained more lower frequency components (<100kHz) compared with signals of H_2 evolution, while more higher frequency components (>200kHz) appeared in the signals of crevice corrosion. Signals of each type in Tests 1 and 3 have the same frequency component distributions. Note that the distributions of the frequency spectrum in this study were made as 0-100kHz, 100-200kHz, 200-300kHz and 300-400kHz, with no further subdivisions. Subtle changes in the signal spectrum due to different specimens' specifications are thus ignored. In addition, it is also noticed that the waveforms of signals from each type in Tests 1 and 3 showed a more distinct difference.

Table 3.6 Frequency component distribution of signals from different mechanisms in Tests 1 and 3

Mechanisms of signals	Frequency component distribution (kHz)		
	<100	100-200	>200
H_2 evolution		√	
Uniform corrosion	√	√	
Crevice corrosion		√	√

Some basic characteristics can be extracted for signal analysis, such as Amplitude (A), Rise Time (RT), Duration (D), Counts (CNTs), Energy (E) and Root Mean Square (RMS). Generally, signals from different mechanisms exhibit the characteristics with different ranges of values. Therefore, these characteristics in time domain can be used for signal classification. However, not all characteristics can be used as a specific parameter to represent a mechanism in some cases. For example, it is meaningless to analyse the characteristic if one set of its value was totally covered by another one or if the distribution areas of values of the two sets significantly overlap. The ideal good

characteristics for signal discrimination should satisfy that the values within a group are compact, while values between groups are distinct.

Coefficient of variation (CoV) is a statistic that measures the dispersion of data distribution, which is always used for the comparison of variation degrees of multiple parameters [164]. The larger the CoV value is, the more dispersed the set of data will be. Based on the known classification results, the CoV values of four groups (data from all signals, signals from H_2 evolution, uniform corrosion and crevice corrosion) were calculated for each characteristic, which are shown in Figure 3.14(a) for Test 1 and Figure 3.14(b) for Test 3. For brevity, the CoV value calculated with all data obtained from Test 1 was abbreviated as SA-CoV, simultaneously; the CoV values calculated with signal data derived from H_2 evolution, uniform corrosion and crevice corrosion obtained from Test 1 were abbreviated as S1-CoV, S2-CoV and S3-CoV, respectively. Similarly, for Test 3 on the big specimen, the CoV values calculated with different groups of data were in turn abbreviated as BA-CoV, B1-CoV, B2-CoV and B3-CoV. For SA-CoV and BA-CoV, a larger CoV value means that the signal represented by the characteristic is distinctive, which is possibly better used for signal discrimination. As for the data within a group, it is better to obtain a smaller CoV value that means this characteristic is representative for this group of signals.
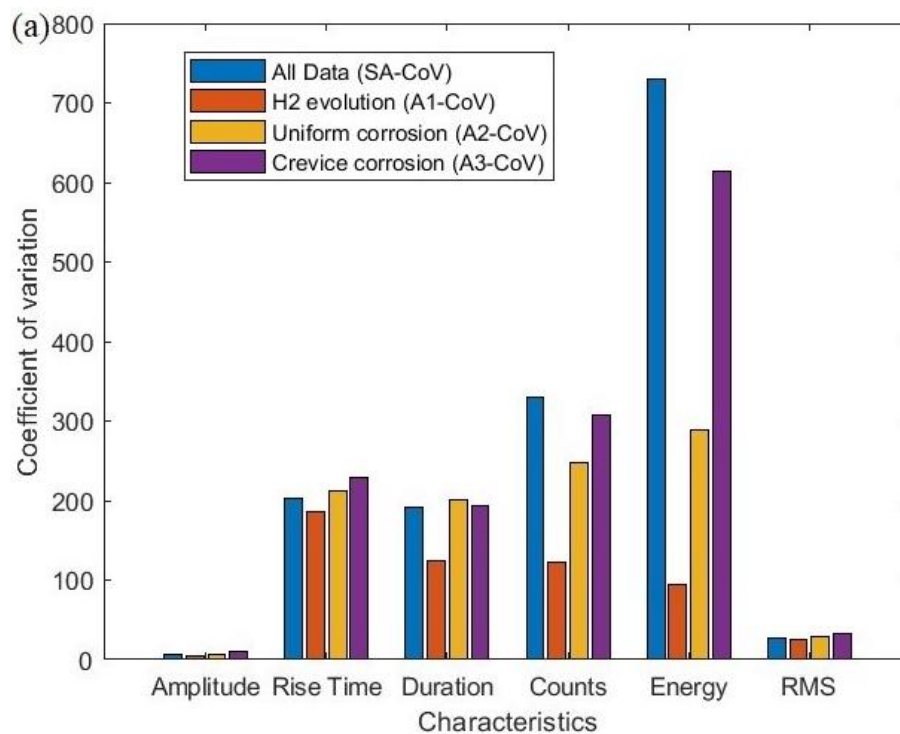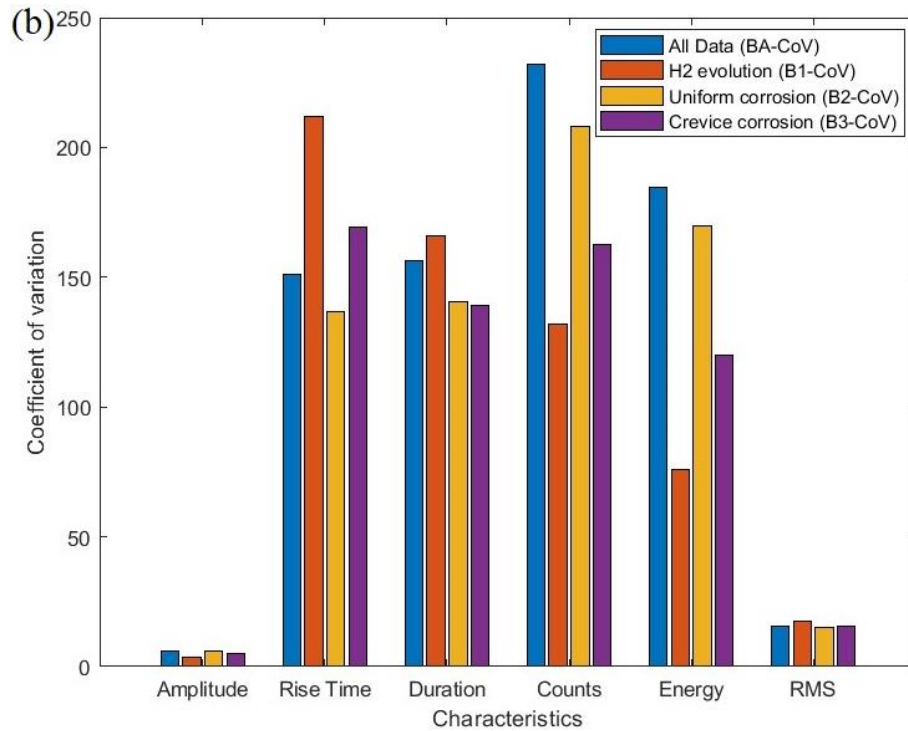
Figure 3.14 CoV of characteristics in time domain of signals from different groups (a) Test 1 with small specimen (b) Test 3 with big specimen

First of all, it can be seen in Figures 3.14(a) and (b) that the SA-CoV and BA-CoV of Rise Time, Duration, Counts and Energy are much higher than those of Amplitude and RMS. It demonstrates that Rise Time, Duration, Counts and Energy are better to be used for signal discrimination. However, for Rise Time, the S1-CoV, S2-CoV and S3-CoV are almost the same as SA-CoV, meanwhile; the B1-CoV and B3-CoV are even higher than BA-CoV. This indicated that RT is not a suitable parameter for signal discrimination because the RT values of signals from different mechanisms were mixed evenly. As for Duration, Counts and Energy, the CoV values calculated with signals from different mechanisms are smaller than CoV value of corresponding parameters calculated with data from all signals. Therefore, Duration, Counts and Energy are considered to be used as the representative parameters in time domain for signal discrimination. Figures 3.15 (a) and (b) show the Duration-Counts-Energy graphs of signals from different mechanisms obtained from the Test 1 and Test 3, respectively. It can be seen that the features' values of signals of uniform corrosion and crevice corrosion distributed widely while those values of signals from H_2 evolution gathered in a certain range. Table 3.7 summarises the ranges of Duration, Counts and Energy of signals derived from H_2 evolution.
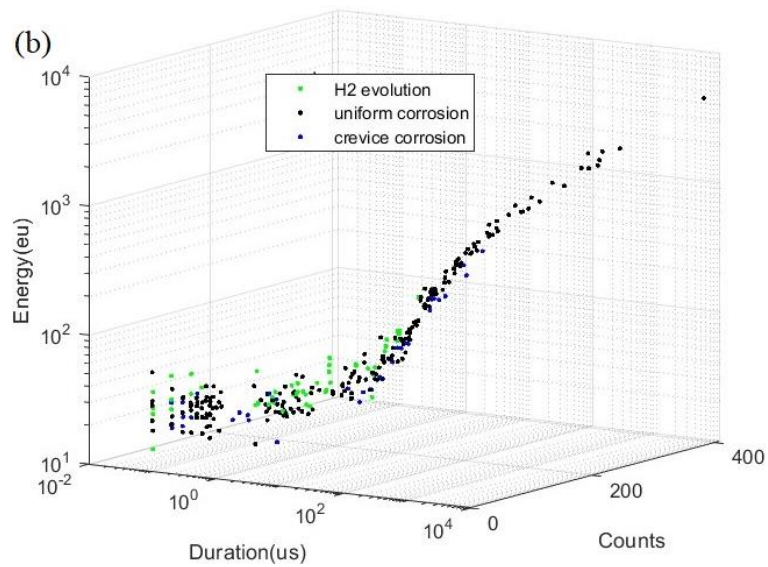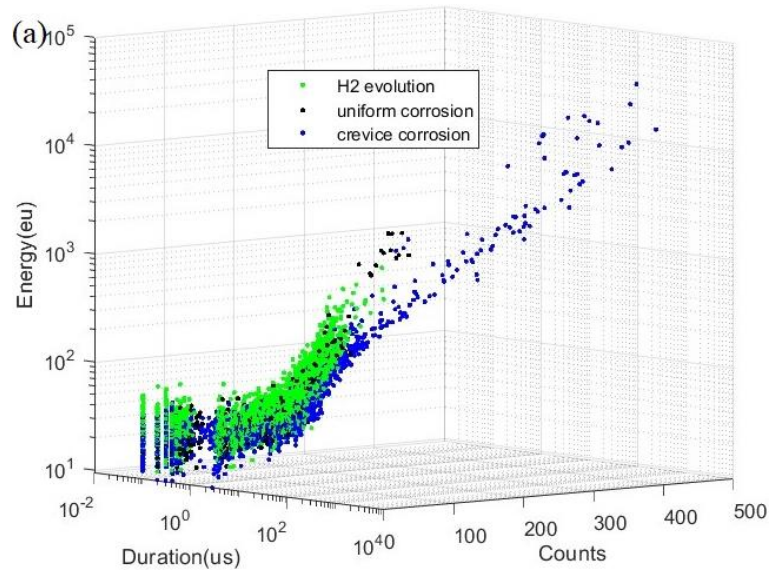
Figure 3.15 Representation of Duration-Counts-Energy of three types of signals (a) Test 1 with small specimen (b) Test 3 with big specimen

Table 3.7 Ranges of Duration, Counts and Energy of signals derived from H_2 evolution

	Duration (us)	Energy (eu)	Counts
Test 1 with small specimen	<400	<400	<25
Test 3 with big specimen	<600	<200	<15

3.3 Experimental Setup and Initial results of ECHC-HIC tests

3.3.1 Experimental setup

Specimens of A516 carbon steel with the dimensions of 200 × 50 × 5mm and 500 × 300 × 5mm were used for ECHC-HIC tests. Figure 3.16 shows the details of the setup with small specimen. The hydrogen charging area was in the middle of the specimen surface that was processed as Figure 3.6 shows. Figure 3.16(b) demonstrates the relative locations of work area and sensors. Four Nano30 sensors are placed around the hydrogen charging area with parallelogram array. The range of work area in the test with small specimen is 21<x<29, 96<y<104 (unit: mm). Similarly, Figure 3.17 shows the details of the setup with big specimen. Noted that the Sensor 3 was hidden by the container in Figure 3.17(a). The range of work area in the test with big specimen is 246<x<254, 146<y<154 (unit: mm). The distance between each sensor and the centre of HIC area on small specimen and big specimen is shown in Table 3.8. Except for the coordinates of work area and sensors, other parameters are the same for tests with small and big specimens. Each test was carried out for 20h with the specimen and platinum mesh being used as cathode and anode separately.
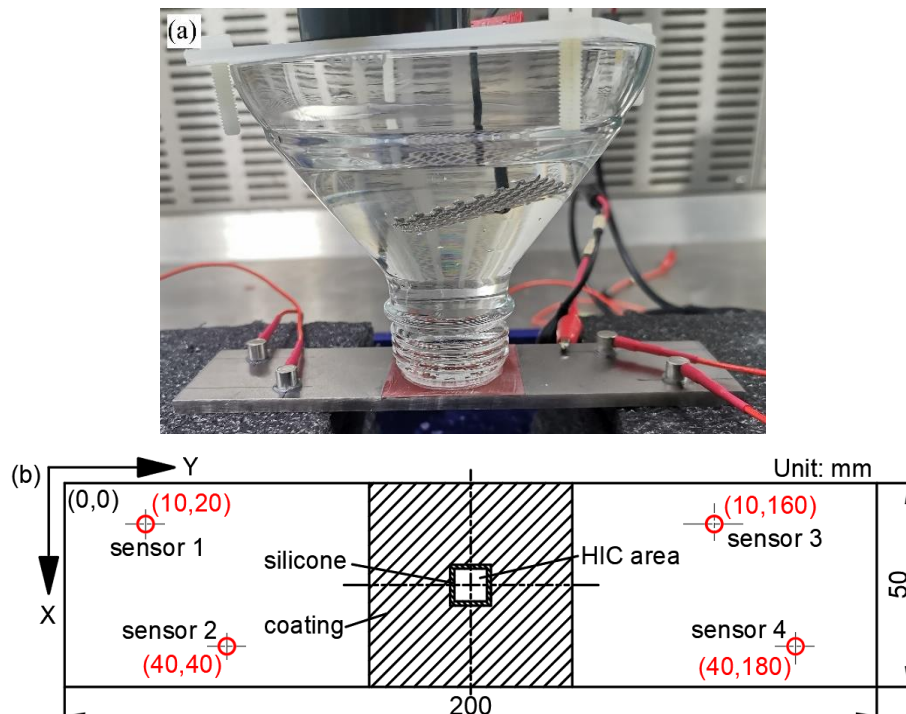
Figure 3.16 Setup of ECHC-HIC test with small specimen (a) physical setup; (b) locations of sensors.
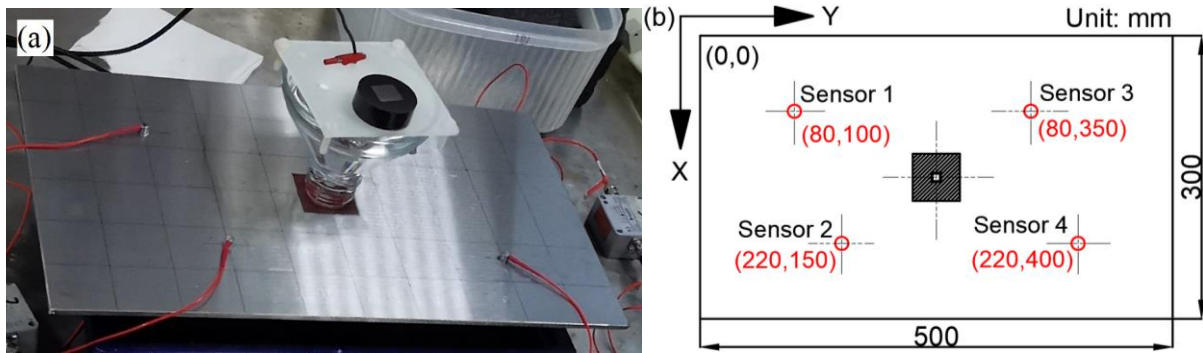
Figure 3.17 Setup of ECHC-HIC test with big specimen (a) physical setup; (b) locations of sensors.

Table 3.8 The distance between each sensor and the centre of HIC area on small specimen and big specimen

Distances(mm)	Sensor 1	Sensor 2	Sensor 3	Sensor 4
Small specimen	81.39	61.85	61.85	81.39
Big specimen	165.53	122.07	122.07	165.53

3.3.2 Observations of initial results

Figures 3.18(a) and 3.18(b) display the observed state of specimen's surface of work area after the testing for both specimens. Three phenomena can be identified in both tests: uniform corrosion at the corners, crevice corrosion at the boundaries and HIC in the square area. The quantity and size of the blisters in both tests are similar. However, the quantity of acquired AE signals from test with small specimen are almost three times than those from test with big specimen, in which the total hits acquired by the four sensors on small specimen was 3914 and that on big specimen was 1715. Figures 3.19(a) and 3.19(b) show the Time-Amplitude graphs of the acquired signals from small and big specimens. It can be seen that the highest amplitude from test with small specimen is 5dB higher than that of test with big specimen. The reasons are supposed to be the strong reflection in small specimen and the signal attenuation in big specimen.
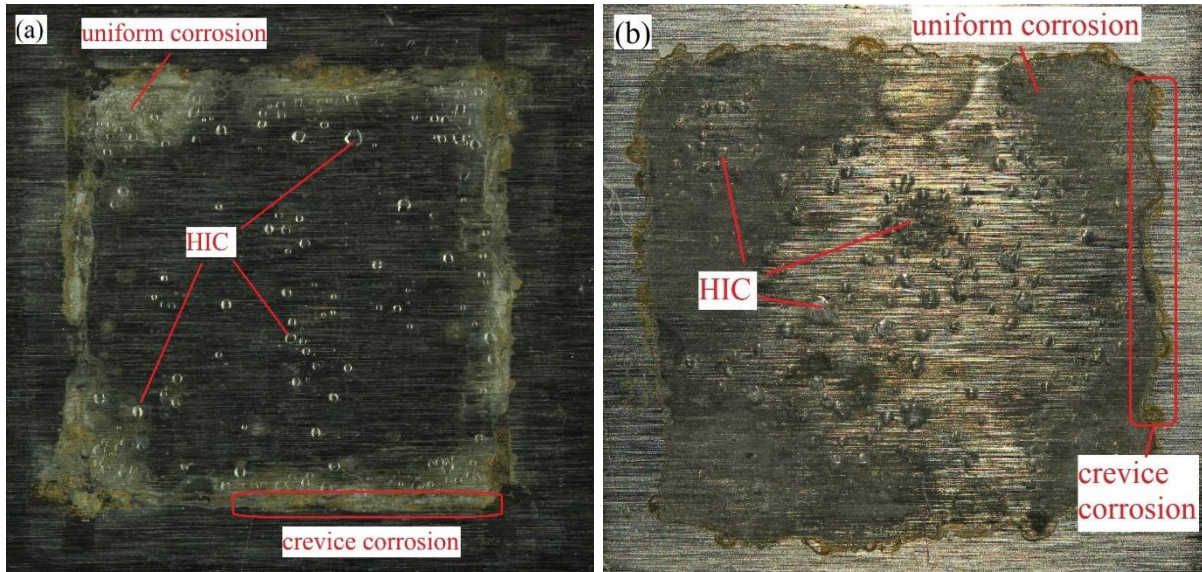
Figure 3.18 Surface observations of ECHC-HIC tests (a) small specimen (b) big specimen
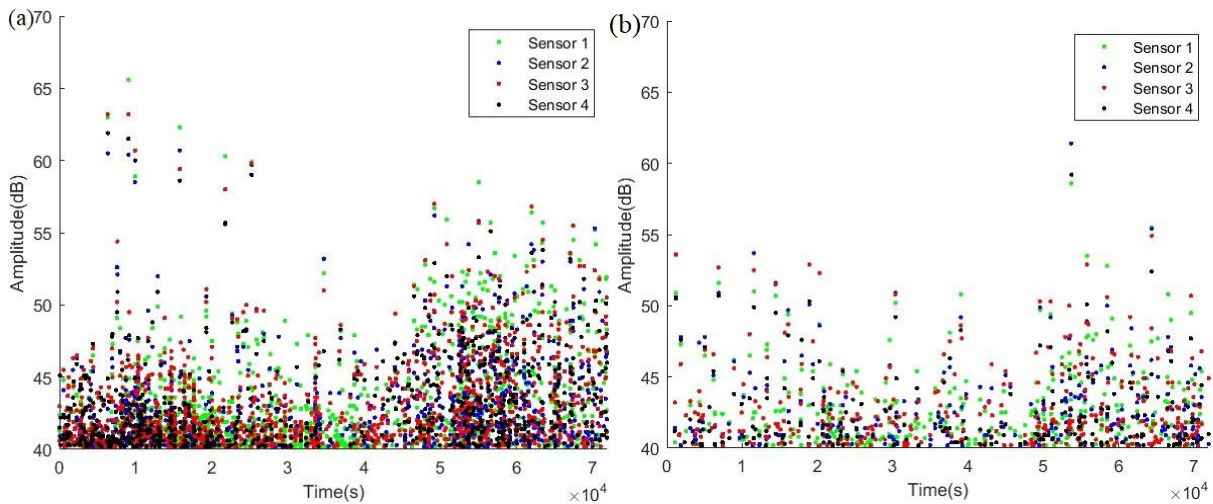
Figure 3.19 Representation of Time-Amplitude of raw signals from four sensors (a) small specimen (b) big specimen

3.4 Signal identification and manual classification

3.4.1 Identification of HIC signals

In the ECHC-HIC tests a new type of AE signal was present in the both small and big specimens, whose waveforms and spectrums are shown in Figure 3.20 and Figure 3.21. Comparing these two signals, the waveforms and spectral distributions are relatively similar, which indicated that this type of signals are from HIC. The difference between these two signals is that the Amplitude of signals acquired from the small-specimen test is higher than that from the big-specimen test, but with shorter Duration.

The reason for this is likely due to superposition of reflected waveforms from the close boundaries not present in the big specimen.
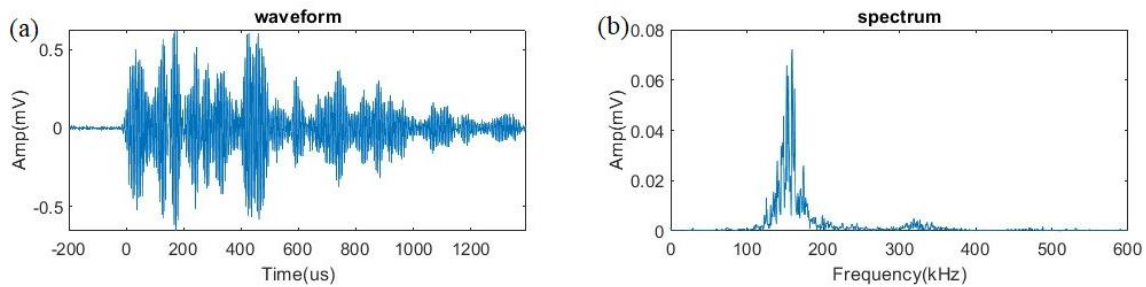
Figure 3.20 A new type of signal related to HIC development obtained from test with small specimen (a) waveform (b) frequency spectrum
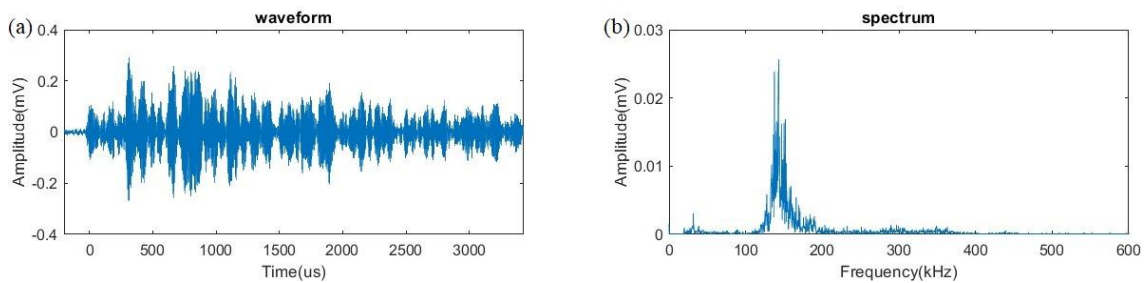
Figure 3.21 A new type of signal related to HIC development obtained from test with big specimen (a) waveform (b) frequency spectrum

Comparing this type of signal with the known ones in Section 3.2 it is easy to distinguish HIC signals from the signals of uniform corrosion and crevice corrosion because of the distinct spectrum. However, the spectral distribution of HIC signal is very similar to signals from H_2 evolution. Therefore, the characteristics in time domain are vital for dividing the signals from HIC and H_2 evolution. Analysing this new type of signals, it can be found that the Duration, Counts and Energy of them are normally bigger than those of signals from H_2 evolution, which can be roughly summarised in Table 3.9.

Table 3.9 Ranges of Duration, Counts and Energy of signals derived from HIC

	Duration (us)	Energy (eu)	Counts
Test 1 with small specimen	>400	>400	>25
Test 3 with big specimen	>600	>200	>15

3.4.2 Manual Classification

The way to classify the four types of signals derived from H_2 evolution, uniform corrosion, crevice corrosion and HIC can be summarized and divided into two steps:

1. According to the different spectral distributions, the mixed signals can be classified into three groups, which are signals of H_2 evolution mixed with HIC signals, signals of uniform corrosion, signals of crevice corrosion.

2. The remaining mixed signals from H_2 evolution and HIC can be divided in the light of characteristics in time domain, which are Duration, Energy and Counts.

For Step 1, it is easy to recognize which mechanism that a signal derived from by looking at its frequency spectrum. However, it is time-consuming to manually check the signals one by one if there are a large amount of data. Two basic characteristics, Peak Frequency and Frequency Gravity, which are extracted from the frequency domain cannot represent all cases well. This is because the peak frequencies of some signals from corrosions may be the same as those from HIC, besides, the calculated frequency gravity is influenced by the selected frequency range. To better express the signals features of frequency domain, the energy spectrum was introduced, which demonstrated the energy of signals changes with frequency [165]. Figure 3.22 shows the energy spectrum of typical signals from HIC, crevice corrosion and uniform corrosion. The spectrums of signals from H_2 evolution had the narrowest band and the lowest energy, which was not visible in this figure. Nevertheless, they are similar to those from HIC whose energy was fully distributed between 100 to 200kHz. It can be seen that the frequency range of all energy distributions is from 0 to 400kHz. Therefore, four partitions on the energy spectrum were divided based on the different distributions of signals from various mechanisms, whose ranges of frequencies are: Part 1 of 0-100kHz, Part 2 of 100-200kHz, Part 3 of 200-300kHz and Part 4 of 300-400kHz. From Figure 3.22, the energy proportions of each part of signals from various mechanisms are distinct. As a result, four parameters were calculated and used for signal classification combining with Peak Frequency: the energy proportion of Part 1 (PE1), Part 2 (PE2), Part 3 (PE3) and Part 4 (PE4). Since the energy spectrum consists of discrete data points, the values of PE1~PE4 were calculated as shown in Equation 3.1:

$$PE1 \sim PE4 = \frac{sum\ of\ energy\ of\ each\ part}{sum\ of\ energy\ of\ four\ parts} \times 100\% \qquad (3.1)$$
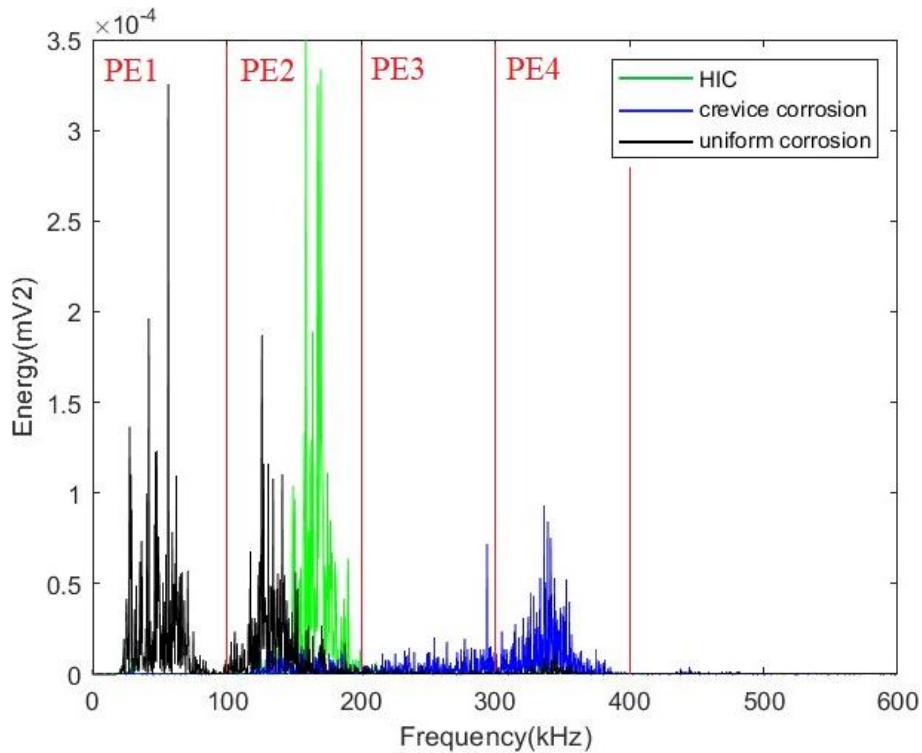
Figure 3.22 Four partitions of energy spectrum of signals in ECHC-HIC tests

3.4.2.1 ECHC-HIC test with small specimen

The energy proportions of four parts of every signal in this test were calculated. Figure 3.23(a) and (b) exhibit the PE1-PE2 and PE1-PE2-Peak Frequency graphs, which can be divided as three areas. Area 1 includes the signals from HIC and H_2 evolution, Area 2 corresponds to the signals from uniform corrosion, whereas Area 3 includes the signals of crevice corrosion. Signals in Area 1 roughly satisfied that the values of PE1 are lower than 8% and the values of PE2 are higher than 90% based on observations. In addition, the value of PE1 of the signal in Area 2 is higher than its values of PE3 and PE4. After manually checking the signals whose values are at the critical line, signals from uniform corrosion and crevice corrosion were classified.
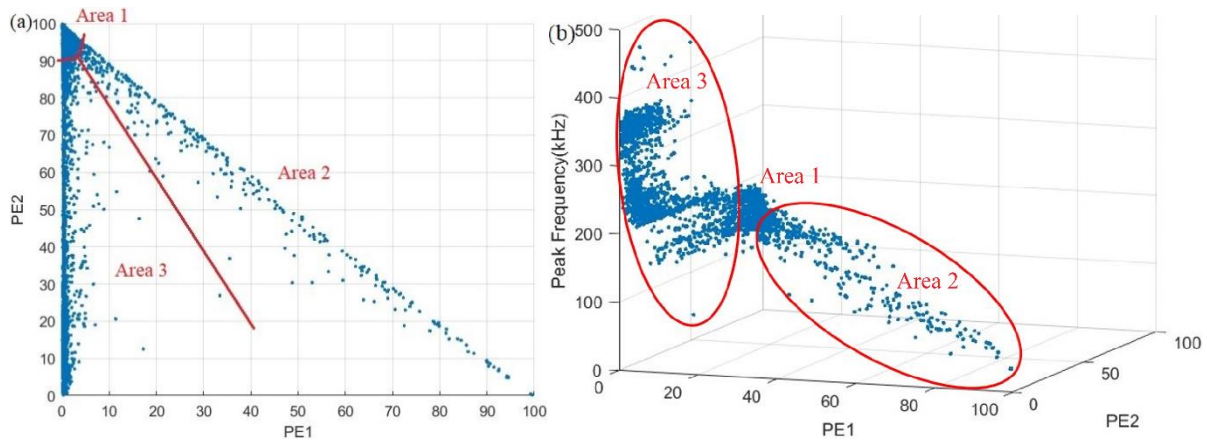
Figure 3.23 Graphs of (a) PE1-PE2 and (b) PE1-PE2-Peak Frequency of signals

In order to differentiate signals from H_2 evolution and HIC, they should be classified in the time domain by Duration, Energy and Counts. As discussed in Section 3.4.1, these characteristics of HIC signals summarily satisfied the conditions: Duration > 400μs, Energy > 400eu and Counts > 25.

Therefore, using this novel approach signals derived from H_2 evolution, HIC, uniform corrosion and crevice corrosion can be classified. In order to observe the HIC progress, the Amplitude of 4 signal clusters and the cumulative Energy of HIC signals vary with time are exhibited in Figure 3.24.
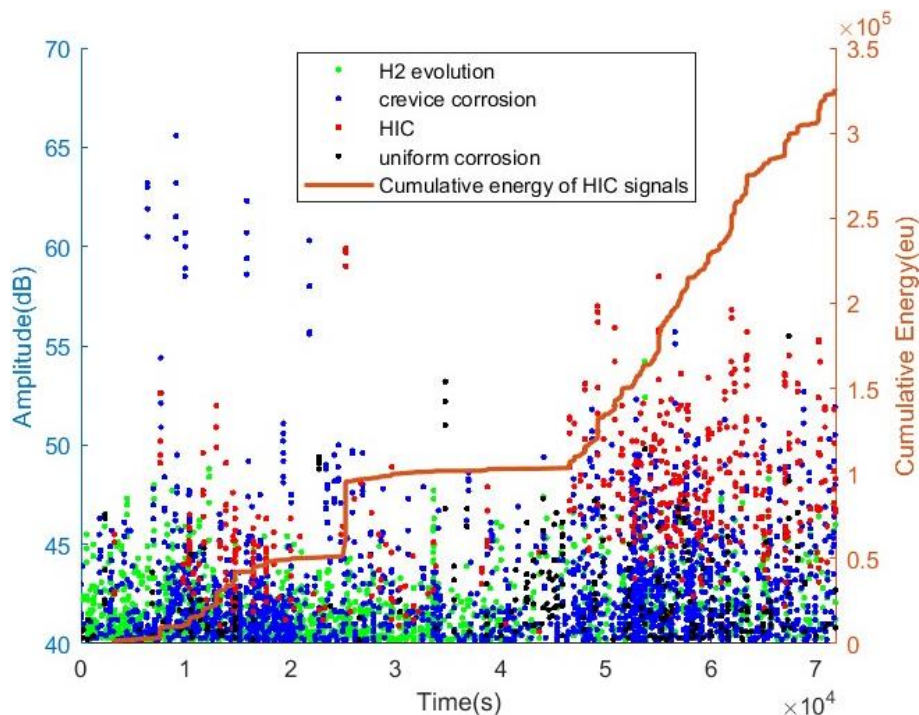
Figure 3.24 Representation of Time-Amplitude of 4 clusters of signals and the Time-Cumulative Energy of HIC signals

3.4.2.2 ECHC-HIC test with big specimen

For the AE results collected from the test on the big specimen, the values of PE1~PE4 of the mixed signals were also calculated. The representation of PE1-PE2 and PE1-PE2-Peak Frequency of signals are shown in Figure 3.25(a) and (b), whose distributions are analogous to those displayed in Figure 3.23, but with less signals. The standard to dividing the Areas 1, 2 and 3 is same as that introduced in Section 3.4.2.1. Noted that the conditions for classify the HIC signals in this test are Duration > 600µs, Energy > 200eu and Counts > 15, which differ than the values used in the analysis of the small specimen.
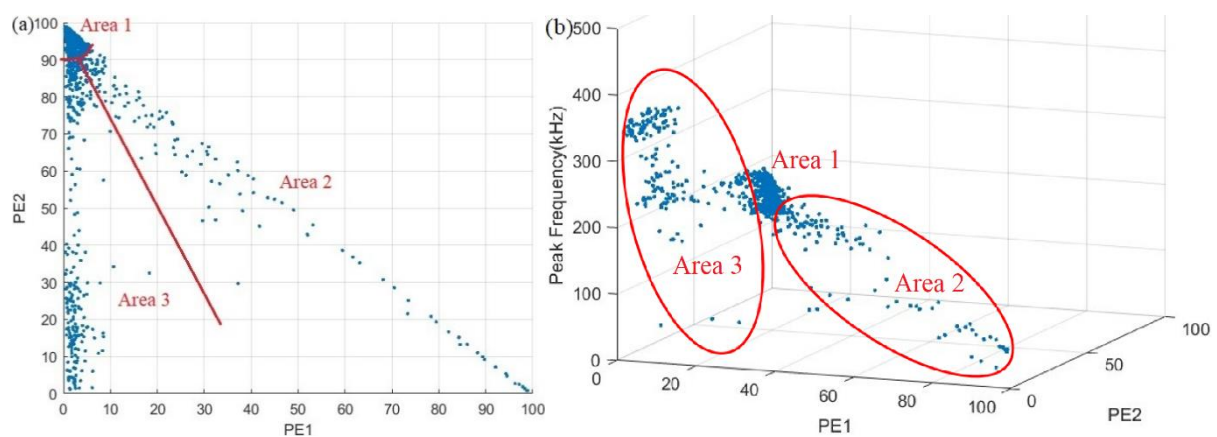
Figure 3.25 Graphs of (a) PE1-PE2 and (b) PE1-PE2-Peak Frequency of signals

After manually classifying the critical signals, four signals clusters were obtained. The Time-Amplitude graph of the 4 clusters of signals in this test is exhibited in Figure 3.26, in which the HIC progress described by cumulative energy of HIC signals is also displayed.
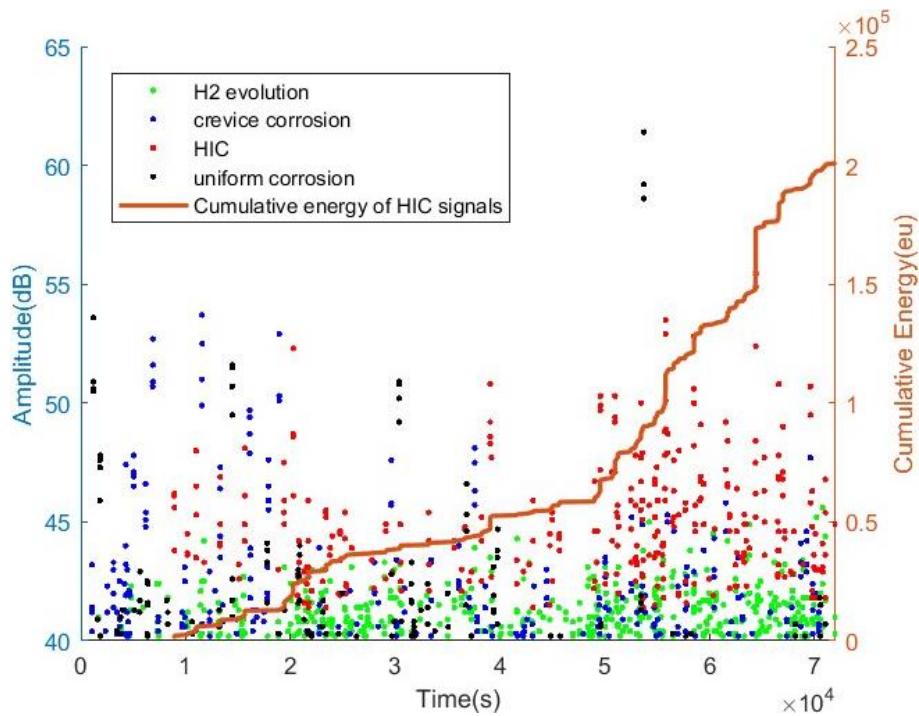
Figure 3.26 Representation of Time-Amplitude of 4 clusters of signals and the Time-Cumulative Energy of HIC signals

3.4.3 Discussions

From Figure 3.24, it can be seen that the first HIC signal was acquired approximately 50mins after the start of test. During the first 7000 seconds, it can be seen that the signals have low amplitude and are primarily from H_2 evolution. From the 2nd hour of the test, a greater number of HIC signals with low amplitude (mostly lower than 50dB) were obtained, which indicated that many small cracks occurred. As the test progresses, more HIC signals with higher amplitude began to be acquired from around the 13th hour of the test. This would indicate the development of bigger crack or the connection of few small cracks.

For the situation on big specimen represented by Figure 3.26, it can be seen that the HIC signals were obtained from the 9000 seconds and more signals with higher amplitude were collected from about 14h in the test. This demonstrated HIC process is similar to that of the small specimen, i.e. small cracks happened in the first 14h of the test, followed by bigger crack growth or the connections of few small cracks occurred in the later of test.

Comparing Figures 3.24 and 3.26, it can be seen that the trends of HIC progression of the tests with small and big specimen are similar under the same experimental

conditions. A large amount of small HIC occurred after hydrogen charging for 2h and bigger cracks or connections among cracks appeared after 12h resulting from the observation of acquired HIC signals with higher amplitude and higher energy. However, it is also obvious that the amplitudes of signals from test with big specimen are generally 5dB lower than those from test with small specimen. Besides, the overall quantity and energy clearly decrease as well, especially the signals from H_2 evolution and crevice corrosion.

The difference in amplitude between these two tests are likely to be caused by two reasons. One is the boundary reflection of signals on the small specimen. Another is signal attenuation because of the long propagation distance on the big specimen, which is the major influence factor. In addition, the threshold set at 40dB also leads to the quantity reduction of signals from the test with big specimen.

To better analyse the effect of specimen's specification on the propagation of the 4 types of signals, the attenuation influence was considered on the AE results obtained from small specimen. In the infinite plate with homogenous medium, the quantity of signals acquired by remote sensor is same as that acquired by proximity sensor (as shown in Figure 3.27(a)) without setting the amplitude threshold. Nevertheless, the amplitude of signals obtained by remote sensor will be lower due to the influence of attenuation. Ideally, the amplitude reductions of signals derived from a same mechanism should be equal. Therefore, the trend of signals' quantity corresponding to each amplitude varying with the amplitude should be the same between proximity and remote sensors. As shown in Figure 3.27(b), the Quantity-Amplitude correlation of remote sensor is parallel to that of proximity sensor in the light of a large numbers of signals from the same mechanism. The amplitude difference (AD) between these two sensors of each signal is thus ideally the same, i.e. AD1=AD2.
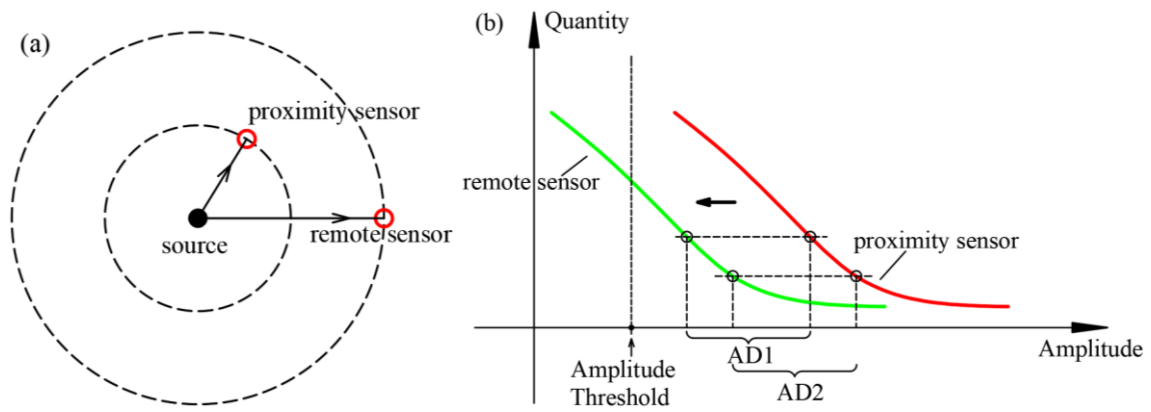
Figure 3.27 (a) signal propagation on an infinite homogenous plate (b) the correlation of Quantity-Amplitude between proximity and remote sensors

As the sensors of the tests on small and big specimen were placed as Figures 3.16 and 3.17 are showing, the Quantity-Amplitude correlation of signals collected with each channel from each mechanism was analysed for detailed comparison. The Quantity-Amplitude curves were obtained by fitting the histogram with appropriate function through observing the Quantity-Amplitude distribution. The comparison of the Quantity-Amplitude curves between the two tests of each channel for each signal mechanism are displayed in Figure 3.28, Figure 3.29, Figure 3.30, Figure 3.31, which represented for H_2 evolution, crevice corrosion, uniform corrosion and HIC, respectively.

However, in this study, the Quantity-Amplitude curves were not complete due to the set amplitude threshold. Besides, boundary reflection on small and big specimen influenced the amplitude significantly. As a result, the Quantity-Amplitude curves obtained from the tests with small and big specimen were not parallel, meanwhile, amplitude difference were calculated as $(AD1 + AD2)/2$ for accuracy.
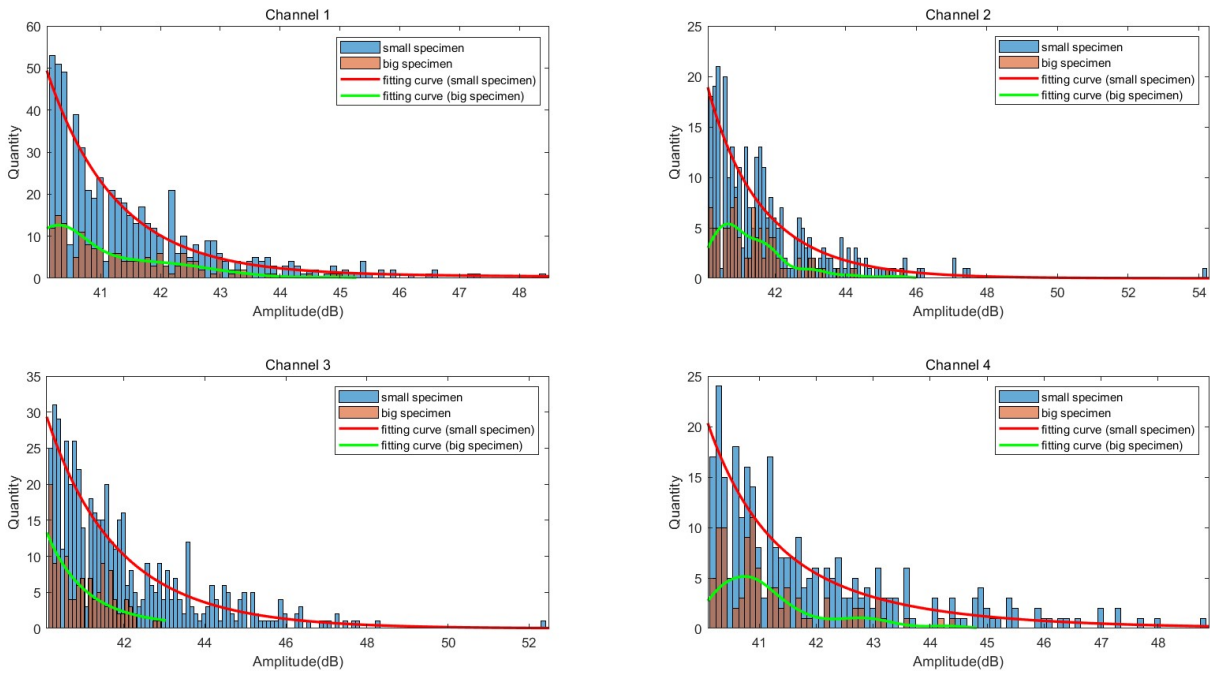
Figure 3.28 Histograms and fitting curves of Quantity-Amplitude of signals from each channel for H₂ evolution
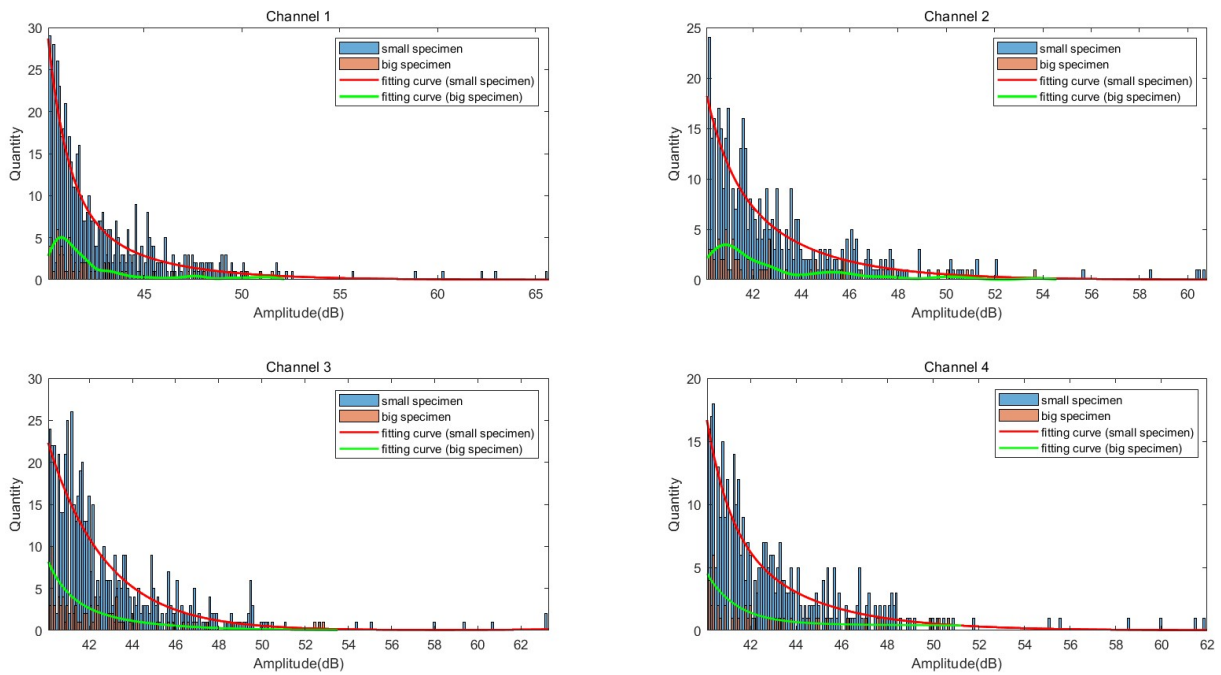
Figure 3.29 Histograms and fitting curves of Quantity-Amplitude of signals from each channel for crevice corrosion
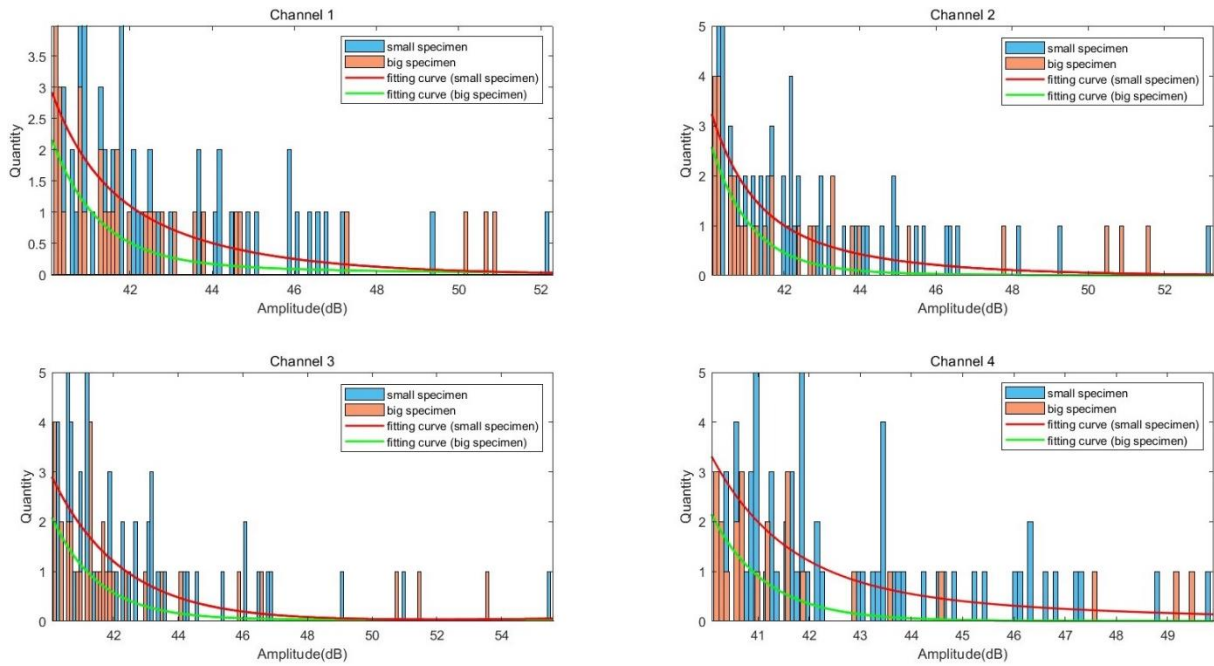
Figure 3.30 Histograms and fitting curves of Quantity-Amplitude of signals from each channel for uniform corrosion
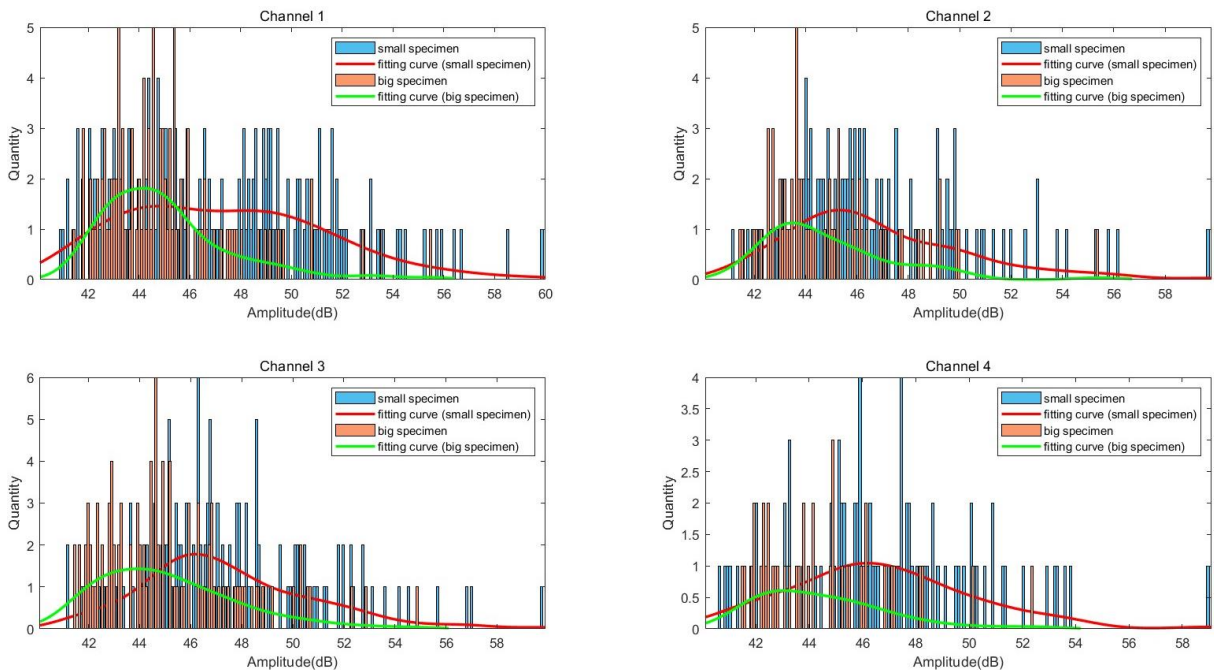
Figure 3.31 Histograms and fitting curves of Quantity-Amplitude of signals from each channel for HIC

In this way, the amplitude differences of signals between tests with small and big specimens of each channel were calculated and displayed in Table 3.10. It can be seen that the attenuation of signals from crevice corrosion was the most severe in this study, which is around 2.7dB. The signals which is least affected by specimen's specification is derived from uniform corrosion. This result demonstrated that signals

containing high frequency components are attenuated more than signals containing low frequency components, which supports the findings of Shehadeh [166]. Based on the values in Table 3.10, the influence of attenuation was applied to the AE results collected from test with small specimen. In the light of Figure 3.14, the two signal characteristics of Counts and Energy are better to express the difference among the various signals. Thus, the energy and counts were recalculated for the attenuated signals. Combining with Peak Frequencies of signals, the Energy-Counts-Peak Frequency graphs of the signals and attenuated signals from the test with small specimen, signals from the test with big specimen were compared in Figures 3.32(a), (b) and (c). At the same time, the changes of signal quantities in the three situations are displayed in Table 3.11.

Table 3.10 The amplitude difference (dB) of signals between tests with small and big specimens of each channel

Amplitude Difference (dB) \ Channels Signal	Channel 1	Channel 2	Channel 3	Channel 4
H$_2$ evolution	1.2	1.2	1.3	0.8
Crevice	2.5	3.0	2.7	2.7
Uniform	1.0	0.6	0.8	0.9
HIC	1.6	1.9	2.3	2.5
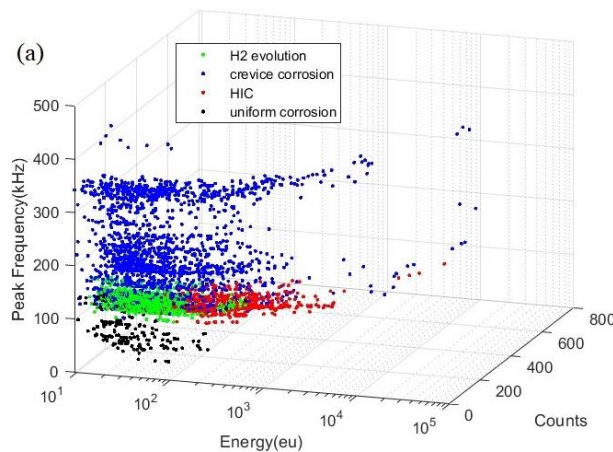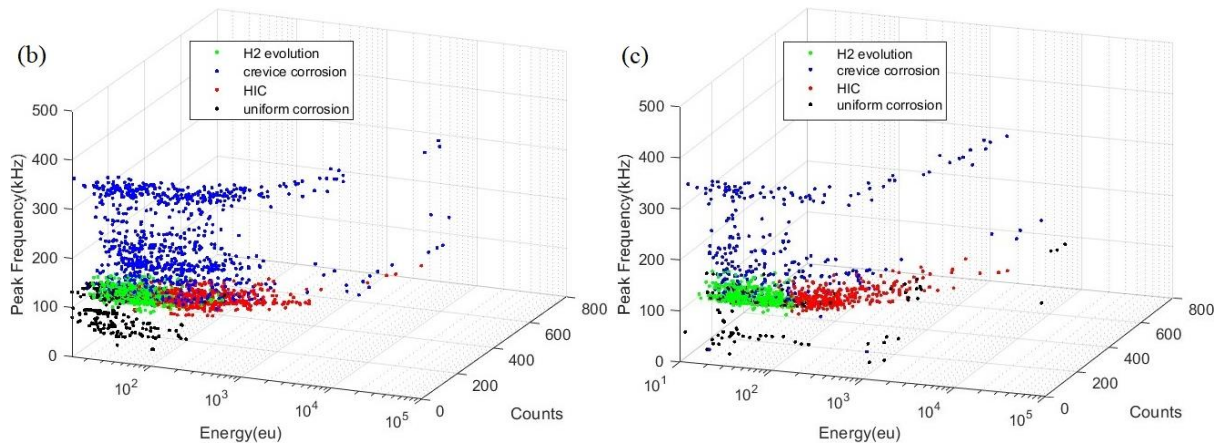
Figure 3.32 Energy-Counts-Peak Frequency graphs of 4 signal clusters (a) Signals from test with small specimen (b) Attenuated signals from test with small specimen (c) Signals from test with big specimen

Table 3.11 The quantity and proportions of 4 signal clusters from tests with small and big specimens

Tests' Results / Four Clusters	Signals from test with small specimen		Attenuated signals from test with small specimen			Signals from test with big specimen	
	Quantity	Proportion	Quantity	Proportion	Reduction rate	Quantity	Proportion
H₂ evolution	1268	32.78%	709	30.17%	44.09%	475	40.16%
Crevice	1835	47.44%	936	39.83%	48.99%	258	21.98%
Uniform	290	7.5%	255	10.85%	12.07%	127	10.82%
HIC	475	12.28%	450	19.15%	5.6%	314	26.75%
Total Quantity	3868		2350			1174	

Comparing Figure 3.32(c) to Figure 3.32(a), too many signals of crevice corrosion existed in the test with small specimen in the light of quantity. After considering the influence of attenuation, it is obvious that a large number of signals with lower amplitude from crevice corrosion were eliminated. The distributions of 4-cluster signals in Figure 3.32(b) are closer to the situation of the results from the test with big specimen, including the value of critical energy which are used to divide the signals from H_2 evolution and HIC. At the same time, the quantity proportion of attenuated signals from each mechanism is more similar to the results from the test with big specimen, which is shown in Table 3.11. Compared the reduction rate of each cluster, the reduced signals basically came from H_2 evolution and crevice corrosion, while the reduction rate of HIC signals was only 5.6%. This indicated that the acquisition of HIC signals were less affected by the specimen's specification with the same other experimental conditions. In addition, it is beneficial to reduce the collection of non-HIC signals by carrying out ECHC-HIC test with bigger specimen. However, the attenuation

results obtained by this method are only applicable to the experimental conditions of this study. Once the specimen's specifications are changed, the exact degree of signal attenuation needs to be recalculated, resulting from the different boundary reflections.

3.5 Velocity Determination of Signal Propagation

In addition to extracting the HIC signals accurately and analysing HIC progress, another important issue is to determinate the location of HIC source. Some commonly used method for source location were introduced in Section 2.3.4.1. However, the velocity of signal propagation on the plate should preferably be known. Generally, Pencil Lead Break (PLB) tests are used to understand the propagation velocity of waves on objects due to their repeatability and simple setup. For this study, the aim is to calculate the velocity of signals from HIC events and locate them then. However, signals from PLB events have a wide band frequency distribution, which are different from HIC signals. Due to the dispersion characteristics of Lamb waves, the wave velocity calculated from the PLB events cannot truly represent the results of the HIC signals. Therefore, two experiments were applied for calculating the propagation velocity of HIC signals on small and big specimen.

For the carbon steel plate of 5 mm thickness used in this study, Figure 3.33 illustrates the dispersion curve of wave propagation with S_0, A_0, and A1 modes. This dispersion curve was calculated by 'Vallen Dispersion' software with three inputs: longitudinal wave velocity of 5900m/ms, shear wave velocity of 3200m/ms and the thickness of 5mm. The higher order modes (S_1, A_2, S_2…) correspond to the frequency components higher than 400kHz, which were not included in any types of signals in the ECHC-HIC tests.
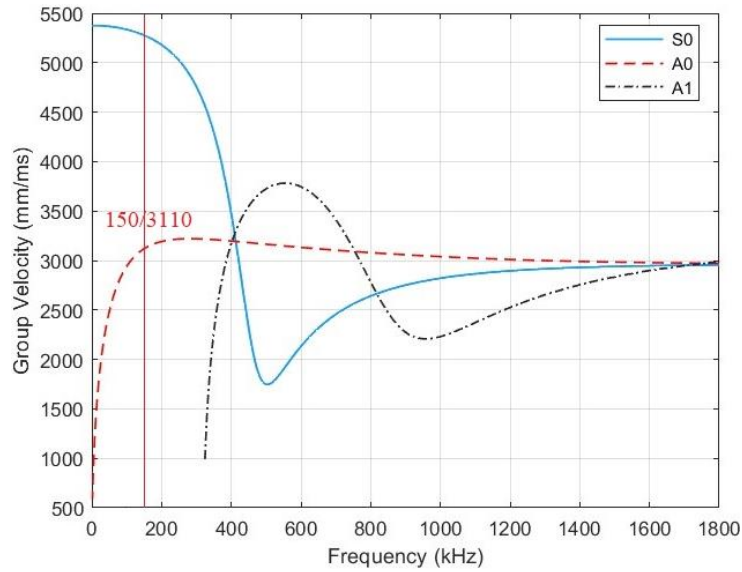
Figure 3.33 Dispersion curve of Lamb wave signals propagating in 5mm thickness A516 plate

3.5.1 Experimental setup

Due to the scale limitation of small specimen, the experimental setup for velocity determination is designed as shown in Figure 3.34 (a), where the same HIC generation setup as used in Figure 3.16 was applied with a fresh specimen. The coordinates of Sensors 1, 2, 3 and 4 are given in Figure 3.34(b). The differences of distance and time between Sensor 4 to Sensors 1, 2 and 3 are marked as d_{14} and t_{14}, d_{24} and t_{24}, d_{34} and t_{34}, respectively. It is noted that the sensor 4 was placed under the work area. Therefore, the velocity of each signal acquired by each sensor can be calculated as $\frac{d_{14}}{t_{14}}$, $\frac{d_{24}}{t_{24}}$ and $\frac{d_{34}}{t_{34}}$.

For big specimen, four sensors were placed as a line across the HIC area. The experimental setup is shown in Figure 3.35(a) and the specific distances are given in Figure 3.35(b). Similarly, the velocity of each signal acquired by each sensor can be calculated as $\frac{d_{12}}{t_{12}}$, $\frac{d_{13}}{t_{13}}$ and $\frac{d_{14}}{t_{14}}$.
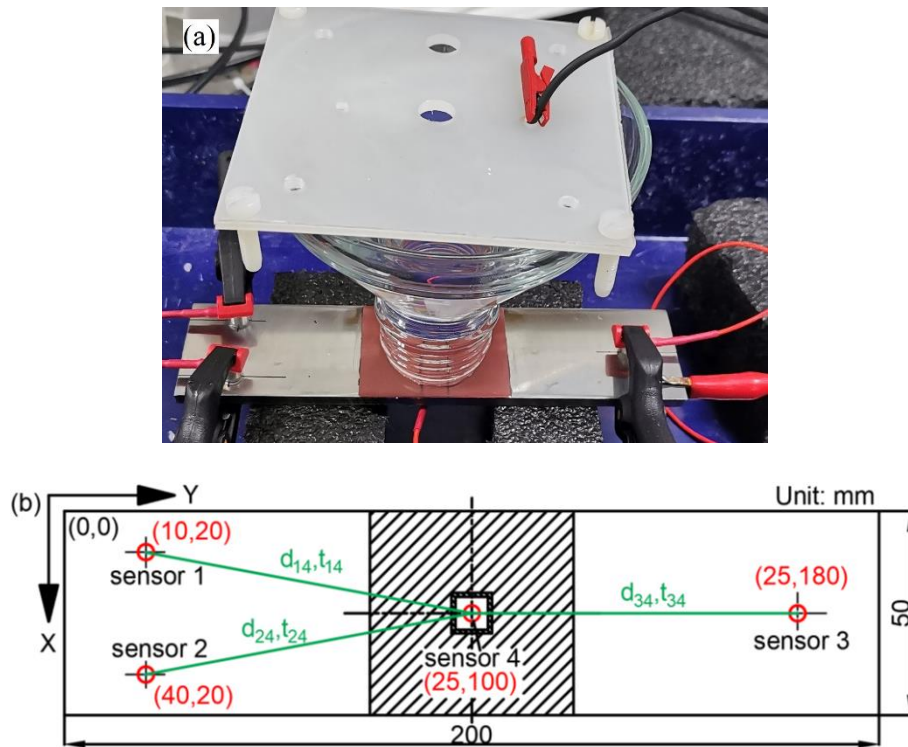
Figure 3.34 Setup of test for propagation velocity with small specimen (a) physical setup; (b) locations of sensors.
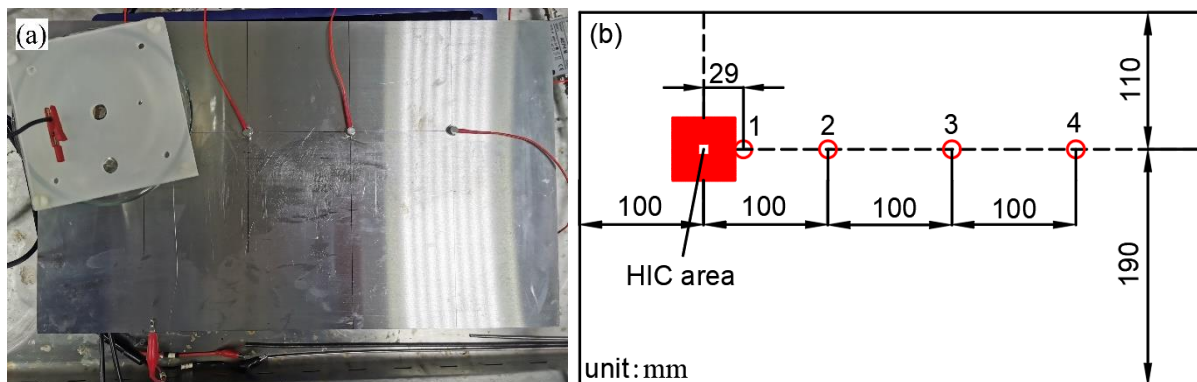
Figure 3.35 Setup of test for propagation velocity with big specimen (a) physical setup; (b) locations of sensors.

3.5.2 Results and Discussions

Signal velocity is the ratio of the distance difference to the time difference between two sensors. The distance difference is known but the time difference needs to be calculated by confirming the onset time of each signal. It can be observed in Figure 3.18 that the diameters of hydrogen blisters were less than 1mm. Due to the small size of HIC developed by electrochemical hydrogen charging method, the released energy was low when the cracks propagate. Despite the background noise was well controlled

under the laboratory conditions, the SNR of the signals was still low. Besides, the signal was attenuated after propagating for a certain distance, which further reduced the SNR. The AIC method, which was introduced in Section 2.3.4.2, is therefore suitable for improving the accuracy of onset time selection of HIC signals. The result is more reliable than that obtained by the threshold-crossing method because AIC method does not depend on any variables. Signals from HIC events in both experiments were manually classified through the approach as introduced in Section 3.4.2. After that, the determination of each signal's onset time was improved by the AIC algorithm. Then, the velocity of each HIC signal was calculated.

The results for these tests with small and big specimen are shown in Figure 3.36 and Figure 3.37, respectively. Figure 3.36(a) and Figure 3.37(a) represent the results calculated from the original onset time which is selected by threshold-crossing method, while Figure 3.36(b) and Figure 3.37(b) demonstrate the results after applying the AIC method. It can be seen that the data distributions in Figure 3.36(a) and Figure 3.37(a) are more scattered, while the data distributions in Figure 3.36(b) and Figure 3.37(b) have a relatively centralized trend, especially in the signals with higher amplitude. This indicates that AIC method does improve the accuracy of velocity calculation and most values of velocity were concentrated around 3000mm/ms. The data that are still scattered after applying AIC method were heavily affected by noises, reflections, propagation paths, incomplete waveforms and other factors, which can be treated as negligible. According to the dispersion curve, there are two propagation modes for waves with the main frequency around 150kHz, which are S0 mode with the velocity of 5300 mm/ms and A_0 mode with the velocity of 3110 mm/ms. In the light of the velocity results from those two tests, it can be summarised that the HIC signals were triggered by mode A_0 and with the velocity of 3110 mm/ms.
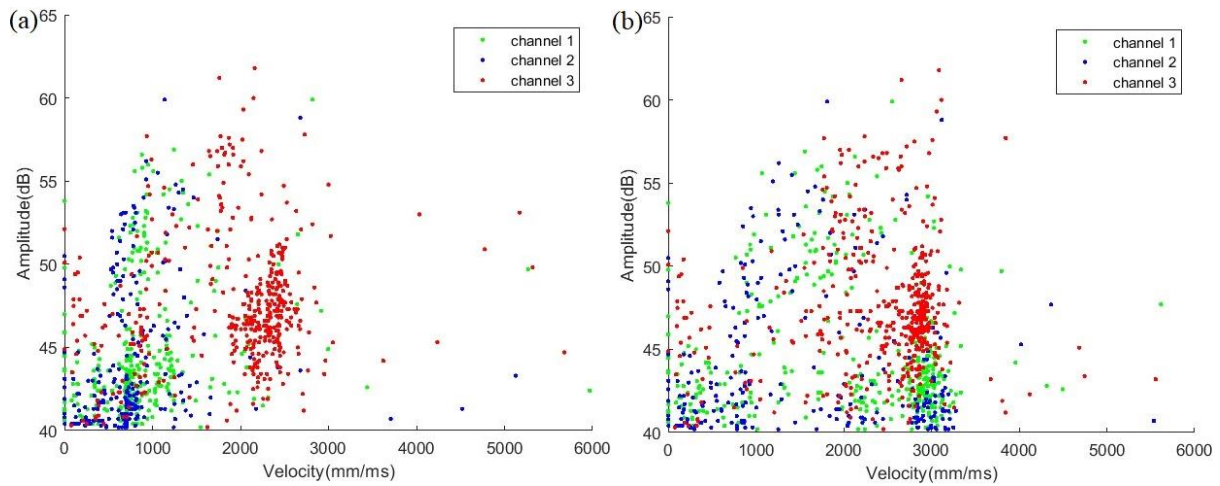
Figure 3.36 Representation of Velocity-Amplitude (a) original results (b) results after applying AIC method
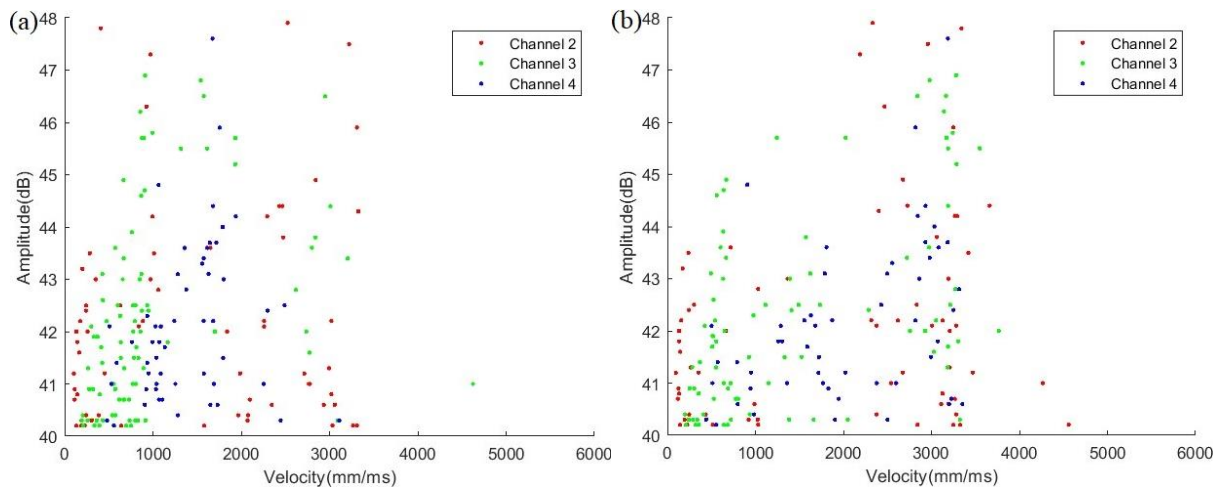
Figure 3.37 Representation of Velocity-Amplitude (a) original results (b) results after applying AIC method

3.6 Source Location

In order to eliminate the influence of non-target events, only signals of HIC were considered for source location analysis. Additionally, only events with signals captured by all four sensors were retained for better localisation. There were thus 118 and 79 HIC events obtained from the tests with small and big specimens, respectively. The onset times of these signals were also selected by AIC method in the same way. Then, the location of each HIC event was determined by Simplex algorithm in this study, which is described in Section 2.3.4.1 in details. The source location results for the tests with small and big specimens were finally exhibited in Figure 3.38 and Figure 3.39, respectively. The work areas for the two tests are indicated by red rectangles. In

addition, the quantity analysis for the source location of HIC events are displayed in Table 3.12.
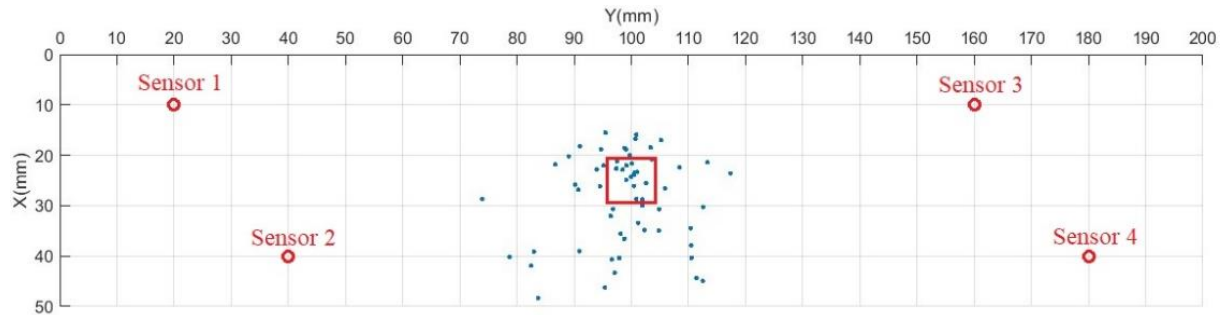
Figure 3.38 Source Location Results for test with small specimen
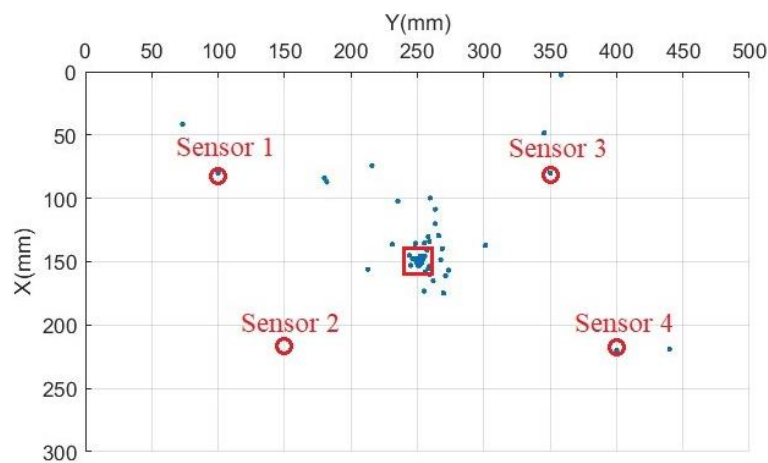
Figure 3.39 Source Location Results for test with big specimen

Table 3.12 Source Location Results summarised

Tests	Total number of HIC events	HIC events located on the plate		HIC events located in the work area	
		Number	Proportion	Number	Proportion
Small specimen	118	64	54.24%	19	16.10%
Big specimen	79	46	58.22%	17	21.52%

It can be seen in Table 3.12 that less than 60% of signals were located on the plate for either the small or the big specimen. The reason that some events were not located on the plates at all is the inaccuracy in the determination of signals' onset time, the errors from the velocity and Simplex method. Compared the quantity results of the two tests, more HIC events located on small plates, but the proportion of events located in the work area is greater in the test with big specimen. From Figures 3.38 and 3.39, it can be seen that the obtained localisation results are more accurate in the Y-axis

direction. This indicates that the boundary reflections also affect the source location accuracy through influencing the signals' onset time. It is demonstrated that the effects of this source location procedure were similar for the tests with small and big specimens, but the localization accuracy is lower on small specimen to some extent resulting from the boundary reflections.

3.7 Conclusions

In this chapter, ECHC method was applied to generate HIC on carbon steel plate under laboratory conditions. Compared with the commonly used hydrogen charging method with H_2S, this method is not only safe and efficient, but also can control experimental parameters and observe experimental progress at any time. The tests with small and big specimens were carried out for providing a basic understanding of the propagation and expression of HIC signals. Signals from HIC were identified by comparing the results of a series of experiments.

It was seen that regardless of whether the HIC signal is propagating on a small plate or a large plate, the frequency distribution was in the range of 100-200kHz with peak frequency at around 150kHz. However, the characteristics of HIC signals from time domain are different. HIC signals propagated on small plate expressed the characteristics of Duration > 400µs, Energy > 400eu and Counts > 25 of while Duration > 600µs, Energy > 200eu and Counts > 15 of HIC signals propagating on big plate. Nevertheless, the HIC progresses described by cumulative energy of two tests were similar.

Moreover, the difference of the number of HIC events between the two tests was not significant, but there were much less non-target signals in the test with big specimen. Therefore, large scale specimen is more suitable to be used in ECHC-HIC test for analysing the mixed signals and HIC development. It should be noted that the distance between the sensor and the work area should not be too far, otherwise too few HIC signals will be collected due to severe attenuation.

The source location results of the two ECHC-HIC tests demonstrated that the parallelogram sensor array and Simplex algorithm worked for source location on 2D plane. Although calculated locations are not very precise, it is enough for the requirement of regional localisation. The error of locations is likely to be primarily

caused by a poor signal to noise ratio, wave reflection, and different propagation directions of the signals, even though the onset time was improved by AIC method.

4 Automatic cluster method for signal clustering of ECHC-HIC experiments

As discussed in Chapter 3, the obtained mixed AE signals were manually classified into 4 groups, which are from H_2 evolution, crevice corrosion, uniform corrosion and HIC, respectively. It was accomplished by applying a series of experimental procedures with small and big specimens. The representative characteristics of signals from different mechanisms were summarized.

However, the characteristics' of signals changed with the parameters of the experimental setup. In order to ensure the accuracy of classification results, the classification procedure needs to be modified for each test with a changed parameter, which is complicated and time-consuming. Therefore, an automatic cluster method is needed for clustering signals directly with the mixed signals acquired from the ECHC-HIC test, similar to machine learning methods.

It was mentioned in Section 2.3.3 that there are mainly two groups of algorithms for clustering, which are supervised learning methods and unsupervised learning methods. Actually, the classification method used in Chapter 3 was essentially equal to the supervised learning method: Decision Tree. However, the basis for splitting each node should be confirmed again to ensure accuracy when the experimental setup is changed. In addition, multiple features need to be used to classify critical signals precisely. This supervised learning method is thus time-consuming.

In this chapter, unsupervised learning methods were considered for clustering signals automatically. The clustering method was explored based on the data from the small and big specimens. The obtained automatic cluster results were then compared with the classification results given in Chapter 3. In addition, more ECHC-HIC tests with different experimental parameters were carried out to verify the proposed unsupervised learning method.

4.1 Automatic cluster method

4.1.1 Investigation of automatic cluster method

The key to cluster a set of data automatically is to determine the unsupervised learning method and input parameters. Several unsupervised clustering methods have been

developed for different situations of data distribution. For the ECHC-HIC tests, the basic characteristics that can be considered for unsupervised learning methods are the Duration, the Energy, the Counts, the Peak Frequency, PE1, PE2, PE3 and PE4. In light of Figure 3.32, the main characteristics that can better represent the four clusters were the Energy, the Counts and the Peak Frequency. Figures 4.1(a) and (b) show the data distributions for the representation of Energy-Counts for all signals acquired on small and big specimens, respectively. It can be concluded that the data distribution exhibited a non-convex shape regardless of the values of Peak Frequency on the z-axis.
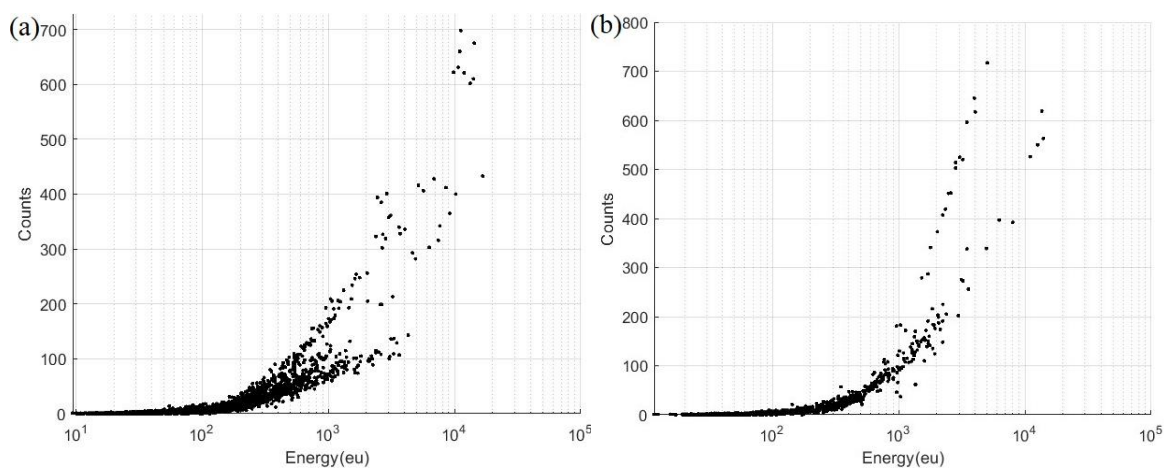
Figure 4.1 Data distributions for the representation of Energy-Counts for all signals (a) Test with small specimen (b) Test with big specimen

This suggests that Density Peaks Clustering (DPC) and Hierarchical Clustering Methods could be considered. The Hierarchical Clustering Method is not appropriate due to the large quantity of data and the existence of outliers. As the critical signals were not identified by Peak Frequency, PE1 and PE2 were used as input data instead of the Peak Frequency. Therefore, the DPC method with the input data of Energy, Counts, PE1 and PE2 was applied for signal clustering. After input data is normalized, the representations of Energy-Counts-Peak Frequency of four signal groups clustered by DPC were displayed in Figure 4.2, in which Figure 4.2(a) was for the Test with the small specimen and Figure 4.2(b) was for the Test with the big specimen.
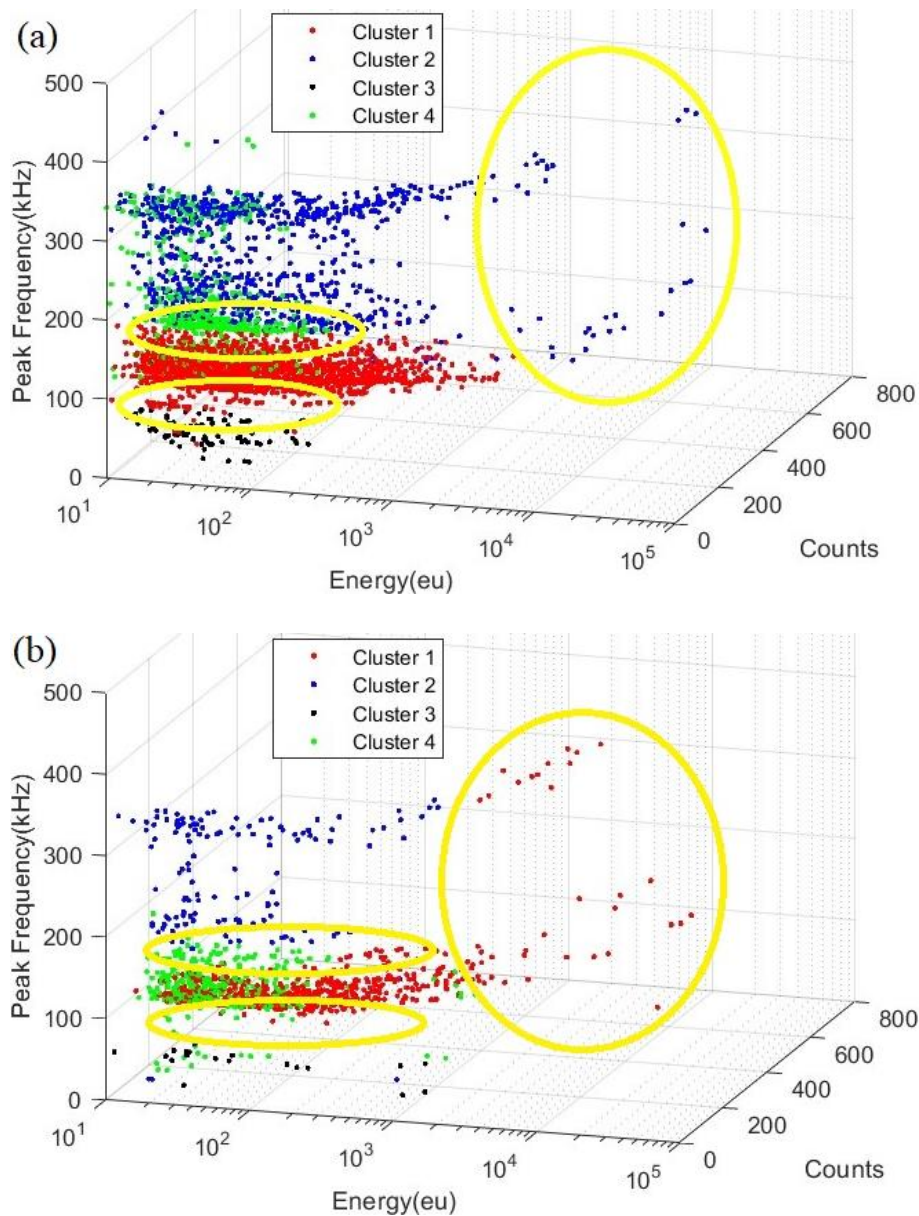
Figure 4.2 Automatic clustering results by DPC method (a) Test with small specimen (b) Test with big specimen

It can be seen in Figure 4.2 that the cluster results were not satisfactory, especially those of the Test with the small specimen. From Figure 4.2(b), the problems were mainly the critical signals among these groups and the signals with higher Energy and Counts, which were marked with yellow circles. As for Figure 4.2(a), in addition to the critical signals, a new group of signals, Cluster 4, was clustered among the Peak Frequency of 200-400kHz, whose signals were mixed with those of Cluster 2. These demonstrated that Energy and Counts have influenced the signal clustering by PE1 and PE2 in the frequency domain.

In Section 3.4.2, the procedure of manual classification involves two steps: signals from uniform corrosion and crevice corrosion were grouped by characteristics in the Frequency domain and signals from H_2 evolution and HIC were then classified by characteristics in the Time domain. The specific manual classification process is shown in the Figure 4.3. Three clusters were obtained by observing the distribution of the values of PE1 and PE2. The data with low values of PE1 but high values of PE2 were assigned in Cluster 1, representing the mixed signals from H_2 evolution and HIC. The data with low values of PE1 and PE2 were assigned in Cluster 2, corresponding to the signals of crevice corrosion. The data with high values of PE1 but low values of PE2 were assigned in Cluster 3, representing the signals from uniform corrosion. The mixed signals in Cluster 1 were then classified by observing the distribution of the values of Duration, Energy and Counts. Signals with lower values of these characteristics were regarded from H_2 evolution, while others were from HIC, marked as Cluster 1-1 and Cluster 1-2, respectively.
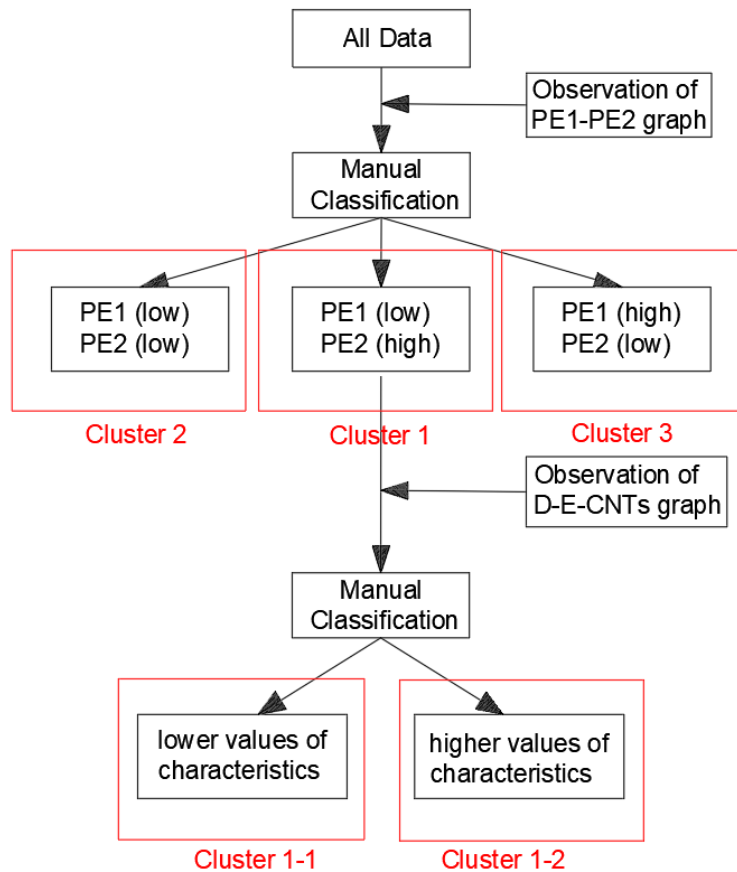
Figure 4.3 The procedure of manual classification method

As a result, the way for automatically clustering signals was considered along the lines of this procedure. Firstly, the distributions of signals of each test on the PE1-PE2 region are shown in Figure 4.4(a) and Figure 4.4(b). It can be seen that the distribution of the mixed signals of H_2 evolution and HIC is much denser than that of signals from the other two mechanisms. The large different density distribution is also the reason the DPC method failed for signal clustering. From the overall view of these signals, it can be regarded as a distribution with two "long tails". Besides, there is only a small overlapped region in the critical area among these three clusters. The Gaussian Mixed Model (GMM) clustering algorithm seems suitable for this kind of distribution. In addition, the process of data normalization is not required because of the same dimension of PE1 and PE2.
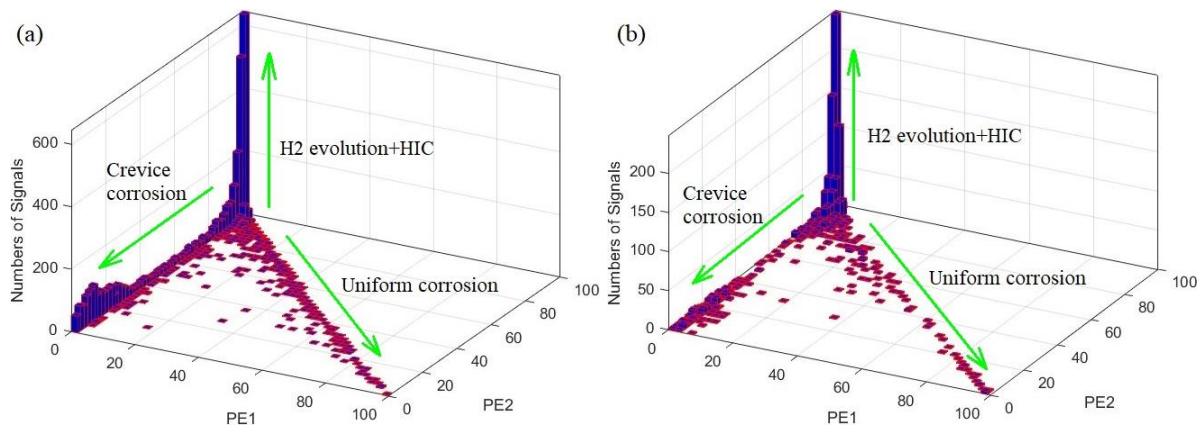
Figure 4.4 Numbers of Signals distributed on PE1-PE2 region (a) Test with small specimen (b) Test with big specimen

The fitgmdist function in Matlab was used for modelling, and the number of clusters was set to three. Some initial conditions were set to improve the accuracy of results clustered by GMM. The initial cluster centres were approximately set as (1.5, 95) for signals of H_2 evolution and HIC, (5, 45) for signals of crevice corrosion, and ((a+5)/2, 50) for signals of uniform corrosion, in which a is the maximum value of PE1.

Figures 4.5(a) and (b) show the representation on PE1-PE2 of GMM cluster results of Tests with small and big specimens, respectively. The signal distributions of 3 clusters on PE1-PE2 are similar to the manual classification, which is displayed in Figure 3.23(a) and Figure 3.25(a). The Energy-Counts-Peak Frequency graphs of these 3 signal clusters for each test were expressed in Figures 4.6(a) and (b). It can be seen that the critical signals were well classified in the z direction. Besides, the signals with high energy were identified with the same label as the manual classification results, which is shown in Figures 3.32(a) and (c).
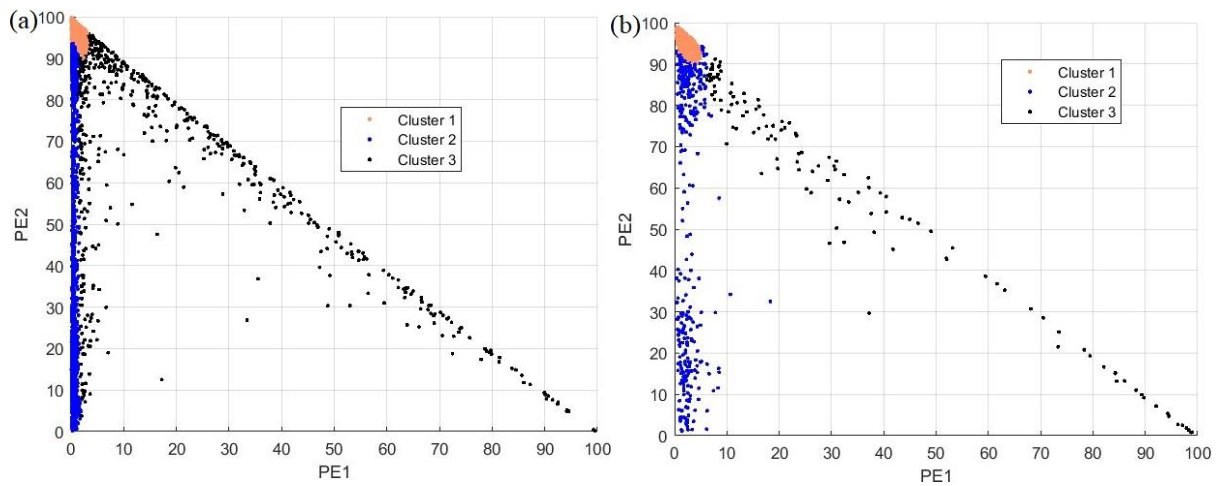
Figure 4.5 Representation on PE1-PE2 of GMM cluster results (a) Test with small specimen (b) Test with big specimen
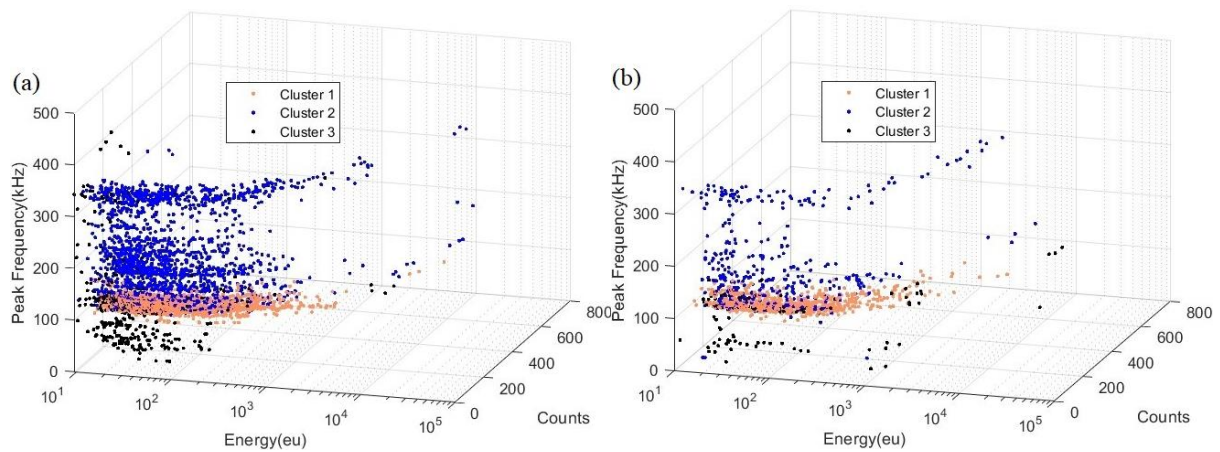
Figure 4.6 Representation of Energy-Counts-Peak Frequency of 3 signal groups clustered by GMM with PE1-PE2 (a) Test with small specimen (b) Test with big specimen

The signals of crevice corrosion and uniform corrosion represented by Clusters 2 and 3 were thus clustered. For the mixed signals derived from H_2 evolution and HIC, the characteristics for identifying these two types of signals were extracted from the Time domain, which are the Duration, the Energy and the Counts. These signal distributions on Duration-Counts-Energy graphs of Tests with small and big specimens are shown in Figure 4.7. It can be seen that there are dense signals in the area close to (0, 0, 0) and scatter distributions towards the diagonal direction in both graphs. This indicated that they are still the kind of distributions with a "long tail" which the GMM algorithm is suitable for. In addition, it was observed that there is a certain correlation between any two characteristics of the three. To make full use of these data and reduce the impact of redundancy, Principle Component Analysis (PCA) was applied for dimensionality

reduction. Besides, it should be noticed that normalization is required before data processing due to the different dimensions of Duration, Energy and Counts.

In this way, the mixed signals of H_2 evolution and HIC were divided. The classification results of each test were shown in Figures 4.8(a) and (b). To better observe these two clusters' signals, the values of Duration and Energy were logarithmic. The values of Duration, Counts and Energy of the critical signals between these two clusters were similar to those obtained by manual classification, but more accurate.
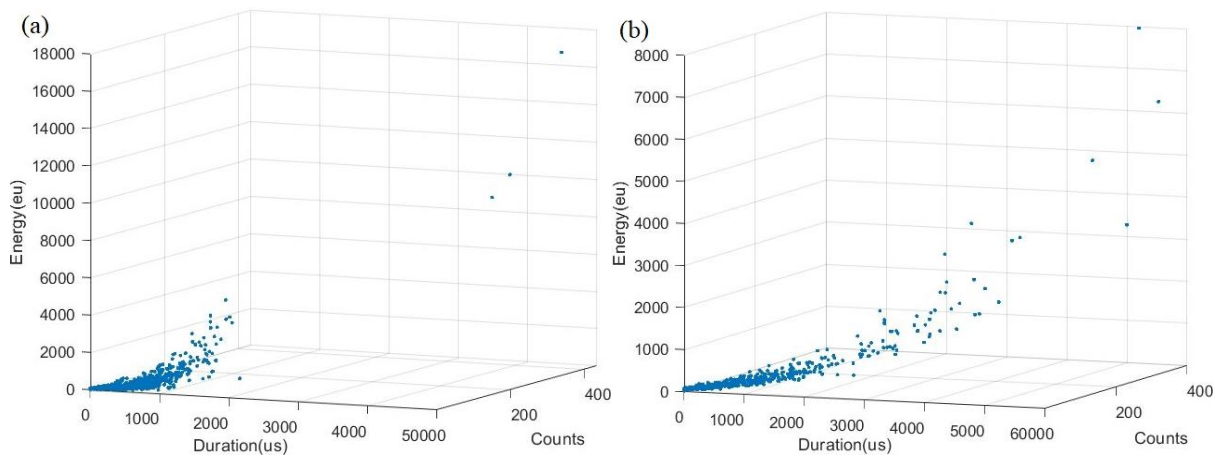
Figure 4.7 Signal distributions of H_2 evolution and HIC on Duration-Counts-Energy graphs (a) Test with small specimen (b) Test with big specimen
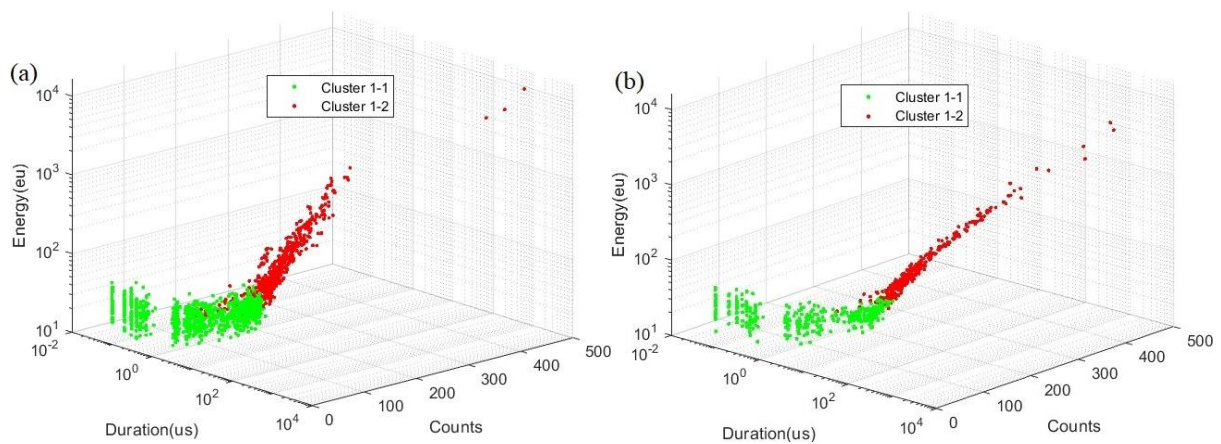
Figure 4.8 Representation of Duration-Counts-Energy of 2 signal groups clustered by GMM with Duration-Counts-Energy(a) Test with small specimen (b) Test with big specimen

Finally, four clusters were thus obtained through the two step-GMM clustering method with different input parameters. The Energy-Counts-Peak Frequency graphs of Tests with small and big specimens are exhibited in Figures 4.9(a) and (b), respectively.

Compared with Figures 3.32(a) and (c), the critical signals among clusters and the signals with higher energy are classified very well.
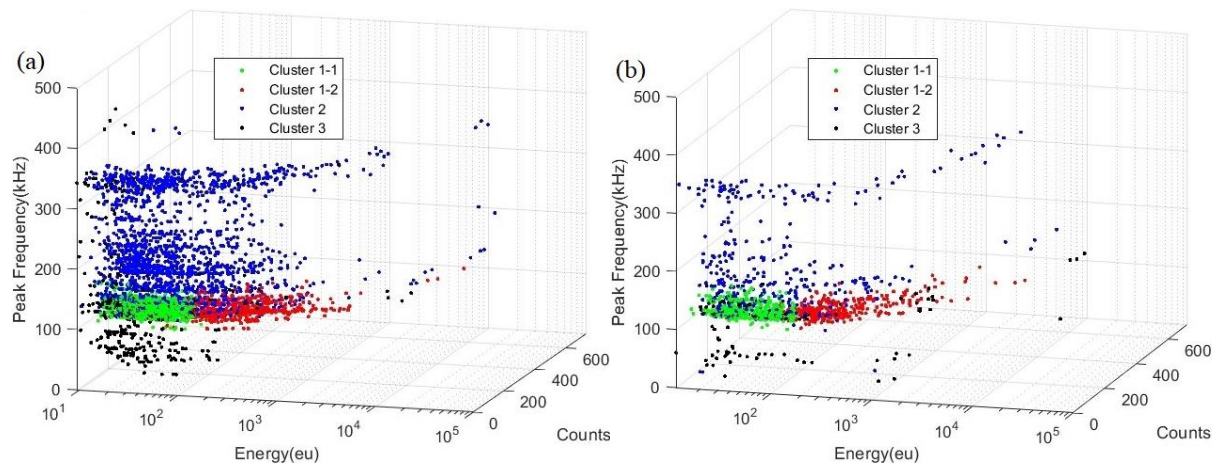
Figure 4.9 Representation of Energy-Counts-Peak Frequency of 4 signal groups clustered by two-step GMM clustering method(a) Test with small specimen (b) Test with big specimen

4.1.2 Evaluation of the automatic cluster results

From Figure 4.9, the automatic clustered results expressed by Energy-Counts-Peak Frequency graphs are similar to the manual classification results. The automatic cluster results are subsequently evaluated in detail with quantitative analysis.

Table 4.1 shows the quantitative comparison between the results of manual classification and the two-step GMM method of each damage mechanism in small-specimen tests. Comparing two signal groups that were from the same mechanism clustered through the two methods, the overlap rate of each group reached 80%, except for signals of uniform corrosion clustered by the two-step GMM method. Combined with Figure 4.5(a), it is shown that the critical signals between uniform corrosion and crevice corrosion were difficult to separate. This is due to the dense distribution of a large number of crevice corrosion signals, resulting in a smaller variance of the established Gaussian model than it should be. Signals located at the edge of the crevice corrosion signals' gathering area were thus considered to belong to uniform corrosion with a greater probability than to belong to crevice corrosion.

For HIC signals classified by the two methods, the overlapping signals accounted for 87.16% and 80.86%, respectively. Figure 4.10 shows that signals' Amplitude/Cumulative Energy of these two results vary with time. Although the number of HIC signals clustered by the two-step GMM method was larger than that by manual

classification, the final cumulative energy was slightly lower. This demonstrates that the energy of the extra signals is very low, which may be the critical signals and were classified into signal groups of H_2 evolution in the manual classification. Notwithstanding, the trends of HIC progress expressed by the two Cumulative Energy-Time curves were quite similar. Besides, the initial HIC signals are the same meaning that the cluster results obtained through the two-step GMM method were reliable for the small-specimen test.

Table 4.1 Quantitative comparison between the results of manual classification and Two-step GMM cluster – Test with small specimen

Damage mechanisms	Methods for classification	Number of signals	Number of overlapped signals	Proportion of overlapped signals
H_2 evolution	Manual	1268	1009	79.57%
	Two-step GMM	1030		97.96%
HIC	Manual	475	414	87.16%
	Two-step GMM	512		80.86%
Crevice corrosion	Manual	1835	1648	89.81%
	Two-step GMM	1770		93.11%
Uniform corrosion	Manual	290	290	100%
	Two-step GMM	556		52.16%
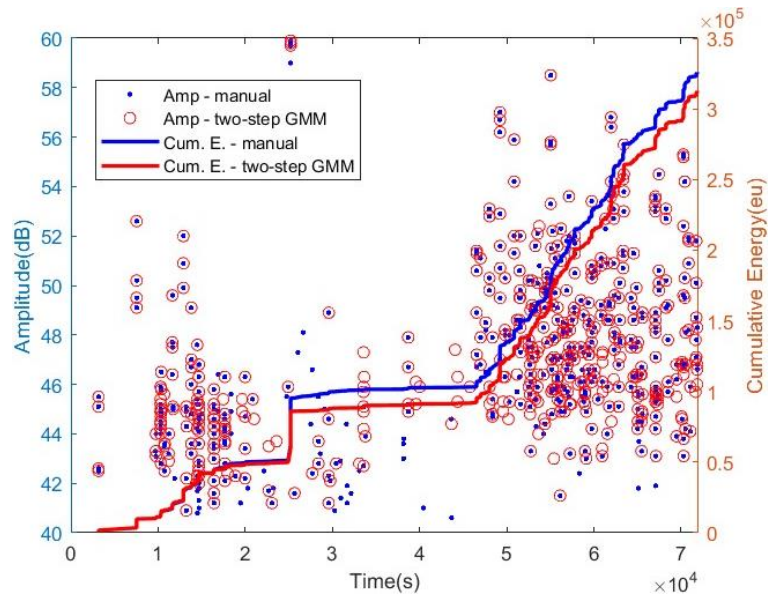
Figure 4.10 Comparison of clustered HIC signals by manual classification and Two-step GMM method about Amplitude/Cumulative Energy varies with Time – Test with small specimen

Similarly, for the test with big specimen, the quantitative comparison between the results of manual classification and the two-step GMM method of each damage mechanism is given in Table 4.2. It can be observed that the signal overlap rates of each group are even better than those of the test with the small specimen. The proportions of overlapping HIC signals are close to 90%. Figure 4.11 exhibits that signals' Amplitude/Cumulative Energy of these two results vary with time. Only a few signals with low amplitude between the two groups were not overlapped, which did not affect the analysis of HIC development. The same initial HIC signal also proved that the cluster results obtained through the two-step GMM method were reliable for the big-specimen test.

Table 4.2 Quantitative comparison between the results of manual classification and Two-step GMM cluster – Test with big specimen

Damage mechanisms	Methods for classification	Number of signals	Number of overlapped signals	Proportion of overlapped signals
H$_2$ evolution	Manual	475		78.74%
	Two-step GMM	384	374	97.40%
HIC	Manual	314	274	87.26%

103

	Two-step GMM	305		89.84%
Crevice corrosion	Manual	258		99.61%
	Two-step GMM	358	257	71.79%
Uniform corrosion	Manual	127		96.85%
	Two-step GMM	125	123	98.40%
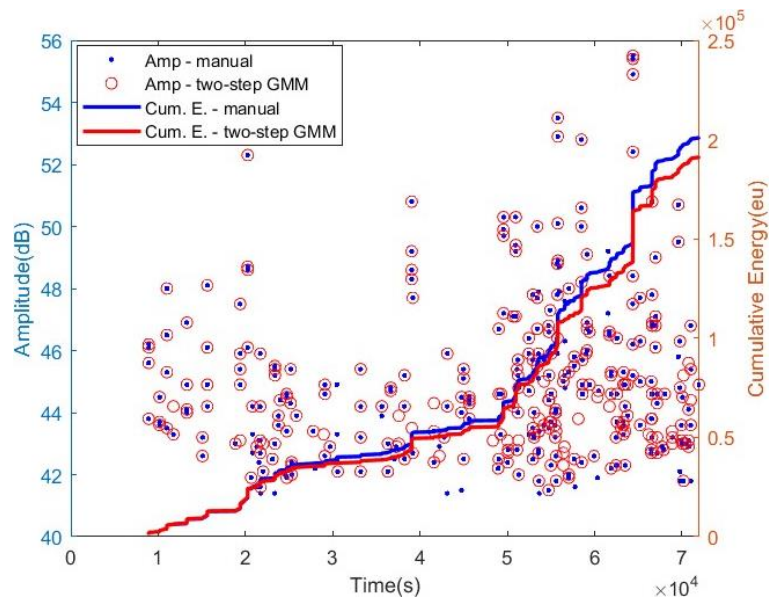
Figure 4.11 Comparison of clustered HIC signals by manual classification and Two-step GMM method about Amplitude/Cumulative Energy varies with Time – Test with big specimen

4.1.3 Procedure of two-step GMM cluster method

The effectiveness of the two-step GMM clustering method was supported by the outcomes of tests with small and big specimens by comparing its cluster results to those of manual classification. The specific procedure of this automatic cluster method is summarized as shown in Figure 4.12.

Firstly, the mixed signals were divided into three clusters by applying the GMM method with the inputs of PE1 and PE2, which are marked as Cluster 1 (signals from H_2 evolution and HIC), Cluster 2 (signals from uniform corrosion) and Cluster 3 (signals from crevice corrosion). To classify signals from H_2 evolution and HIC, the values of Duration, Energy and Counts were selected as the input parameters. To eliminate the differences among evaluation indicators with different units, the data are scaled and

converted into decimals between (-1, 1). This step is called standardization. In addition, since Duration, Energy and Counts are positively correlated, the normalized data was processed by PCA to reduce redundant information and improve calculation speed. Finally, two clusters, Cluster 1-1 (signals from H_2 evolution) and Cluster 1-2 (signals from HIC), were obtained by the GMM method with the input of the processed data.
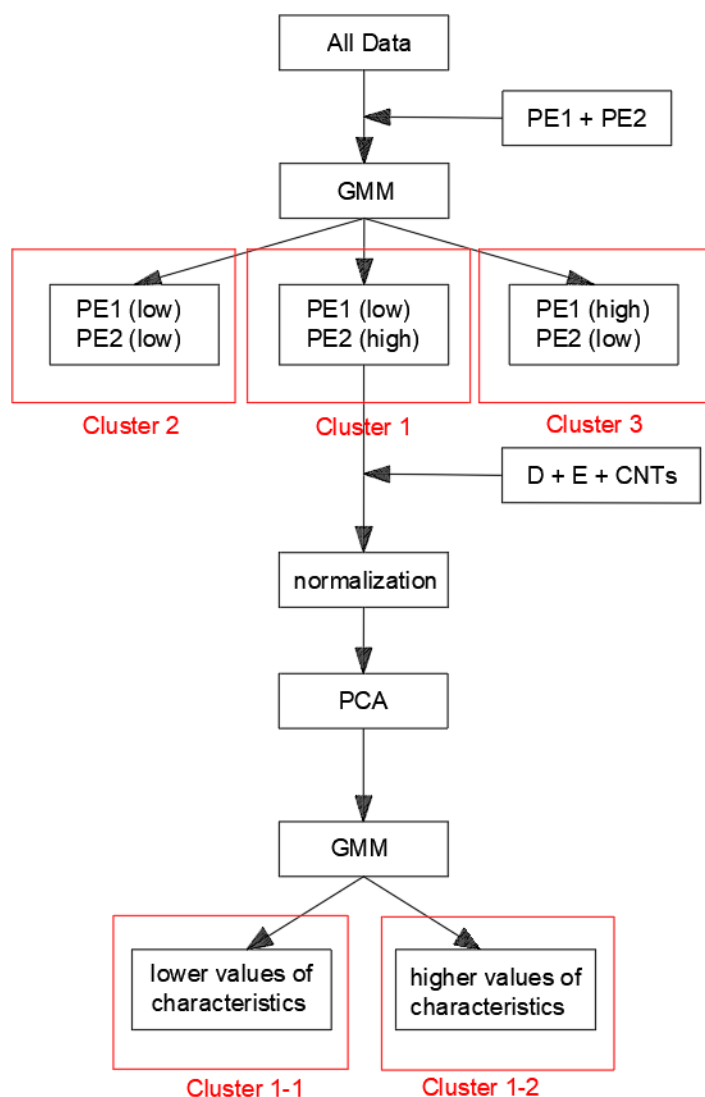
Figure 4.12 The procedure of stepped automatic clustering method

To verify the universal applicability of this method for tests under the same setup, three tests were carried out with different parameters. In the first test, the current of 50mA/cm^2 was applied for electrochemical hydrogen charging to make different hydrogen concentrations. This changed the quantitative ratio among four kinds of signals. In the second test, the amount of non-HIC signals was increased and the distances between working areas and sensors were changed. This caused a

proportional reduction in the number of HIC signals, and the characteristics' values in Time domain changed accordingly. In the third test, different AE sensors (VS150-RIC) were applied, which have a different frequency response range than Nano30 sensors. All these tests were done with a big specimen of the same specification to minimize the effect of boundary reflections.

4.2 Test with different hydrogen concentration

4.2.1 Experimental setup and initial results

The aim of this test is to confirm whether the proposed two-step GMM method is suitable for the ECHC-HIC test with different external hydrogen concentrations. The test setup is the same as shown in Figure 3.17 and only the applied current was changed to 50mA/cm². After 20 hours, the specimen was taken off and cleaned with alcohol. Figure 4.13(a) shows the condition of the work area after the test. Many more hydrogen blisters were observed. Meanwhile, severe uniform corrosion and crevice corrosion occurred as well. The most intuitive result of this phenomenon on the AE result is the substantial increase in the number of acquired signals, which is about 3.5 times the number of signals of the test with a current of 5mA/cm². Figure 4.13(b) shows the AE results in a Time-Amplitude graph. It can be seen that signals with higher amplitude appeared at a very early stage and lasted until about the 14th hour of the test. This is different from the results shown in Figure 3.26 of the test with a current of 5mA/cm², meaning that bigger cracks may appear earlier.
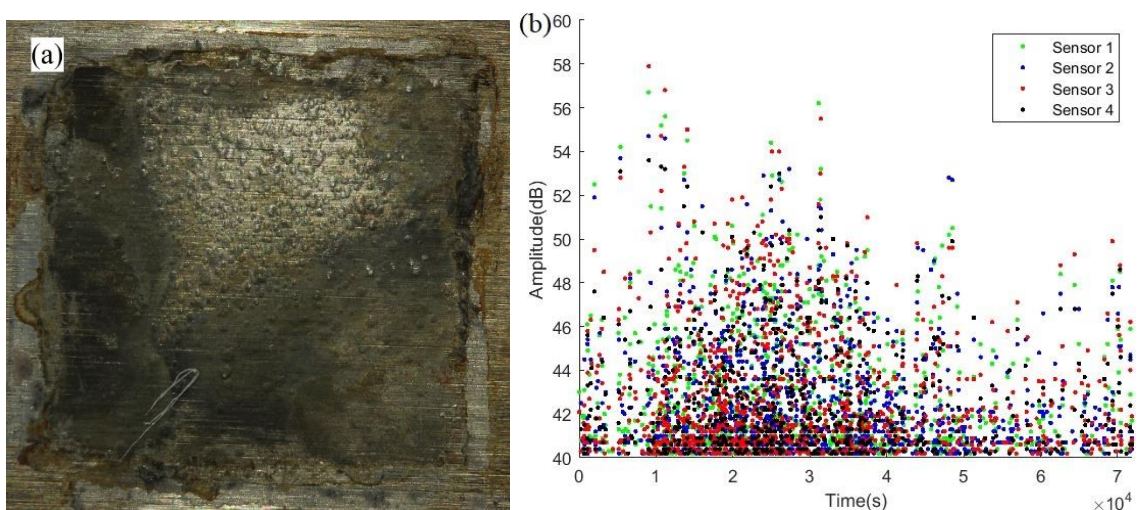
Figure 4.13 Initial results after 20h (a) Observation of HIC area (b) AE results represented by Time-Amplitude graph

4.2.2 Rough manual classification results

To provide correct and comparable classification results for the cluster results obtained by the two-step GMM method, manual classification was applied for this test first. However, there is no prior knowledge of the critical values of PE1 and PE2 to divide the signals for this test. Therefore, the partitions of signals from the three groups, which are mixed signals from H_2 evolution and HIC, signals from crevice corrosion, and signals from uniform corrosion. These were divided in light of signal distribution on the PE1-PE2 graph and the experience obtained from Section 3.4.2.2. Figure 4.14(a) shows the three areas on the PE1-PE2 graph for those three signal groups. Figure 4.14(b) shows the two areas on Duration-Counts-Energy graph for signals from H_2 evolution and HIC. The final distributions of four signal groups were given in Figure 4.15 represented by the Time-Amplitude of all signals and the Time-Cumulative Energy curve of HIC signals.
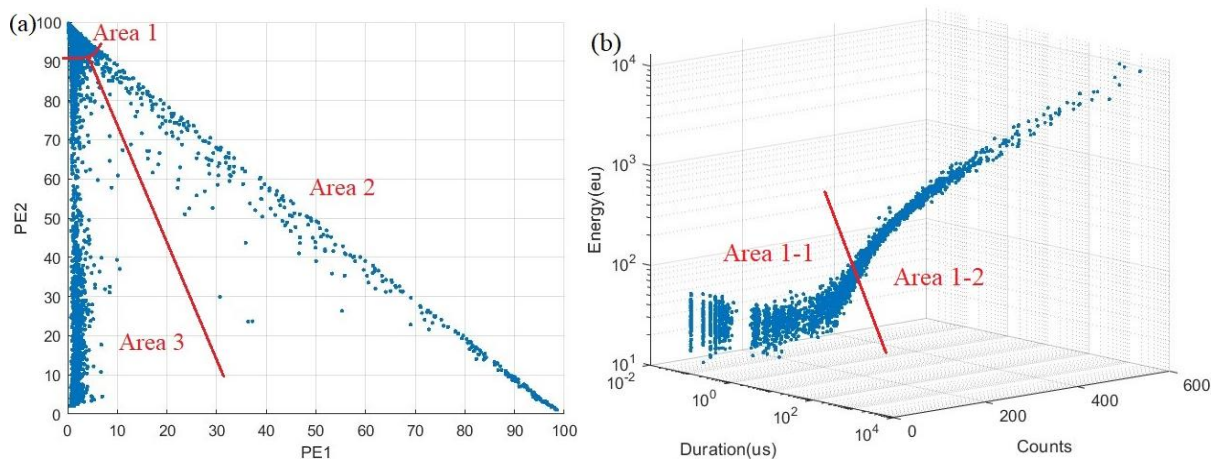
Figure 4.14 Area partitions for signals (a) PE1-PE2 graph of all signal data (b) Duration-Counts-Energy graph of signals from H_2 evolution and HIC
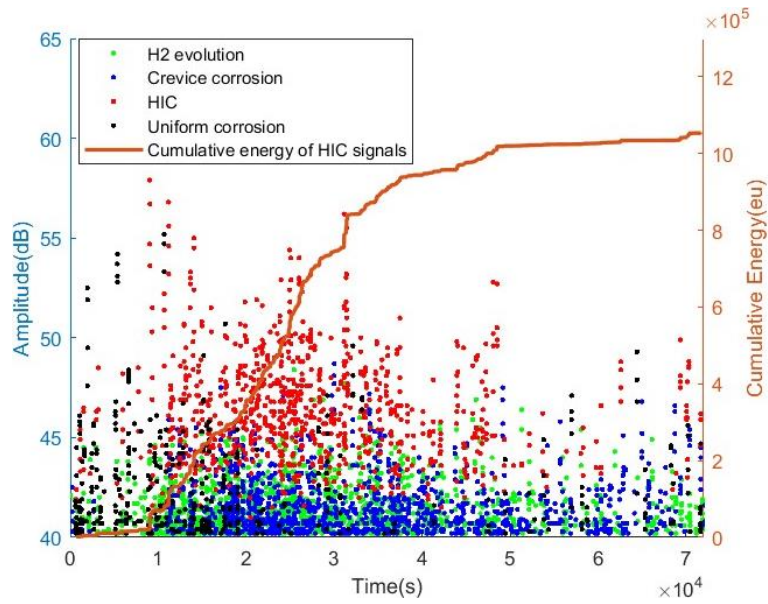
Figure 4.15 Representation of Time-Amplitude of 4 clusters of signals and the Time-Cumulative Energy of HIC signals

Comparing the results of tests with a current of 5mA/cm^2 (which is shown in Figure 3.26), although the highest amplitudes of HIC signals of these two tests are similar, the number of HIC signals whose amplitude higher than 45dB in this test are significantly greater than that of low-current tests. Besides, the first HIC signal was acquired at 675s, and a large number of signals with higher amplitude were obtained from 2.5 hours. This demonstrates that bigger cracks in this test have already occurred at 2.5h, which is much earlier than that in low-current tests. In addition, the hydrogen charging reached equilibrium after 14h while there was no equilibrium state reflected in the low current test. This difference is logical for increasing the 10 times current in this test.

4.2.3 Automatic cluster results and discussions

After processing the data through the proposed two-step GMM cluster method, the results were shown in Figures 4.16(a) and (b), respectively. Comparing Figure 4.16(a) to Figure 4.14(a), it can be seen that most signals that were divided into Area 1 in manual classification were assigned to the other two clusters after the GMM method. In Figure 4.16(b), the critical signals between the two areas in Figure 4.14(b) were adjusted by the GMM method as well. Ultimately, four signal groups are displayed in the representation of Energy-Counts-Peak Frequency in Figure 4.17, in which Figure

4.17(a) is the results obtained from manual classification while Figure 4.17(b) is the results from the two-step GMM cluster method.
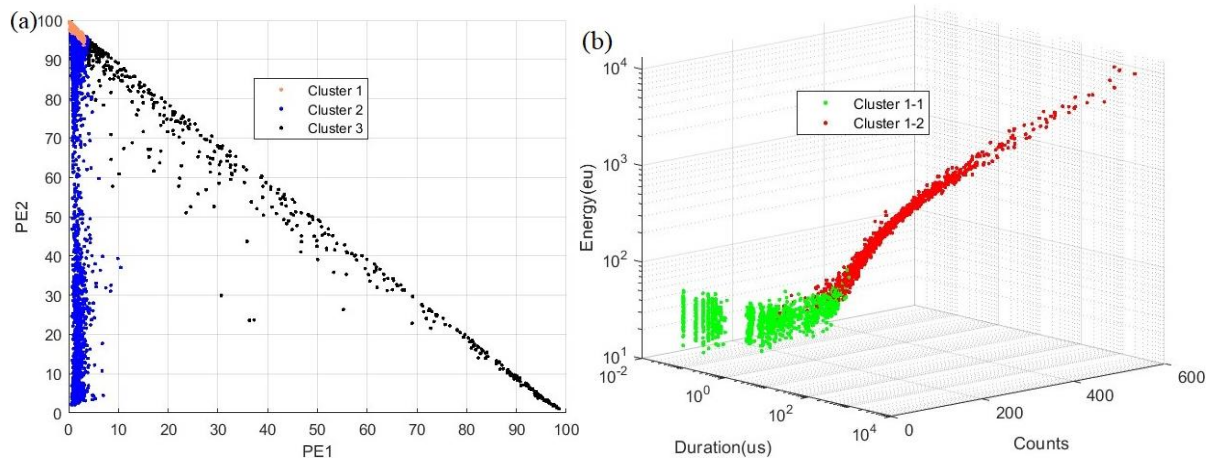
Figure 4.16 (a) Cluster result of first GMM algorithm on PE1-PE2 (b) Cluster result of second GMM algorithm on Duration-Counts-Energy of signals from H$_2$ evolution and HIC
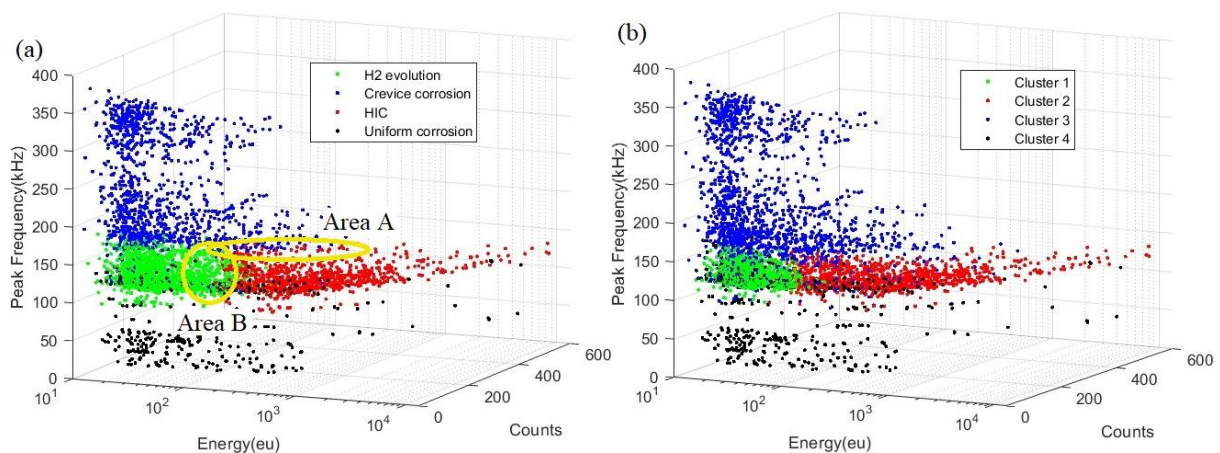
Figure 4.17 Energy-Counts-Peak Frequency graphs of 4 signal clusters (a) manual classification (b) two-step GMM cluster method

The cluster results from the two approaches were similar but still two small parts need to be examined further, which were circled in Figure 4.17(a) and marked as Area A and Area B. For Area A, the problem is that some signals were distributed to the HIC group by manual classification, but were assigned to the crevice corrosion group through the two-step GMM method. These signals were thus observed individually and the waveform and spectrum of a typical example is shown in Figure 4.18. From its frequency spectrum, although there is only a small amount of high-frequency components, the dominant frequency is close to 200kHz. Combined with the waveform of a continuous style, it is regarded to be a signal from crevice corrosion. For signals

in Area B, the waveform and spectrum of a typical signal are shown in Figure 4.19. It has a longer duration of 797.9us and a wider frequency band than normal H_2 evolution signals, resulting in a great likelihood of belonging to the HIC signal group. Even though a small part of the signals in Area B were indeed from H_2 evolution, the cluster results from the two-step GMM method were more reliable. It is because the probability of each point belonging to a Gaussian model was calculated and compared by the two-step GMM method while the other one was the manual cut only based on the distribution of signals. To sum up, the cluster results from the two-step GMM method were more accurate than those from manual classification.
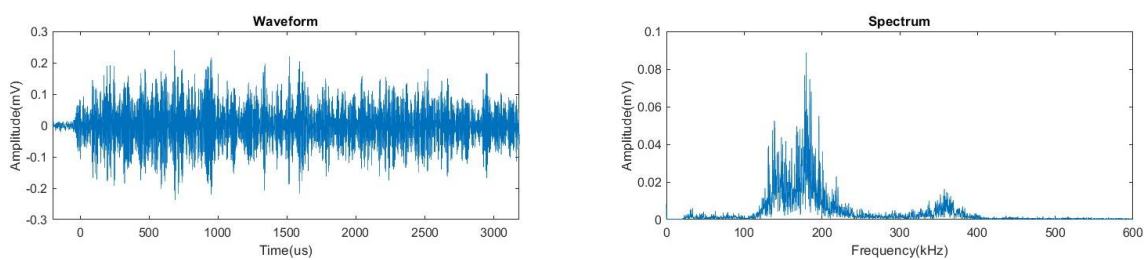
Figure 4.18 The waveform and spectrum of a typical signal in Area A
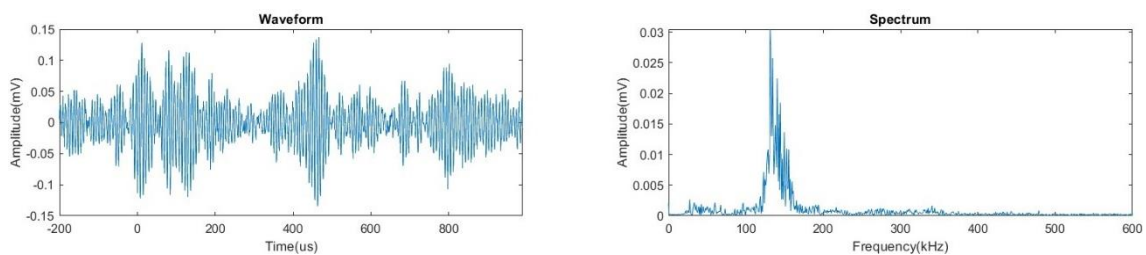
Figure 4.19 The waveform and spectrum of a typical signal in Area B

Figure 4.20 demonstrates the HIC development represented by Time-Amplitude/Cumulative energy of HIC signals clustered by the two methods. It can be seen that the initial HIC signals and signals with higher amplitude clustered by the two methods were identical. The difference is concentrated in low-amplitude signals which were mostly signals in Area B in Figure 4.17(a). However, this does not have much impact on HIC progress represented by cumulative energy due to their low energy. Nevertheless, the situation of HIC development expressed by the two-step GMM results is more accurate, which is conducive to subsequent assessments of the severity of cracks.
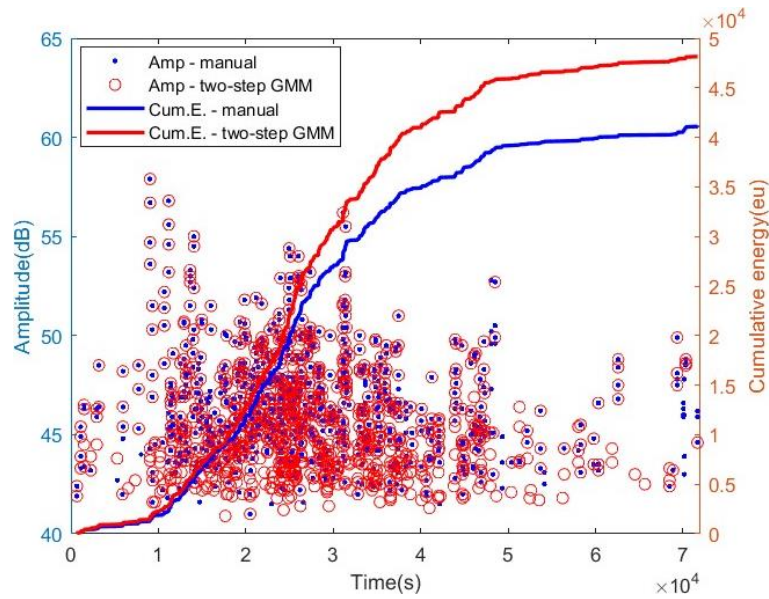
Figure 4.20 Time-Amplitude/Cumulative energy of HIC signals clustered by two methods

4.3 Test with increasing non-HIC signals

4.3.1 Experimental setup and initial results

For this test, another area of the same size on the specimen for corrosion was selected to provide more non-HIC signals. Figure 4.21(a) shows the setup of this test, and Figure 4.21(b) gives the coordinates of the four sensors. The range of HIC area in the test is 121<x<129, 196<y<204 and that of corrosion area is 171<x<179, 296<y<304 (unit: mm). The current for generating HIC was still 5mA/cm^2. For the corrosion area, the solution was the same as the electrolyte, but with no current applied. Under this setup, more signals of crevice corrosion were expected due to the inhibitory effect of NaAsO$_2$ on uniform corrosion, resulting in a more unbalanced number of signals from different mechanisms. In addition, the values of characteristics extracted from the Time domain of signals varied with different source locations. The aim of this test is therefore to confirm whether the proposed two-step GMM method is suitable for the ECHC-HIC test with increasing non-HIC signals in different locations.
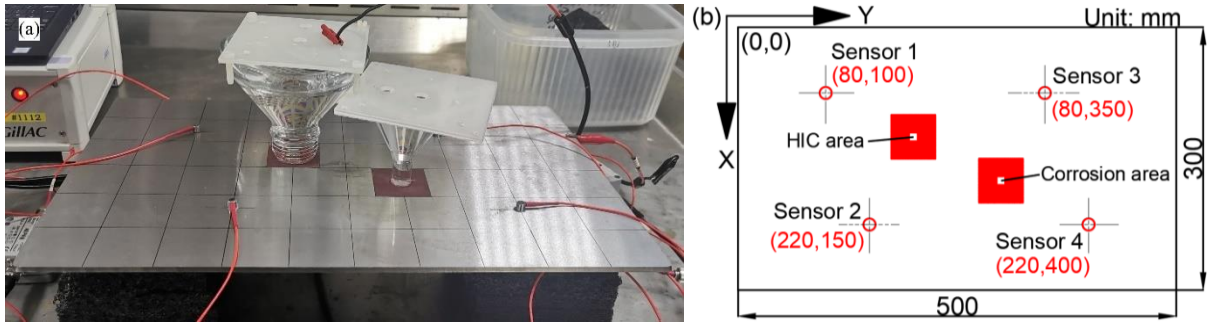
Figure 4.21 Setup of ECHC-HIC test with increasing non-HIC signals in different location (a) physical setup; (b) locations of sensors

Images of these two areas after 20h are shown in Figure 4.22(a) for the HIC area and Figure 4.22(b) for the corrosion area. It can be seen in Figure 4.22(b) that severe crevice corrosion was developed, which is in line with expectations.
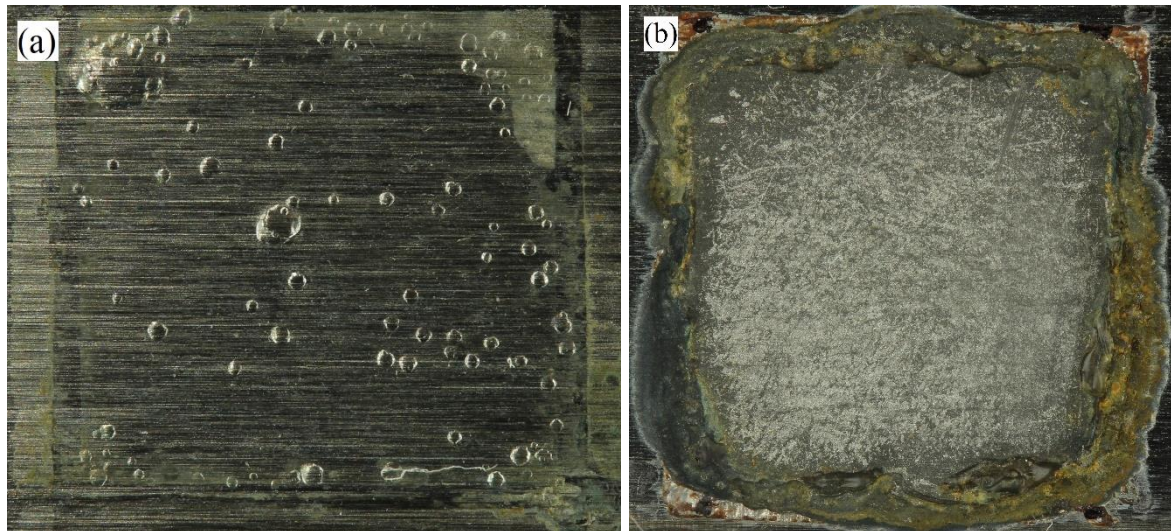
Figure 4.22 Observations on specimen's surface after 20h (a) HIC area (b) corrosion area

4.3.2 Rough manual classification results

The manual classification was first carried out on the basis of signals' distributions to provide a comparable cluster result. Signals from the three groups were divided as exhibited in Figure 4.23(a), and two signal groups of H_2 evolution and HIC were shown in Figure 4.23(b). The distributions of four signal groups are shown in Figure 4.24, in terms of the Time-Amplitude of all signals and the Time-Cumulative Energy curve of HIC signals.
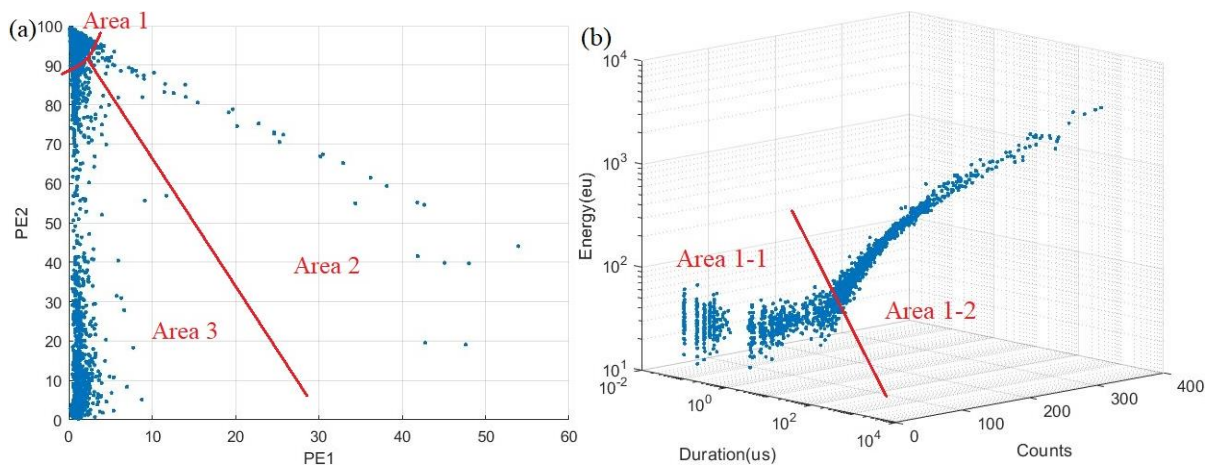
Figure 4.23 Area partitions for signals (a) PE1-PE2 graph of all signal data (b) Duration-Counts-Energy graph of signals from H_2 evolution and HIC
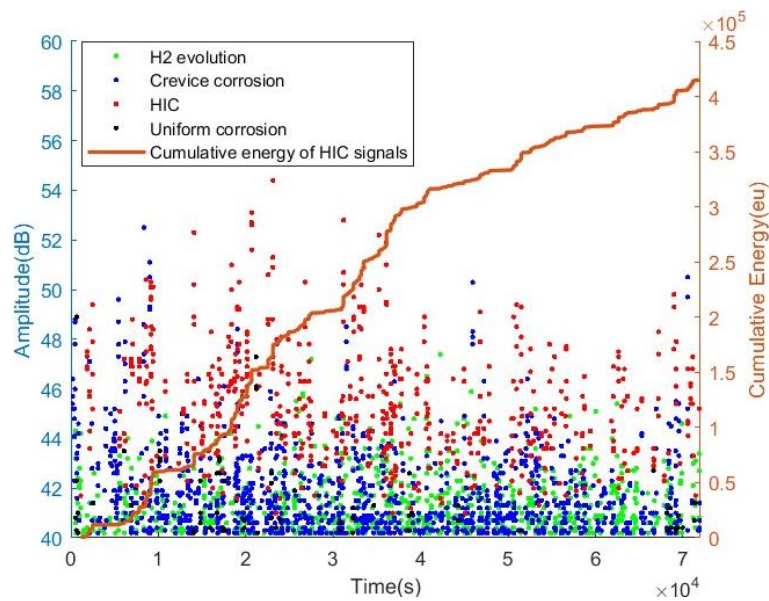
Figure 4.24 Representation of Time-Amplitude of 4 clusters of signals and the Time-Cumulative Energy of HIC signals predicted through manual classification

From Figure 4.24, it can be seen that the initial HIC signal was acquired after about 20 minutes, which is about two hours earlier than the time shown in Figure 3.26, even though the same current of 5mA/cm^2 was applied in the two tests. This is supposed to be due to the closer distance between the HIC area and sensors 1 and 2. More signals from small cracks were then collected at an early stage of the test which would have been too attenuated to be collected in the prior test. The cumulative energy still increased in the late hours of the test. This trend is similar to that in Figure 3.26, which demonstrates that the results of the extracted HIC signals by manual classification were credible.

4.3.3 Automatic cluster results and discussions

After processing the data through the proposed two-step GMM cluster method, the results were shown in Figures 4.25(a) and (b), respectively. Comparing Figure 4.25(a) to Figure 4.23(a), the divided areas seem similar with the manual partitions, as well as the results of Figure 4.25(b). Ultimately, the four signal groups are displayed in terms of Energy-Counts-Peak Frequency in Figure 4.26, in which Figure 4.26(a) is for the results obtained from manual classification while Figure 4.26(b) is for the results from the two-step GMM cluster method. The distributions expressed by the two graphs in Figure 4.26 are almost the same, except for the critical signals from H_2 evolution and HIC.
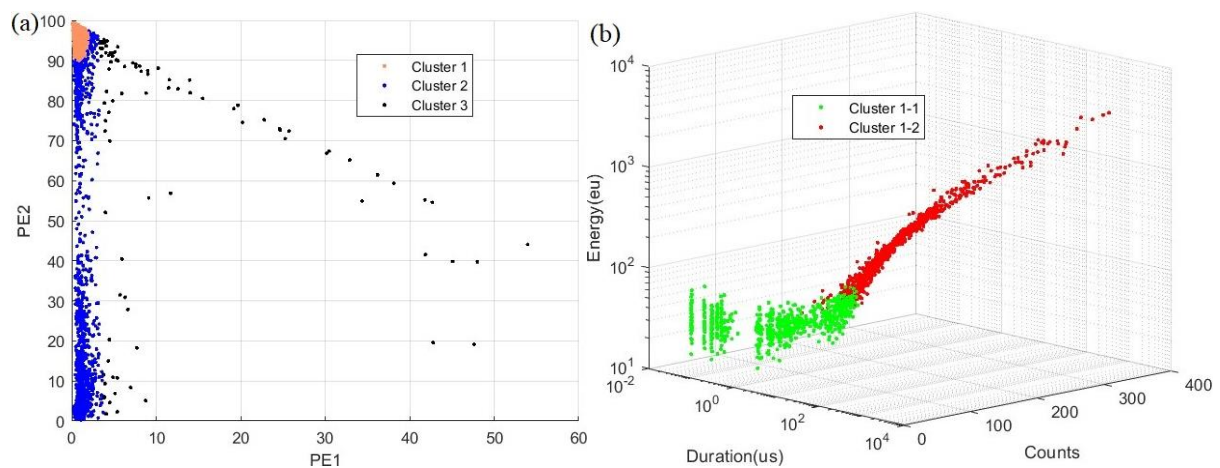
Figure 4.25 (a) Cluster result of first GMM algorithm on PE1-PE2 (b) Cluster result of second GMM algorithm on Duration-Counts-Energy of signals from H_2 evolution and HIC
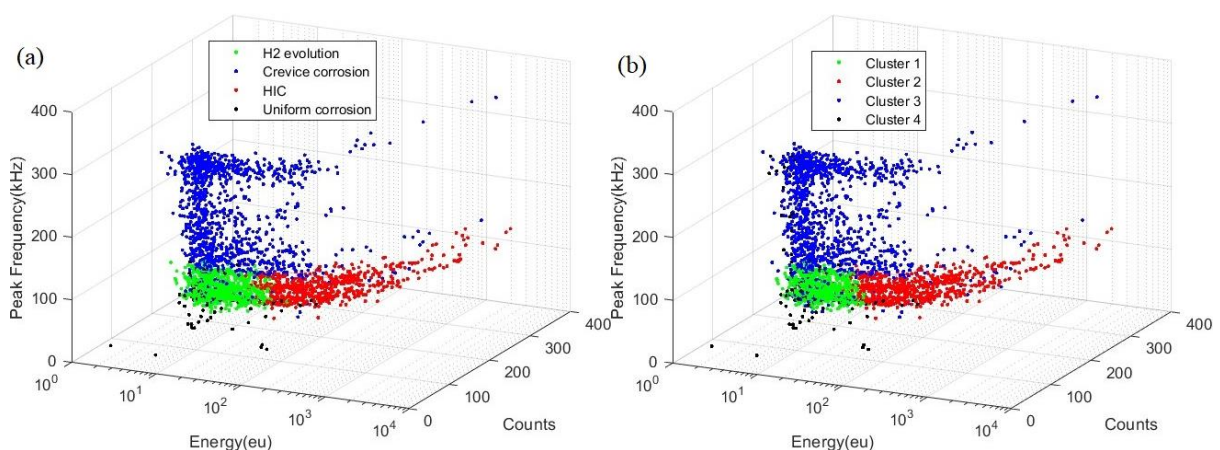
Figure 4.26 Energy-Counts-Peak Frequency graphs of 4 signal clusters (a) manual classification (b) two-step GMM cluster method

Figure 4.27 shows the conditions of Time-Amplitude/Cumulative energy of HIC signals clustered by the two methods. The initial signal determined by the two-step GMM method was about 10mins earlier than that by manual classification. However, different signals between these two results were generally low-energy, which do not heavily influence HIC progression. This also indicates the high efficiency of the proposed automatic cluster method.
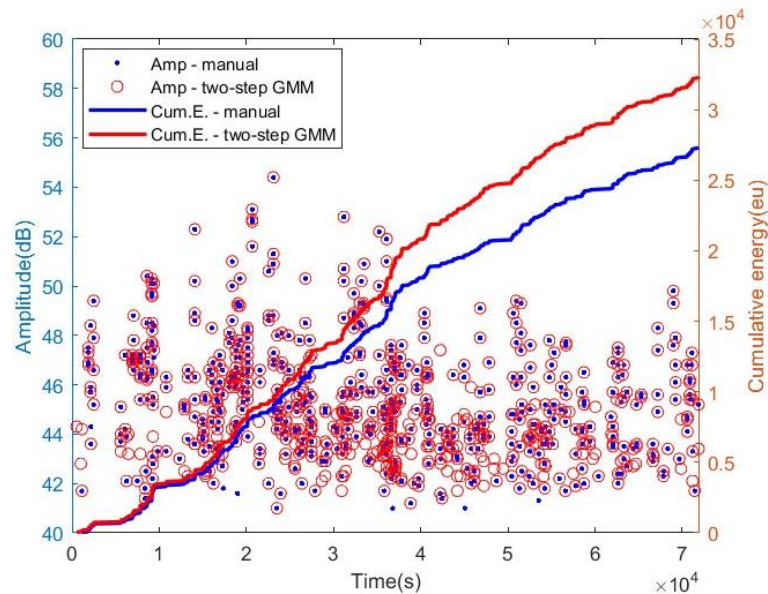
Figure 4.27 Time-Amplitude/Cumulative energy of HIC signals clustered by the two methods

4.4 Test with different type of sensors

4.4.1 Experimental setup and initial results

The type of sensor is also an important factor affecting the expression of signals due to their different frequency responses. It is known that the dominant frequency of HIC signals acquired by Nano30 is around 150kHz. In order to highlight the HIC signals, VS150-RIC sensors (Vallen Systeme GmbH, diameter of 28mm) with a resonant frequency of 150kHz were used for ECHC-HIC tests. The response curve of VS150-RIC sensor is shown in Figure 4.28 whereas for the Nano30 in Figure 3.3. To better identify the signals obtained by VS150-RIC from different mechanisms, Nano30 and VS150-RIC sensors were applied for the test simultaneously. Figure 4.29(a) shows the physical setup of this test, and Figure 4.29(b) gives the coordinates of eight sensors, in which the red circles represent Nano30 and the blue ones are VS150-RIC sensors.
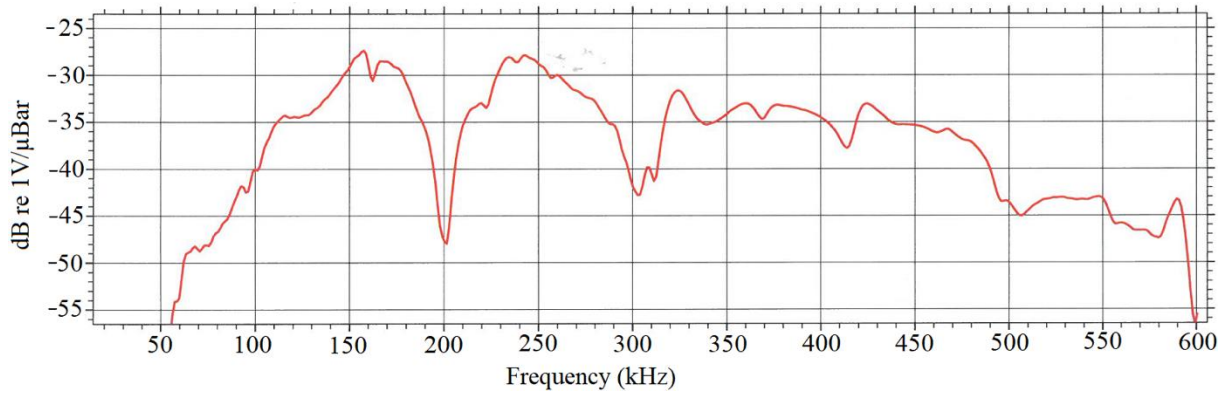
Figure 4.28 Response curves of VS150-RIC sensor used in this study
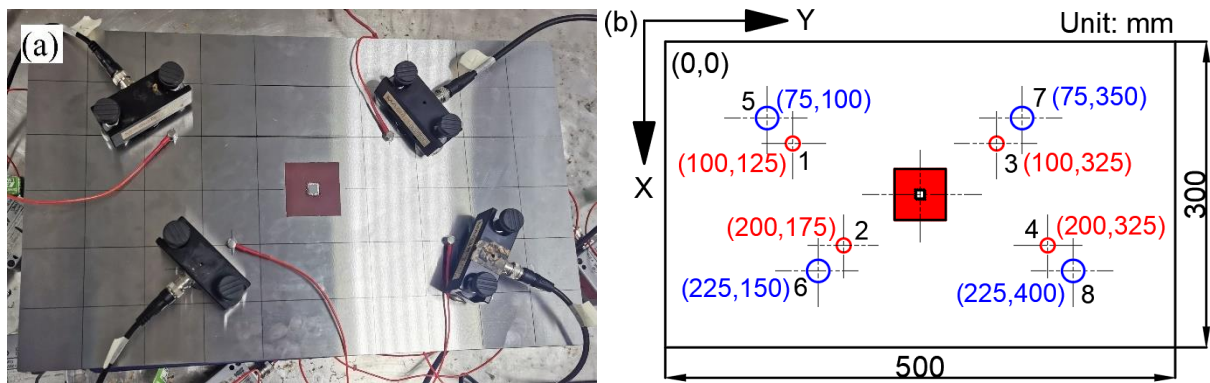
Figure 4.29 Setup of ECHC-HIC test with two types of sensors (a) physical setup; (b) locations of sensors

The applied current was 5mA/cm^2 and the test duration was still 20h. The AE results are shown in Figure 4.30. From Figure 4.30(a), the amplitudes of signals obtained by VS150-RIC are seen to be about 5dB higher than those of Nano30. Figure 4.30(b) demonstrates that the number of signals obtained by VS150-RIC was around four times that of Nano30 because of the higher sensitivity of VS150-RIC.
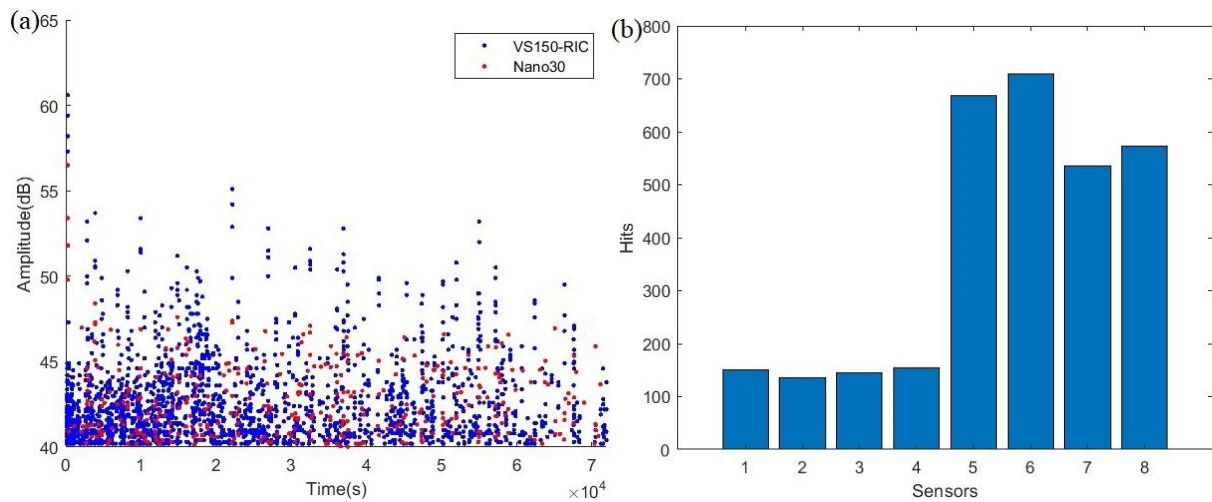
Figure 4.30 Results of test (a) Time-Amplitude graph of signals (b) Number of Hits of each sensor

There were still three kinds of frequency distributions of signals obtained by VS150-RIC sensors. Compared to the signals from the same event obtained by those of the Nano30 sensors, the features of signals from different mechanisms were similar except for some signals of uniform corrosion. Figure 4.31 shows the waveforms (a, b), frequency spectrums (c, d) and energy spectrums (e, f) of two signals from Nano30 and VS150-RIC of the same uniform corrosion event. It can be seen that the duration and amplitude of the signal obtained by VS150-RIC were higher than those of Nano30, but their waveforms look similar. Comparing Figure 4.31(b) and (c), the low-frequency component of signal from VS150-RIC was almost negligible. Corresponding to the energy spectrums, the PE1 and PE2 were 32.94%, 64.76% and 6.44%, 92.81% of signals from Nano30 and VS150-RIC, respectively. Therefore, the characteristics (PE1 and PE2) of this uniform corrosion signal obtained by VS150-RIC are closer to those of HIC signals, which may make mistakes in signal classification.
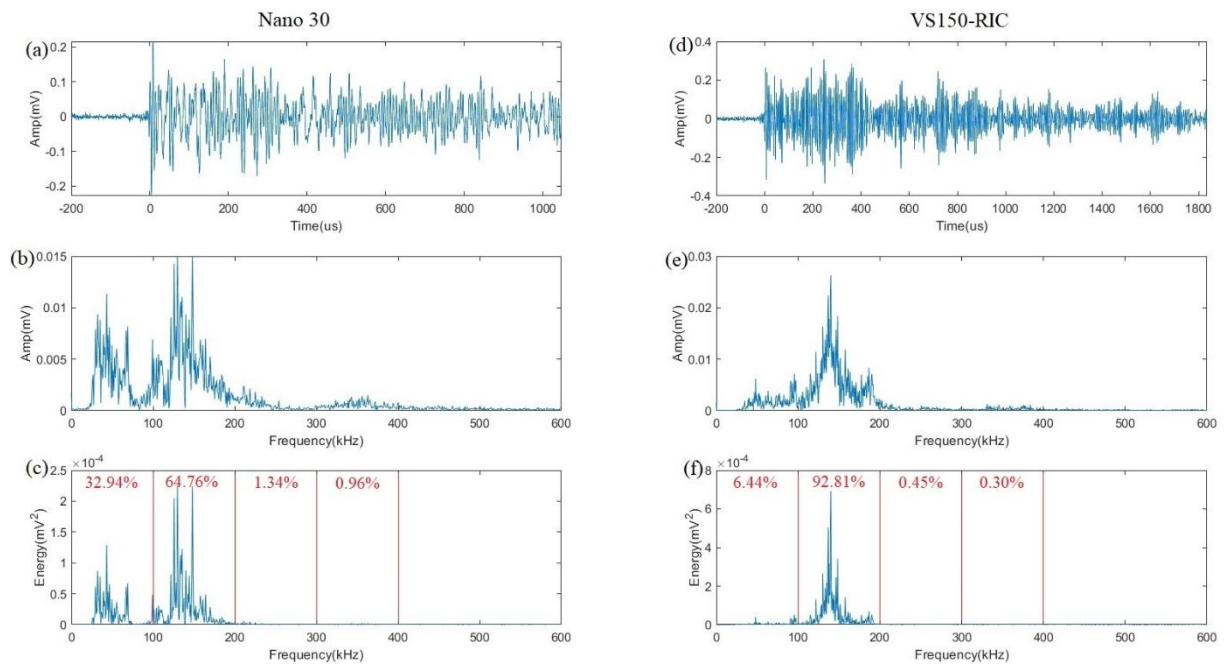
Figure 4.31 The waveforms, frequency spectrum and energy spectrum of signals from same one uniform corrosion event obtained by Nano30 (a, b, c) and VS150-RIC sensors (d, e, f)

Figure 4.32 shows the waveform and energy spectrum of a representative HIC signal acquired by VS150-RIC. It is difficult to discriminate the signals from HIC and uniform corrosion only based on the value of PE1-PE4. In this case, the comparison in the time domain is vital. The waveform from uniform corrosion signal is closer to a typical burst signal than that of HIC signal shown in Figure 4.32(a). However, there was no value of representative parameters in the time domain that can clearly discriminate these two waveforms. In addition, it is also hard to observe the style of waveform if the signal's Duration is too short.
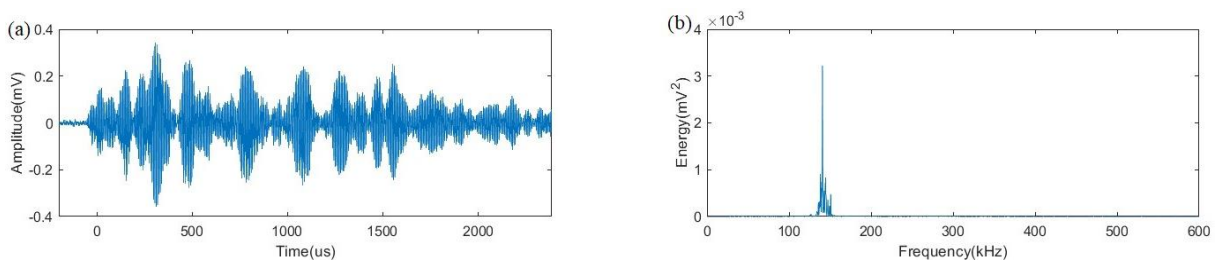
Figure 4.32 The (a) waveform and (b) energy spectrum of HIC signals obtained by VS150-RIC sensors

Nevertheless, the situation shown in Figure 4.31 is rare in this test, it is thus not such time-consuming to manually identify the critical signals. The proposed two-step GMM method was still carried out for evaluation under this condition.

4.4.2 Rough manual classification results

The partitions of PE1 and PE2 of all signals obtained by VS150-RIC are shown in Figure 4.33(a) according to the data distribution. It can be seen that signals like those shown in Figure 4.30(d) were critical signals. Figure 4.33(b) exhibits the divisions of signals derived from H_2 evolution and HIC with their distributions in terms of Duration-Counts-Energy. The final manual classification results are shown in Figure 4.34 in Time-Amplitude for all signals and in Time-Cumulative Energy of HIC signals. The HIC progress expressed by the cumulative energy is similar to those in previous tests with 5mA/cm^2 current. However, the initial HIC signal was found at the time of 159s which is too early, and therefore unlikely to actually be due to HIC. Unfortunately, there are no signals acquired by Nano30 of this event to further confirm whether it is derived from HIC or uniform corrosion.
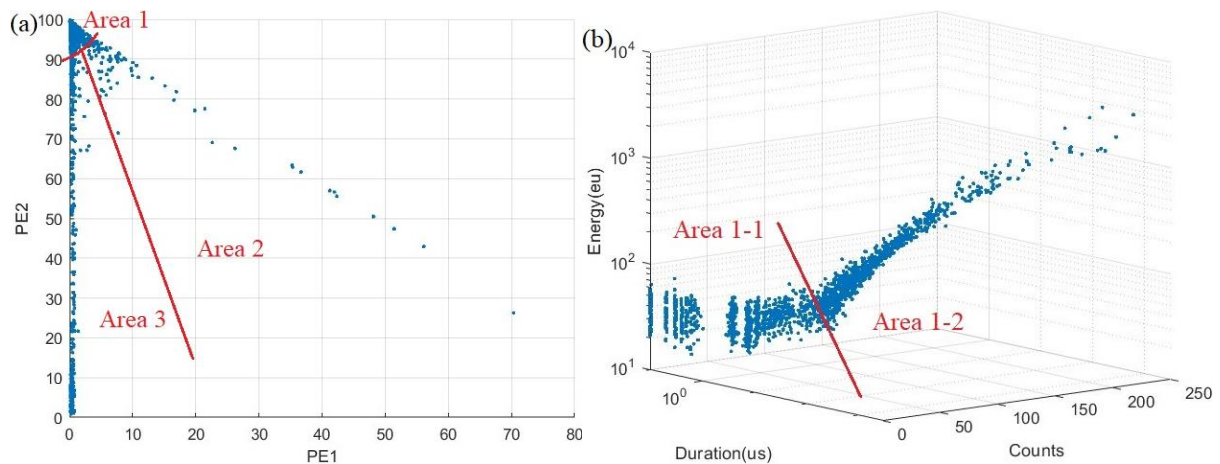
Figure 4.33 Area partitions for signals (a) PE1-PE2 graph of all signal data (b) Duration-Counts-Energy graph of signals from H_2 evolution and HIC
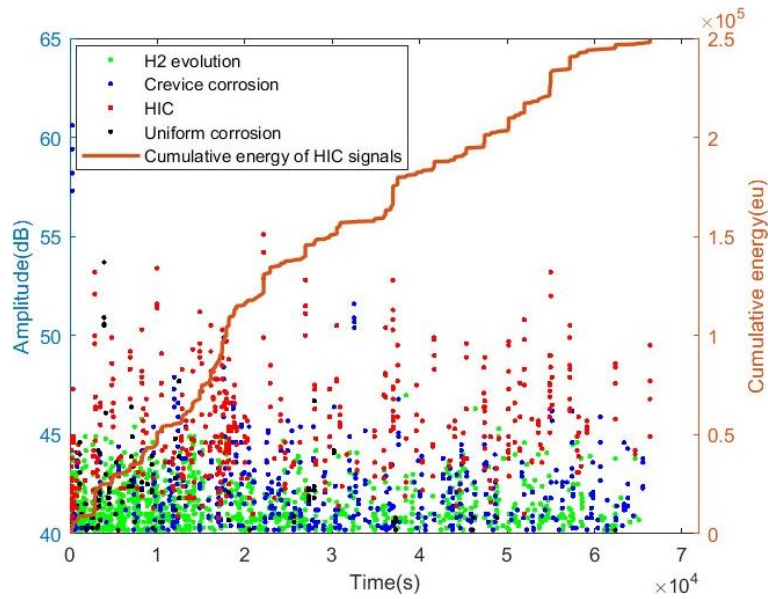
Figure 4.34 Representation of Time-Amplitude of 4 clusters of signals and the Time-Cumulative Energy of HIC signals

4.4.3 Automatic cluster results and discussions

With the proposed two-step GMM cluster method, the results after twice GMM methods were shown in Figure 4.35(a) and (b), respectively. It can be seen that the critical signals were adjusted in both results, especially the more concentrated data in cluster 1. The ultimate clustering results were displayed in the form of Energy-Counts-Peak Frequency in Figure 4.36(a) of manual classification and Figure 4.36(b) of automatic clustering. The big difference between these two results is the low-energy signals of uniform corrosion signals. For instance, the signal shown in Figure 4.31(b) was assigned to the group of HIC signals by manual classification while it is in the group of uniform corrosion signals by automatic clustering.
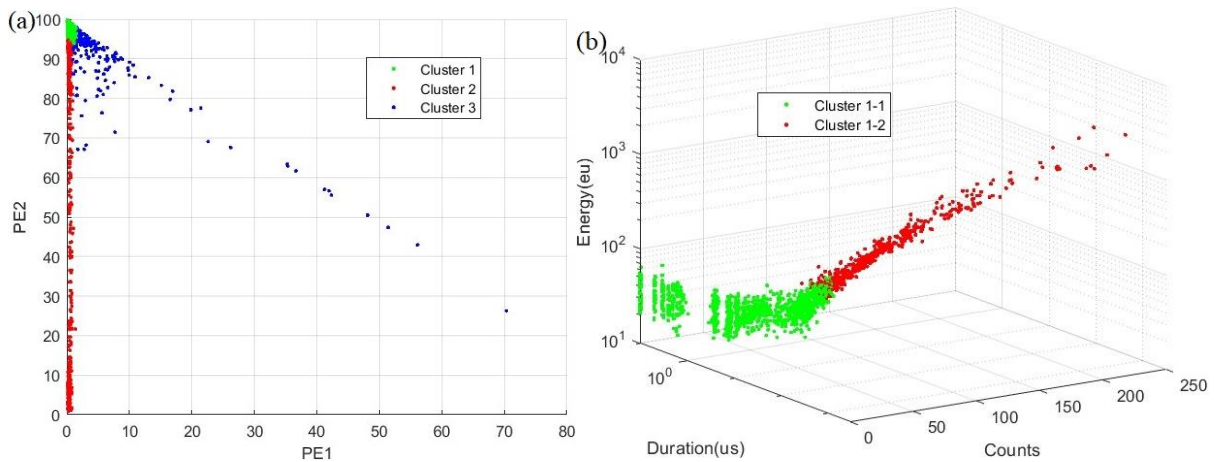
Figure 4.35 Cluster result of first GMM algorithm on PE1-PE2 (b) Cluster result of second GMM algorithm on Duration-Counts-Energy of signals from H_2 evolution and HIC
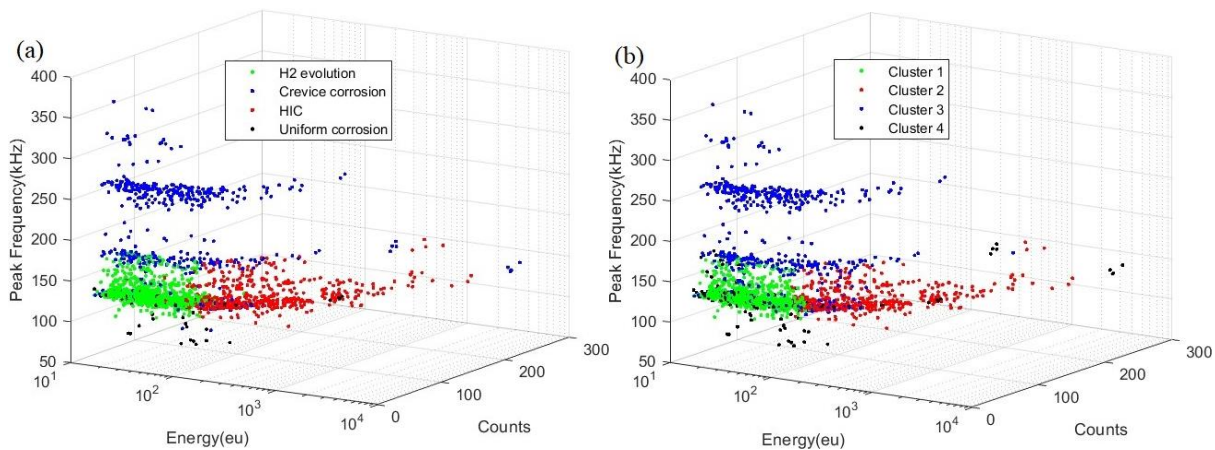
Figure 4.36 Energy-Counts-Peak Frequency graphs of 4 signal clusters (a) manual classification (b) two-step GMM cluster method

Figure 4.37 gives the Time-Amplitude/Cumulative energy of HIC signals clustered by the two methods. The initial HIC signal picked by the automatic cluster method occurred at 252s which was 93s later than the results by manual classification. The manually selected initial HIC signal was regarded as a uniform corrosion signal in the results of automatic clustering. From its waveform and frequency spectrum which are shown in Figure 4.38, it is preferred to be regarded as non-HIC signals. However, this was not certain due to the short duration. For non-overlapping signals between the two results, the influence of low-energy signals on HIC progress can be ignored. For those who have higher energy and higher amplitude, analysis of each signal verified that the results of the automatic clustering method were more accurate. For example, Figure 4.39(a-b) depicts the waveform and frequency of the signal circled in Figure 4.37. The event recorded by one of the Nano30 sensors is also shown in Figure 4.39

(c-d). It is clear that this signal should be classified as a uniform corrosion signal, which is consistent with the results of the automatic method.
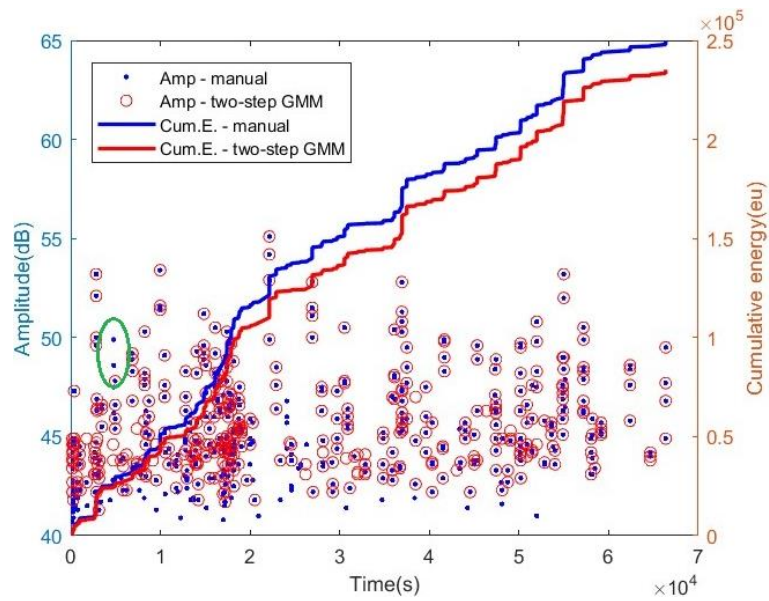
Figure 4.37 Time-Amplitude/Cumulative energy of HIC signals clustered by two methods
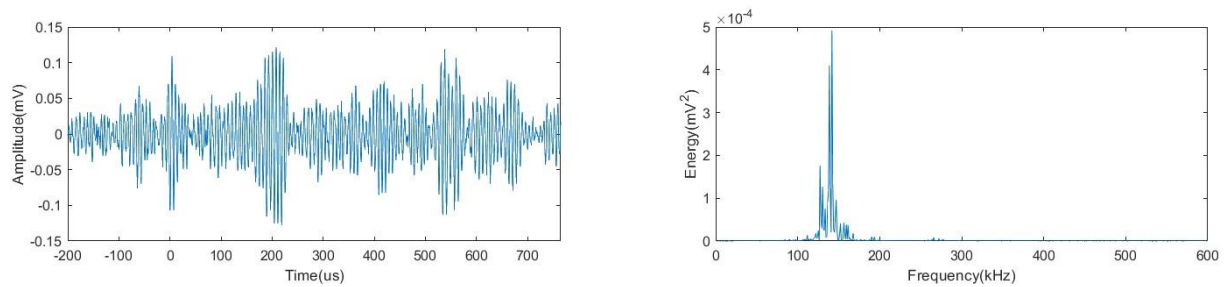
Figure 4.38 The waveform and frequency spectrum of initial HIC signals identified by manual classification
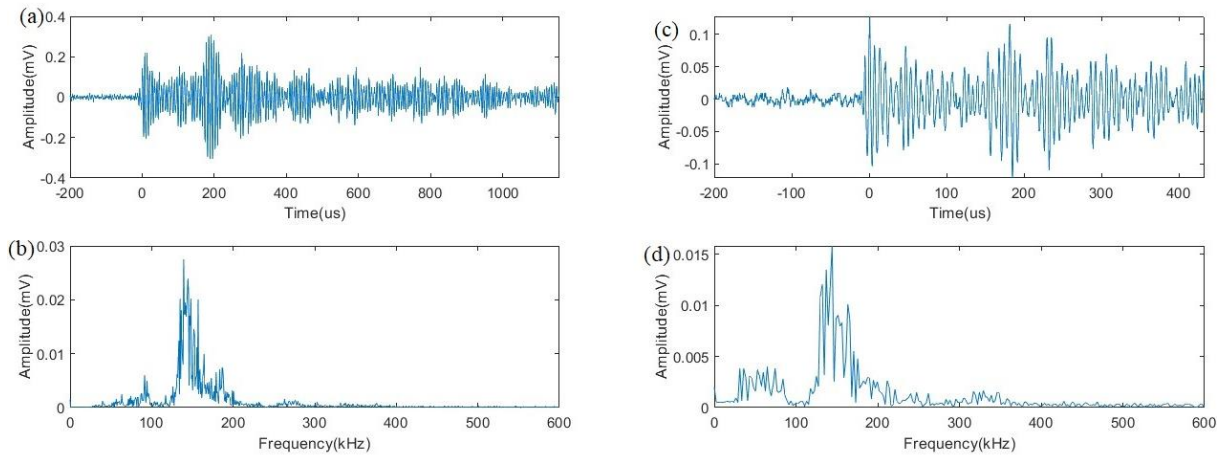
Figure 4.39 The waveforms and frequency spectrum of signals from same one event obtained by VS150-RIC (a, b) and Nano30 sensors (c, d)

Nevertheless, the frequency distributions of some uniform corrosion signals might appear similar to those of HIC signals by VS150-RIC sensors. At the same time, there was no signal acquired by Nano30 for comparison and confirmation. Under this condition, these uniform corrosion signals will be assigned to the HIC group mistakenly. For example, it is uncertain whether the selected initial HIC signal was derived from HIC or uniform corrosion. Therefore, it is necessary to have a good understanding of signals from different mechanisms acquired by VS150-RIC sensors, like the identification procedure of signals obtained by Nano30 illustrated in Chapter 3. Detailed analysis of signals acquired by VS150-RIC is given in Chapter 5.

4.5 Conclusions

In this chapter, a two-step GMM clustering method was proposed for automatic clustering of mixed signals from the ECHC-HIC test under this experimental setup. As the signals from ECHC-HIC tests with small and big specimens were well classified manually in Chapter 3, their results were used as references to derive a suitable automatic cluster method. Subsequently, another three ECHC-HIC tests with different parameters were analysed to verify the proposed method. It is proved that the mixed signals were well clustered by the two-step GMM clustering method with shorter time and better assignment of critical signals than manual classification. For the unsupervised signal clustering method, the two most important aspects are the cluster algorithm and the input data. For signal clustering under this setup, the biggest difference among all signals is the frequency distributions. The best parameter to

describe is found to be the proportion of energies in different ranges of frequency. In addition, the results of tests introduced in Sections 4.2 and 4.3 illustrate that the proposed cluster method is always adaptable regardless of the relationship between the quantities of the three types of signals.

However, for different types of sensors used in the tests, it seems that the acquired signals change because of the different resonant frequencies of the sensors. Although the automatic cluster method was still reliable under this test conditions, the results might be different if there were more corrosion events. This problem will be discussed in more detail in Chapter 5.

5 Influence of different specimen's thickness and sensor's type on signals of ECHC-HIC tests

In previous sections, the basic concept of signals derived from ECHC-HIC tests with various parameters was illustrated, such as the different 2D specifications of specimens, the applied current and the number of non-HIC signals. However, two other vital parameters, specimens' thickness and sensors' type, were not investigated in detail. These two parameters may influence the signals essentially. For example, changes in the specimen's thickness will change the wave propagation mode, while using different sensors will change the parameters in the frequency and time domains of electrical signals. These contents will thus be covered in a separate chapter for a more complete analysis.

5.1 Tests for non-HIC signals identification method

As the thickness of specimens and sensors' type changed, the basic characteristics of non-HIC signals unclear. Therefore, short-time tests for non-HIC signals identification were necessary. Table 5.1 shows the details of these tests.

Table 5.1 Details for short-time tests for each specimen

Tests	Thickness	Solution	Current	Theoretically Signal Sources
5.1	5mm		$5mA/cm^2$	H_2 bubble + crevice corrosion + uniform corrosion (possible)
5.2	10mm	0.5mol/L H_2SO_4	×	H_2 bubble + crevice corrosion + uniform corrosion (numerous)
5.3			$5mA/cm^2$	H_2 bubble + crevice corrosion + uniform corrosion (possible)
5.4	20mm		×	H_2 bubble + crevice corrosion + uniform corrosion (numerous)
5.5			$5mA/cm^2$	H_2 bubble + crevice corrosion + uniform corrosion (possible)

The duration of all these five tests were one hour. For the 5mm-thick specimen, signals from different sources acquired by Nano30 sensors have been identified. Thus, the signals obtained by VS150-RSC sensors can be recognized by comparing the signals from Nano30 of the same event. As for the specimens of 10mm and 20mm thickness, two short-time tests with or without current for each specimen were implemented. Figure 5.1 shows the locations of sensors and work areas for these 5 tests, in which sensors 1 and 2 are Nano30 and 3 and 4 are VS150-RSC sensors. The threshold of AE acquisition was 40dB and other parameters were set the same as in Figure 3.5.
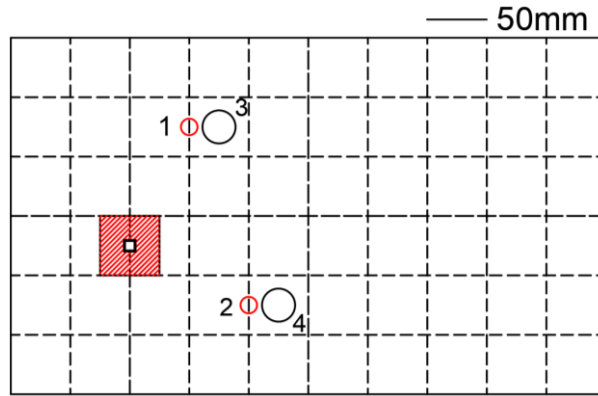
Figure 5.1 The locations of sensors for short-time tests

5.1.1 Specimen of 5mm thickness

As the characteristics of signals from different mechanisms acquired by Nano30 sensors have been summarised, it is feasible to compare individual signals obtained by VS150-RSC with the signal by Nano30 of the same event. Therefore, only the events captured by all four sensors were retained. After clustering the signals from Nano30, the corresponding signals acquired by VS150-RSC were then classified. Figure 5.2 demonstrates the signals' distributions in the PE1-PE2-Energy graph.
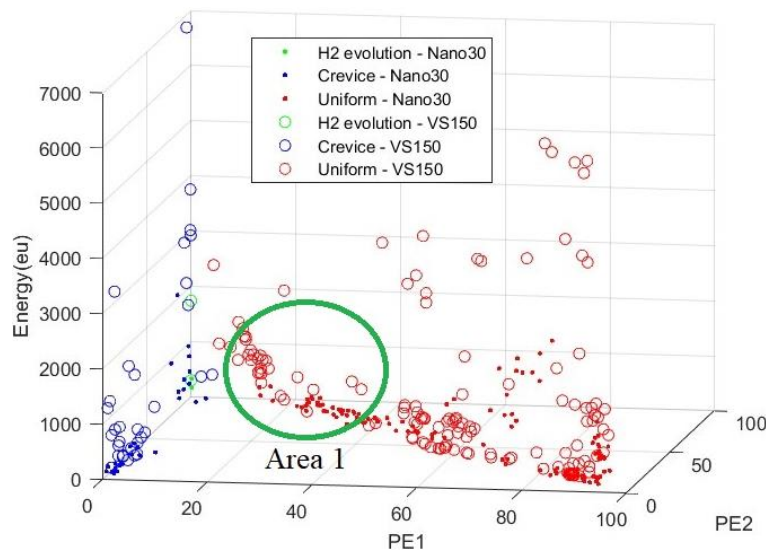
Figure 5.2 PE1-PE2-Energy graph of three signal clusters from Test 5.1

From Figure 5.2, it can be seen that the frequency distributions of the three types of signals obtained by VS150-RSC were similar to those signals from Nano30. For the signals of uniform corrosion acquired by VS150-RSC, they still presented a heavier proportion of low-frequency components (50-100 kHz) than other kinds of signals, which is confirmed in Chapter 4. However, compared to the uniform corrosion signals

from Nano30, the low-frequency features exhibited by some of them were not obvious, especially the signals in Area 1. In Area 1, signals acquired by Nano30 had a PE1 of at least 18%, but the PE1 of the corresponding signals obtained by VS150-RSC was as low as 5%, which is very close to that value of the HIC signal. This makes the critical conditions of the uniform corrosion signal and the HIC signals more blurred, causing more difficulty in signal identification.

5.1.2 Specimen of 10mm thickness

For Tests 5.2 and 5.3 with 10mm thickness specimens, there were also found three types of signals according to the frequency distribution. Figure 5.3 shows the results of PE1-PE2-Energy of Test 5.2 (Figure 5.3 (a)) and Test 5.3 (Figure 5.3 (b)) of these three kinds of signals. It can be seen that there were numerous Type 3 signals in Test 5.2 whilst a significant reduction in Test 5.3. In the light of the theoretical signal sources, the signals of Type 3 were from uniform corrosion. Their frequency spectrums contain heavier low-frequency components, which is the same as the uniform corrosion signals obtained in a 5mm-thickness specimen. Based on the results from Test 5.1, the energy of H_2 evolution signals is generally lower than that of crevice corrosion signals. Type 1 thus presented signals of H_2 evolution and Type 3 signals were from crevice corrosion.
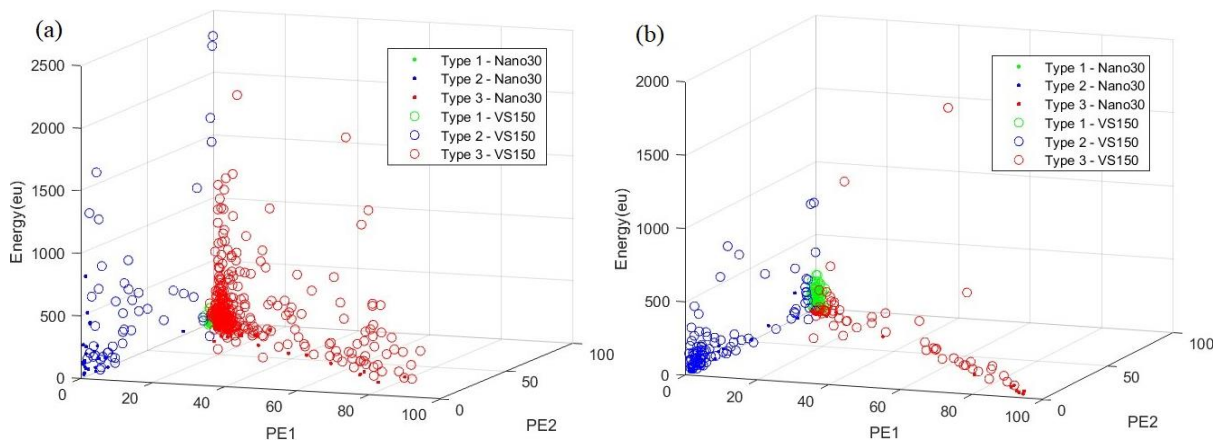
Figure 5.3 PE1-PE2-Energy graph of three signal clusters from (a) Test 5.2 and (b) Test 5.3

5.1.3 Specimen of 20mm thickness

Tests 5.4 and 5.5 with a 20mm-thickness specimen were analysed in the same way. Figure 5.4 shows the results of PE1-PE2-Energy of Test 5.2 (Figure 5.4(a)) and Test 5.3 (Figure 5.4(b)) of the different kinds of signals. Type 1 signals were deduced to be from H_2 evolution, Type 2 signals were from crevice corrosion and Type 3 signals were

from uniform corrosion. It is noted that no Type 1 signals were obtained by Nano30 in Test 5.4 whereas three signals were identified as Type 1 in Test 5.5. This is mainly due to the different physical phenomena in these two tests. A lot of H_2 bubbles were produced in Test 5.5 due to the cathode protection process. They merged into a bigger size bubble quickly and then broke with a higher energy. Due to larger bubbles and faster hydrogen evolution, the probability of acquiring H_2 evolution signals in Test 5.5 is therefore higher.
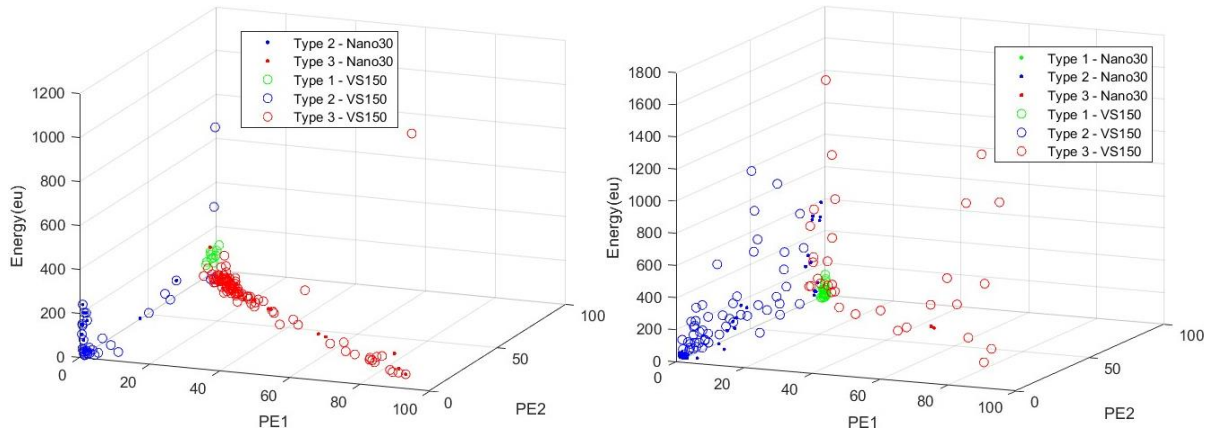
Figure 5.4 PE1-PE2-Energy graph of three signal clusters from (a) Test 5.4 and (b) Test 5.5

5.1.4 Discussions

As the test evolutions of Tests 5.1, 5.3 and 5.5 were closer to the ECHC-HIC tests, only the results of these three tests are to be discussed. Tests 5.2 and 5.4 were used as compared tests for identifying signal sources.

The various thicknesses of specimens do not affect the frequency distribution of the three types of signals. However, the energy and number of acquired signals reduce with increasing thickness, especially the signals from uniform corrosion. This demonstrated that low-energy uniform corrosion signals were relatively dominant, whose amplitudes were mostly below 40dB.

Different types of sensors, Nano30 and VS150-RSC, influence the frequency distributions on uniform corrosion and crevice corrosion signals. Figure 5.5 shows the PE1-PE2-Peak Frequency graphs of crevice corrosion signals acquired by Nano30 (Figure 5.5(a)) and VS150-RSC (Figure 5.5(b)). It is clear that the peak frequency centres around 350kHz of signals from Nano30 whereas about 250kHz from VS150-RSC. This indicated that the frequency distribution of the signal will be concentrated towards 150kHz, which is decided by the resonant frequency of VS150-RSC sensors.

In addition, for a same event, the energy of signals from VS150-RSC is higher than that from Nano30, which is because of the higher sensitivity of the VS150-RSC sensor.
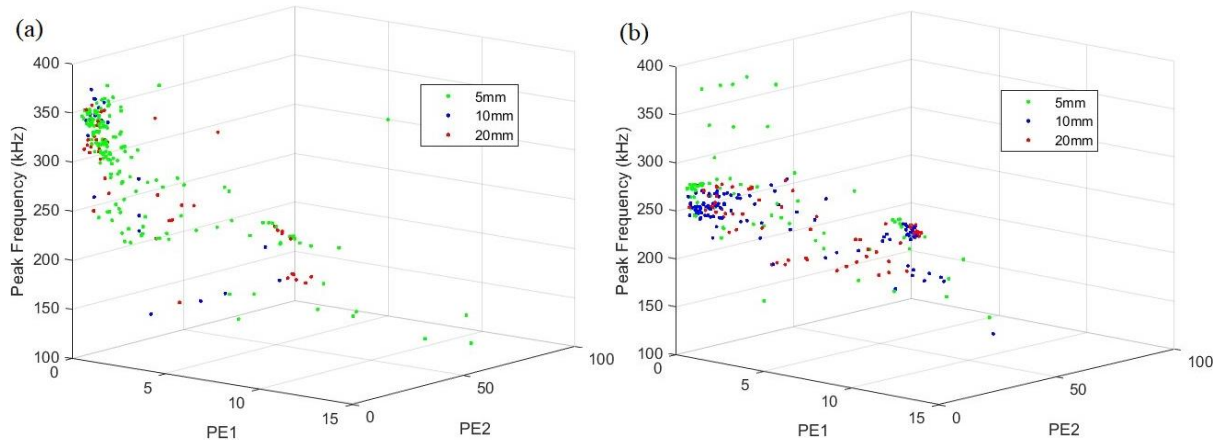
Figure 5.5 PE1-PE2-Peak Frequency graphs of crevice corrosion signals acquired by (a) Nano30 and (b) VS150-RSC

5.2 ECHC-HIC tests for the detailed analysis on signals

5.2.1 Experimental setup

As the non-HIC signals have been identified, the ECHC-HIC tests on specimens with various thicknesses were carried out for distinguishing HIC signals. To better analyse the signals' propagations, four sensors of each type were placed as a line with a gap of 100mm, as shown in Figure 5.6. Sensors 1, 2, 3 and 4 are Nano30 and Sensors 5, 6, 7 and 8 are VS150-RSC. It is noted that Sensor 5 was attached to the reverse surface under the work area. The test duration was 20h and the AE threshold was 40dB. All other AE parameters were set as Figure 3.5 shows.
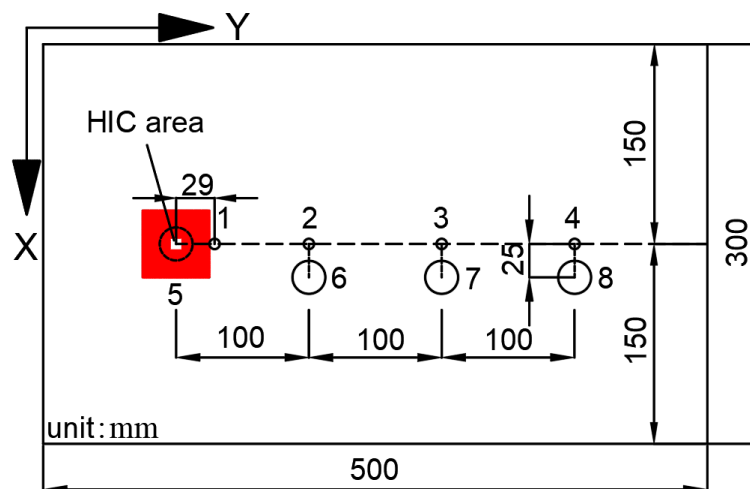
Figure 5.6 The setup of ECHC-HIC tests

5.2.2 Results of signal identification

According to the results obtained in Section 5.1, signals from four mechanisms in ECHC-HIC tests on each specimen can be identified. Figures 5.7-5.18 display the typical signals of each kind of event on each specimen.

5.2.2.1 Signals of H_2 evolution

The main characteristics of signals from H_2 evolution are low Energy, low Counts and Peak Frequency around 130-180kHz with a narrow band. Figure 5.7(a) and Figure 5.8(a) display the signals' waveforms and spectrums acquired by Nano30 sensors on 5mm and 10mm thickness specimens. Figure 5.7(b), Figure 5.8(b) and Figure 5.9(b) show the waveforms and spectrums from VS150-RSC sensors on 5mm, 10mm and 20mm-thick specimens. In Figure 5.7, it can be seen that all four VS150-RSC sensors were triggered while only two Nano30 sensors (Sensor 1 and Sensor 2) were triggered by the H_2 evolution event. On 10mm-thick specimen, one Nano30 sensor and three VS150-RSC sensors acquired the signals. And in Figure 5.9, even only two VS150-RSC sensors were triggered. There are mainly three reasons that caused the phenomena. Firstly, the energies emitted by H_2 evolution events were low, resulting in short distance propagation on specimens. Secondly, Nano30 sensors have lower sensitivity than VS150-RSC sensors, causing missing data acquired from Nano30 sensors. Finally, the attenuation increased with the specimens' thicknesses increased.
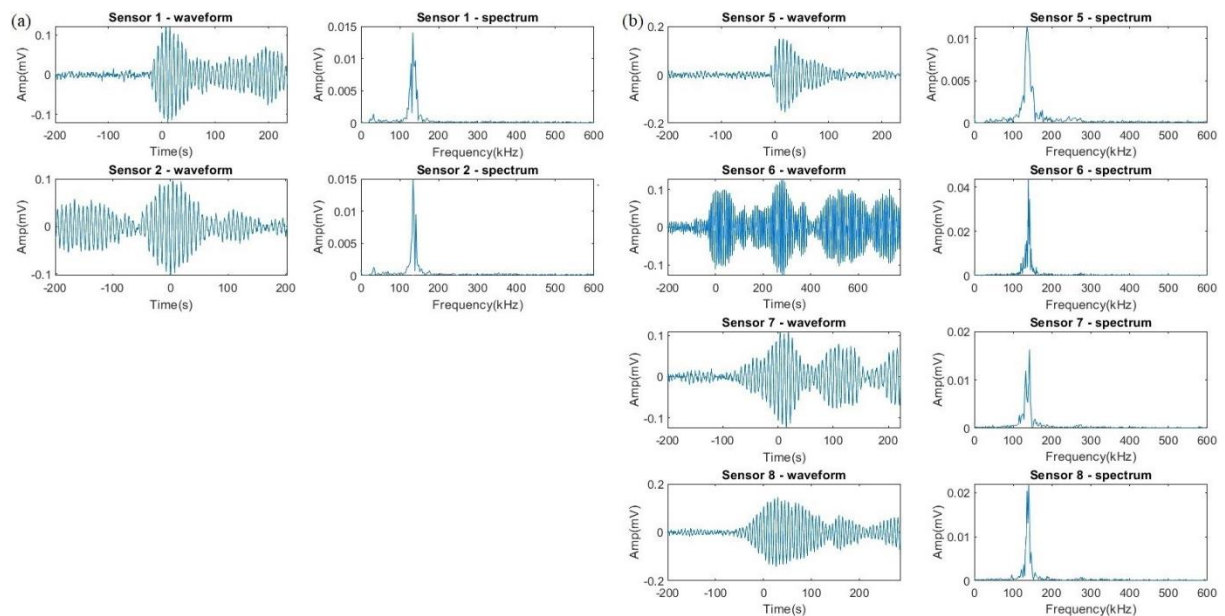
Figure 5.7 The waveforms and spectrums from the same event of H_2 evolution acquired by (a) Nano30 sensors (b) VS150-RSC on 5mm-thick specimen
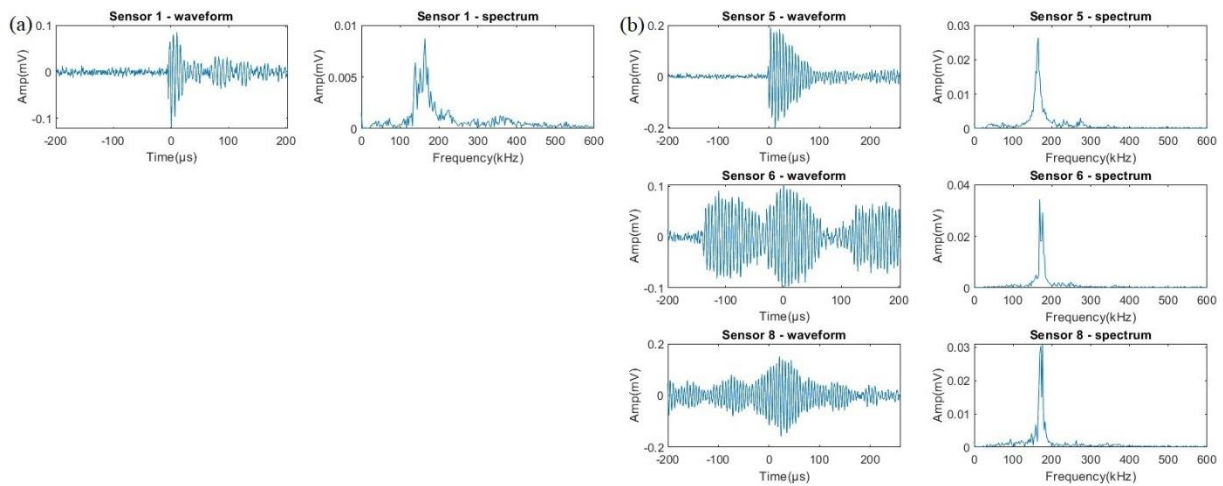
Figure 5.8 The waveforms and spectrums from the same event of H_2 evolution acquired by (a) Nano30 sensors (b) VS150-RSC on 10mm-thick specimen
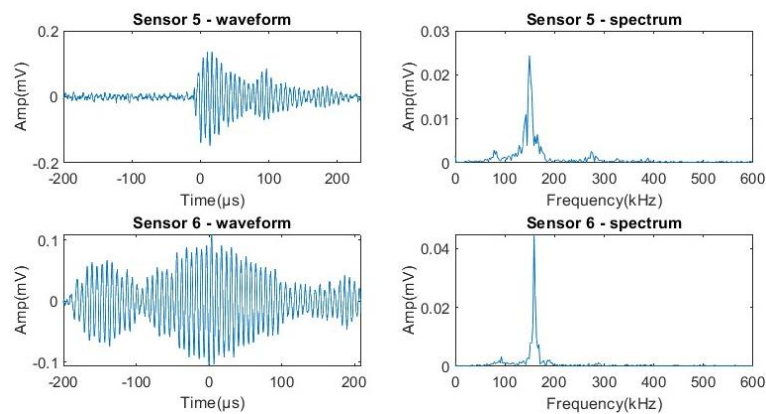
Figure 5.9 The waveforms and spectrums of H_2 evolution acquired by VS150-RSC on 20mm-thick specimen

5.2.2.2 Signals of crevice corrosion

Higher frequency components (>200kHz) are the main characteristics used to identify signals of crevice corrosion. Figure 5.10(a), Figure 5.11(a) and Figure 5.12(a) show the signals' waveforms and spectrums acquired by Nano30 sensors. Figure 5.10(b), Figure 5.11(b) and Figure 5.12(b) show the waveforms and spectrums from VS150-RSC sensors.
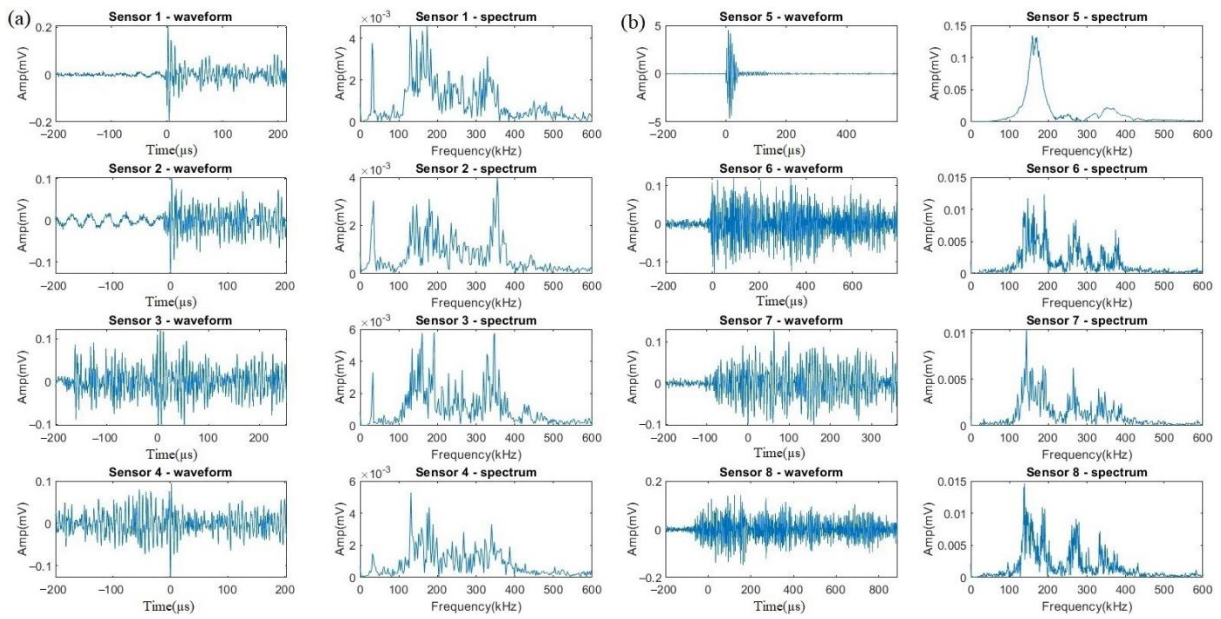
Figure 5.10 The waveforms and spectrums from the same event of crevice corrosion acquired by (a) Nano30 sensors (b) VS150-RSC on 5mm-thick specimen
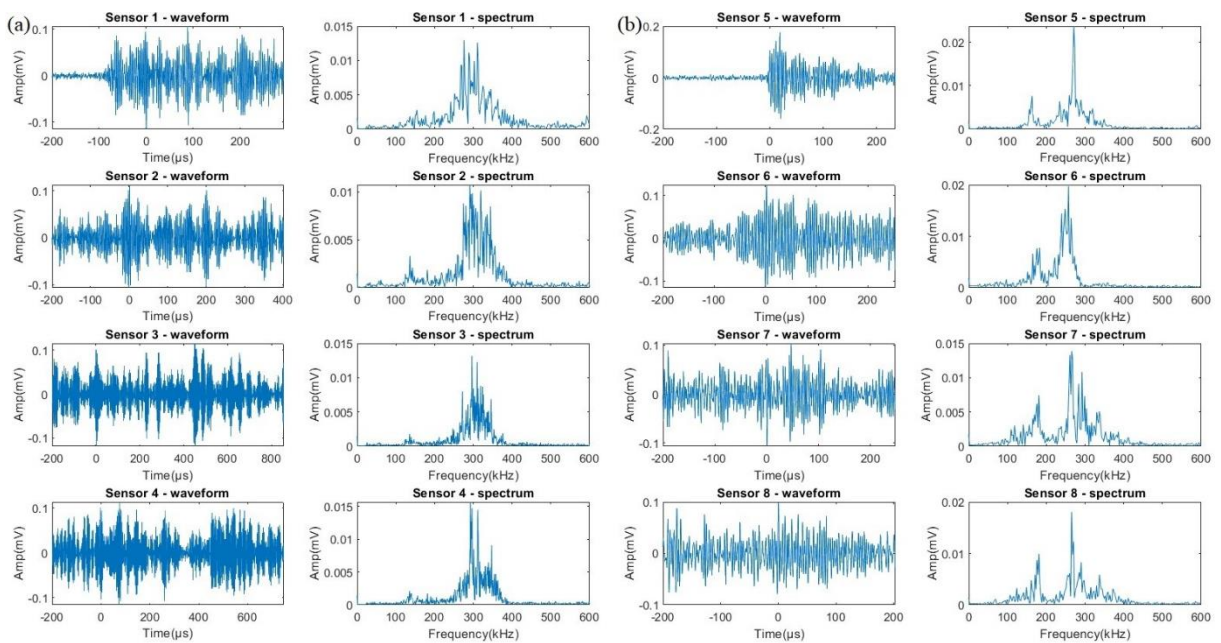
Figure 5.11 The waveforms and spectrums from the same event of crevice corrosion acquired by (a) Nano30 sensors (b) VS150-RSC on 10mm-thick specimen
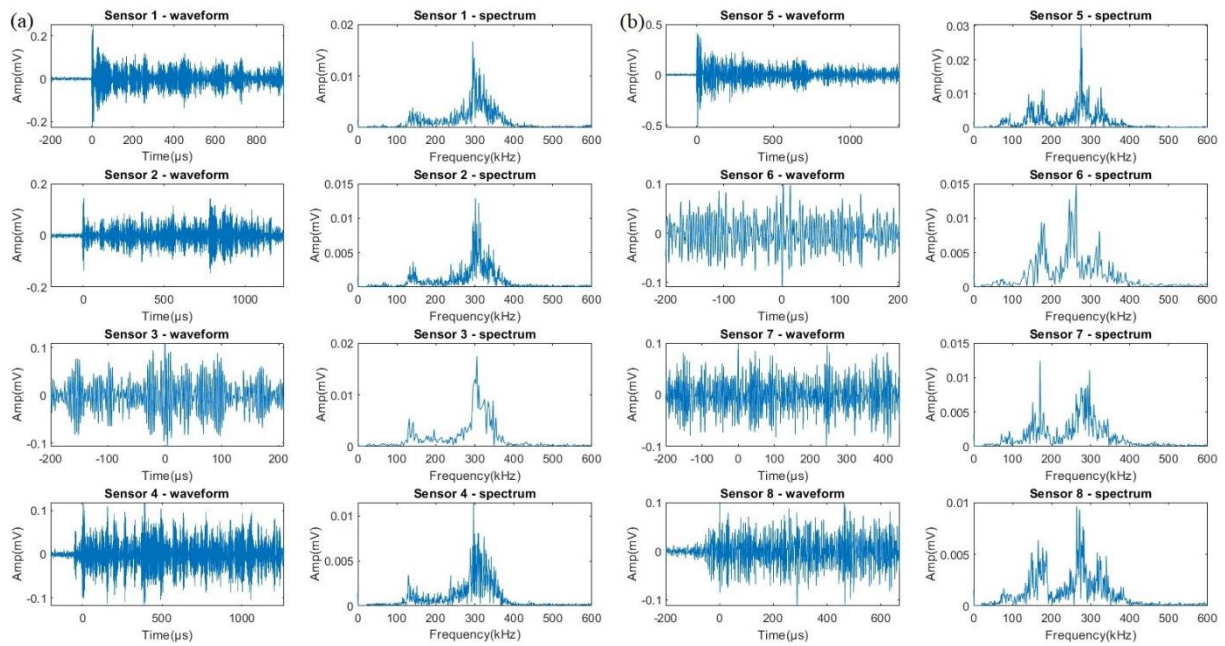
Figure 5.12 The waveforms and spectrums from the same event of crevice corrosion acquired by (a) Nano30 sensors (b) VS150-RSC on 20mm-thick specimen

5.2.2.3 Signals of uniform corrosion

Lower frequency components (<100kHz) are the main characteristics used to identify signals of uniform corrosion. Figure 5.13(a), Figure 5.14(a) and Figure 5.15(a) display the signals' waveforms and spectrums acquired by Nano30 sensors on 5mm and 10mm thickness specimens. Figure 5.13(b), Figure 5.14(b) and Figure 5.15(b) show the waveforms and spectrums from VS150-RSC sensors on the three different thickness specimens.
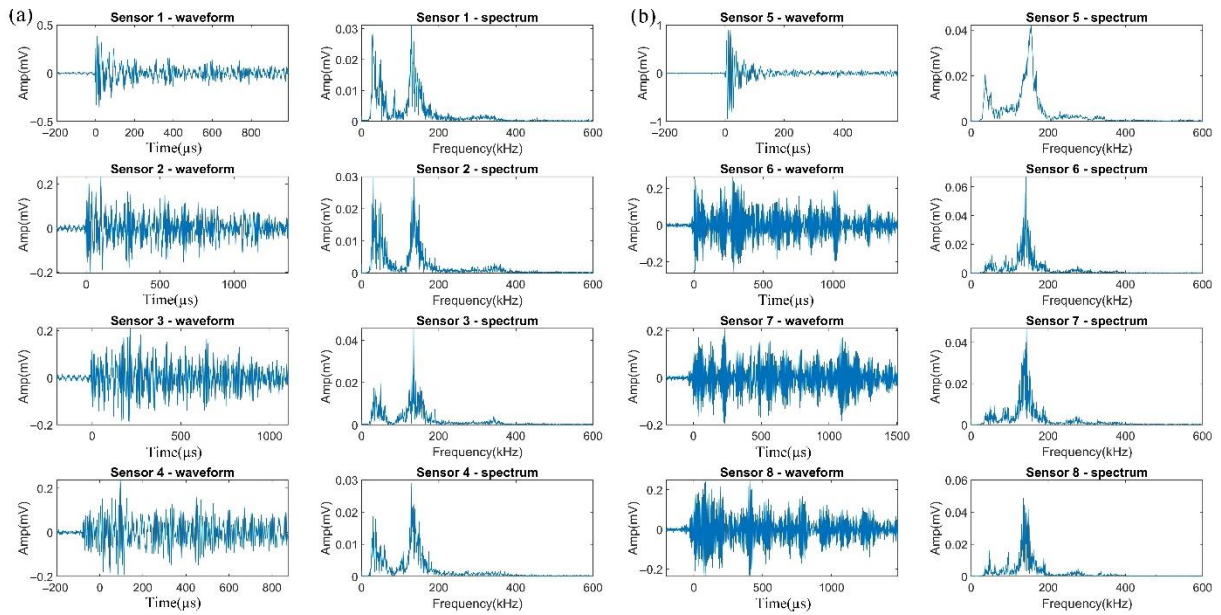
Figure 5.13 The waveforms and spectrums from the same event of uniform corrosion acquired by (a) Nano30 sensors (b) VS150-RSC on 5mm-thick specimen
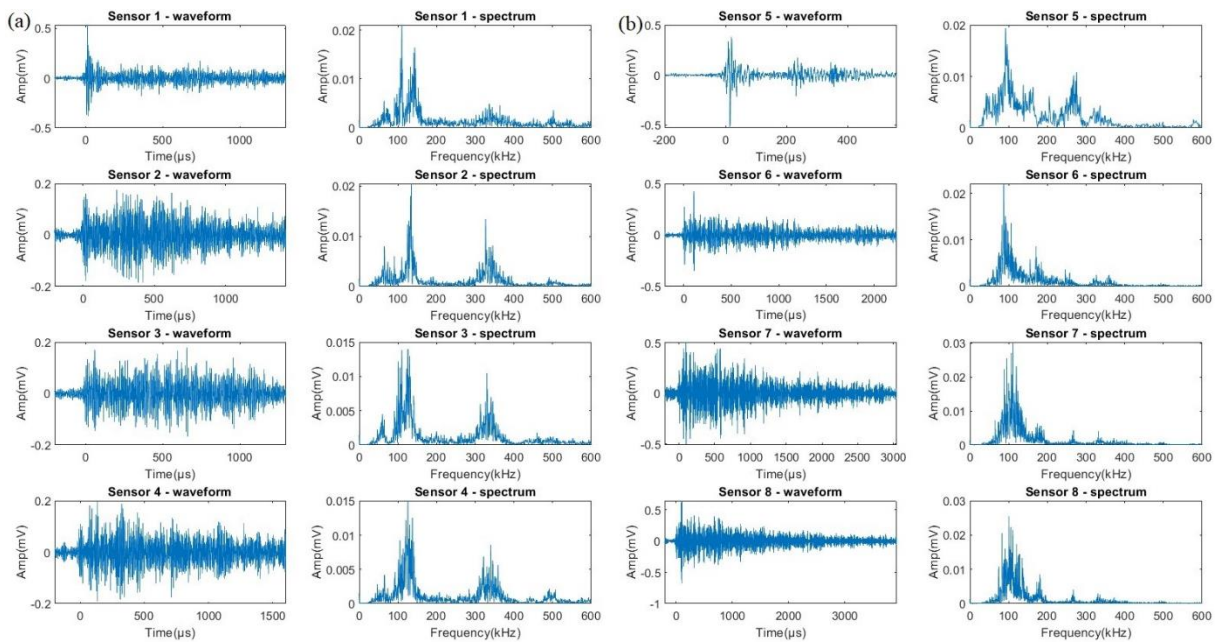
Figure 5.14 The waveforms and spectrums from the same event of uniform corrosion acquired by (a) Nano30 sensors (b) VS150-RSC on 10mm-thick specimen
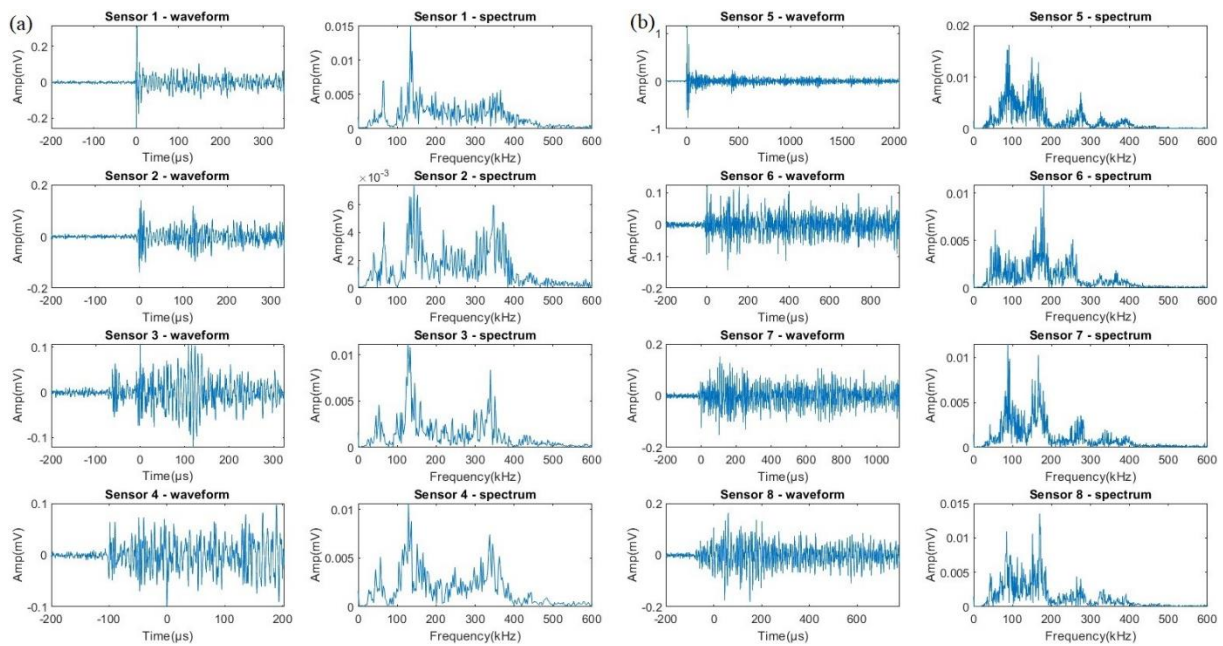
Figure 5.15 The waveforms and spectrums from the same event of uniform corrosion acquired by (a) Nano30 sensors (b) VS150-RSC on 20mm-thick specimen

5.2.2.4 Signals of HIC

A new group of signals, which is represented by HIC signals, was acquired. by both types of sensors on the three specimens. The main characteristics of these HIC signals obtained by both types of sensors on the three specimens are the same: higher Energy, higher Counts and Peak Frequency around 120-180kHz. Figure 5.16(a), Figure 5.17(a) and Figure 5.18(a) show example waveforms and spectrums acquired by Nano30 sensors. Figure 5.16(b), Figure 5.17(b) and Figure 5.18(b) exhibited waveforms and spectrums from VS150-RSC sensors.
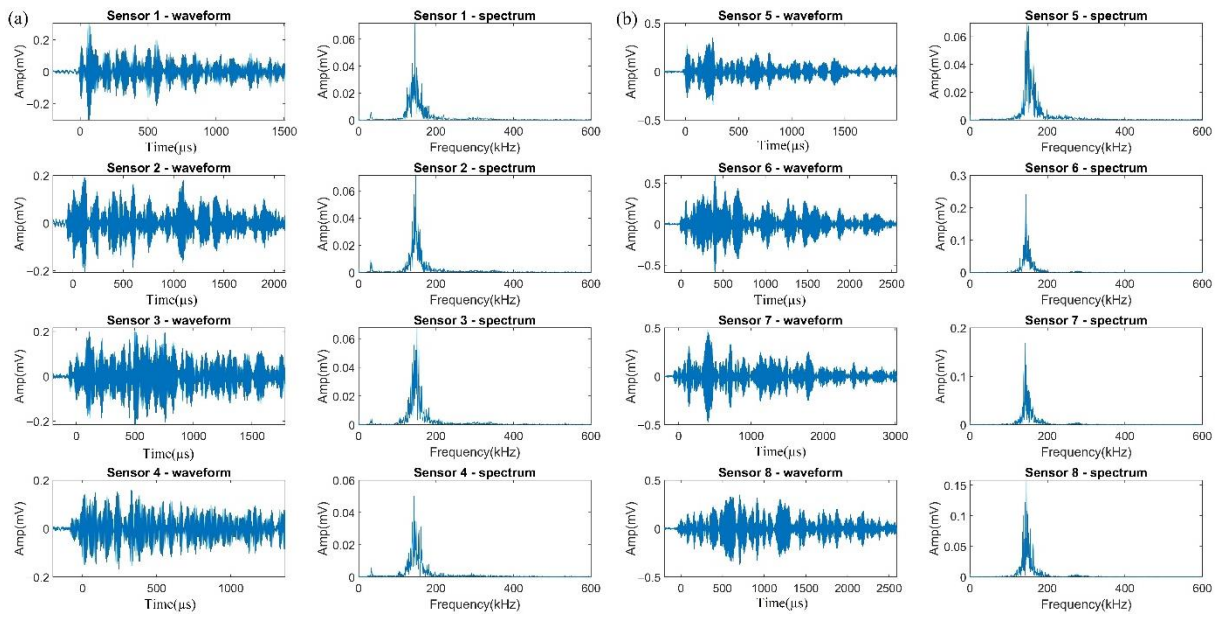
Figure 5.16 The waveforms and spectrums from the same event of HIC acquired by (a) Nano30 sensors (b) VS150-RSC on 5mm-thick specimen
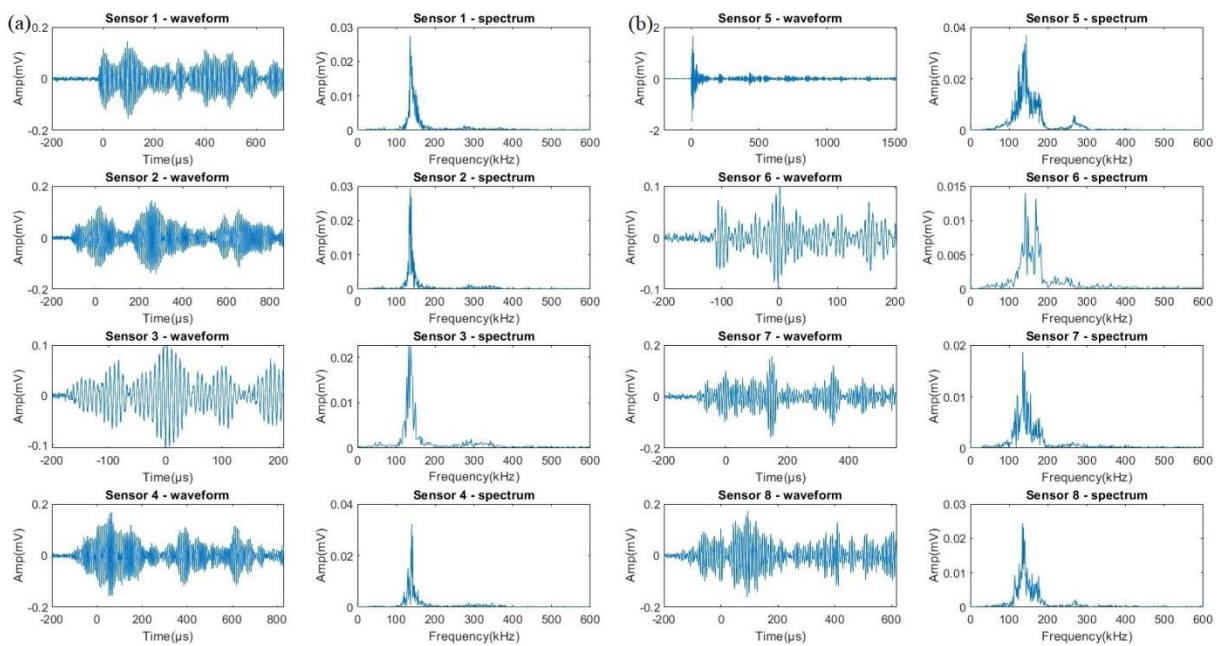
Figure 5.17 The waveforms and spectrums from the same event of HIC acquired by (a) Nano30 sensors (b) VS150-RSC on 10mm-thick specimen
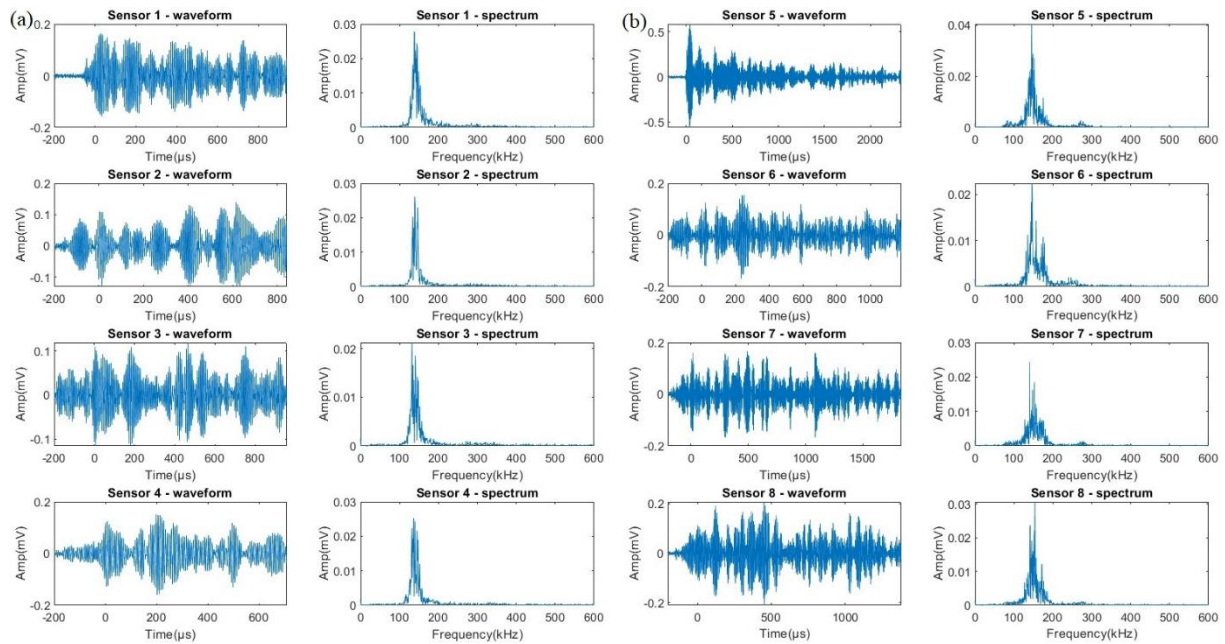
Figure 5.18 The waveforms and spectrums from the same event of HIC acquired by (a) Nano30 sensors (b) VS150-RSC on 20mm-thick specimen

5.2.3 Discussions on parameters' influences

The difference between non-HIC signals acquired by two types of sensors has been discussed in Section 5.1. As for HIC signals, it can be seen from Figures 5.16-5.18 that the frequency distributions of signals acquired by Nano30 and VS150-RSC on the same specimen were almost the same, especially on the specimen with a thickness of 5mm. On 10mm and 20mm-thick specimens, the frequency distributions of signals from Nano30 were the same as those on 5mm-thick specimen. However, for VS150-RSC, the bandwidths of frequency spectrums were bigger, which had more components of 170-200kHz. The main differences between HIC signals collected by the two kinds of sensors were the parameters in the time domain. Figure 5.19 demonstrates the values of some primary parameters, Duration, Counts and Energy, which were extracted from both sensors on three specimens. It can be seen that the Duration and Energy from VS150-RSC were an order of magnitude higher than those from Nano30. Combined with the more complete waveforms acquired by VS150-RSC, it can be inferred that the results of source location prediction by VS150-RSC will be more accurate because of the more accurate selection of onset time.
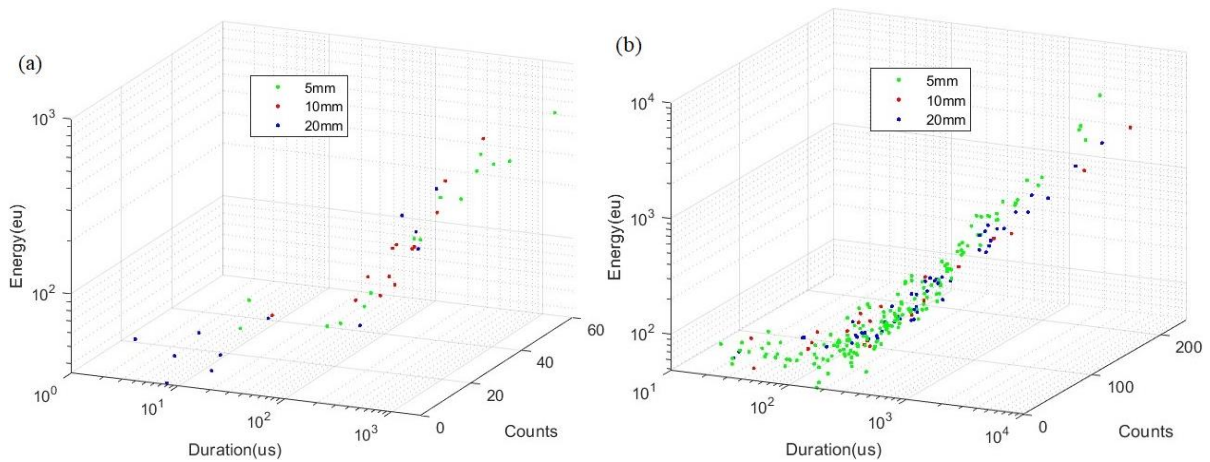
Figure 5.19 Representation of Duration-Counts-Energy of HIC signals acquired by (a) Nano30 and (b) VS150-RSC on three specimens

5.2.4 Velocity of signals propagation

Velocity is another important parameter for better understanding the propagation of signals, not only for source location, but also can be used for simply identifying the mode of Lamb wave which is crossing the threshold and triggering the AE system. In Section 3.5, it is shown that Nano30 were triggered by the A_0 mode of HIC signals propagating on a 5mm-thick specimen and the velocity of the waveform is about 3110mm/ms. Both mode and velocity and known to change with various thicknesses of specimens. In this study, only signals from HIC events were analysed.

From the work of Hamstad [167], the approximate frequency below which a Rayleigh wave cannot propagate versus thickness of steel plate is demonstrated, which is shown in Figure 5.20. When the thickness of the steel plate is less than 20mm, the HIC signal with a frequency of about 150kHz propagates in the form of Lamb waves. Therefore, the research methodology in Section 3.5 is still suitable for the HIC signals acquired on 10mm and 20mm-thick specimens.
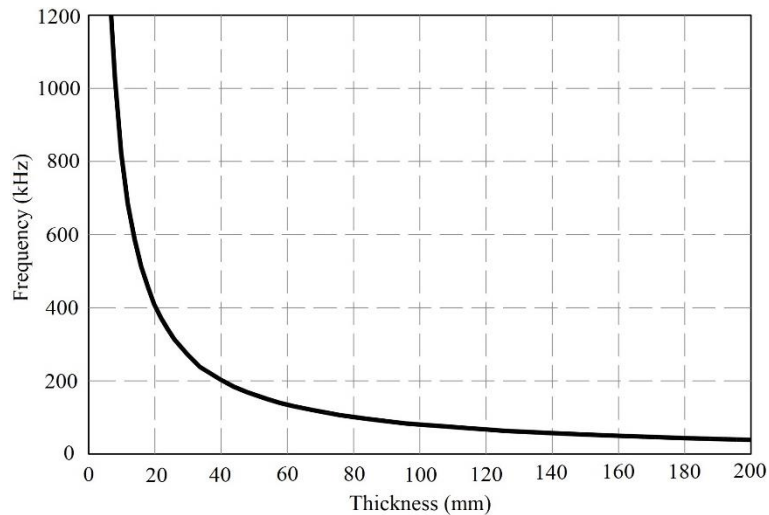
Figure 5.20 Approximate frequency below which a Rayleigh wave cannot propagate versus thickness of steel plate [167]

To improve accuracy, the onset time of each signal was determined by the AIC method. However, for some signals with incomplete waveforms, such as the signals' waveforms shown in Figure 5.18, the onset time can still not be accurately picked with the AIC method. Generally, there are more complete waveforms of signals with higher peak amplitudes due to higher energies. Besides, the impact of events that generate high-energy signals on the state of the structure is more worth considering. Therefore, for analysing the velocity results, more attention should be paid to velocities where most data is concentrated as well as the velocities obtained from signals with high peak amplitudes.

Figure 5.21 shows the Velocity-Amplitude graph of HIC events acquired by Nano30 (Figure 5.21(a)) and VS150-RSC (Figure 5.21(b)) on a 5mm-thick specimen. For Nano30 sensors, the velocities were calculated according to the time difference of the signals collected by Sensors 2, 3, and 4 related to Sensor 1 from a same event. As for VS150-RSC sensors, the velocities were calculated according to the time difference of the signals collected by Sensors 6, 7, and 8 related to Sensor 5 from the same event. It can be seen that the velocities calculated from the signals with higher amplitude are concentrated around 3000mm/ms. From Figure 3.33 (the dispersion curve), the velocity of HIC on a 5mm-thick specimen can be determined as 3110mm/ms, whether acquired by Nnao30 or VS150-RSC sensors.
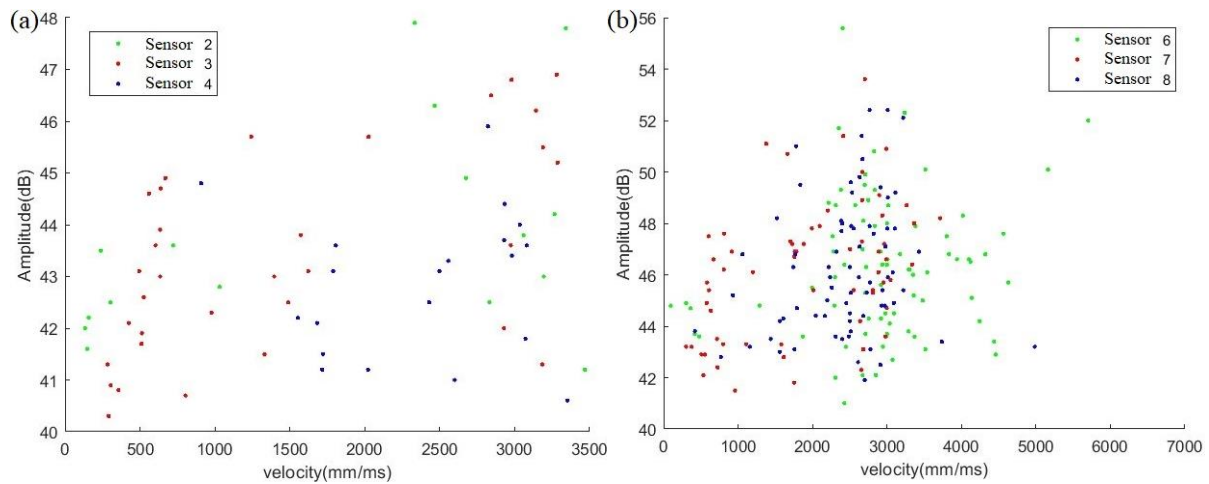
Figure 5.21 Velocity-Amplitude results of HIC events after applying AIC method on 5mm-thick specimen (a) Nano30 (b) VS150-RSC

Figure 5.22 presents the Velocity-Amplitude graph of HIC events acquired by Nano30 (Figure 5.22(a)) and VS150-RSC (Figure 5.22(b)) on a 10mm-thick specimen in the same way. Most results from Sensors 3 and 4 were concentrated at 3200mm/ms, while the results from Sensor 2 were concentrated around 500mm/ms (signals with lower amplitude) or 3600mm/ms (signals with higher amplitude). It is strange that the velocity calculated by the signals from Sensor 2 was about 300mm/ms while that from Sensors 3 or 4 was 3200mm/ms from the same event. A detailed study was carried out on the event whose signal's propagation speed was about 500mm/ms in Sensor 2. It was found that the emitted signal was first acquired by Sensor 4 and then was obtained by Sensors 3 and 2. Figure 5.23 displays the waveforms and 2D Colour Contour Diagram of WT Coefficients (from -160us to 20us) of signals from Sensor 4 (a, c) and Sensor 2(b, d) from an event in this situation. It can be seen that the part waveform (from -160us to 20us) in Figure 5.23(b) corresponds to the waveform between -40us to 20us in Figure 5.23(a), but with apparent attenuation. This is likely to be the reflected signals from the edge. The velocity calculated in this situation is not correct because the time difference and distance difference calculated relative to the signal of channel 1 do not match correctly. Therefore, the velocity range is 3100-3700mm/ms after filtering those signals.

As for the results from VS150-RSC, it can be seen that there is a central tendency at 3100mm/ms. In terms of the signals with lower propagation velocity from Sensor 6, the velocities calculated with the corresponding signals from Sensors 7 and 8 were also low. This indicates that the low velocity is caused by an incomplete waveform,

rather than the situation shown in Figure 5.23(a). Overall, the velocity of HIC propagating on a 10mm-thick specimen was about 3200mm/ms. Figure 5.24 depicts the dispersion curve of Lamb wave signals propagating on a 10mm-thick plate. Corresponding to this curve, the velocity of HIC signals with higher energy was determined as 3220mm/ms and sensors were triggered by A_0 mode.
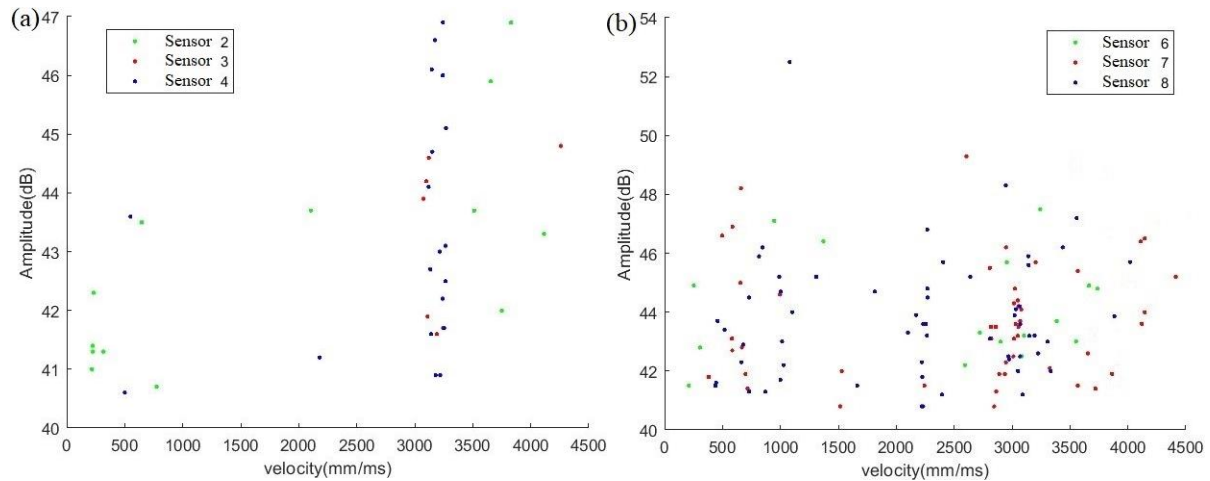
Figure 5.22 Velocity-Amplitude results of HIC events after applying AIC method on 10mm-thick specimen (a) Nano30 (b) VS150-RSC
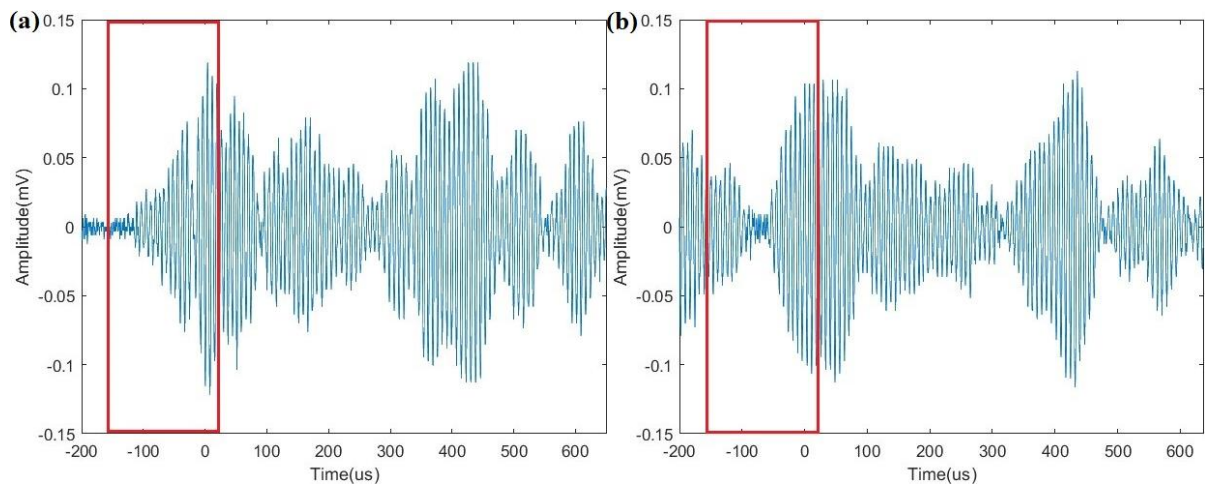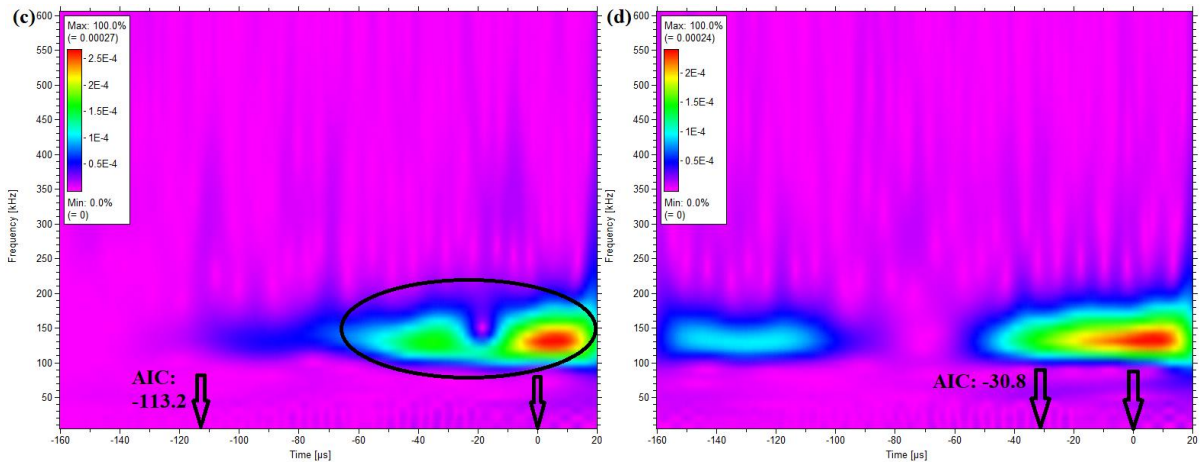
Figure 5.23 The waveforms and 2D Colour Contour Diagram of WT Coefficients of signals from channel 4 (a, c) and channel 2(b, d) from an event
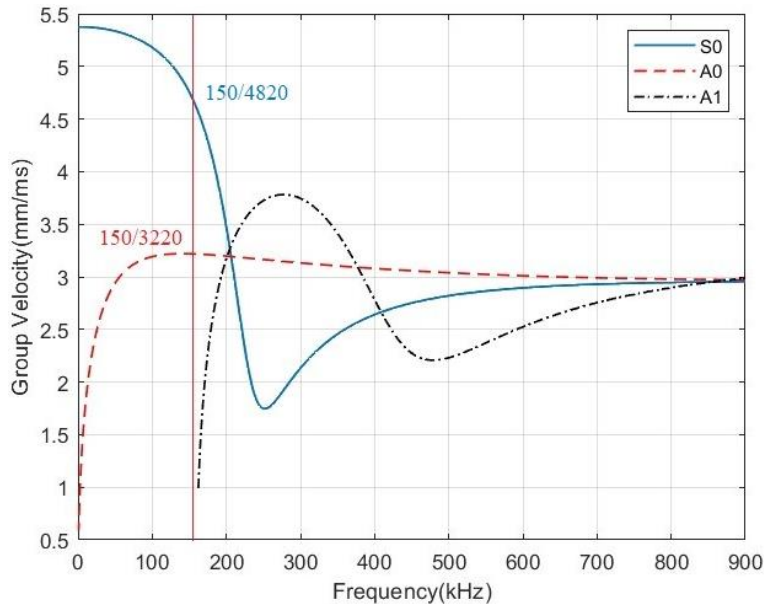
Figure 5.24 Dispersion curve of Lamb wave signals propagating in 10mm thickness plate

Figure 5.25 presents the Velocity-Amplitude graph of HIC events acquired by Nano30 and VS150-RSC on the 20mm-thick specimen. The results from Nano30 sensors are not representative due to too few signals and high numbers of incomplete waveform. The analysis of results from VS150-RSC will therefore be the focus. From Figure 5.25(b), the velocities were lower than 3000mm/ms and most results from signals with higher amplitudes were concentrated around 2000mm/ms. According to the dispersion curve which is shown in Figure 5.26, the trigger mode should be S_0 and the velocity can be determined as 2200mm/ms. One typical signal from channel 6 was analysed in details by wavelet analysis combined with a dispersion curve, which is shown in Figure 5.27. Figure 5.27(a) gave the waveform of the signal which is totally complete.

The 2D Colour Contour Diagram of WT Coefficients with the normal max scale of colour coding (100%) is shown in Figure 5.27(c), in which the duration was selected from -32us to 19us. However, the specific distribution is not clear due to the heavy attenuation on this plate. The maximum scale of colour coding is thus adjusted to 10%, which is better for observation with the combination of a dispersion curve (Figure 5.27(b)). Therefore, with the onset time selected by the AIC algorithm (-8us), it is clear that the trigger mode is S_0.
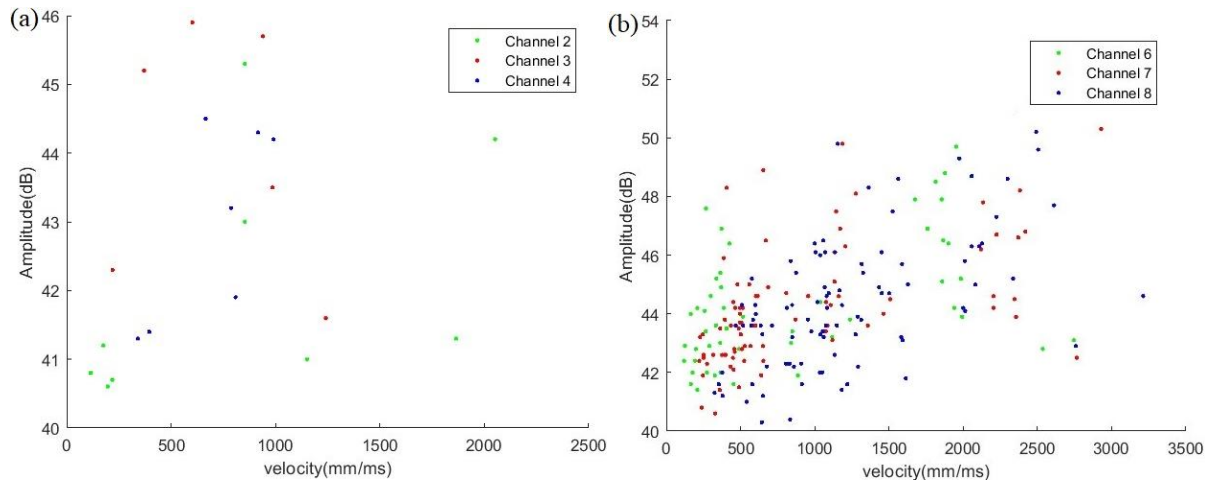
Figure 5.25 Velocity-Amplitude results of HIC events after applying AIC method on 20mm-thick specimen (a) Nano30 (b) VS150-RSC
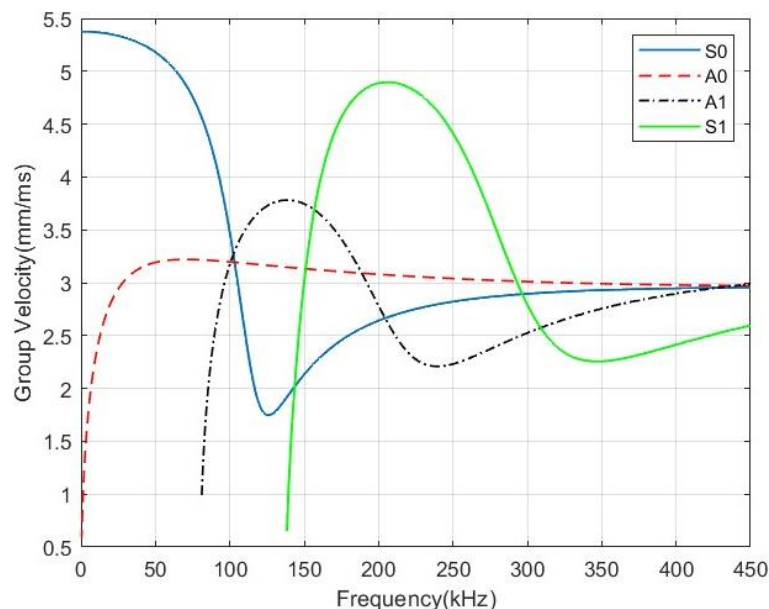
Figure 5.26 Dispersion curve of Lamb wave signals propagating in 20mm thickness plate
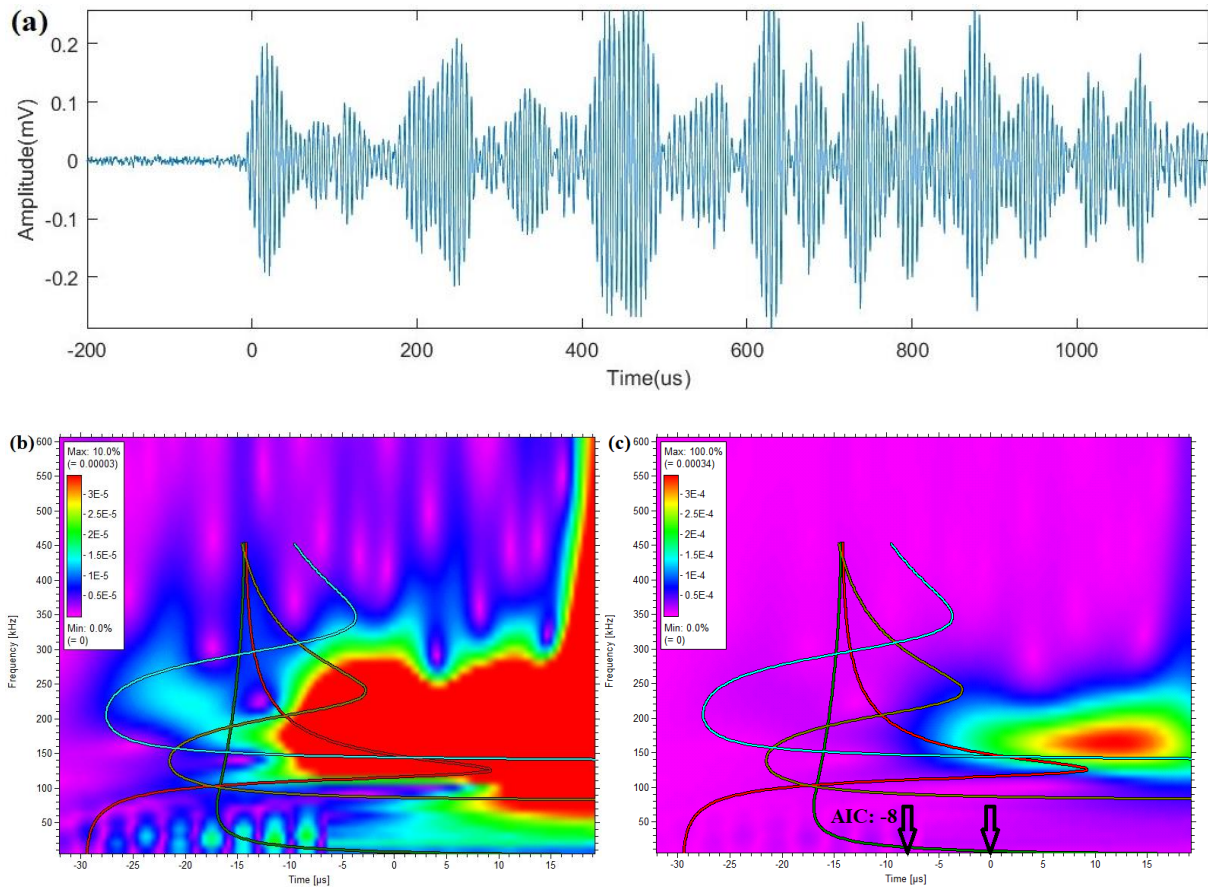
Figure 5.27 2D Colour Contour Diagram of WT Coefficients of signals from channel 6 (a) waveform (b) max scale of colour coding of 10% (b) max scale of colour coding of 100%

5.3 ECHC-HIC tests for application

The propagation and expression of signals produced during the ECHC-HIC test on three different thickness specimens acquired with Nano30 and VS150-RSC sensors were thoroughly analysed in Section 5.2. The velocities of HIC signals propagating on the different specimens were also calculated. In this section, the propagation and localisation of HIC events on different thickness specimens is investigated to evaluate AE monitoring method. At the same time, Ultrasonic Testing (UT) was applied to support the AE results.

5.3.1 Experimental setup

Figure 5.28 (a) demonstrates the setup of this ECHC-HIC test of three parts: UT system, potentiostat for ECHC method and experimental area. Figure 5.28(b) shows the locations of sensors and work areas. To better simulate the practical environment, a non-HIC area was added to the specimen as a distraction to ensure localisation was effective. Table 5.2 gives the exact coordinates of sensors and work areas.

It can be calculated that the shortest distance between sensors to HIC area is 111.8mm and the longest distance is 246.2mm. From the results above, it is known that few events can be acquired for such a long distance under the setup with previous parameters, especially on 20mm-thick specimen. Therefore, the current was increased to 50mA/cm^2 which Section 4.2 confirmed produced more HIC events. For AE parameters, the threshold was reduced to 35dB and the pre-trigger time was set as 300us to ensure more complete signals.

For UT technology, a 150kHz UT probe was placed on the opposite surface under the HIC area to detect the progress of HIC every 30s.
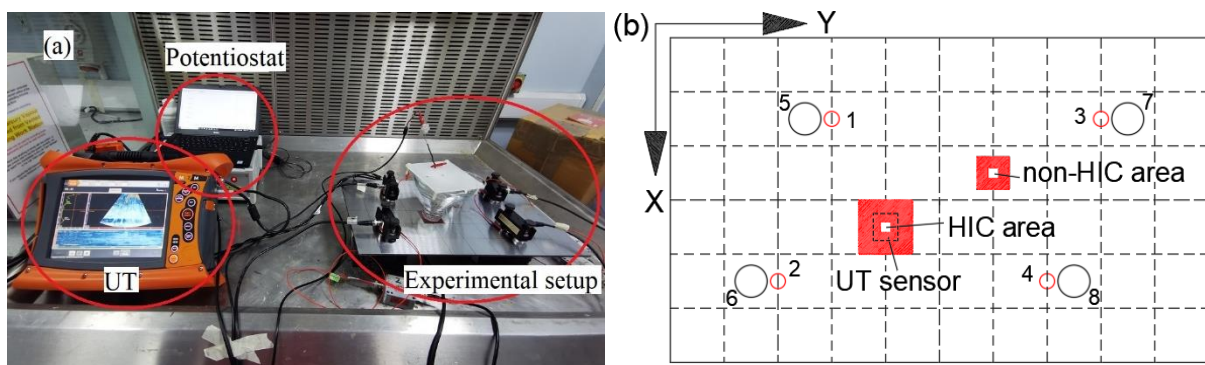
Figure 5.28 ECHC-HIC tests with UT system (a) physical setup (b) locations of sensors

Table 5.2 The coordinates of sensors and HIC/non-HIC areas

Type of sensors	Number	Coordinates	Type of sensors	Number	Coordinates
Nano30	1	(75,150)	VS150-RSC	5	(75,125)
	2	(225,100)		6	(225,75)
	3	(75,400)		7	(75,425)
	4	(225,350)		8	(225,375)
HIC area centre/UT sensor		(175,200)	Non-HIC area centre		(125,300)

5.3.2 Observation on specimens and UT results

After 20h, the equipment was removed and the specimens were rinsed with 0.5mol/L NaOH solution and deionized water. They were then air-dried after rinsing with alcohol. Figures 5.29(a)-(c) show pictures of HIC areas' surfaces on specimens of 5mm, 10mm and 20mm thicknesses, respectively. Figure 5.29(d) shows an image of the non-HIC area of a 20mm-thick specimen. The phenomena of all non-HIC areas of the three specimens are the same because of the same conditions. Therefore, only one representative image of that was displayed here.

It can be seen that corrosion phenomena were aggravated on three specimens because of higher applied currents. The area covered by uniform corrosion on the 5mm-thick specimen is the biggest. Simultaneously, lots of hydrogen blisters were observed. For the specimens with thicknesses of 5mm and 10mm, the density of blisters was higher and most sizes were small. As for Figure 5.29(c), the blisters were less but generally of greater size. To better analyse the physical phenomena, the cross-section of HIC area of each specimen was observed by optical microscope (OM). Figures 5.30-5.32 show the results of specimens with 5mm, 10mm and 20mm, respectively, in which (a) shows the whole cross-section under the work area and (b) shows the crack which is deepest. It can be seen that the generated cracks get closer to the surface as the thickness of the specimen increases. The number of cracks in Figure 5.32(a) is also significantly reduced, as well as the size of cracks was smaller in Figure 5.32(b).
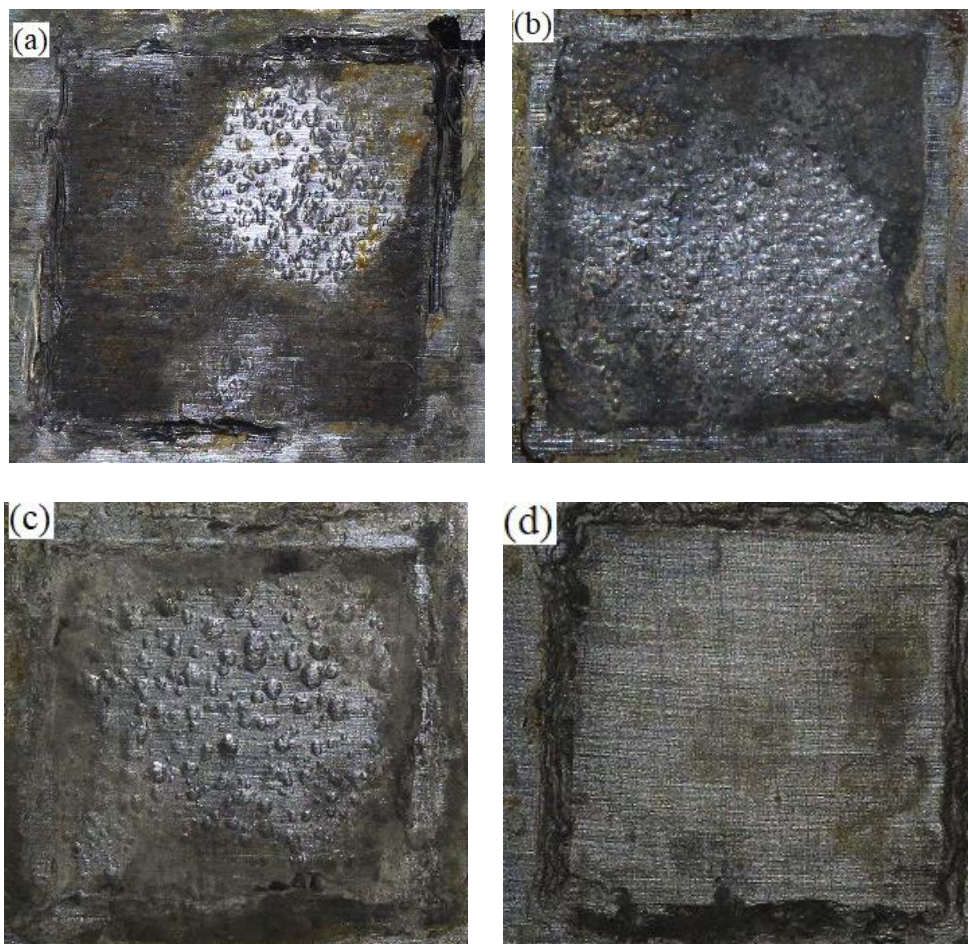
Figure 5.29 Pictures of HIC area on specimens' surface (a)5mm (b) 10mm (c) 20mm and non-HIC area on 20mm
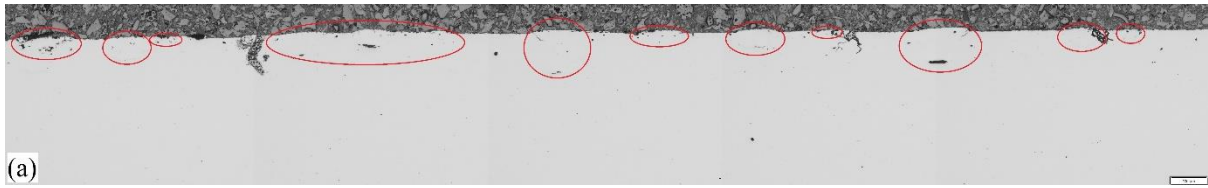
Figure 5.30 Optical Microscope observations of 5mm-thick specimen (a) the whole cross-section (b) the deepest crack
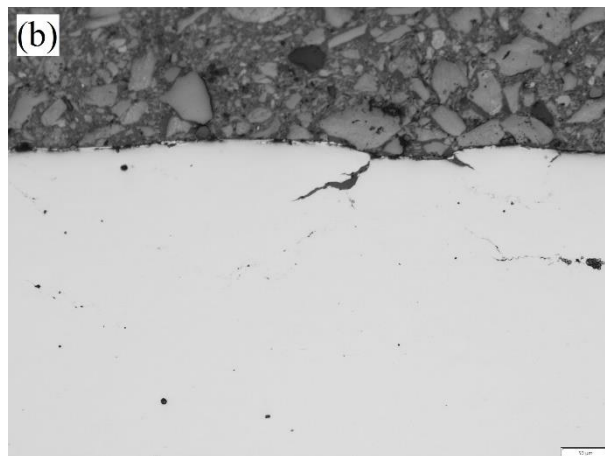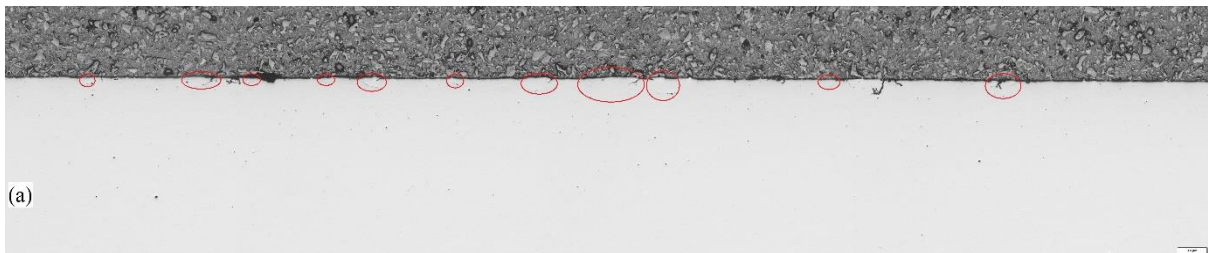
Figure 5.31 Optical Microscope observations of 10mm-thick specimen (a) the whole cross-section (b) the deepest crack
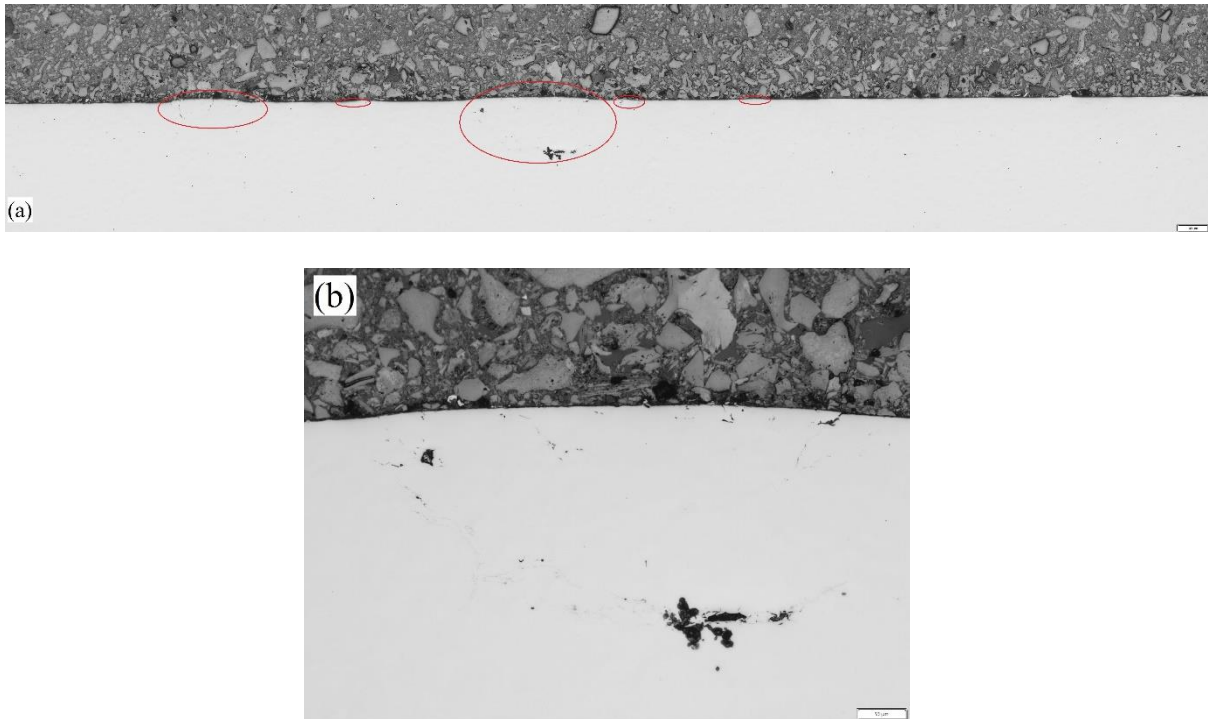
Figure 5.32 Optical Microscope observations of 20mm-thick specimen (a) the whole cross-section (b) the deepest crack

In addition, UT technology was also applied to monitor the development of HIC. Figures 5.33-5.35 give the UT images of HIC areas on specimens with thicknesses of 5mm, 10mm and 20mm, respectively, in which (a) was captured at 0s and (b) was captured at 20h.

The red region at the bottom of each image is called backwall, which is exactly the surface of HIC area. It is obvious that the backwalls changed a lot in Figures 5.33-5.35(b). This is because of the existence of blisters that block the penetration of ultrasound. It can be seen that only the colour in the backwall changed, which means only blisters on the surface or close to the surface were detected by UT. Therefore, the HIC progress can be expressed by calculating the reduction of the red region with time, which will be illustrated later with AE results.
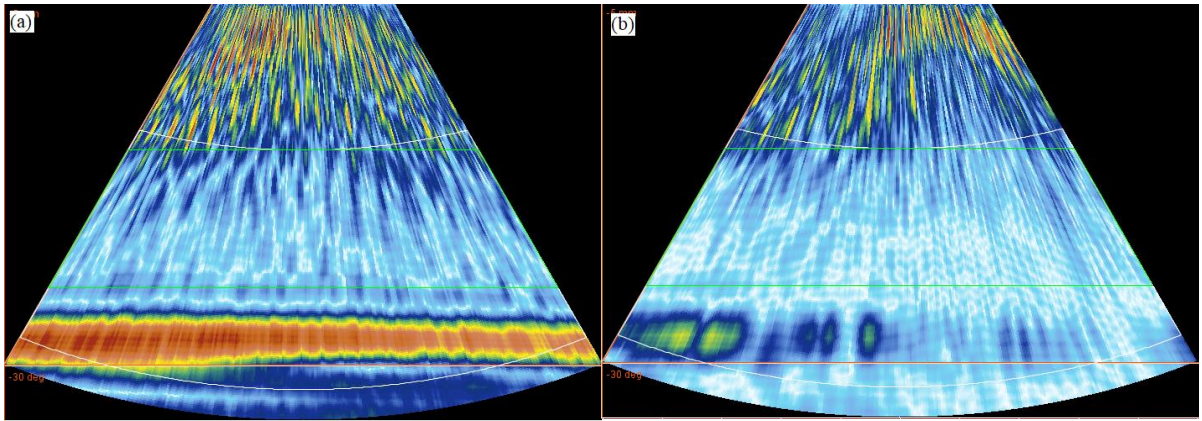
Figure 5.33 UT images of HIC area on 5mm-thick specimen (a) 0h (b) 20h
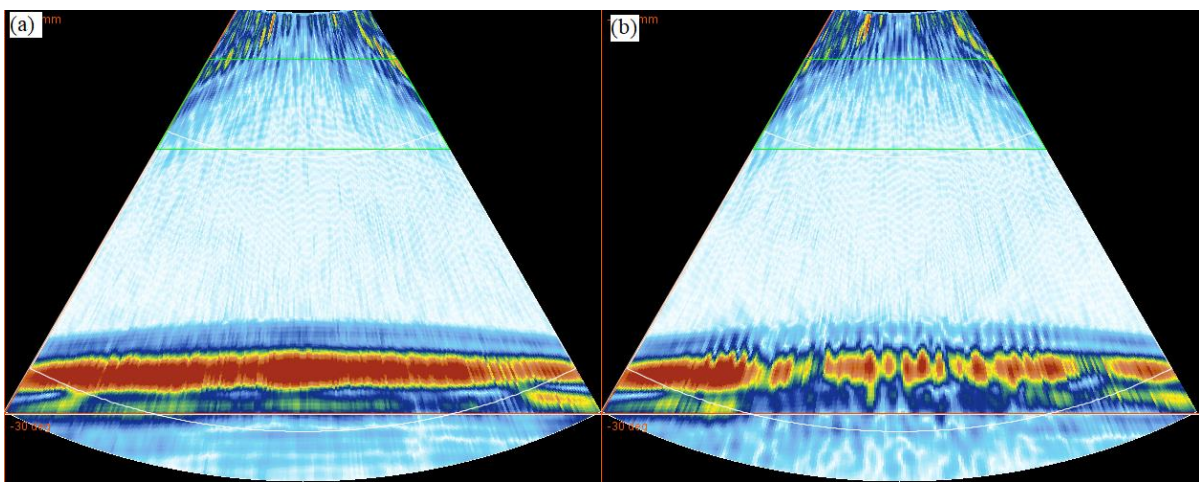
Figure 5.34 UT images of HIC area on 10mm-thick specimen (a) 0h (b) 20h
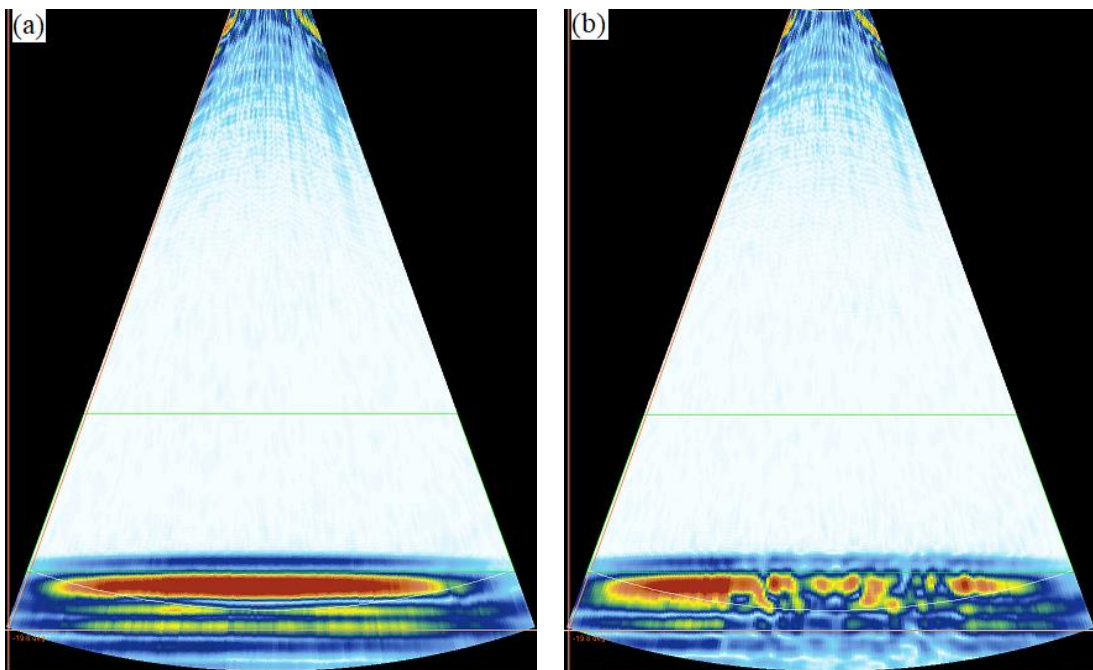
Figure 5.35 UT images of HIC area on 20mm-thick specimen (a) 0h (b) 20h

149

5.3.3 Analysis of HIC development with AE and UT

In order to reduce unnecessary processing work, the raw data from AE was filtered. Only an event whose emitted wave was captured by at least three sensors of the same type was reserved. According to the summarized characteristics of each kind of event, the mixed signals can be clustered. It has been verified that the two-step GMM clustering method proposed in Chapter 4 was effective in classifying signals. Therefore, this method was applied to classify the four groups' signals from Nano30 and VS150-RSC sensors. The critical signals were then checked manually. In addition, the development of HIC was represented by the changes in the cumulative energy of HIC events with time. For UT results, HIC progress can be quantified by the change of colour in the backwall. To better compare its result with that of AE, the increment of the other two colours' element was calculated based on the image at 0s instead of the reduction of the red element.

5.3.3.1 Specimen with thickness of 5mm

Figure 5.36(a) and (b) illustrate the results of Time-Amplitude/Cumulative Energy of HIC of classified signals acquired by Nano30 and VS150-RSC. A greater number of signals were acquired by VS150-RSC than by Nano30, no matter from which kind of events. The amplitudes of signals from VS150-RSC were generally 5dB higher than those from Nano30. Even though the phenomena of corrosion were aggravated, the amplitude of most signals from two types of corrosion was under 40dB as well as the signals of H_2 evolution. Therefore, for this 5mm-thick specimen, most non-HIC signals can be well filtered with the threshold settled at 40dB. This will not influence the expression of HIC development too much because the energy of a signal with a low amplitude was technically low. However, the determination of the initial HIC signal may be affected.

The Cumulative Energy of HIC signals indicates HIC development during hydrogen charging. The progress of HIC given by both types of sensors was similar even though the total energy differed by an order of magnitude. During 0-6120s, the cumulative energy increased rapidly and smoothly which demonstrated that lots of small cracks occurred. In 6120s-39960s, the cumulative energy growth rate slows down but with some small fluctuations. This meant that the crack started to grow steadily. Larger energy may be released by the formation of bigger cracks or the connection of

adjacent cracks, resulting in several fluctuations in the cumulative energy curves. From 39960s to the end, the cumulative energy curve gradually flattens. It is assumed that the saturation of hydrogen permeation makes the cracks basically stop growing.
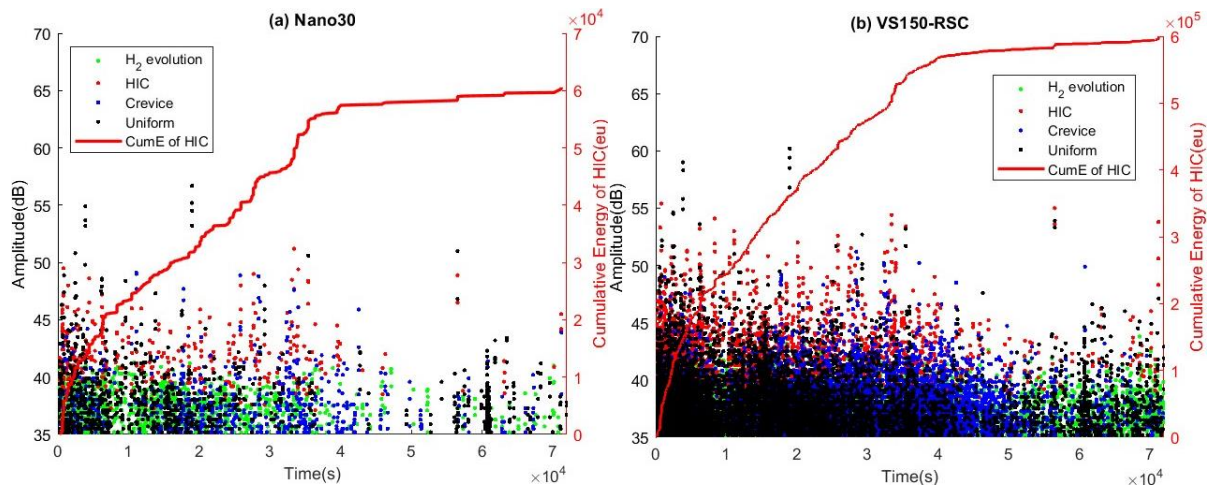
Figure 5.36 Time-Amplitude/Cumulative Energy of HIC of 4 kinds of signals on 5mm-thick specimen (a) Nano30 and (b) VS150-RSC

The HIC progresses represented by AE results from two types of sensors and UT results are compared in Figure 5.37. The gap in the energy between signals from two types of sensors was observed more intuitively. It is further clarified that the sensitivity of VS150-RSC to HIC signals. As for UT results, it is concluded that lots of HIC events were detected within the first three hours, the reduction of red element was as high as 93%, which is consistent with AE results. However, in the next three hours, no crack growth was observed. The red element increased by another 20% even at 23760s and always fluctuated till the end of the test. It is speculated resulting from the couplant problem between the UT probe and specimen. Moreover, the edge of a crack revealed in UT images was not very clear. Two adjacent but not connected cracks may already be considered as one large crack in the UT images. This is also considered to be the reason why no further crack growth was detected after three hours. Furthermore, the initial HIC signals were found at 190s, 234s and 510s by VS150-RSC, Nano30 and UT technology. The results were quite similar, except that the UT detection was less sensitive.
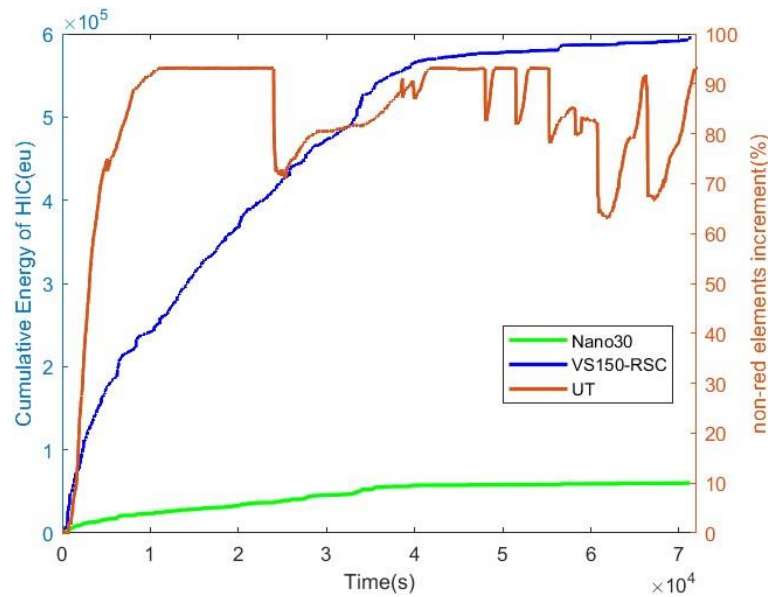
Figure 5.37 Comparison of AE results represented by Cumulative Energy of HIC events -Time and UT results of the non-red elements increment-Time on 5mm-thick specimen

5.3.3.2 Specimen with thickness of 10mm

Figure 5.38(a) and (b) illustrate the results of Time-Amplitude/Cumulative Energy of HIC of classified signals acquired by Nano30 and VS150-RSC. Similarly, signals acquired by VS150-RSC were still much more than those acquired by Nano30. Nevertheless, the HIC progress expressed by Nano30 and VS150-RSC were still similar. During the first 50mins, the cumulative energy increased rapidly which corresponds to the occurrence of small cracks on or close to the surface. After that, there were gentle curves lasting about 4320s in both results which are different from the results on a 5mm-thick specimen. This should be a process of hydrogen diffusion to the deeper inside of the plate. Cracks grew between 7560s-43920s, and then gradually stopped till the end of the test. It can be seen that the curve obtained from VS150-RSC included more details and only several HIC events with high energy were acquired by Nano30.
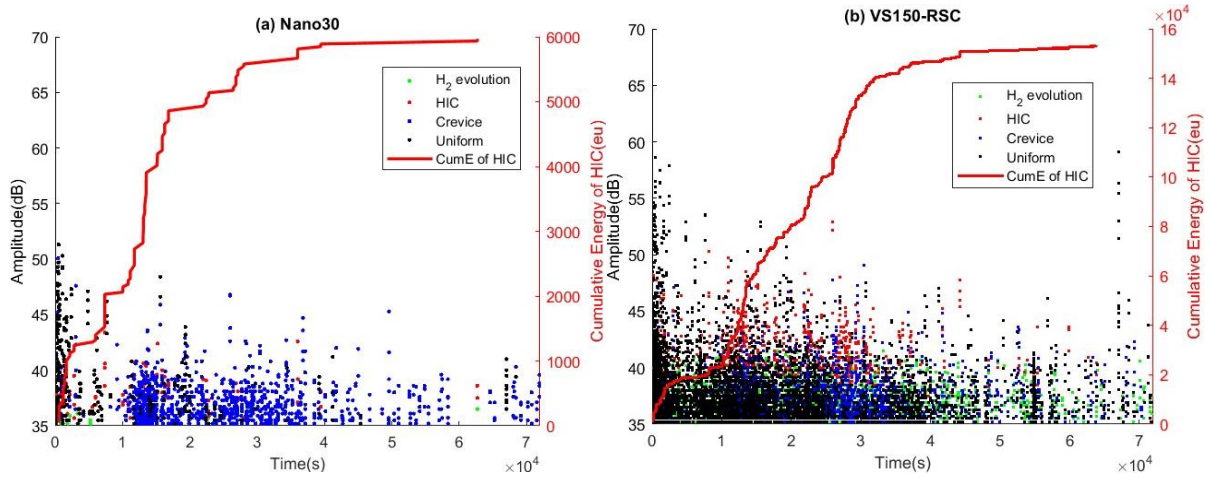
Figure 5.38 Time-Amplitude graphs of 4 kinds of signals on 10mm-thick specimen (a) Nano30 and (b) VS150-RSC

Figure 5.39 displays the HIC progress represented by AE results from two types of sensors and UT results. Within the beginning of 5040s, the red element represented the backwall kept decreasing, which indicated the appearance of cracks close to the surface. As in Figure 5.37, the subsequent curve barely rises. In addition, the highest percentage of non-red elements increment was only 32% which is different from the curve in Figure 5.37. This demonstrated that the total crack area on a 10mm-thick specimen was smaller than that on a 5mm-thick specimen. The initial HIC signals were found at 165s, 220s and 330s by VS150-RSC, Nano30 and UT technology.
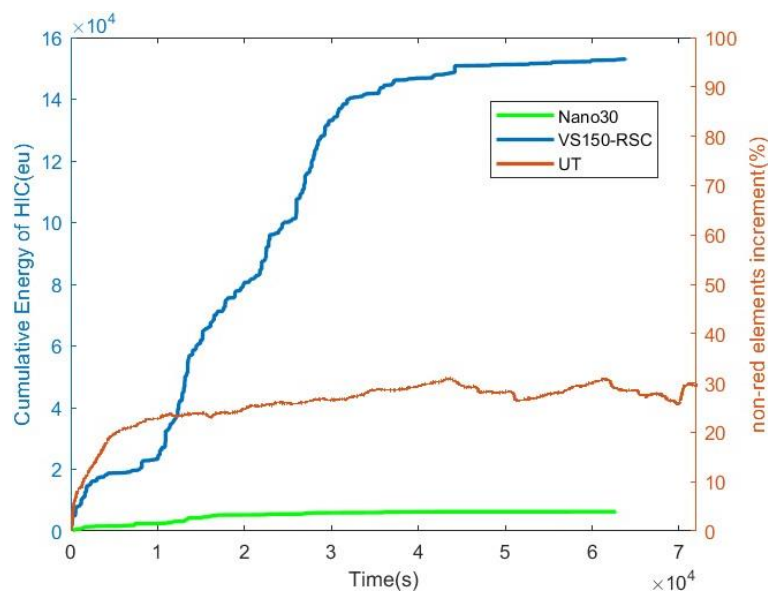
Figure 5.39 Comparison of AE results represented by Cumulative Energy of HIC events -Time and UT results of the non-red elements increment-Time on 10mm-thick specimen

5.3.3.3 Specimen with thickness of 20mm

Figure 5.40(a) and (b) illustrate the results of Time-Amplitude/Cumulative Energy of HIC of classified signals acquired by Nano30 and VS150-RSC. Compared with Figures 5.36 and 5.38, the number of signals from both types of sensors had a large reduction. Few HIC signals were acquired by Nano30 and the final cumulative energy was only 2000eu. The first HIC signal was found at 9000s and the HIC progress was analysed with only 11 HIC events, which was not a reliable result. As for VS150-RSC sensors, the development of HIC could still be depicted by the curve of cumulative energy. The main HIC events had still been acquired by these sensors in light of the level of cumulative energy. The HIC progress described in Figure 5.40(b) is similar to that in Figure 5.38(b). However, at 3000s, the curve gradually flattens and lasts longer. This revealed that the process of hydrogen diffusion into the plate lasted longer. After the process of crack growth, the curve no longer rises uniformly but with some small bursts. It is indicated that the crack growth has not stopped, but has grown very slowly in the 20mm-thick plate.
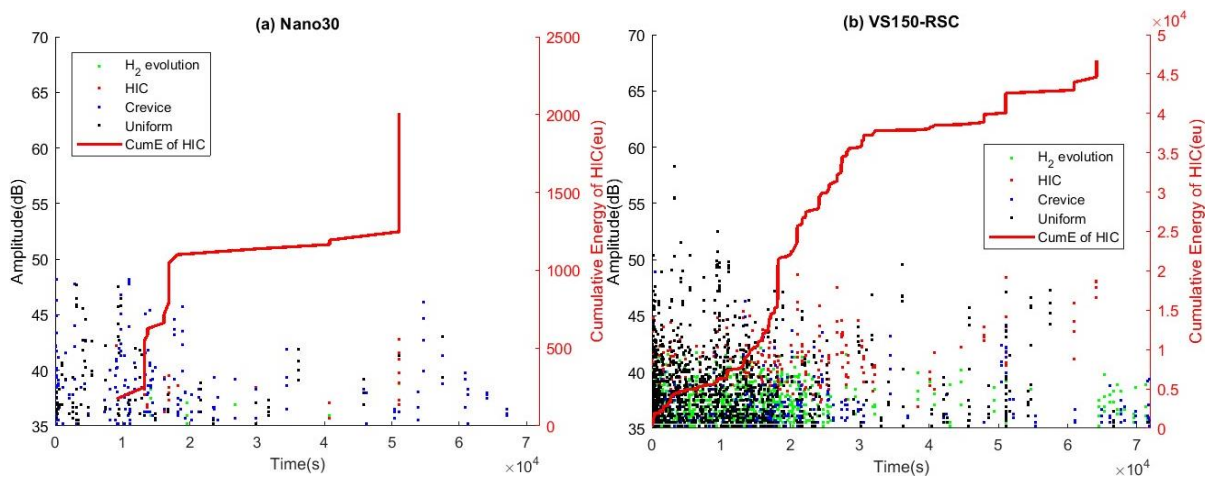
Figure 5.40 Time-Amplitude graphs of 4 kinds of signals on 20mm-thick specimen (a) Nano30 and (b) VS150-RSC

Figure 5.41 displayed the HIC progress represented by AE results from two types of sensors and UT results. The initial HIC signals were found at 218s, 9000s and 330s by VS150-RSC, Nano30 and UT technology.
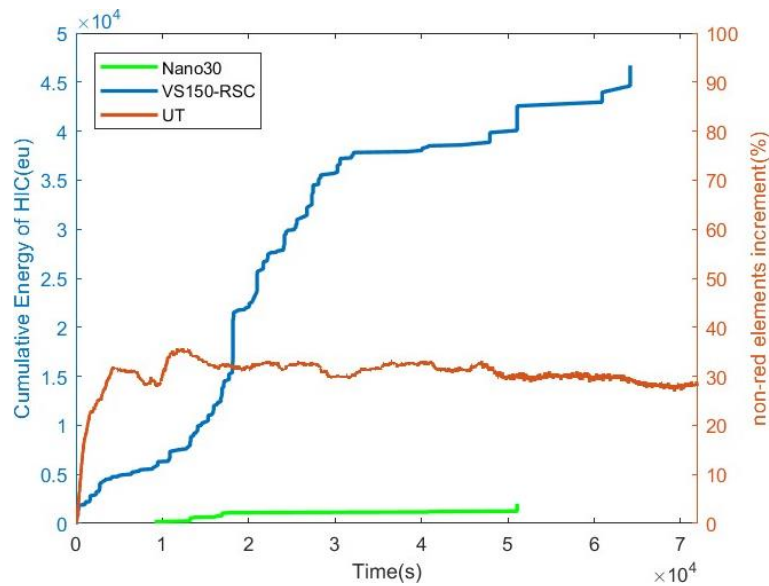
Figure 5.41 Comparison of AE results represented by Cumulative Energy of HIC events -Time and UT results of the non-red elements increment-Time on 20mm-thick specimen

In conclusion, compared to the UT technique, there can be seen more details from AE results, not only the occurrence of initial HIC event, but also the growth information in the number of HIC events. However, with the increase in specimens' thickness, the results from Nano30 sensors were not too instructive because few signals were obtained. In this case, the initial HIC event is better determined by UT results rather than from AE with Nano30 sensors. Nevertheless, the corrosion phenomena on the surface influence the disappearance of backwall in UT images as well. Therefore, it is a good choice to monitor the HIC development by AE with VS150-RSC sensors, especially in the case of thick specimens and long distances.

5.3.4 Source localisation

For a planar source location using AE technology, at least three sensors are needed which are not in a line. Therefore, for each type of sensor, an HIC event whose emitted wave was captured by three or four sensors was reserved. Signals of HIC have been classified in Section 5.3.3. The onset time of every signal was picked by the AIC method. The location of each event was calculated by the Simplex method with the known velocity from Section 5.2.4. Finally, the results of source localisation on three specimens are shown in Figures 5.42-5.44.

It can be seen that the distributions of locations on three specimens were concentrated around the coordinate of (175, 200), which was exactly where the HIC area was.

Evidently, the number of accurately localized HIC events gradually decreases as the thickness of specimen increases. Table 5.3 shows the details of source localisation of HIC events on each specimen by three kinds of numbers. These are the total number of HIC events, and the number of HIC events located within the whole plate, the number of HIC events located within the work area. However, there were errors in calculations caused by the calculations of onset time and velocity. Therefore, a HIC event located in the range of 160<x<180, 185<y<215 was considered to be located within the work area.
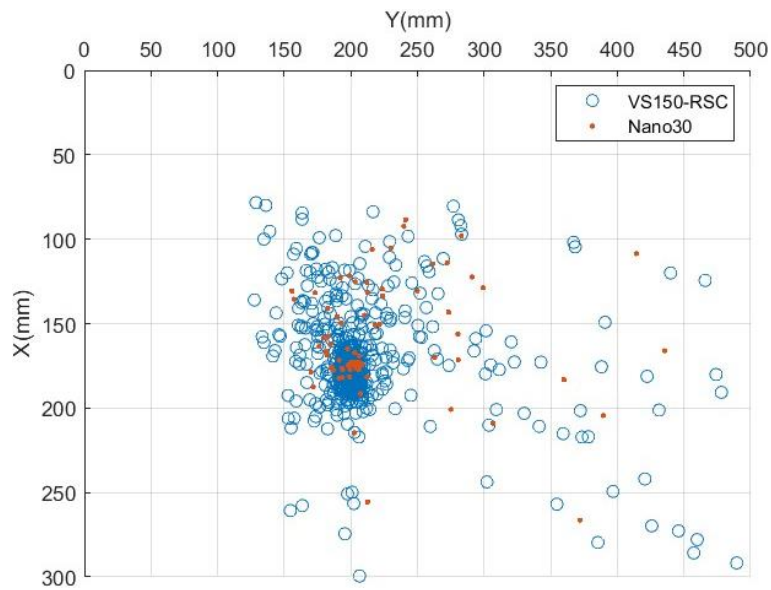
Figure 5.42 Location results of HIC events on 5mm-thickness specimen
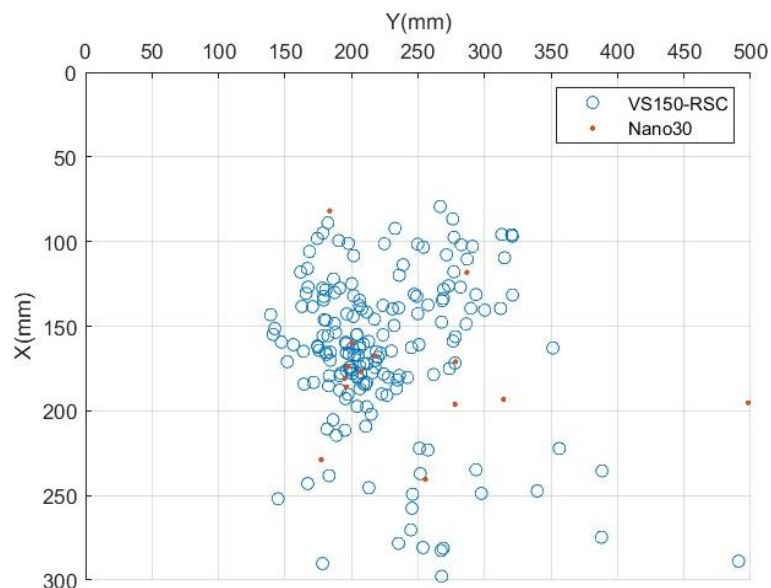
Figure 5.43 Location results of HIC events on 10mm-thickness specimen
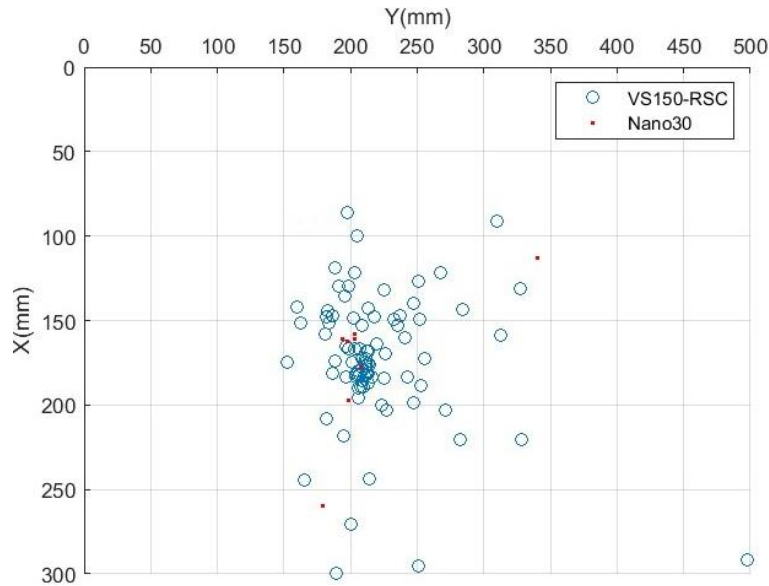
Figure 5.44 Location results of HIC events on 20mm-thickness specimen

Table 5.3 Details of the number of HIC events' source localisation on each specimen

Specimens	Sensors	Total number	Located within the specimen	Located within work area
5mm	Nano 30	103	82	30
	VS150-RSC	714	643	207
10mm	Nano 30	28	13	5
	VS150-RSC	215	179	21
20mm	Nano 30	11	8	4
	VS150-RSC	138	86	16

From Table 5.3, for a 5mm-thick specimen, the localisation effects of both sensors were comparable. The quantity proportions of HIC events located in the work area acquired by Nano30 and VS150-RSC were 29.13% and 28.99%, respectively. However, as for the specimens with thicknesses of 10mm and 20mm, few HIC events were acquired by Nano30. These events were easier to be localised accurately because they were emitted with higher energy, and therefore more complete waveforms were acquired. Thus, it is pointless to compare the localisation accuracy between two kinds of sensors.

To analyse the influence of thickness on source location, only events from VS150-RSC were considered. With the thickness increases, the quantity proportions of HIC events located in the work area were 28.99%, 9.7% and 11.59%. The results on 10mm and 20mm thickness specimens are similar, which is because more signals with lower energy were acquired on the 10mm-thick specimen. Although less signals were

acquired on the 20mm-thick specimen, the obtained signals had higher energies and more complete waveforms. It can be concluded in this test condition that as the thickness increases, its influence on the accuracy of source localisation gradually decreases.

5.4 Conclusions

In this chapter, ECHC-HIC tests were carried out on three specimens with different thicknesses, 5mm, 10mm and 20mm. At the same time, two kinds of sensors, Nano30 and VS150-RSC, were applied to acquire signals. The analysis of the influence of these two parameters on the AE results made this study more systematic and complete.

Various thicknesses of specimens did not influence the frequency distributions of signals from four kinds of sources. In addition, thickness indeed significantly influenced the parameters of signals' time domain, such as the integrity of waveform, Duration, Counts, Energy, etc., because of the severe energy loss during propagation. In addition, the accuracy of HIC event location was thus influenced.

Signals acquired by Nano30 and VS150-RSC exhibited some different frequency distributions of corrosion signals. For corrosion signals acquired by VS150-RSC, their energy was concentrated to the components at around 150kHz. This phenomenon was exacerbated by an increase in specimens' thickness, which is not conducive to distinguishing the signals from different mechanisms. In addition, it was noticed that HIC signals acquired by VS150-RSC on 10mm and 20mm thickness specimens had more components of 160-190kHz, indicating a sensor resonant to a higher frequency may be more sensitive. In the time domain, signals with more complete waveforms and higher energies were acquired by VS150-RSC, which indicated that VS150-RSC sensors were more suitable for source localisation and long-distance monitoring.

6 Investigation of HIC events monitoring on complex plate

The behaviour of HIC developed by the electrochemical hydrogen charging method has been investigated on simple carbon steel plates with different specifications. However, in practical industry, HIC always occurs on complex structures, such as storage tanks with holes, pipes with welding or flanges, etc. This chapter presents the study on signals propagation and HIC events localisation on a complex plate.

6.1 Experimental setup

For the purpose of better comparing the change of signals caused by different structural features, a hole with a radius of 30mm and a seam through the thickness with length of 60mm were cut on a plate of the dimension of 500 x 300 x 5mm, shown in Figure 6.1. Figure 6.1(b) demonstrates the specific size of the seam. The work area for generating HIC was in the centre of the plate. Four VS150-RSC sensors were placed symmetrically around the centre. The vertical distance between each sensor and its two adjacent edges was 75mm. In addition, another VS150-RSC (Sensor 5) was attached on the opposite surface under the HIC area. The experimental parameters were the same as before: the applied current was 50mA/cm^2, the threshold was 35dB and the test duration was 20h.
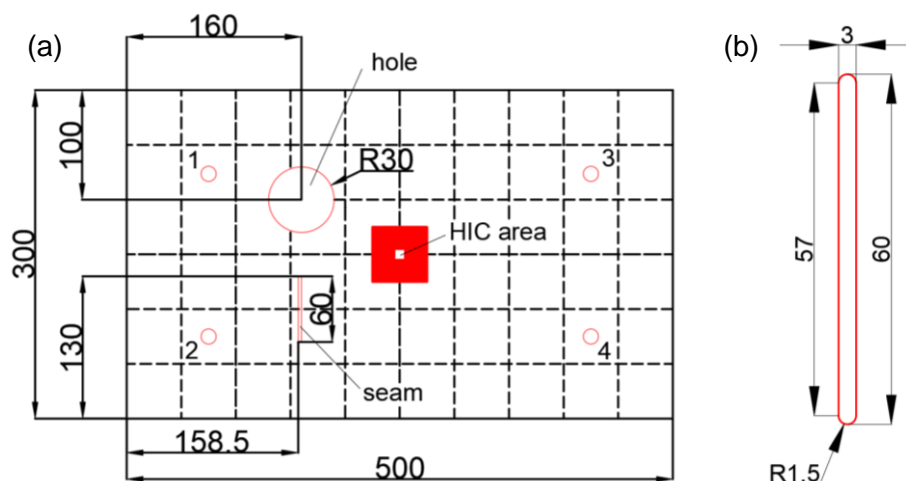
Figure 6.1 Specification of specimen (a) and the seam (b) (unit: mm)

6.2 Experimental results and discussions

6.2.1 Signal acquisition

Figure 6.2 shows the numbers of events acquired by the Sensors 1 to 4 after 20h. It can be seen that the number of signals acquired by Sensor 3 or 4 is approximately twice that of Sensor 1 or 2 which are close to the hole and the seam, respectively. In addition, the number of events collected by Sensor 2 is about 600 less than that of Sensor 1, indicating that the seam caused a bigger influence than the hole. The parameter, Hits, showed the overall impact of the hole/seam on the collected data volume. This may be due to the seam cutting off some signals, while the hole changed the signal's propagation path. Although the propagation path of the signal was increased, Sensor 1 can still receive the signal. However, for lower energy events, the greater attenuation caused by the longer path prevented the sensor from being triggered.

To understand the influence of the defects or structural features on specific signals from the same event, energy is a good choice for evaluation because it is not affected by the threshold. The results presented by a few events are not representative. Therefore, the data is filtered to only retain events in which all four sensors were triggered. Figure 6.3 shows the Time-Cumulative Energy curves of the filtered signals from four sensors. It can be seen that the values of energy from Sensor 3 and 4 were the highest and quite similar to each other, while the signal collected by Sensor 2 had the lowest energy. However, there is a sharp increase at 38789s corresponding to the signals from a uniform corrosion event. The signal acquired by Sensor 2 from this event had the highest energy, indicating that the influence of the seam on uniform corrosion signals was smaller. More details about the effects of the hole/seam on the characteristics of each type of signal will be introduced in Section 6.2.2.

Therefore, it can be concluded that the hole and the seam indeed affected the acquisition of signals. Under the same size level, the influence of the seam was greater than that of the hole under this experimental setup.
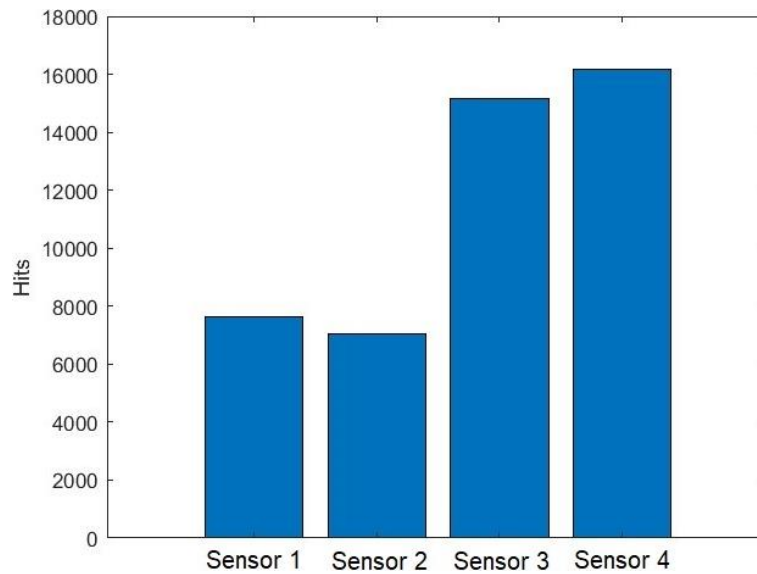
Figure 6.2 The number of Hits of each sensor
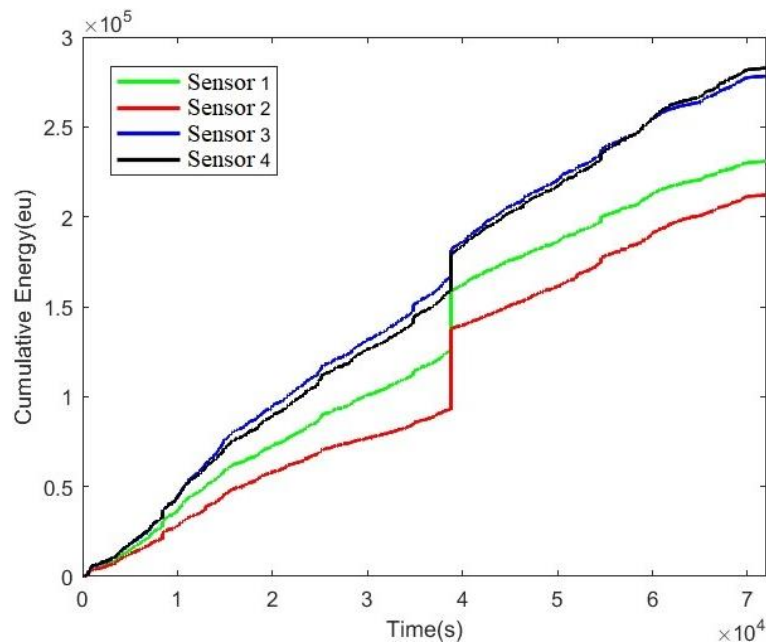
Figure 6.3 Representation of Time-Cumulative Energy of the filtered signals from 4 channels

6.2.2 Signal identification

It is known that the signals from the four mechanisms mainly expressed three distributions in frequency domain. In addition, it has been verified that the proposed automatic clustering method in Chapter 4 was suitable for clustering on simple plates. Three clusters in signals from uniform corrosion, crevice corrosion, H_2 evolution and HIC could be classified with the values of PE1 and PE2 by the GMM method. However, from Chapter 5, it was noted that the critical signals among these three clusters are not clear in the signals acquired by VS150-RSC. Therefore, critical signals need to be manually identified after using the GMM method.

Under this experimental setup, only the signals acquired by Sensor 3 and 4 are suitable to be classified by the introduced method. Figure 6.4(a) shows the three clusters of signals from Sensor 3 and 4 represented by the PE1-PE2 graph. The signals from H_2 evolution and HIC were then automatically clustered with the values of Duration, Counts and Energy, as shown in Figure 6.4(b).
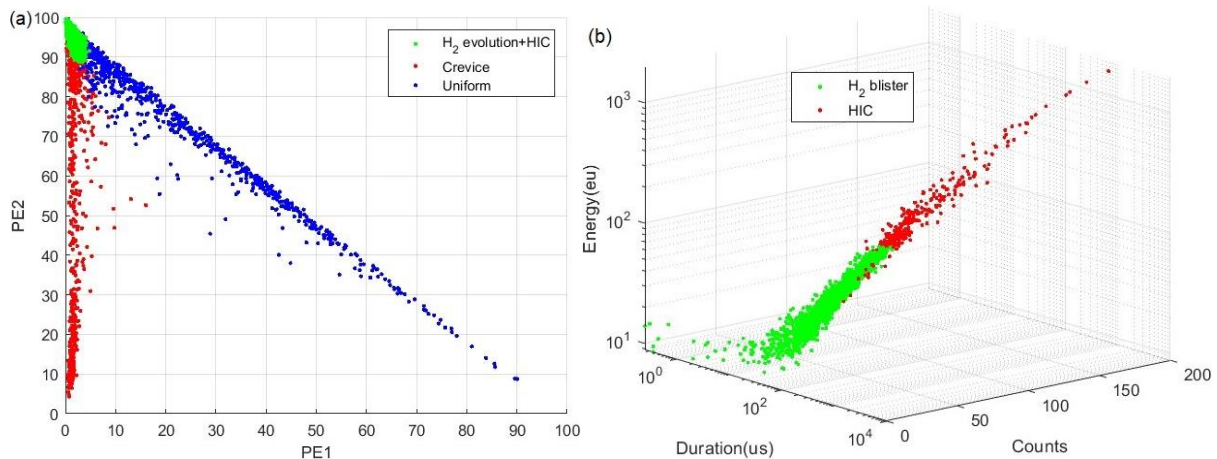
Figure 6.4 Cluster results from the signals acquired by Sensors 3 and 4 represented by (a) PE1-PE2 (b) Duration-Counts-Energy

In this way, signals from Sensor 3 and 4 were classified into 4 clusters. The corresponding signals collected by Sensor 2 and 3 from the same event are therefore classified as well. In order to investigate the signals collected by the 4 sensors, the characteristics in both the frequency domain represented by PE1-PE2 and the time domain represented by Time-Cumulative Energy were selected for comparison.

Figure 6.5 shows the results of signals from H_2 evolution. From Figure 6.5(a), it can be seen that PE1 and PE2 of most signals from Sensor 1, 3 and 4 were in the ranges of 0-5% and 90-100%, respectively. However, the PE1-PE2 distribution of signals from Sensor 2 is different and scattered, in which the value of PE2 decreases and that of PE1 increases. This means that there were more low-frequency components in signals from Sensor 2. Figure 6.5(b) expresses the cumulative energy in terms of time. The cumulative energy of signals from Sensor 3 and 4 increases rapidly, while the energy of signals obtained from Sensor 2 is the lowest and grows slowest.
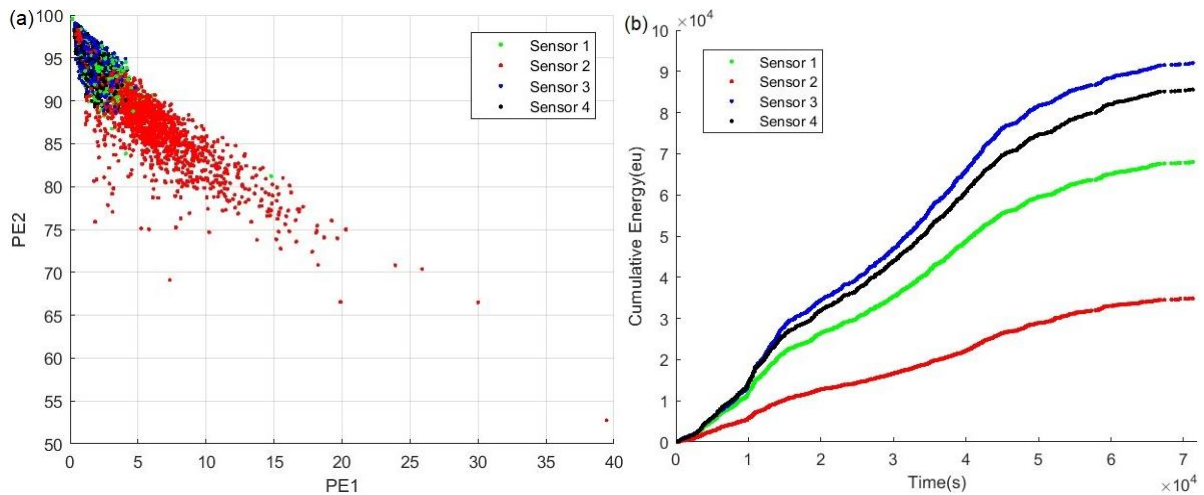
Figure 6.5 Representation of (a) PE1-PE2 (b) Time-Cumulative Energy of signals from 4 sensors from H₂ evolution

Figure 6.6 gives the results of signals from HIC events. The relative distribution of PE1-PE2 shown in Figure 6.6(a) among the four sensors is similar to that in Figure 6.5(a). The PE1-PE2 distribution of HIC signals collected by Sensor 2 is still the most dispersed. Compared with signals acquired by other sensors, signals obtained by Sensor 2 contained more low-frequency components. Figure 6.6(b) exhibits that the cumulative energy varies with the time of signals from each sensor. Similarly, the energy of signals obtained from Sensor 2 was the lowest.
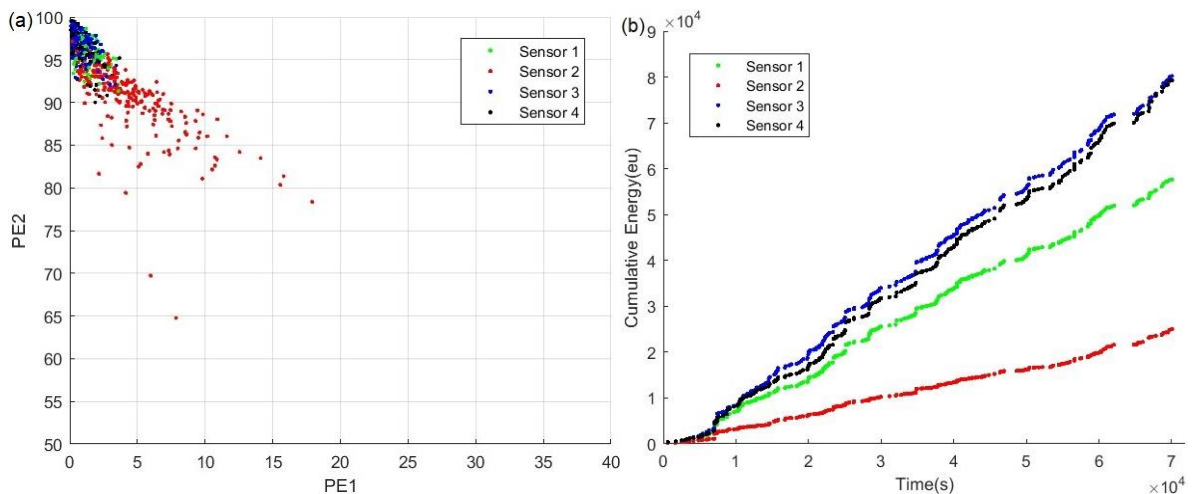
Figure 6.6 Representation of (a) PE1-PE2 (b) Time-Cumulative Energy of signals from 4 sensors from HIC

Figure 6.7(a) shows a PE1-PE2 graph of signals from crevice corrosion, which contain more higher-frequency components. It can be seen that the PE1-PE2 distributions of signals from the 4 sensors were comparable. This means that the hole/seam had little

effect on the spectral distribution of the crevice corrosion signals. In addition, from Figure 6.7(b) which reveals the Time-Cumulative Energy correlations, the energy of signals acquired by Sensor 2 was as high as those from Sensor 3 and 4, even increased faster after 12h.
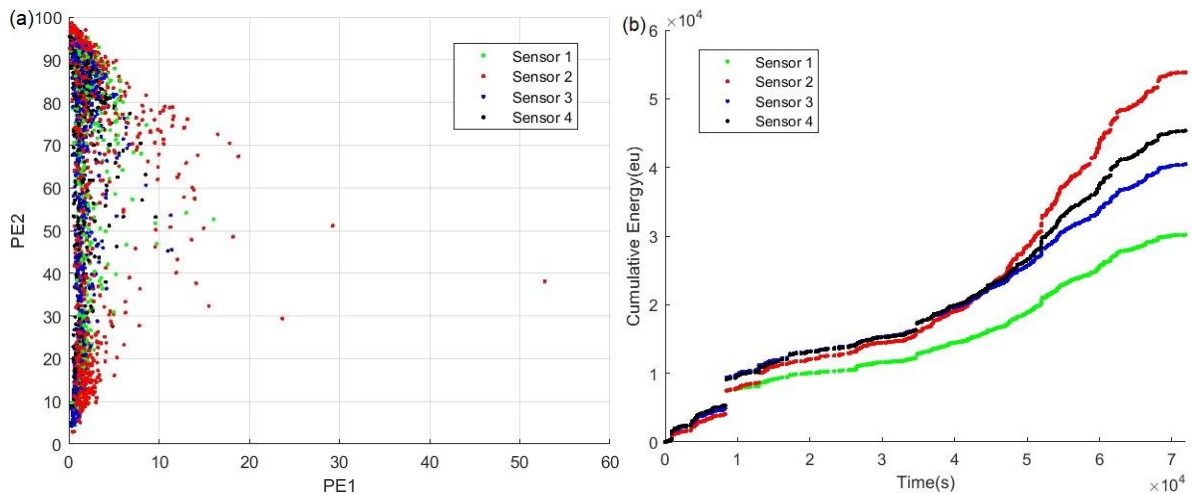
Figure 6.7 Representation of (a) PE1-PE2 (b) Time-Cumulative Energy of signals from 4 sensors from Crevice corrosion

Figure 6.8 exhibits the results of signals from uniform corrosion. The PE1-PE2 distributions of signals from the 4 sensors are quite similar, except that signals from Sensor 2 are more concentrated in the area where the PE1 value is greater than 50%. Nevertheless, the increase in cumulative energy of signals from Sensor 2 is almost identical to those from Sensor 3 and 4, in addition to a specific event that occurred around 4×10^4 seconds.
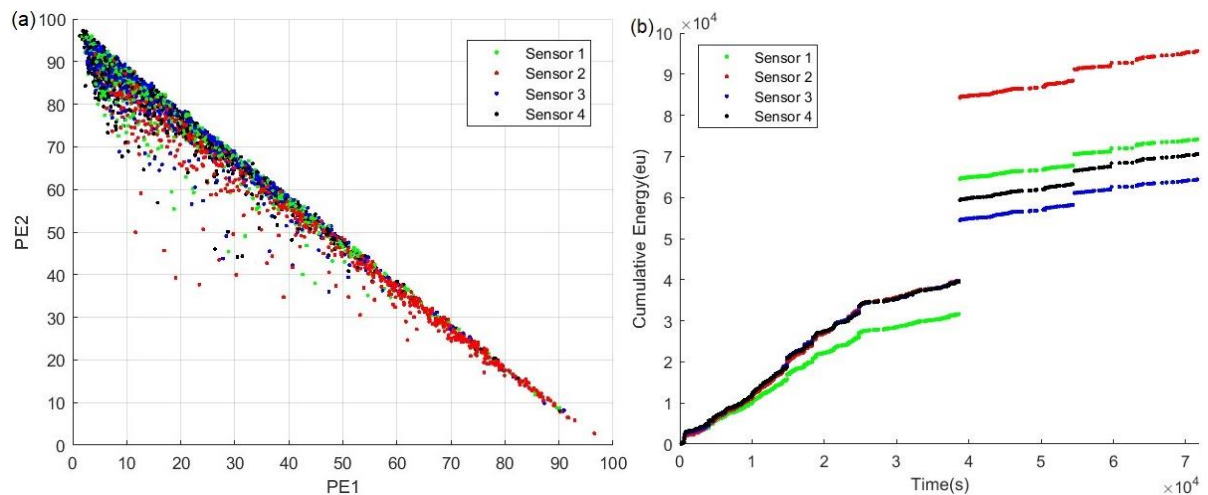
Figure 6.8 Representation of (a) PE1-PE2 (b) Time-Cumulative Energy of signals from 4 sensors from Uniform corrosion

In summary, from Figures 6.5-6.8(a) which demonstrate the frequency spectrums of signals, it can be known that the influence of the hole was small, while the seam affected the frequency distributions to a greater extent. There were more low-frequency components in signals acquired by Sensor 2, especially the signals from H_2 evolution and HIC whose frequency were dominated by 150kHz. From Figures 6.5-6.8(b) which indicate the correlations between the Cumulative energy and Time, it can be seen that the energy of signals acquired by Sensor 1 was always smaller than those from Sensor 3 and 4, no matter which mechanisms the signals came from. As for signals from Sensor 2 which were influenced by the seam, the energies of signals from H2 evolution and HIC were much lower than those from Sensor 3 and 4. However, there was little effect of the seam on energies of signals from crevice corrosion or uniform corrosion.

For the HIC signals that were heavily affected by the hole and the seam, Figure 6.9 displays the waveforms and frequency spectrums of signals from each sensor from one same event. For the parameters in time domain, the value of duration of signal from Sensor 2 was the smallest, as well as the value of amplitude. As for the spectrums, the peak frequencies of the four signals were all at around 150kHz. However, there were more components of 100-200kHz in signal from Sensor 2, while others had narrow bands between 130kHz to 170kHz.
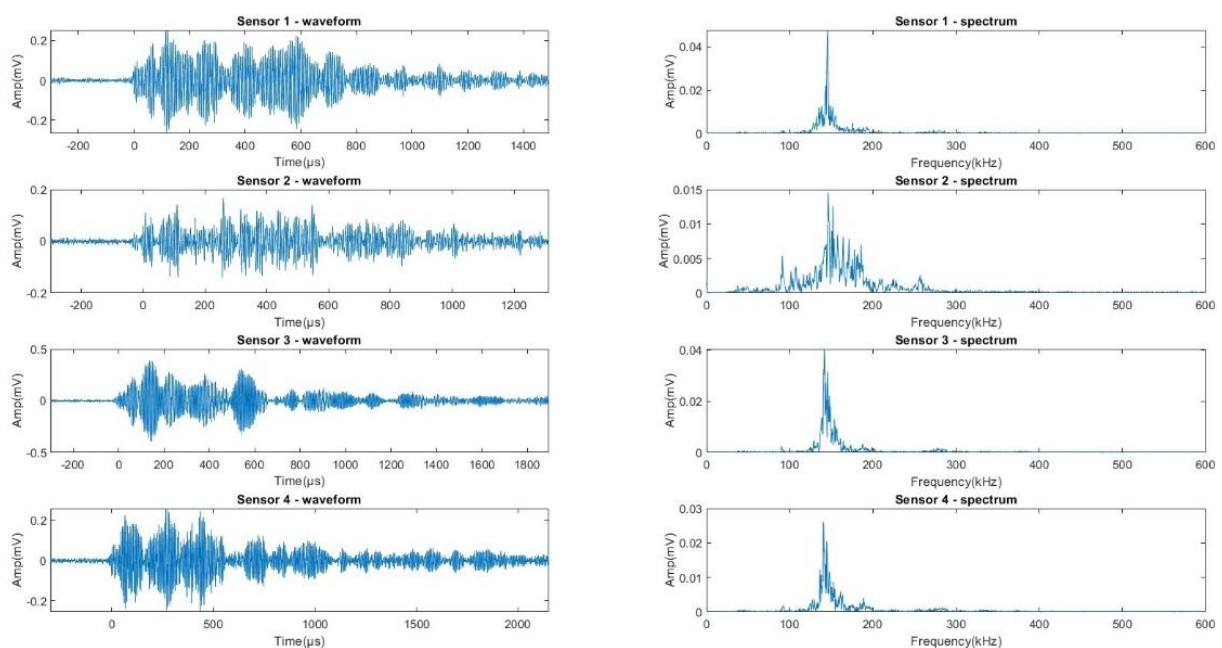
Figure 6.9 Typical waveforms and frequency spectrums of signals from one same HIC event from 4 sensors

6.2.3 Velocity of wave propagation

The calculation of velocities and source locations was focused on signals from HIC events. The velocity was calculated by the time difference between the signals from each sensor and Sensor 5 from one event. As before, the onset time of each signal was determined by the AIC method. The Velocity-Amplitude chart of signals from each sensor is shown in Figure 6.10. It can be seen that most of the velocities were concentrated around 3000mm/ms, especially the signals from Sensor 3 and 4. Besides, for signals with higher amplitude acquired by Sensor 3 and 4, their propagation velocities tended to be gathered around 3200mm/ms, which were consistent to the results in Chapters 3 and 5. The velocity of HIC signals on the 5mm-thick simple plate is determined as 3110mm/ms, in which the sensors were triggered by A_0 mode. For signals obtained by Sensor 2, although the characteristics in the time domain and the frequency domain were heavily influenced by the existence of the seam, velocities were still concentrated around 3000mm/ms. However, velocities of signals collected by Sensor 1 were mainly gathered about 2600mm/ms or even lower. It shows that the hole had little impact on signals' characteristics but a greater effect on source locations compared with the influence of the seam.
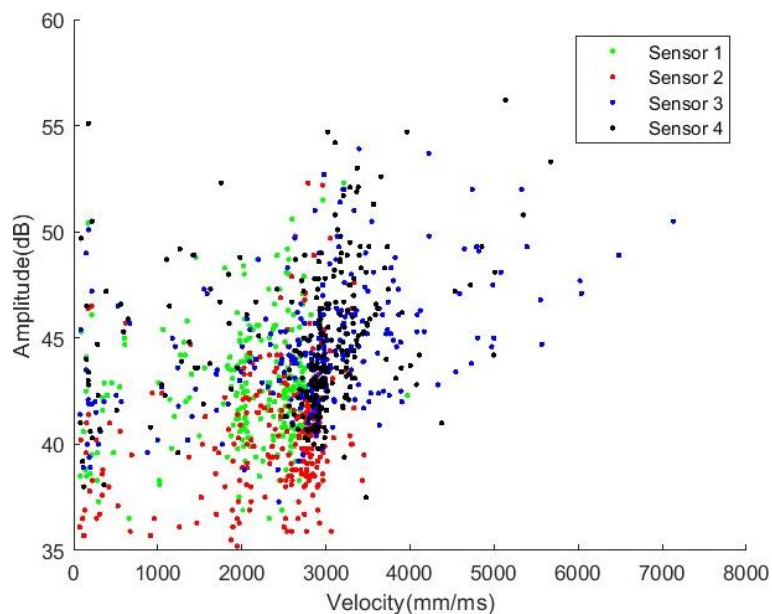
Figure 6.10 Wave propagation velocity of HIC signals from 4 sensors

6.2.4 Source location by simplex method

The locations of HIC events were initially calculated by the Simplex method, as done in earlier Sections. Figure 6.11 shows the source locations of HIC events. It can be

seen that the calculated results indicate the location on the right of the actual HIC occurrence area, which were closer to Sensors 3 and 4. Table 6.1 gives the results of source locations, including the numbers of events on the plate and the work area. Due to errors of calculation caused by the determinations of the onset time and the velocity, a HIC event located in the range of 140<x<160, 240<y<260 was considered to be within the work area. It was found that the proportion of events located in the work area was only 8.65%, which was much lower than that obtained in Chapter 5.
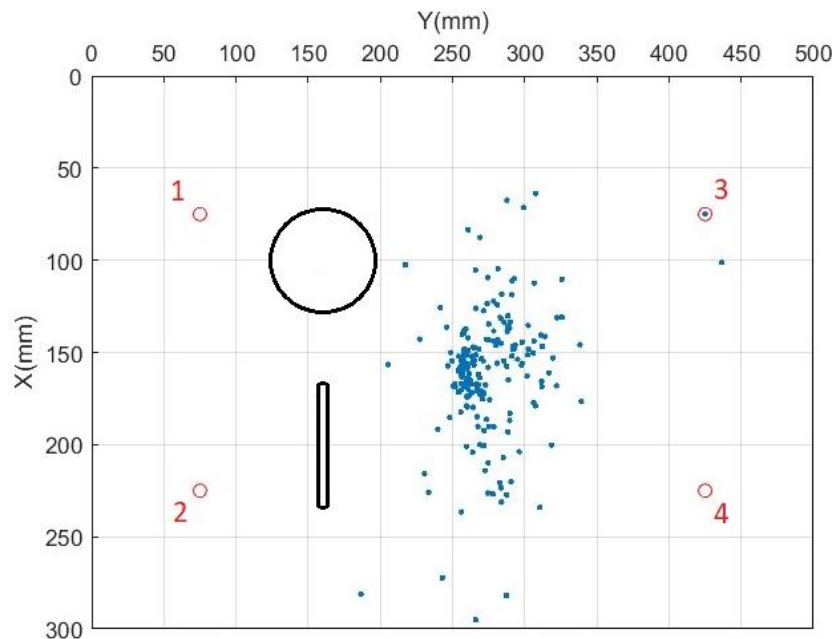
Figure 6.11 Source location of HIC events calculated by simplex method

Table 6.1 Source location results of HIC events

	All HIC events	HIC events located on the plate	HIC events located in work area
Numbers of events	266	203	23
Proportions	100%	76.32%	8.65%

In light of the results, it is not suitable to calculate the source locations of HIC events with the Simplex method on complex plates. The reason is that the propagation paths varied in different directions due to the impacts of the hole and the seam. For the conditions with inhomogeneous structures, the delta-T mapping source location method is a good choice introduced in Section 2.3.4.1.

To build a delta-T map for HIC events on this specimen, time differences between each pair of sensors from HIC events at different locations are required. Therefore, a training grid was needed within the square area surrounded by the four sensors. From

Pearson's work [168], a grid spacing of 20mm is sufficient to satisfy the requirement of accuracy. Figure 6.12 gives the grid for the locations of AE source, i.e., the points where HIC occurs.

Baxter et al. [92] completed the delta-T map through PLB experiments conducted at different locations on the specimen. However, it is impossible to carry out an ECHC-HIC test at each node in the grid which is time-consuming and costly. To overcome this problem, a good choice is to collect simulated data from the numerical models. Nevertheless, before producing the delta-T map by numerical method, it is necessary to prove the accuracy of the time difference of sensor pair obtained from the model.
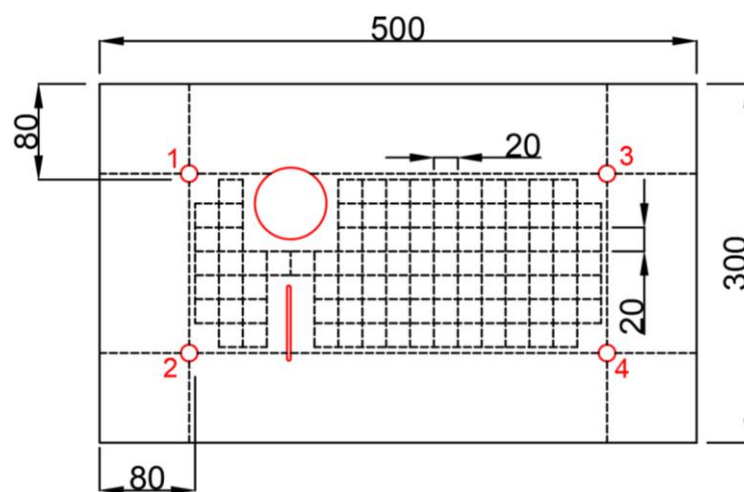
Figure 6.12 The positions of applied force for producing Delta-T map

6.3 Simulation of HIC signal on the complex specimen

It has been demonstrated that reliable PLB source signals can be obtained on the surface of the plate through numerical simulations [108], which was introduced in Section 2.4. A model was created in Abaqus in which the specification of specimen and the positions of four sensors were consistent with those shown in Figure 6.1(a).

Due to the response frequency bandwidth of VS150-RSC sensor (Vallen Systems GmbH, Germany) is 100-450 kHz, the maximum frequency of the simulated wave was thus set as 500 kHz. Under this condition, a grid size of 1mm is sufficient to accurately model the propagation of AE waves in the frequency range of 500 kHz [169]. The hexahedral elements, C3D8R, were used to mesh the model. The FE model and mesh are shown in Figure 6.13.
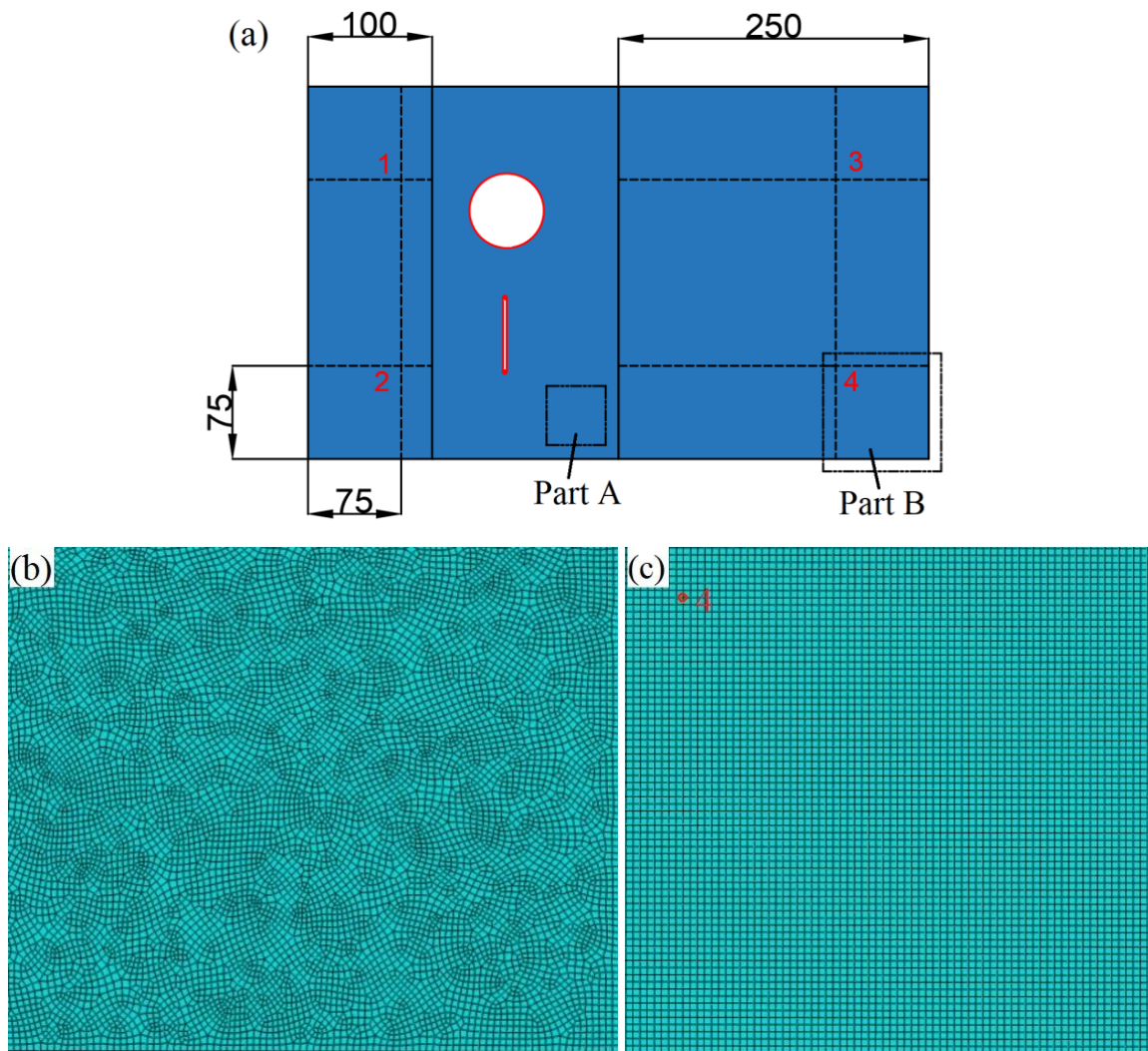
Figure 6.13 (a) FE model in Abaqus (Unit: mm) and the mesh of (b) Part A (c) Part B

The frequency range of the obtained simulated signals is from 0 to 500kHz. However, according to Figure 6.9, the main frequency ranges of experimental HIC signals acquired by Sensor 1, 3 and 4 were 120-170kHz and those from Sensor 2 were 130-185kHz. Therefore, frequency filtering was applied to simulate signals to get the simulated HIC signals. Figure 6.14 shows the data filtering process. Simulated signals in the frequency domain were obtained by applying Fast Fourier Transform (FFT) to signals in the time domain. A frequency band-pass filter with the range of 120-180kHz was used, followed by the Inverse Fast Fourier Transform (IFFT) to get the filtered signals in the time domain. The latter was regarded as the simulated HIC signal.
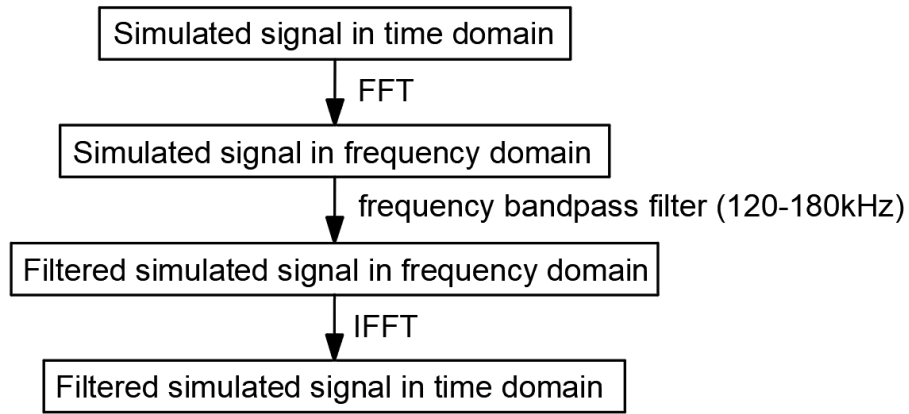
Figure 6.14 Data filtering process

To verify this simulation method, the simulated signals at the positions of the four sensors were compared with the experimental HIC signals when the force was applied at (150, 250) in the model. Figure 6.15(a) exhibits the raw simulated signal at the position of Sensor 1, and Figure 6.15(b) shows the waveform from 30us to 70us where the S_0 mode and A_0 model can be observed clearly.
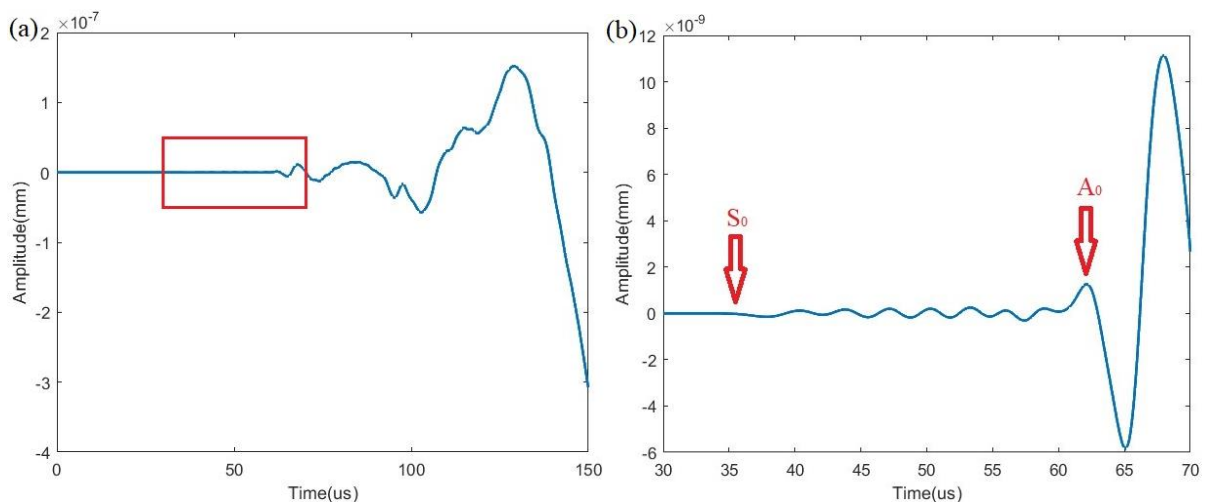
Figure 6.15 Simulated signals at Sensor 1 (a) completed signal in time domain (b) signal in time domain from 30us to 70us

Figure 6.16(a) and (b) represent the filtered simulated signal at Sensor 1 in the time and frequency domain, respectively. In light of the dispersion curve on the 5mm-thick specimen, there are only two modes (S_0 and A_0) of the signal when the components between 120-180kHz dominant its frequency distribution. The modes of S_0 and A_0 were thus divided in Figure 6.16(a), which is supported by Figure 6.15(b). Figure 6.16(c) represents part of a typical experimental HIC signal acquired by Sensor 1 in time domain and the corresponding frequency distribution in Figure 6.16(d).
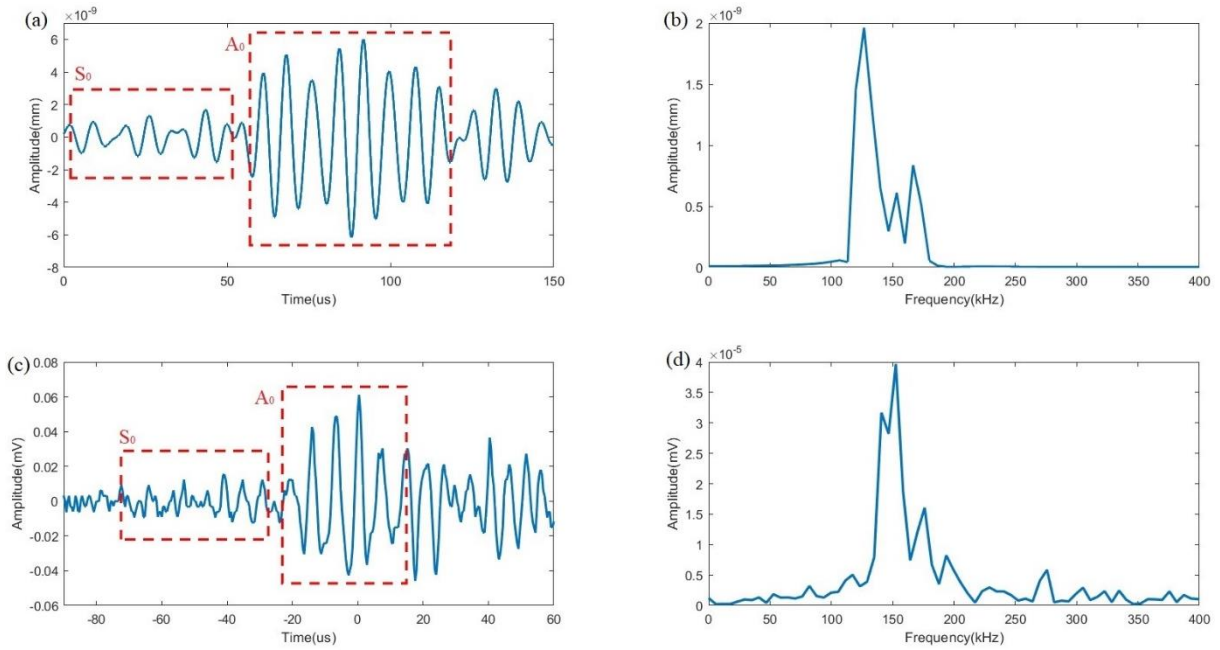
Figure 6.16 Signals at Sensor 1 - Filtered simulated signal (a) in time domain (b) in frequency domain; Experimental signal from -90us to 60us (a) in time domain (b) in frequency domain

Similarly, the raw simulated signals in time domain at the positions of Sensor 2, 3 and 4 are shown in Figure 6.17, Figure 6.19 and Figure 6.21, respectively. The comparisons between the filtered simulated signals and the experimental signal in time domain and frequency domain from Sensor 2, 3 and 4 are exhibited in Figure 6.18, Figure 6.20 and Figure 6.22, respectively.
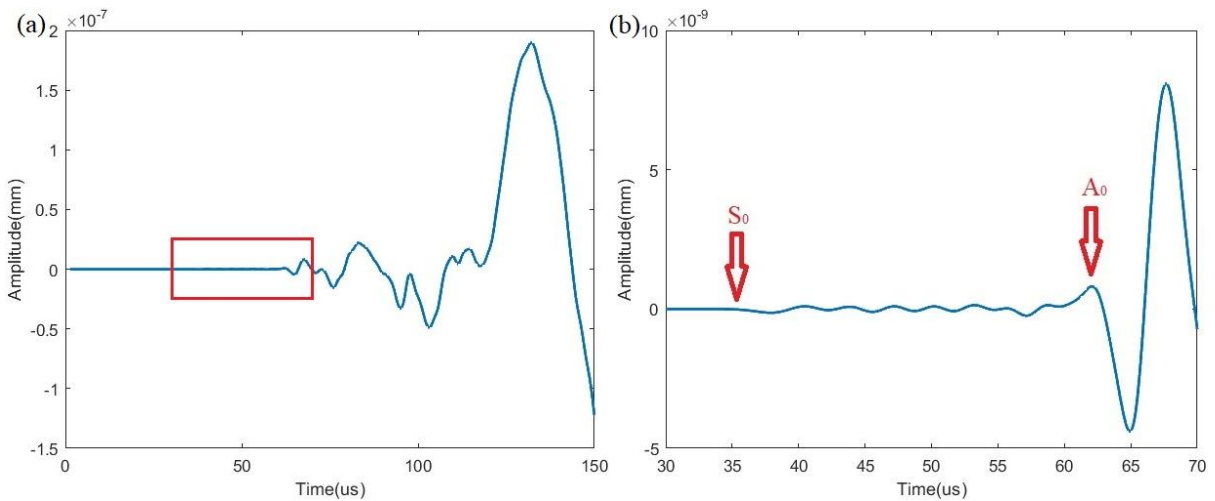
Figure 6.17 Simulated signals at Sensor 2 (a) completed signal in time domain (b) signal in time domain from 30us to 70us
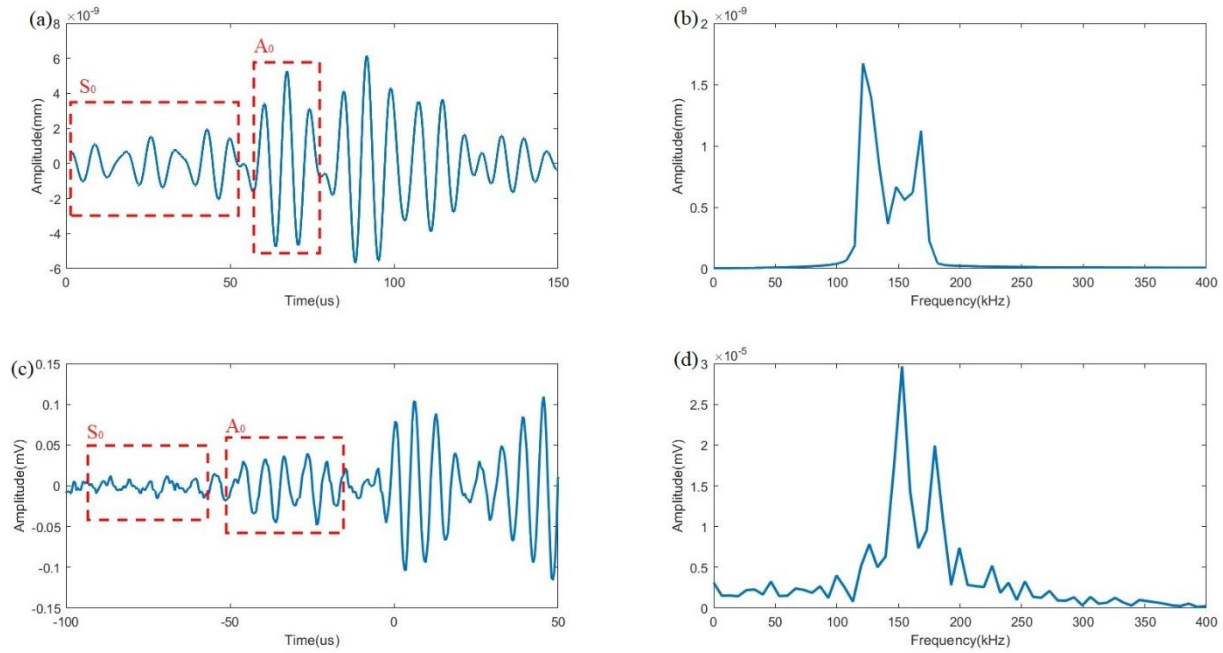
Figure 6.18 Signals at Sensor 2 - Filtered simulated signal (a) in time domain (b) in frequency domain;
Experimental signal from -100us to 50us (a) in time domain (b) in frequency domain
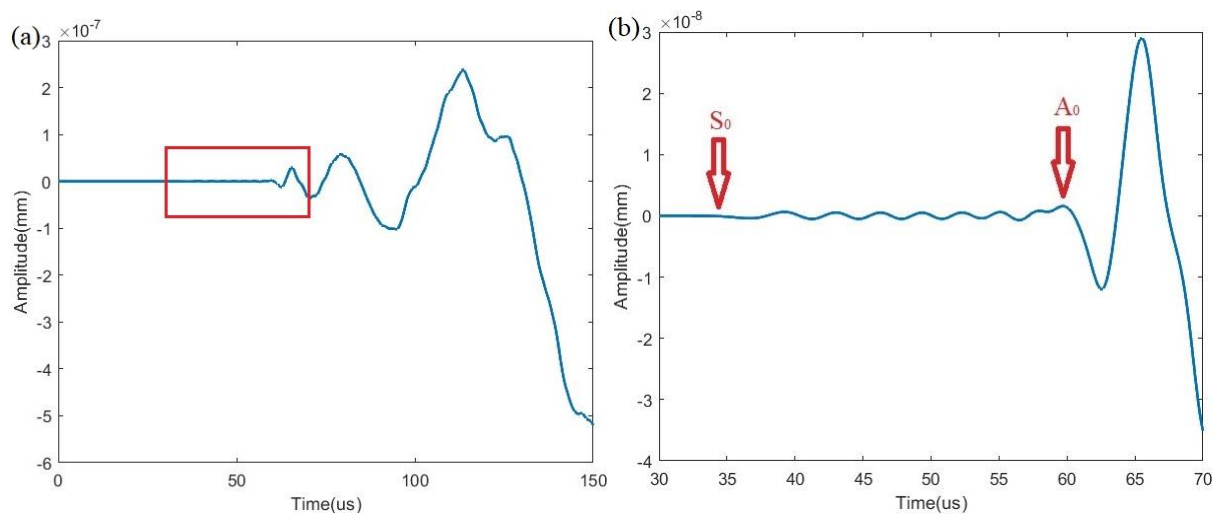
Figure 6.19 Simulated signals at Sensor 3 (a) completed signal in time domain (b) signal in time
domain from 30us to 70us
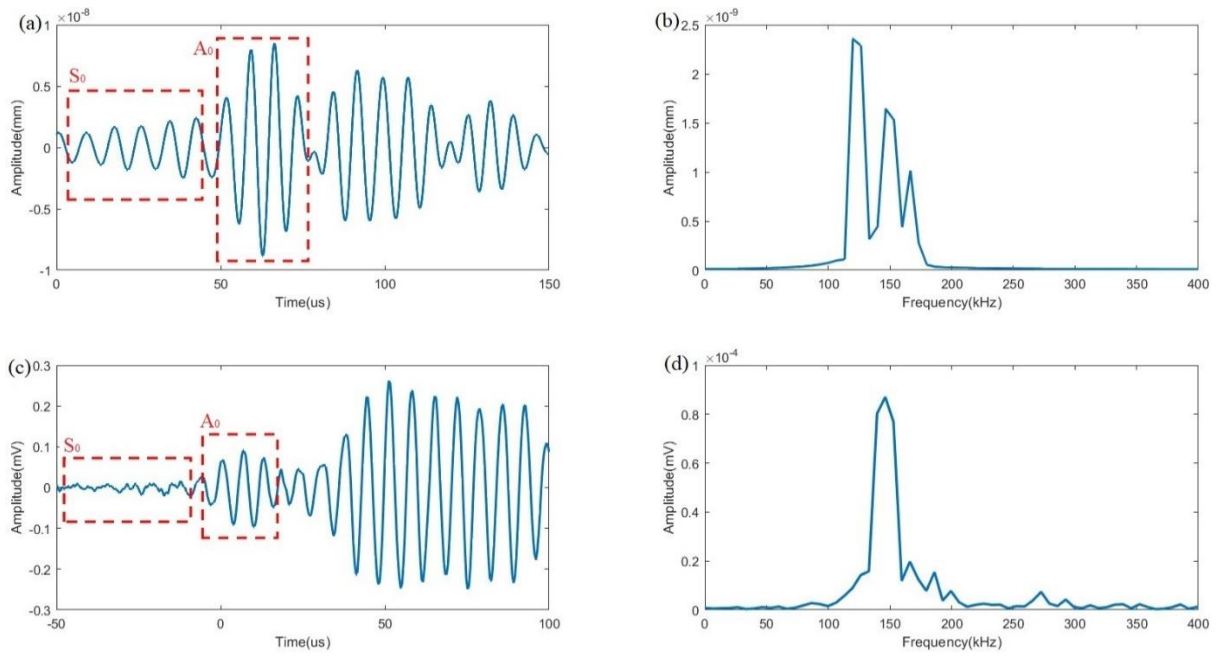
Figure 6.20 Signals at Sensor 3 - Filtered simulated signal (a) in time domain (b) in frequency domain; Experimental signal from -50us to 100us (a) in time domain (b) in frequency domain
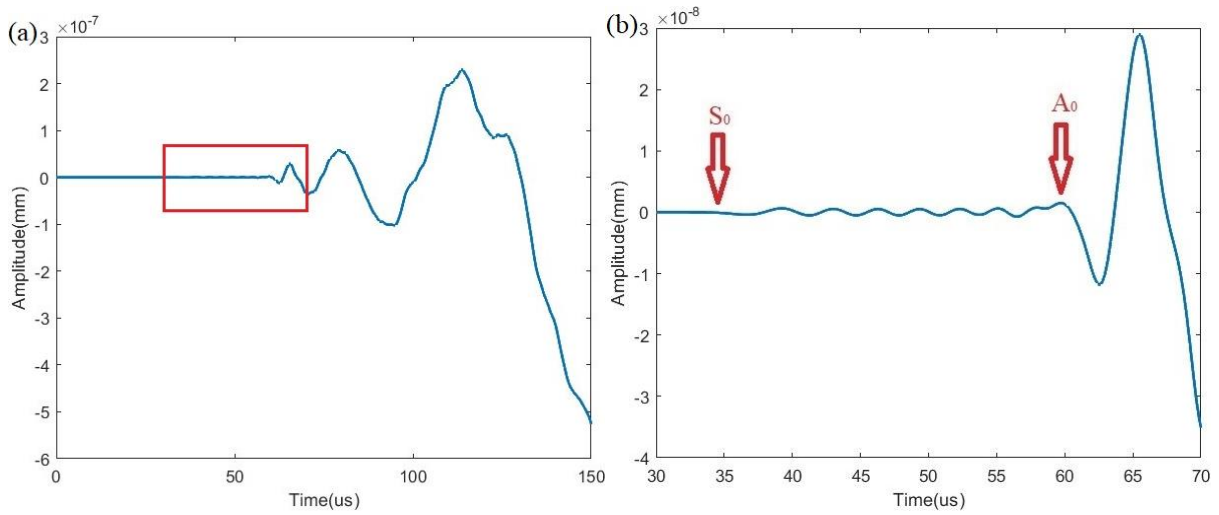
Figure 6.21 Simulated signals at Sensor 4 (a) completed signal in time domain (b) signal in time domain from 30us to 70us

173
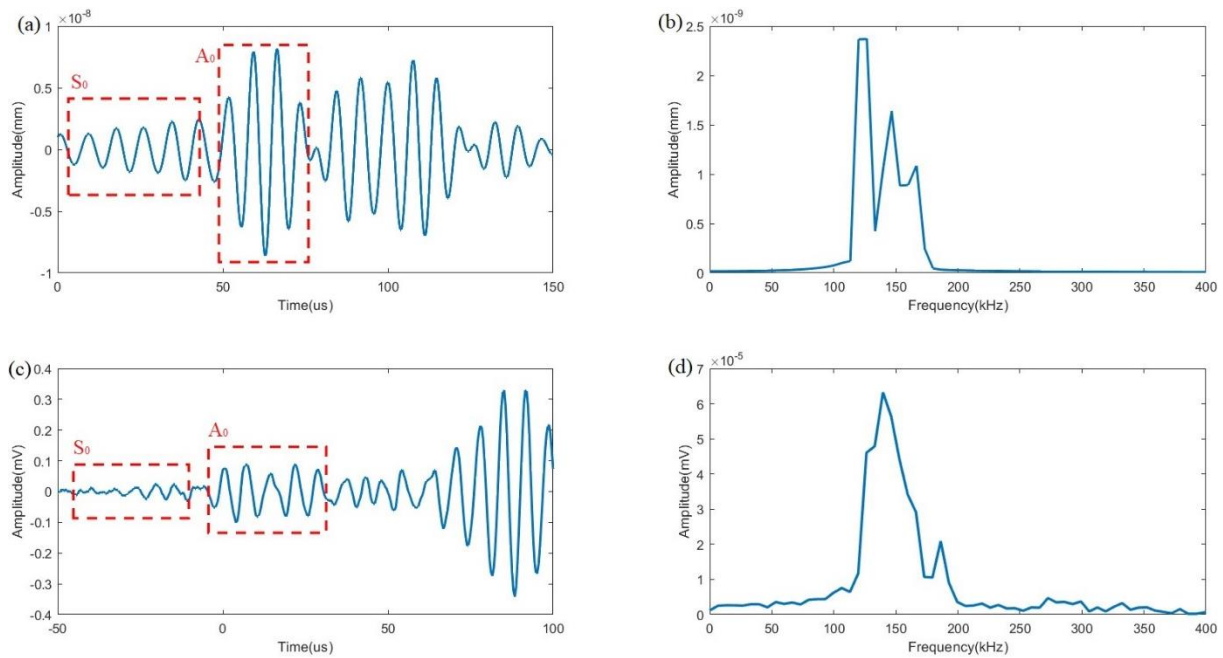
Figure 6.22 Signals at Sensor 4 - Filtered simulated signal (a) in time domain (b) in frequency domain; Experimental signal from -50us to 100us (a) in time domain (b) in frequency domain

By comparing the amplitudes of the simulated signals, it can be deduced that the order of energy of these four signals from high to low is: signal at position 3 and 4 in Figure 6.12, signal at position 2 and signal at position 1. This is consistent with the order of energy of experimental signals acquired by the four sensors. In addition, the frequency spectrum and the waveform of each simulated signal were similar to those of corresponding experimental signals. These verifications indicated that FE modelling is a reliable simulation approach for HIC signals.

By observing the waveforms of the simulated HIC signals, the AIC algorithm is still effective in determining the arrival time of the simulated HIC signal. The simulated signal at Position 3 was taken as an example to show the result of TOA determination, which is presented in Figure 6.23. The arrival time for this signal was determined to be 50.41us. Similarly, the arrival times of the simulated HIC signals at Position 1 to 4 were 59.1us, 56.5us, 50.41us and 50.44us, respectively. Figure 6.24 illustrates the comparison of experiments and simulations for the time difference between each pair of sensors. Due to the errors in HIC signal identification and TOA determination, the experimental time differences in all HIC events are distributed in a range. The histograms in Figure 6.24 clearly show the distribution and concentration of experimental time differences for each pair of sensors. It can also be seen that the simulation results were very close to the actual experimental results, which proved the

reliability of the HIC signal simulation method and the time difference of each pair of sensors obtained by the numerical method.
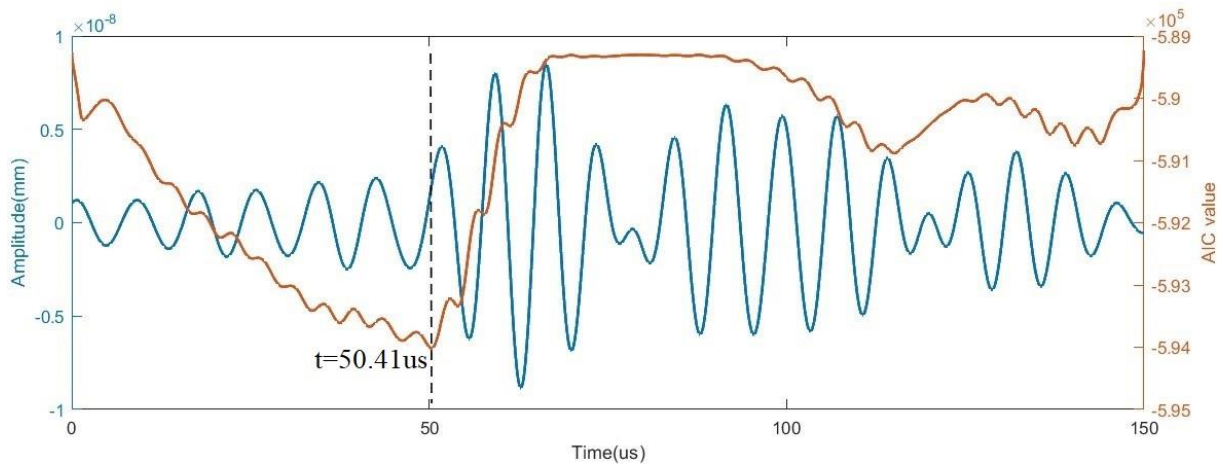
Figure 6.23 Time of Arrival determination by AIC algorithm of simulated HIC signal at the position 3
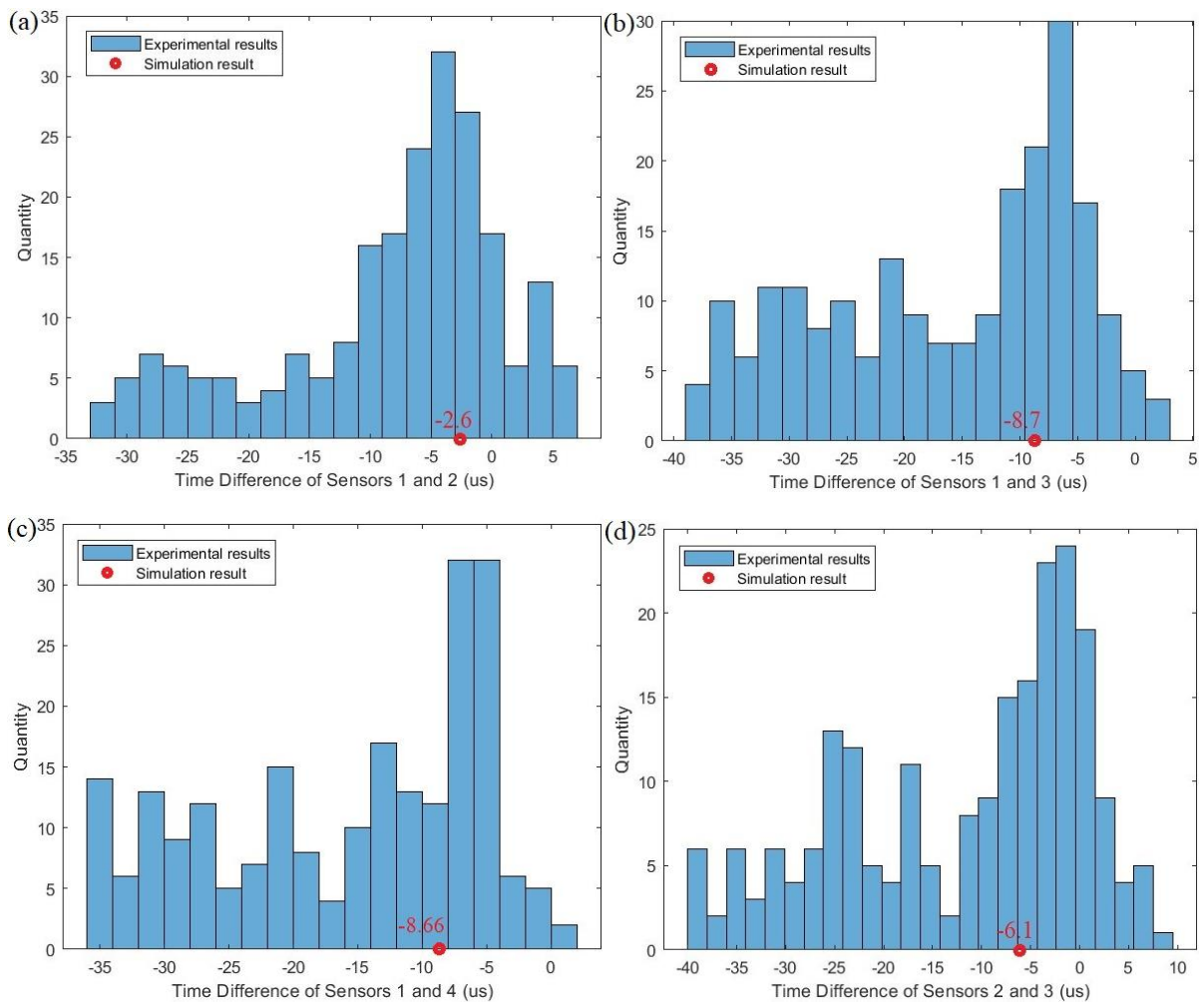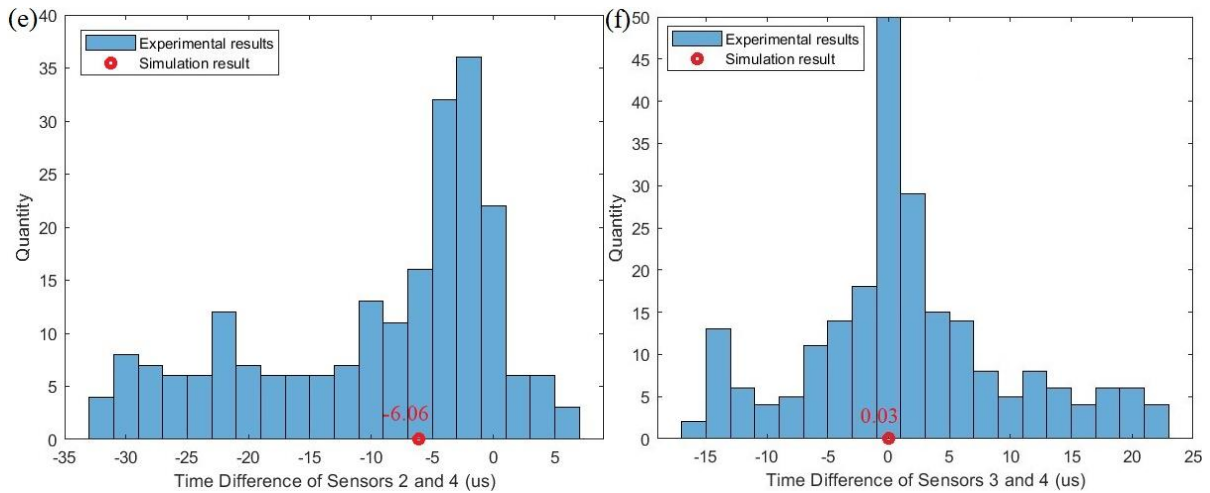
Figure 6.24 Time difference between each pair of sensors of experiments and simulation (a) Sensors 1 and 2 (b) Sensors 1 and 3 (c) Sensors 1 and 4 (d) Sensors 2 and 3 (e) Sensors 2 and 4 (f) Sensors 3 and 4

6.4 Simulation of delta-T map for HIC events

After processing each signal obtained at the 4 positions in Figure 6.12, the arrival times were picked up and time differences of each pair of sensors were calculated. Interpolation was applied to supplement data between two grid points. A delta-T map can thus be produced for each sensor pair by connecting the grid points with the similar value of time difference, in which the error band was defined as $\pm 0.1 us$. Figures 6.25-6.28 show the delta-T map between sensor pair 1 and 3, 1 and 4, 2 and 3, 2 and 4, respectively.
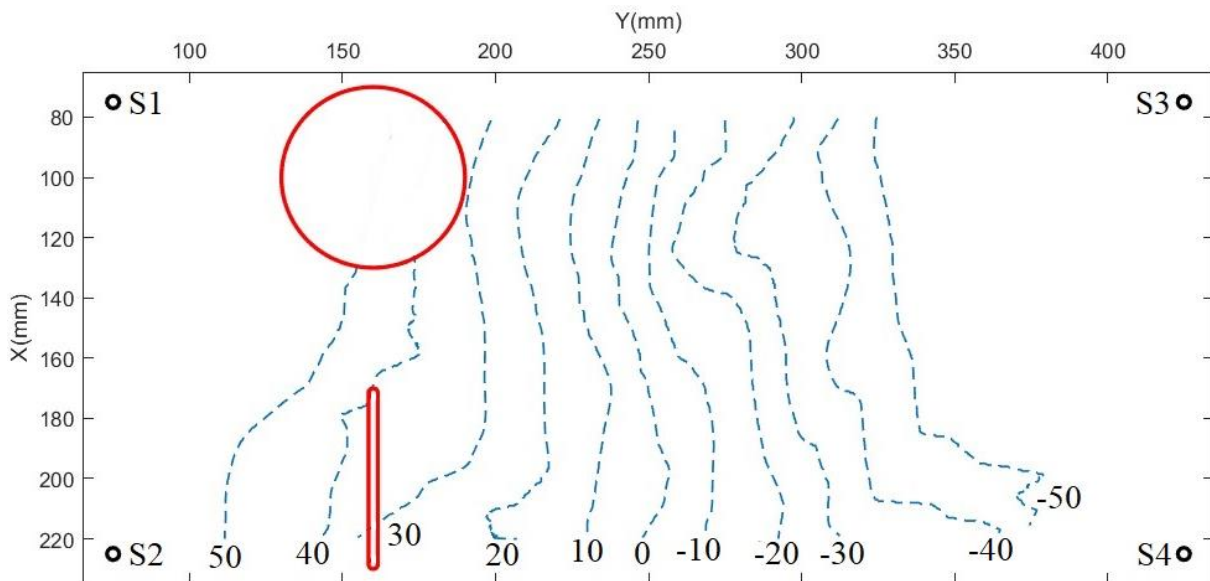
Figure 6.25 Delta-T map between Sensors 1 and 3
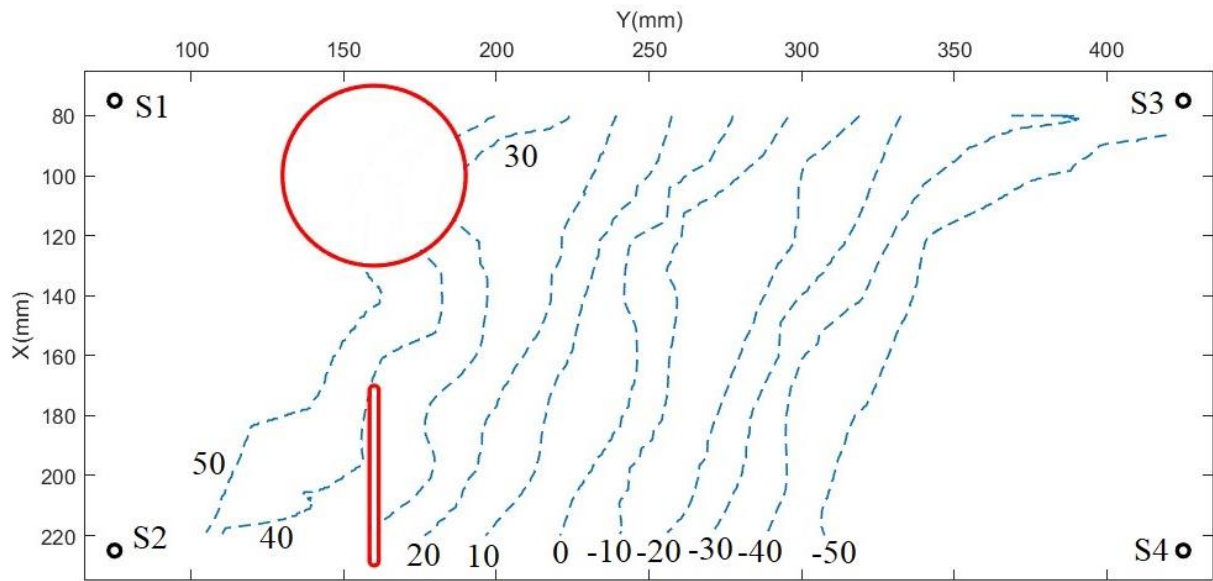
Figure 6.26 Delta-T map between Sensors 1 and 4
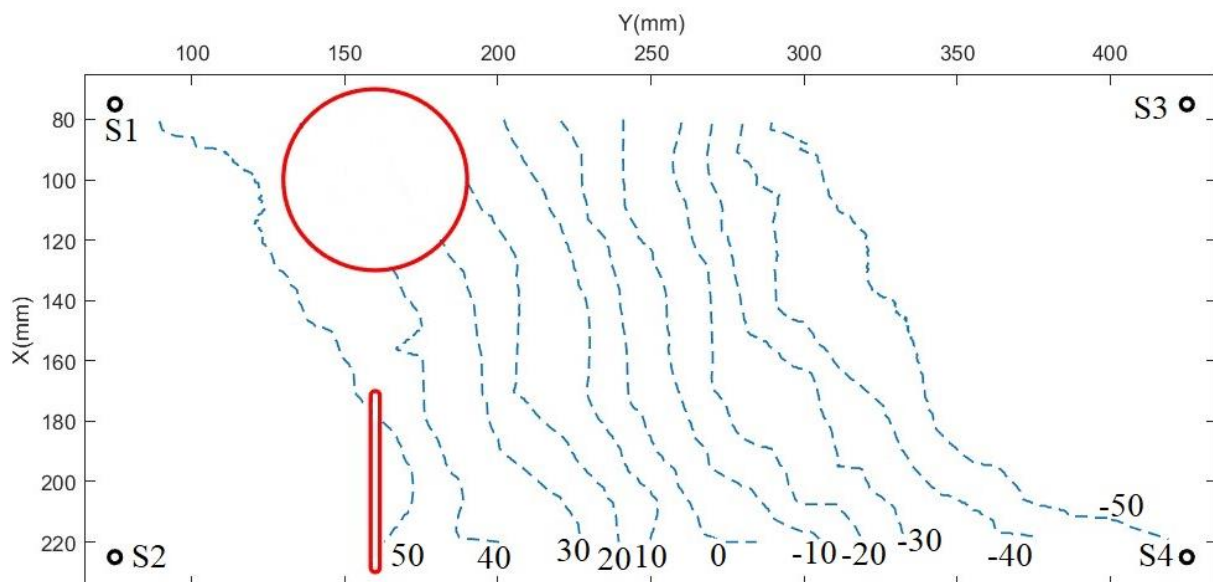
Figure 6.27 Delta-T map between Sensors 2 and 3
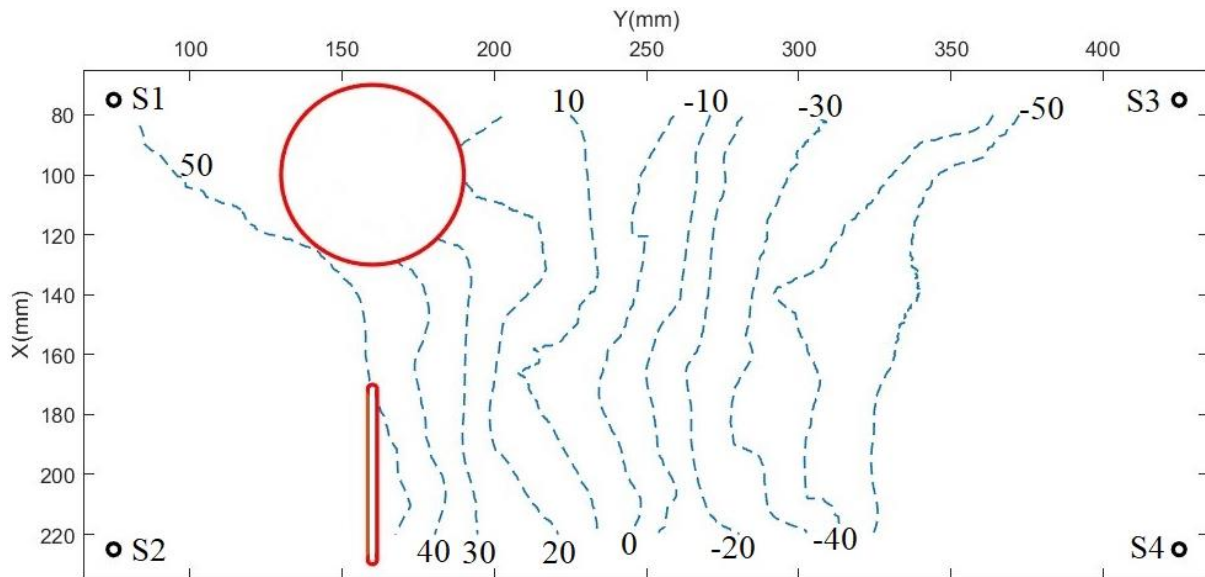
Figure 6.28 Delta-T map between Sensors 2 and 4

For the sensor pair 1 and 2, and 3 and 4, it is too complex to produce the delta-T map with contour lines because both signals were influenced by the hole and the seam. Figure 6.29 shows the pseudocolor plot using the values of time differences between Sensor 3 and 4. It can be seen that in the area where the Y value is greater than 200mm, the values of time differences were symmetrical about the straight line X=150mm. However, in the area where Y value is smaller than 200mm, the distribution of the time difference values changes due to the existence of the hole and the seam. Nevertheless, from an overall perspective, the delta-T map with some contour lines can still be roughly depicted.

For Sensor 1 and 2, at least 90% of signals were affected by the complex features, i.e., the hole and the seam. The pseudocolor plot using the values of time difference between Sensor 1 and 2 was described in Figure 6.30. As can be seen, it is too messy to depict the contour lines of the delta-T map.
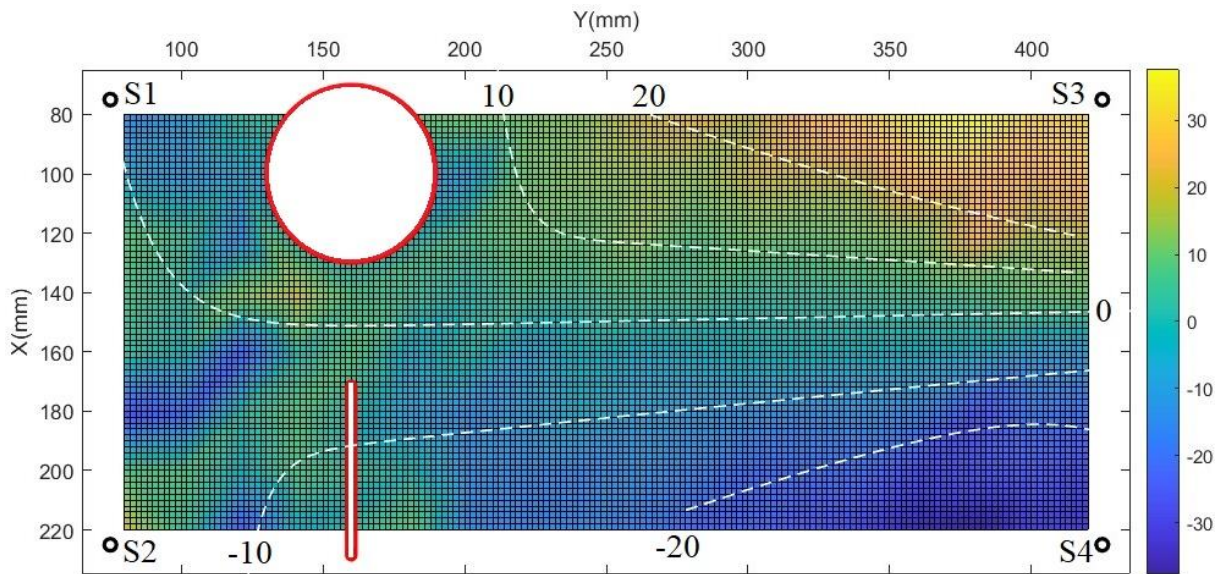
Figure 6.29 Delta-T map between Sensors 3 and 4
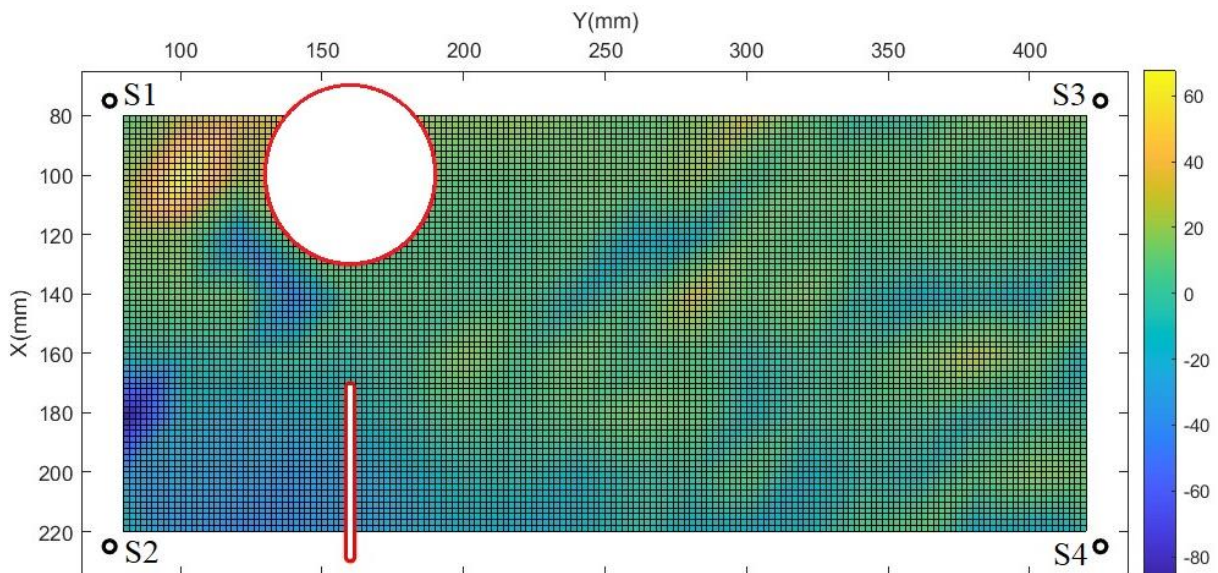
Figure 6.30 Delta-T map between Sensors 1 and 2

6.5 Verification by experimental results

Based on Figures 6.25-6.30, a real event can be located by overlapping all lines corresponding to the values of time difference of each sensor pair. A typical experimental HIC event was selected to verify the accuracy of the delta-T mapping method. This HIC event was located at (160.0936, 257.2063) by the Simplex method, which was in the localisation event concentrated area in Figure 6.11. By overlapping the corresponding lines from the delta-T map of each sensor pair, the location of this HIC event was determined at (150.33, 248.92) with the average coordinates of intersection points. Figure 6.31 presents the comparison of localisation results

calculated by the Simplex method (Point 1) and the Delta-T mapping method (Point 2). Due to the occurrence of experimental HIC events in a square area of 146<X<154mm and 246<Y<254mm, it is concluded that the delta-T method greatly improved the accuracy of the localisation results.
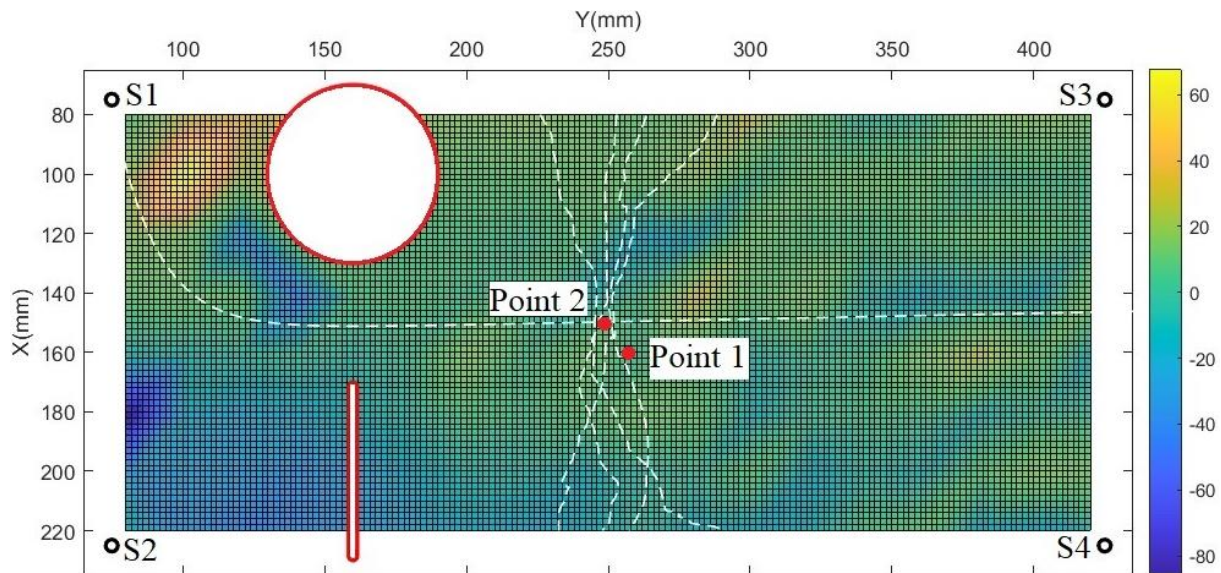
Figure 6.31 The comparison of localisation results calculated by Simplex method (Point 1) and Delta-T mapping method (Point 2) for a typical experimental HIC event

6.6 Conclusions

In this chapter, the ECHC-HIC test was carried out on a complex specimen with a hole and a seam by monitoring using AE technology. The influences of the two structural features, a hole and a seam, on AE signals were investigated. The seam has a greater effect on signals in perspectives of the energy, the peak amplitude and the frequency distribution, especially for the signals from H_2 evolution and HIC events. Compared with the seam, the hole has little impact on the expression of signals in both the time and frequency domains. The propagation time for the signal to reach the sensor is greatly extended through the hole, resulting in inaccurate localisation by the Simplex method.

The Delta-T map method proved to be a reliable means to locate PLB events on the complex specimen. However, due to the complexity of HIC experiments, experimental data cannot be collected at every node on the specimen. This study obtained the HIC signal at each node through numerical methods and created a complete HIC event delta-T diagram. The experimental results verify the simulated HIC signal at the central

node. For the actual HIC events in the test, the localisation results obtained from the simulated delta-T mapping method had a higher accuracy compared with those calculated by the Simplex method.

7 Conclusions and future work

7.1 Conclusions

This research investigated the acoustic emission (AE) technology monitoring of hydrogen-induced cracking (HIC) development on carbon steel plates with simple and complex geometries. Perspectives of analyse include pattern recognition, automatic clustering, wave propagation and source localisation, which were carried out by experiments with different parameters and numerical modelling.

• The monitoring of HIC growth by AE was studied comprehensively. In previous work, most studies used H_2S gas to generate HIC, in which good sealing was required because H_2S is very toxic to the human body. Moreover, the period to obtain HIC was very long in this way, at least 96 hours. In this work, the HIC in plate was generated under laboratory condition through the Electrochemical Hydrogen Charging (ECHC) method, in which the solution was mixed with 0.5mol/L H_2SO_4 and 0.5g/L $NaAsO_2$. This method produced a large amount of HIC within 24 hours. Besides, the experimental progress can be observed at any time during the experiment due to its safety. In addition, most studies only investigated the growth of HIC under one experimental condition. This work created different experimental scenarios, such as different specimen specifications, different hydrogen concentrations, different sensor positions and other conditions. Tests were monitored by Nano30 sensors. Four defect mechanisms were found to generate elastic waves during a test, which were H_2 evolution, HIC, crevice corrosion and uniform corrosion. An experimental procedure was designed for pattern recognition of these mixed signals. Two short-time tests with or without current were carried out using only 0.5mol/L H_2SO_4 solution for identifying non-HIC signals. It was found that the frequency distribution was the best characteristics to distinguish the defect mechanisms. The frequency of the H_2 evolution signal was concentrated around 150kHz with a narrow band. There were more high-frequency (250-400kHz) components in crevice corrosion signals, while signals of uniform corrosion had more low-frequency (50-100kHz) components. A new group of signals appeared in the ECHC-HIC test, which was derived from HIC. Their frequency spectrums were similar to those of H_2 evolution, but with longer Duration, higher Amplitude, more Counts and higher Energy in the time domain. These characteristics were the basic elements for signals identification, irrespective of the

specifications of the plate, the value of the applied current, and the locations of the sensors. Thus, this investigation on monitoring HIC growth with AE was more complete, which almost covered every experimental setup. The work exhibited a systematic method for researchers to study signals' propagations, characteristics and HIC development.

• A robust automatic clustering method was proposed to cluster the signals of different mechanisms under this test setup. Most literature introduced the manual clustering method by using different signals' characteristics. However, each time the test setup changes, such as specifications or sensors' types, the criteria for manual classification will change. To ensure accuracy, the test procedure needs to be carried out again, which is time-consuming and may include human errors. Some researchers used automatic methods to classify signals, but only for one test setup.Under this experimental setup, a two-step GMM clustering method was proposed for automatically clustering the mixed signals, which is suitable for almost all different test setups. The parameters of PE1 and PE2 obtained from the frequency domain were first available for identifying signals from corrosions, and Duration, Counts and Energy were then used to distinguish signals between H_2 evolution and HIC. This method was verified by experiments with different setup parameters. In addition, due to the effectiveness, this method is also conducive to data storage. For a different type of sensors (VS150-RSC), the frequency distributions of signals from each mechanism still follow the above criteria generally. However, no matter whether the signals were derived from the uniform corrosion or the crevice corrosion, more signal components were acquired by the VS150-RSC which are concentrated at 150kHz than those from the Nano30 sensors. Therefore, the accuracy rate of the proposed automatic method becomes lower because of the closer frequency distribution among the critical signals. For this situation, it was necessary to check the critical signals manually for more accurate identification.

• This research investigated the source localisation of HIC events on simple plate under different experimental setup, including the specifications of specimen and the type of sensors. The Simplex method was used to calculate the location based on the parallelogram sensor array. The onset time of each signal was determined by the AIC method to improve the accuracy. When the thickness of specimen plate was 5mm, it was more accurate to locate the HIC events on the specimen with a bigger planar size

due to less reflection from plate edges. Moreover, when the plate thickness increases, fewer signals were acquired by Nano30 sensor resulting from its low sensitivity. In comparison, VS150-RSC sensors were more suitable to monitor HIC development in thick plate specimens and for long distances between cracks and sensors.

• Most literature investigated the monitoring of HIC growth on a simple plate, however, the structures of material used for energy pipelines include holes, seams, welds and others in industry. Based on the experimental procedure, an ECHC-HIC test was carried out on a plate with complex features including a hole and a seam. It was concluded that the seam structure influenced the characteristics of HIC signals in both the time and frequency domains, while the hole-structure influenced the arrival time of signals resulting in inaccurate source localisations if using the Simplex method. Delta-T mapping method is a good way to locate AE sources on complex structures which has been proven by others' research. However, they verified it with repeatable PLB experiments to construct the mapping. For my work, the numerical method carried out by Abaqus was used to achieve the repeatability of HIC tests. The numerical delta-T mapping method is proved to be a more reliable way to locate HIC events on complex structures more quickly and more accurately. A complete delta-T map was produced for HIC events under this experimental study. The success of this method means that it is possible to simulate the monitoring of HIC growth in more complex environments, which is more accurate and time-saving. A numerical delta-T mapping would help technicians locate damaged areas quickly, providing a good guide and reference for future research directions.

7.2 Future work

Three perspectives of future work were recommended based on the study carried out by this research.

• Although several factors influencing HIC signals have been studies, there are still broader situations that have not been considered. For example, the ECHC-HIC tests can be carried out with more complex structures with different defects, like welding lines, flanges and pipe steel and so on. In addition, the background noises were well controlled in the laboratory condition. In practice, background noises are also a vital factor which may significantly influence the identification of target signals. For this

situation, the used sensors can be improved in light of signal characteristics generated by different noises.

• In this work, the FE modelling was successfully completed and verified by real signals HIC events. However, in practical applications, more details are needed to be considered, such as more complex geometry conditions, and anisotropy of materials. Also, only simulated HIC signals were verified in this study, the simulated signals of other mechanisms with different characteristics should also be investigated, such as those from corrosions, to better understand and analyse the damage process with multiple mechanisms.

• Although the overall progress of HIC development was able to be reflected by the cumulative energy of the HIC signals obtained by the AE technology, the hydrogen charging characteristics during the experiment were not investigated to be related to the information from AE, such as the amount of the charged hydrogen, the increment of crack growth and the depth of HIC cracks, etc. The outcomes of this investigation will be conducive to understand the mechanism of HIC and to detect small-scale HIC in early stages. This research can be enhanced further by conducting multiple short-term hydrogen charging experiments, with more accurate control of the electrochemical hydrogen charging process.

The experimental procedure for identifying HIC signals developed in this work is safe, time-saving and easy to operate. The proposed unsupervised classification method is generally applicable for classifying the mixed signals obtained during ECHE-HIC tests with different setups. Modelling technology creates large datasets for quickly depicting Delta-T maps for complex geometries. Target events can be accurately and quickly located in practice, showing the high effectiveness. This shows the potential for creating virtual environments based on Lamb wave damage monitoring. With the support of large amounts of data, using digital twin technology to realize virtual models of physical objects is an inspiring development direction. This will be of great help for operators in controlling the status of energy pipelines and their life cycles.

Reference

[1]   W. H. Johnson, "On some remarkable changes produced in iron and steel by the action of hydrogen and acids," *Nature*, p. 393, 1875.

[2]   O. Reynolds, "On the effect of acid on the interior of iron wire," *J. Frankl Inst.*, vol. 99, no. 1, pp. 70–72, 1875.

[3]   J. H. Andrew, A. K. Bose, G. A. Geach, H. Lee, and A. G. Quarrell, "The formation of hair-line cracks," *Jl. Iron and Steel Inst.*, vol. 145, no. 2, pp. 193–202, 1942.

[4]   A. Pundt and R. Kirchheim, "Hydrogen in metals: Microstructural aspects," *Annu Rev Mater Res*, vol. 36, pp. 555–608, 2006, doi: 10.1146/annurev.matsci.36.090804.094451.

[5]   S. Lynch, "Hydrogen embrittlement phenomena and mechanisms," *Corrosion Reviews*, vol. 30, no. 3–4, pp. 105–123, Jun. 2012, doi: 10.1515/corrrev-2012-0502.

[6]   R. J. Walter, R. P. Jewett, and W. T. Chandler, "On the mechanism of hydrogen-environment embrittlement of iron- and nickel-base alloys," *Materials Science and Engineering*, vol. 5, no. 2, pp. 99–110, 1970, doi: 10.1016/0025-5416(70)90039-X.

[7]   P. Cotterill, "The hydrogen embrittlement of metals," *Progress in Metal Physics*, vol. 9, no. 4, pp. 205–301, 1961.

[8]   M. H. Bartz and C. E. Rawlins, "Effects of hydrogen generated by corrosion of steel," *Corrosion*, vol. 4, no. 5, pp. 187–206, 1948.

[9]   C. A. Zapfpe, J. Member, and C. E. Sims, "Hydrogen Embrittlement, Internal Stress and Defects in Steel," *Transactions of the Metallurgical Society of AIME*, vol. 145, pp. 225–271, 1941.

[10]   T. H. Nam, J. H. Lee, S. R. Choi, J. B. Yoo, and J. G. Kim, "Graphene coating as a protective barrier against hydrogen embrittlement," *Int J Hydrogen Energy*, vol. 39, no. 22, pp. 11810–11817, Jul. 2014, doi: 10.1016/j.ijhydene.2014.05.132.

[11]   J. Ćwiek, "Prevention methods against hydrogen degradation of steel," *J. Achievements in Materials and Manufacturing Engineering*, vol. 43, no. 1, pp. 214–221, 2010, [Online]. Available: www.journalamme.org

[12]   H. K. D. H. Bhadeshia, "Prevention of hydrogen embrittlement in steels," *ISIJ International*, vol. 56, no. 1, pp. 24–36, 2016, doi: 10.2355/isijinternational.ISIJINT-2015-430.

[13]   J. H. Andrew, H. Lee, A. K. Mallik, and A. G. Quarrell, "The Removal of Hydrogen from Steel," *J. Iron Steel Inst.*, vol. 153, pp. 67–113, 1946.

[14]   Y. Chung, "Validity of Caltrans' environmental hydrogen embrittlement tests on Grade BD Anchor Rods in the SAS Span," 2014.

[15]   "Why does hydrogen embrittlement fracture occur in steel?," Pipe Fittings Manufacturer – Yaang Pipe Industry .

[16]   "Background Reference: Malaysia," Sep. 2021.

[17]   M. R. Walsh *et al.*, "Preliminary report on the commercial viability of gas production from natural gas hydrates," *Energy Econ*, vol. 31, no. 5, pp. 815–823, Sep. 2009, doi: 10.1016/j.eneco.2009.03.006.

[18]   L. T. Popoola, A. S. Grema, and G. K. Latinwo, "Corrosion Mitigation for Complex Environments," Houston, USA, 2012.

[19]   "How much does it cost to begin pipeline maintenance and construction- Discover the capital expenditures involved," Finmodelslab.

[20]   Y. Qiu, H. Yang, L. Tong, and L. Wang, "Research progress of cryogenic materials for storage and transportation of liquid hydrogen," *Metals (Basel)*, vol. 11, no. 7, Jul. 2021, doi: 10.3390/met11071101.

[21]   Y. Chen, S. Zhao, H. Ma, H. Wang, L. Hua, and S. Fu, "Analysis of hydrogen embrittlement on aluminum alloys for vehicle-mounted hydrogen storage tanks: A review," *Metals (Basel)*, vol. 11, no. 8, Aug. 2021, doi: 10.3390/met11081303.

[22]   G. M. Pressouyre, "A Classification of Hydrogen Traps in Steel," *Metallurgical Transactions A*, vol. 10, no. 10, pp. 1571–1573, 1979.

[23]   M. Nagumo, *Fundamentals of Hydrogen Embrittlement*. Tokyo: Springer, 2016.

[24]   R. Ma, S. Xiang, X. Zhang, and J. Wu, "Rapid dehydrogenation of metallic materials under external electric field," *Mater Today Commun*, vol. 31, Jun. 2022, doi: 10.1016/j.mtcomm.2022.103350.

[25]   M. A. Mohtadi-Bonab and H. Ghesmati-Kucheki, "Important Factors on the Failure of Pipeline Steels with Focus on Hydrogen Induced Cracks and Improvement of Their Resistance: Review Paper," *Metals and Materials International*, vol. 25, no. 5, pp. 1109–1134, Sep. 2019, doi: 10.1007/s12540-019-00266-7.

[26]   R. D. Kane and M. S. Cayard, "NACE committee report 8X294: review of published literature on wet H2S cracking," 1999.

[27]   F. F. Dear and G. C. G. Skinner, "Mechanisms of hydrogen embrittlement in steels: Discussion," *Philosophical Transactions of the Royal Society A: Mathematical, Physical and Engineering Sciences*, vol. 375, no. 2098. Royal Society, Jul. 28, 2017. doi: 10.1098/rsta.2017.0032.

[28]   M. A. Dyrud, "Familiarizing the Unknown: Three Unusual Engineering Cases," in *2011 ASEE Annual Conference & Exposition*, 2011, pp. 22.710.1-22.710.16.

[29]   S. Narayanan, "I-35W Mississippi river bridge failure-Is it a wake up call?," *The India Concrete Journal*, pp. 29–38, 2008, [Online]. Available: https://www.researchgate.net/publication/292870482

[30]   M. Saeedifar and D. Zarouchas, "Damage characterization of laminated composites using acoustic emission: A review," *Compos B Eng*, vol. 195, Aug. 2020, doi: 10.1016/j.compositesb.2020.108039.

[31]   E. Dascotte, J. Strobbe, and U. T. Tygesen, "Continuous stress monitoring of large structures," in *5th International Operational Modal Analysis Conference*, Guimarães, Portugal, 2013.

[32]   V. I. Travush, O. A. Shulyat'ev, S. O. Shulyat'ev, A. M. Shakhraman'yan, and Y. A. Kolotovichev, "Analysis of the Results of Geotechnical Monitoring of 'Lakhta Center'

Tower," *Soil Mechanics and Foundation Engineering*, vol. 56, no. 2, pp. 98–106, May 2019, doi: 10.1007/s11204-019-09576-9.

[33]   W. Sikorski, *Acoustic Emission.* InTech, 2012.

[34]   Y. He *et al.*, "An overview of acoustic emission inspection and monitoring technology in the key components of renewable energy systems," *Mech Syst Signal Process*, vol. 148, Feb. 2021, doi: 10.1016/j.ymssp.2020.107146.

[35]   G. Ciaburro and G. Iannace, "Machine-Learning-Based Methods for Acoustic Emission Testing: A Review," *Applied Sciences (Switzerland)*, vol. 12, no. 20, Oct. 2022, doi: 10.3390/app122010476.

[36]   G. Manthei and K. Plenkers, "Review on in situ acoustic emission monitoring in the context of structural health monitoring in mines," *Applied Sciences (Switzerland)*, vol. 8, no. 9. MDPI AG, Sep. 09, 2018. doi: 10.3390/app8091595.

[37]   X. Lei and S. Ma, "Laboratory acoustic emission study for earthquake generation process," *Earthquake Science*, vol. 27, no. 6, pp. 627–646, Dec. 2014, doi: 10.1007/s11589-014-0103-y.

[38]   A. Carpinteri, F. Asce, and G. Lacidogna, "Structural Monitoring and Integrity Assessment of Medieval Towers", doi: 10.1061/ASCE0733-94452006132:111681.

[39]   G. Cloutier, F. Destrempes, F. Yu, and A. Tang, "Quantitative ultrasound imaging of soft biological tissues: a primer for radiologists and medical physicists," *Insights Imaging*, vol. 12, no. 1, Dec. 2021, doi: 10.1186/s13244-021-01071-w.

[40]   S. W. Rienstra and A. Hirschberg, "An Introduction to Acoustics," *Eindhoven University of Technology*. 2020.

[41]   T. K. Worden, "Rayleigh and Lamb Waves = Basic Principles," *Strain*, vol. 37, no. 4, pp. 167–172, 2001.

[42]   A. Burtin, N. Hovius, and J. M. Turowski, "Seismic monitoring of torrential and fluvial processes," *Earth Surface Dynamics*, vol. 4, no. 2, pp. 285–307, Apr. 2016, doi: 10.5194/esurf-4-285-2016.

[43]   Richard B. Hetnarski and Jozef Ignaczak, *The Mathematical Theory of Elasticity, Second Edition*, Second Edition. CRC Press, 2011.

[44]   O. Novotny, "Seismic Surface Waves," Bahia, 1999.

[45]   F. R. S. Lamb, "On waves in an elastic plate," 1906.

[46]   L. Zeng and J. Lin, "Structural damage imaging approaches based on lamb waves: A review," in *ICQR2MSE 2011 - Proceedings of 2011 International Conference on Quality, Reliability, Risk, Maintenance, and Safety Engineering*, 2011, pp. 986–993. doi: 10.1109/ICQR2MSE.2011.5976769.

[47]   J. L. Rose, *Ultrasonic Guided Waves in Solid Media*. Cambridge University Press , 2014. [Online]. Available: www.cambridge.org/9781107048959

[48]   C. U. Grosse and M. Ohtsu, *Acoustic emission testing: Basics for Research-Applications in Civil Engineering.* Springer Berlin Heidelberg, 2008. doi: 10.1007/978-3-540-69972-9.

[49] K. Nakamura, *Ultrasonic transducers: materials and design for sensors, actuators and medical applications*. Woodhead Publishing, 2010.

[50] G. Gautschi, *Piezoelectric Sensorics: Force, Strain, Pressure, Acceleration and Acoustic Emission Sensors Materials and Amplifiers*. Springer, 2002.

[51] J. C. Drury, *Ultrasonic Flaw Detection for Technicians*, 3rd Edition. Imex Group Limited, 2004.

[52] R. S. Konovalov, S. I. Konovalov, and A. G. Kuz'menko, "Influence of the Design Features of a Piezoelectric Transducer on Probing Signal Duration," *Russian Journal of Nondestructive Testing*, vol. 54, no. 8, pp. 546–555, Aug. 2018, doi: 10.1134/S1061830918080053.

[53] W. Caesarendra, B. Kosasih, A. K. Tieu, H. Zhu, C. A. S. Moodie, and Q. Zhu, "Acoustic emission-based condition monitoring methods: Review and application for low speed slew bearing," *Mech Syst Signal Process*, vol. 72–73, pp. 134–159, May 2016, doi: 10.1016/j.ymssp.2015.10.020.

[54] C. R. Ramirez-Jimenez, N. Papadakis, N. Reynolds, T. H. Gan, P. Purnell, and M. Pharaoh, "Identification of failure modes in glass/polypropylene composites by means of the primary frequency content of the acoustic emission event," *Compos Sci Technol*, vol. 64, no. 12, pp. 1819–1827, Sep. 2004, doi: 10.1016/j.compscitech.2004.01.008.

[55] D. G. Aggelis, S. De Sutter, S. Verbruggen, E. Tsangouri, and T. Tysmans, "Acoustic emission characterization of damage sources of lightweight hybrid concrete beams," *Eng Fract Mech*, vol. 210, pp. 181–188, Apr. 2019, doi: 10.1016/j.engfracmech.2018.04.019.

[56] W. Hwang, S. Bae, J. Kim, S. Kang, N. Kwag, and B. Lee, "Acoustic emission characteristics of stress corrosion cracks in a type 304 stainless steel tube," *Nuclear Engineering and Technology*, vol. 47, no. 4, pp. 454–460, 2015, doi: 10.1016/j.net.2015.04.001.

[57] F. G. Rivera, G. Edwards, E. Eren, and S. Soua, "Acoustic emission technique to monitor crack growth in a mooring chain," *Applied Acoustics*, vol. 139, pp. 156–164, Oct. 2018, doi: 10.1016/j.apacoust.2018.04.034.

[58] L. Toubal, H. Chaabouni, P. Bocher, and C. Jianqiang, "Monitoring fracture of high-strength steel under tensile and constant loading using acoustic emission analysis," *Eng Fail Anal*, vol. 108, Jan. 2020, doi: 10.1016/j.engfailanal.2019.104260.

[59] L. Calabrese, G. Campanella, P. Longo, and E. Proverbio, "Corrosione Damage analysis of stress corrosion test of pretensioning steel strands by AE monitoring," *La Metall. Ital.*, vol. 106, pp. 41–45, 2014.

[60] N. N. Kencanawati, S. Iizasa, and M. Shigeishi, "Fracture process and reliability of concrete made from high grade recycled aggregate using acoustic emission technique under compression," *Materials and Structures/Materiaux et Constructions*, vol. 46, no. 9, pp. 1441–1448, Sep. 2013, doi: 10.1617/s11527-012-9986-z.

[61] Z. Yang, W. Yan, L. Jin, F. Li, and Z. Hou, "A novel feature representation method based on original waveforms for acoustic emission signals," *Mech Syst Signal Process*, vol. 135, Jan. 2020, doi: 10.1016/j.ymssp.2019.106365.

[62] F. T. Santo, T. P. Sattar, and G. Edwards, "Validation of acoustic emissionwaveform entropy as a damage identification feature," *Applied Sciences (Switzerland)*, vol. 9, no. 19, Oct. 2019, doi: 10.3390/app9194070.

[63] R. V. Sanchez, P. Lucero, J. C. Macancela, M. Cerrada, D. Cabrera, and R. Vasquez, "Gear Crack Level Classification by Using KNN and Time-Domain Features from Acoustic Emission Signals under Different Motor Speeds and Loads," in *Proceedings - 2018 International Conference on Sensing, Diagnostics, Prognostics, and Control, SDPC 2018*, Institute of Electrical and Electronics Engineers Inc., Mar. 2019, pp. 465–470. doi: 10.1109/SDPC.2018.8664979.

[64] A. Habib, C. H. Kim, and J. M. Kim, "A crack characterization method for reinforced concrete beams using an acoustic emission technique," *Applied Sciences (Switzerland)*, vol. 10, no. 21, pp. 1–21, Nov. 2020, doi: 10.3390/app10217918.

[65] K. Hattori and M. Takahashi, "A new nearest-neighbor rule in the pattern classification problem," *Pattern Recognit*, vol. 32, pp. 425–432, 1999.

[66] L. Breiman, J. H. Friedman, R. A. Olshen, and C. J. Stone, *Classification and Regression Trees*. Florida: Chemical Rubber Company Press, 1984.

[67] F. Mejia, M. L. Shyu, and A. Nanni, "Data quality enhancement and knowledge discovery from relevant signals in acoustic emission," *Mech Syst Signal Process*, vol. 62, pp. 381–394, Oct. 2015, doi: 10.1016/j.ymssp.2015.02.017.

[68] K. Xu, J. Lyu, and S. Manoochehri, "In situ process monitoring using acoustic emission and laser scanning techniques based on machine learning models," *J Manuf Process*, vol. 84, pp. 357–374, Dec. 2022, doi: 10.1016/j.jmapro.2022.10.002.

[69] A. Rodriguez and A. Laio, "Clustering by fast search and find of density peaks," *Science (1979)*, vol. 344, no. 6191, pp. 1492–1496, 2014, doi: 10.1126/science.1242072.

[70] T. Kohonen, "Self-Organized Formation of Topologically Correct Feature Maps," *Biol. Cybern*, vol. 43, pp. 59–69, 1982.

[71] L. Calabrese, G. Campanella, and E. Proverbio, "Use of cluster analysis of acoustic emission signals in evaluating damage severity in concrete structures," *J. Acoustic Emission*, vol. 28, p. 129, 2010.

[72] J. Vesanto, "Neural Network Tool for Data mining: SOM Toolbox," 2000.

[73] F. Pashmforoush, R. Khamedi, M. Fotouhi, M. Hajikhani, and M. Ahmadi, "Damage Classification of Sandwich Composites Using Acoustic Emission Technique and k-means Genetic Algorithm," *J Nondestr Eval*, vol. 33, no. 4, pp. 481–492, Oct. 2014, doi: 10.1007/s10921-014-0243-y.

[74] V. Emamian, M. Kaveh, A. H. Tewfik, Z. Shi, L. J. Jacobs, and J. Jarzynski, "Robust Clustering of Acoustic Emission Signals Using Neural Networks and Signal Subspace Projections," 2003.

[75] R. de Oliveira and A. T. Marques, "Health monitoring of FRP using acoustic emission and artificial neural networks," *Comput Struct*, vol. 86, no. 3–5, pp. 367–373, Feb. 2008, doi: 10.1016/j.compstruc.2007.02.015.

[76] M. Chai, X. Hou, Z. Zhang, and Q. Duan, "Identification and prediction of fatigue crack growth under different stress ratios using acoustic emission data," *Int J Fatigue*, vol. 160, Jul. 2022, doi: 10.1016/j.ijfatigue.2022.106860.

[77] S. Rippengill, K. Worden, K. M. Holford, and R. Pullin, "Automatic classification of acoustic emission patterns," *Strain*, vol. 39, no. 1, pp. 31–41, Feb. 2003, doi: 10.1046/j.1475-1305.2003.00041.x.

[78] M. Ercolino, A. Farhidzadeh, S. Salamone, and G. Magliulo, "Detection of onset of failure in prestressed strands by cluster analysis of acoustic emission," *Structural Monitoring and Maintenance*, vol. 2, no. 4, pp. 339–355, Dec. 2015, doi: 10.12989/smm.2015.2.4.339.

[79] W. Harizi, S. Chaki, G. Bourse, and M. Ourak, "Damage mechanisms assessment of Glass Fiber-Reinforced Polymer (GFRP) composites using multivariable analysis methods applied to acoustic emission data," *Compos Struct*, vol. 289, Jun. 2022, doi: 10.1016/j.compstruct.2022.115470.

[80] K. Ono, "Review on structural health evaluation with acoustic emission," *Applied Sciences (Switzerland)*, vol. 8, no. 6. MDPI AG, Jun. 11, 2018. doi: 10.3390/app8060958.

[81] E. Karasözen and B. Karasözen, "Earthquake location methods," *GEM - International Journal on Geomathematics*, vol. 11, no. 1. Springer, Dec. 01, 2020. doi: 10.1007/s13137-020-00149-9.

[82] J. A. Nelder and R. Mead, "A simplex method for function minimization," *Computer Journal*, vol. 7, pp. 308–313, 1965.

[83] A. Prugger and D. J. Gendzwill, "Microearthquake location: a nonlinear approach that makes use of a simplex stepping procedure.," *Bulletin - Seismological Society of America*, vol. 78, no. 2, pp. 799–815, 1988, doi: 10.1785/bssa0780020799.

[84] M. Ge, "Analysis of source location algorithms Part II: Iterative methods," *J. Acoustic Emission*, vol. 21, p. 29, 2003.

[85] P. Mottahed, "Improved Determination of Microseismic Source Location Using a Simplex Technique," *IEEE Trans Ind Appl*, vol. 24, no. 4, pp. 666–671, 1988, doi: 10.1109/28.6119.

[86] M. Ge, "Analysis of source location algorithms Part I: Overview and non-iterative methods," *J. Acoustic Emission*, vol. 21, p. 14, 2003.

[87] R. O. Schmidt, "A new approach to geometry of range difference location," *IEEE Trans Aerosp Electron Syst*, vol. AES-8, no. 6, pp. 821–835, 1972, doi: 10.1109/TAES.1972.309614.

[88] B. Friedlander, "A Passive Localization Algorithm and Its Accuracy Analysis," *IEEE Journal of Oceanic Engineering*, vol. 12, no. 1, pp. 234–245, 1987, doi: 10.1109/JOE.1987.1145216.

[89] J. O. Smith and J. S. Abel, "Closed-Form Least-Squares Source Location Estimation from Range-Difference Measurements," *IEEE Transactions on Acoustics, Speech, and Signal Processing*, vol. 35, no. 12. pp. 1661–1669, 1987. doi: 10.1109/TASSP.1987.1165089.

[90]   J. O. Smith and J. S. Abel, "The Spherical Interpolation Method of Source Localization," *IEEE Journal of Oceanic Engineering*, vol. 12, no. 1, pp. 246–252, 1987, doi: 10.1109/JOE.1987.1145217.

[91]   Y. T. Chan and K. C. Ho, "A Simple and Efficient Estimator for Hyperbolic Location," *IEEE Transactions on Signal Processing*, vol. 42, no. 8, pp. 1905–1915, 1994, doi: 10.1109/78.301830.

[92]   Baxter, M.G.; Pullin, R.; Holford, K.M.; Evans, S.L. Delta T Source Location for Acoustic Emission. Mech. Syst. Signal Process. 2007, 21, 1512–1520.

[93]   M. Leonard, "Comparison of Manual and Automatic Onset Time Picking," *Bulletin of the Seismological Society of America*, vol. 90, pp. 1384–1390, 2000.

[94]   G. Kitagawa and H. Akaike, "A procedure for the modeling of non-stationary time serise," *Ann. Inst. Statist. Math*, vol. 30, pp. 351–363, 1978.

[95]   Z. Zhou *et al.*, "An improved onset time picking method for low SNR acoustic emission signals," *IEEE Access*, vol. 8, pp. 47756–47767, 2020, doi: 10.1109/ACCESS.2020.2977885.

[96]   P. Sedlak, Y. Hirose, M. Enoki, and J. Sikula, "Arrival time detection in thin multilayer plates on the basis of Akaike Information Criterion," *J. Acoustic Emission*, vol. 26, p. 182, 2008.

[97]   J. H. Kurz, C. U. Grosse, and H. W. Reinhardt, "Strategies for reliable automatic onset time picking of acoustic emissions and of ultrasound signals in concrete," *Ultrasonics*, vol. 43, no. 7, pp. 538–546, Jun. 2005, doi: 10.1016/j.ultras.2004.12.005.

[98]   A. Carpinteri, J. Xu, G. Lacidogna, and A. Manuello, "Reliable onset time determination and source location of acoustic emissions in concrete structures," *Cem Concr Compos*, vol. 34, no. 4, pp. 529–537, Apr. 2012, doi: 10.1016/j.cemconcomp.2011.11.013.

[99]   N. Maeda, "A Method for Reading and Checking Phase Time in Auto-Processing System of Seismic Wave Data," *Zisin*, vol. 38, pp. 365–379, 1985.

[100] E. Fallahmohammadi, G. Fumagalli, G. Re, F. M. Bolzoni, and L. Lazzari, "Study on hydrogen diffusion in pipeline steels," in *EuroCorr2011*, 2011. [Online]. Available: https://www.researchgate.net/publication/236325746

[101] R. Courant. Variational methods for the solution of problems of equilibrium and vibrations. 1-23, 1943.

[102] Gary, J., & Hamstad, M. A. On the far-field structure of waves generated by a pencil lead break on a thin plate. *Journal of acoustic emission*, *12*(3-4), 157-170, 1994.

[103] Aki, K., Richards, P.G.: Quantitative Seismology, Theory and Methods. University Science Books, Sausalito, 1980.

[104] Lysak, M. V. Development of the theory of acoustic emission by propagating cracks in terms of fracture mechanics. Engineering fracture mechanics, 55(3), 443-452, 1996.

[105] Ono, K., & Ohtsu, M. A generalized theory of acoustic emission and Green's functions in a half space. Journal of Acoustic Emission, 3, 27-40, 1984.

[106]   Hamstad, M. A. On lamb modes as a function of acoustic emission source rise time. Journal of acoustic emission, 28, 2010.

[107]   Hamstad, M. A., O'Gallagher, A., & Gary, J. Modeling of buried acoustic emission monopole and dipole sources with a finite element technique. Journal of acoustic emission, 17(3-4), 97-110, 1999.

[108]   Hamstad, M. A. Acoustic emission signals generated by monopole (pencil lead break) versus dipole sources: finite element modeling and experiments. J. Acoust. Emiss, 25, 92-106, 2007.

[109]   Moser, F., Jacobs, L. J., & Qu, J. Modeling elastic wave propagation in waveguides with the finite element method. Ndt & E International, 32(4), 225-234, 1999.

[110]   Sause, M. G., & Richler, S. Finite element modelling of cracks as acoustic emission sources. Journal of nondestructive evaluation, 34, 1-13, 2015.

[111]   Lee, C. K., Wilcox, P. D., Drinkwater, B. W., Scholey, J. J., Wisnom, M. R., & Friswell, M. I. Acoustic emission during fatigue crack growth in aluminium plates. Proceedings of the ECNDT, Berlin, Germany, 25-29, 2006.

[112]   D. Rudomilova, T. Prošek, and G. Luckeneder, "Techniques for investigation of hydrogen embrittlement of advanced high strength steels," *Corrosion Reviews*, vol. 36, no. 5. De Gruyter, pp. 413–434, Sep. 25, 2018. doi: 10.1515/corrrev-2017-0106.

[113]   V. Olden, C. Thaulow, and R. Johnsen, "Modelling of hydrogen diffusion and hydrogen induced cracking in supermartensitic and duplex stainless steels," *Mater Des*, vol. 29, no. 10, pp. 1934–1948, Dec. 2008, doi: 10.1016/j.matdes.2008.04.026.

[114]   R. A. Orianit, "The diffusion and trapping of hydrogen in steel," *Acta. Metall.*, vol. 18, pp. 147–157, 1970.

[115]   E. I. Galindo-Nava, B. I. Y. Basha, and P. E. J. Rivera-Díaz-del-Castillo, "Hydrogen transport in metals: Integration of permeation, thermal desorption and degassing," *J Mater Sci Technol*, vol. 33, no. 12, pp. 1433–1447, Dec. 2017, doi: 10.1016/j.jmst.2017.09.011.

[116]   M. Dadfarnia, P. Sofronis, and T. Neeraj, "Hydrogen interaction with multiple traps: Can it be used to mitigate embrittlement?," *Int J Hydrogen Energy*, vol. 36, no. 16, pp. 10141–10148, Aug. 2011, doi: 10.1016/j.ijhydene.2011.05.027.

[117]   M. A. Mikolaichuk and A. G. Knyazeva, "Effect of stresses and strains on impurity redistribution in a plate under uniaxial loading," *Journal of Applied Mechanics and Technical Physics*, vol. 51, no. 3, pp. 422–430, 2010.

[118]   A. Traidia, E. Chatzidouros, and M. Jouiad, "Review of hydrogen-assisted cracking models for application to service lifetime prediction and challenges in the oil and gas industry," *Corrosion Reviews*, vol. 36, no. 4, pp. 323–347, Jul. 2018, doi: 10.1515/corrrev-2017-0079.

[119]   H. P. Van Leeuwen, "The kinetics of hydrogen embrittlement: A quantitative diffusion model," *Eng Fract Mech*, vol. 6, pp. 141–161, 1974.

[120]   P. Sofronis and R. M. Mcmeeking, "Numerical analysis of hydrogen transport near a blunting crack tip," *J. Mech. Phys. Solids*, vol. 37, no. 3, pp. 317–350, 1989.

[121] A. H. M. Krom, R. W. J. Koers, and A. Bakker, "Hydrogen transport near a blunting crack tip," *J Mech Phys Solids*, vol. 47, pp. 971–992, 1999.

[122] A. Taha and P. Sofronis, "A micromechanics approach to the study of hydrogen transport and embrittlement," *Eng Fract Mech*, vol. 68, pp. 803–837, 2001, [Online]. Available: www.elsevier.com/locate/engfracmech

[123] V. Olden, C. Thaulow, T. Berstad, and E. Østby, "Prediction of hydrogen embrittlement in 25% Cr duplex stainless steel based on cohesive zone simulation," in *ASME2009 28th International Conference on Ocean, Offshore and Arctic Engineering*, 2009. [Online]. Available: http://asmedigitalcollection.asme.org/OMAE/proceedings-pdf/OMAE2009/43468/209/4574122/209_1.pdf

[124] S. Serebrinsky, E. A. Carter, and M. Ortiz, "A quantum-mechanically informed continuum model of hydrogen embrittlement," *J Mech Phys Solids*, vol. 52, no. 10, pp. 2403–2430, Oct. 2004, doi: 10.1016/j.jmps.2004.02.010.

[125] V. Olden, C. Thaulow, and R. Johnsen, "Modelling of hydrogen diffusion and hydrogen induced cracking in supermartensitic and duplex stainless steels," *Mater Des*, vol. 29, no. 10, pp. 1934–1948, Dec. 2008, doi: 10.1016/j.matdes.2008.04.026.

[126] J.-S. Wang, "The thermodynamics aspects of hydrogen induced embrittlement," *Eng Fract Mech*, vol. 68, pp. 647–669, 2001, [Online]. Available: www.elsevier.com/locate/engfracmech

[127] V. Olden, A. Alvaro, and O. M. Akselsen, "Hydrogen diffusion and hydrogen influenced critical stress intensity in an API X70 pipeline steel welded joint-Experiments and FE simulations," *Int J Hydrogen Energy*, vol. 37, no. 15, pp. 11474–11486, Aug. 2012, doi: 10.1016/j.ijhydene.2012.05.005.

[128] N. Erarslan, "Analysing mixed mode (I–II) fracturing of concrete discs including chevron and straight-through notch cracks," *Int J Solids Struct*, vol. 167, pp. 79–92, Aug. 2019, doi: 10.1016/j.ijsolstr.2019.03.005.

[129] W. Y. Chu *et al.*, *Hydrogen embrittlement and stress corrosion cracking*. Beijing Science Press, 2013.

[130] X. C. Ren *et al.*, "The effects of atomic hydrogen and flake on mechanical properties of a tyre steel," *Materials Science and Engineering A*, vol. 491, no. 1–2, pp. 164–171, Sep. 2008, doi: 10.1016/j.msea.2008.02.002.

[131] A. R. Troiano, "The Role of Hydrogen and Other Interstitials in the Mechanical Behavior of Metals: (1959 Edward De Mille Campbell Memorial Lecture)," *Metallography, Microstructure, and Analysis*, vol. 5, no. 6, pp. 557–569, Dec. 2016, doi: 10.1007/s13632-016-0319-4.

[132] C. L. Fu and G. S. Painter, "First principles investigation of hydrogen embrittlement in FeAl," *J. Mater. Res.*, vol. 6, no. 4, pp. 719–723, 1991, [Online]. Available: http://journals.cambridge.org

[133] C. D. Beachem, "A New Model for Hydrogen-Assisted Cracking (Hydrogen 'Embrittlement')," *Metallurgical Transactions*, vol. 3, pp. 437–451, 1972.

[134] H. K. Birnbaum and P. Sofronis, "Hydrogen-enhanced localized plasticity-a mechanism for hydrogen-related fracture," *Materials Science and Engineering*, vol. 176, pp. 191–202, 1994.

[135] NACE International., *Standard test method : evaluation of pipeline and pressure vessel steels for resistance to hydrogen-induced cracking*. NACE International, 2003.

[136] K. O. Findley, M. K. O'Brien, and H. Nako, "Critical assessment 17: Mechanisms of hydrogen induced cracking in pipeline steels," *Materials Science and Technology*, vol. 31, no. 14, pp. 1673–1680, Nov. 2015, doi: 10.1080/02670836.2015.1121017.

[137] G. Domizzi, G. Anteri, J. Ovejero-Garc, D. Materiales, and G. Desarollo, "Influence of sulphur content and inclusions distribution on the hydrogen induced blister cracking in pressure vessel and pipeline steels," *Corros Sci*, vol. 43, pp. 325–339, 2001, [Online]. Available: www.elsevier.com/locate/corsci

[138] F. Huang, J. Liu, Z. J. Deng, J. H. Cheng, Z. H. Lu, and X. G. Li, "Effect of microstructure and inclusions on hydrogen induced cracking susceptibility and hydrogen trapping efficiency of X120 pipeline steel," *Materials Science and Engineering A*, vol. 527, no. 26, pp. 6997–7001, Oct. 2010, doi: 10.1016/j.msea.2010.07.022.

[139] S. Zheng, C. Chen, and L. Chen, "Influence of S Contents on the Hydrogen Blistering and Hydrogen Induced Cracking of A350LF2 Steel," *Materials Sciences and Applications*, vol. 02, no. 07, pp. 917–921, 2011, doi: 10.4236/msa.2011.27122.

[140] D. P. Dunne, D. Hejazi, A. A. Saleh, A. J. Haq, A. Calka, and E. V. Pereloma, "Investigation of the effect of electrolytic hydrogen charging of X70 steel: I. The effect of microstructure on hydrogen-induced cold cracking and blistering," *Int J Hydrogen Energy*, vol. 41, no. 28, pp. 12411–12423, Jul. 2016, doi: 10.1016/j.ijhydene.2016.04.114.

[141] X. S. Du, W. B. Cao, C. D. Wang, S. J. Li, J. Y. Zhao, and Y. F. Sun, "Effect of microstructures and inclusions on hydrogen-induced cracking and blistering of A537 steel," *Materials Science and Engineering A*, vol. 642, pp. 181–186, Aug. 2015, doi: 10.1016/j.msea.2015.06.085.

[142] M. A. Mohtadi-Bonab, J. A. Szpunar, R. Basu, and M. Eskandari, "The mechanism of failure by hydrogen induced cracking in an acidic environment for API 5L X70 pipeline steel," *Int J Hydrogen Energy*, vol. 40, no. 2, pp. 1096–1107, Jan. 2015, doi: 10.1016/j.ijhydene.2014.11.057.

[143] J. S. Park, J. W. Lee, J. K. Hwang, and S. J. Kim, "Effects of alloying elements (C, Mo) on hydrogen assisted cracking behaviors of A516-65 steels in sour environments," *Materials*, vol. 13, no. 18, Sep. 2020, doi: 10.3390/MA13184188.

[144] R. Padmanabhan, N. Suriyayothin, and W. E. Wood, "Grain Size-Acoustic Emission Relationships in Hydrogen Induced Delayed Cracking," *Metallurgical Transactions A*, vol. 14A, pp. 2357–2362, 1983.

[145] H. L. Dunegan and A. S. Tetelman, "Non-destructive characterization of hydrogen-embrittlement cracking by acoustic emission techniques," *Eng Fract Mech*, vol. 2, pp. 387–402, 1971.

[146] A. K. Bhattacharya, N. Parida, and P. C. Gope, "Monitoring hydrogen embrittlement cracking using acoustic emission technique," 1992.

[147] C. K. Soundararajan, A. Myhre, A. Sendrowicz, X. Lu, and A. Vinogradov, "Hydrogen-induced degradation behavior of nickel alloy studied using acoustic emission technique," *Materials Science and Engineering A*, vol. 865, Feb. 2023, doi: 10.1016/j.msea.2023.144635.

[148] T. Shiraiwa, M. Kawate, F. Briffod, T. Kasuya, and M. Enoki, "Evaluation of hydrogen-induced cracking in high-strength steel welded joints by acoustic emission technique," *Mater Des*, vol. 190, May 2020, doi: 10.1016/j.matdes.2020.108573.

[149] J. Kittel, V. Smanio, M. Fregonese, L. Garnier, and X. Lefebvre, "Hydrogen induced cracking (HIC) testing of low alloy steel in sour environment: Impact of time of exposure on the extent of damage," *Corros Sci*, vol. 52, no. 4, pp. 1386–1392, 2010, doi: 10.1016/j.corsci.2009.11.044.

[150] V. Smanio, M. Fregonese, J. Kittel, T. Cassagne, F. Ropital, and B. Normand, "Contribution of acoustic emission to the understanding of sulfide stress cracking of low alloy steels," *Corros Sci*, vol. 53, no. 12, pp. 3942–3949, Dec. 2011, doi: 10.1016/j.corsci.2011.07.041.

[151] V. Smanio, M. Fregonese, J. Kittel, T. Cassagne, F. Ropital, and B. Normand, "Wet hydrogen sulfide cracking of steel monitoring by acoustic emission: Discrimination of AE sources," *J Mater Sci*, vol. 45, no. 20, pp. 5534–5542, 2010, doi: 10.1007/s10853-010-4613-2.

[152] D. Merson, S. Dement'ev, A. Ioffe, P. Suvorov, and A. Vinogradov, "Acoustic Emission during Hydrogen Charging of a Pipeline Steel," 2011.

[153] G. Shen, L. Li, and W. Zhang, "Investigation on Acoustic Emission of Hydrogen Induced Cracking for Carbon Steel Used in Pressure Vessel," 2008, pp. 25–28.

[154] L. fei Li, Z. Zhang, G. tian Shen, and Z. wen Wu, "Acoustic Emission as a Technique to Study Hydrogen Induced Cracking Behavior of Low-Carbon Steel," in *2010 3rd International Congress on Image and Signal Processing (CISP2010)* , 2010, pp. 4002–4005.

[155] R. D. Kane and M. S. Cayard, "Roles of H2S in the behavior of engineering alloys: a review of literature and experience," in *In Proceedings of the CORROSION 98*, San Diego, CA, USA, Mar. 1998.

[156] D P. Dunne, D. Hejazi, A. A. Saleh, A. J. Haq, A. Calka, and E. V. Pereloma, "Investigation of the effect of electrolytic hydrogen charging of X70 steel: I. The effect of microstructure on hydrogen-induced cold cracking and blistering," *Int J Hydrogen Energy*, vol. 41, no. 28, pp. 12411–12423, Jul. 2016, doi: 10.1016/j.ijhydene.2016.04.114.

[157] M. A. Hamstad, "Some observations on Rayleigh waves and acoustic emission in thick steel plates," *J. Acoustic Emission*, p. 27, 2009.

[158] User's Instruction Manual of Model Nano30; Mistras Group: Texas, TX, USA, 2021.

[159] A. Prateepasen and C. Jirarungsatian, "Implementation of Acoustic Emission Source Recognition for Corrosion Severity Prediction," *CORROSION*, vol. 67, no. 5, 2011.

[160] H. Bi, D. Hu, Z. Li, Q. Niu, I. Toku-Gyamerah, and J. Chen, "Monitoring Uniform Corrosion of Storage Tank Bottom Steel by Acoustic Emission technique," *Int. J.*

Electrochem. Sci, vol. 10, pp. 6946–6958, 2015, [Online]. Available: www.electrochemsci.org

[161] D. Merson, S. Dement'ev, A. Ioffe, P. Suvorov, and A. Vinogradov, "Acoustic Emission during Hydrogen Charging of a Pipeline Steel," 2011.

[162] V. Smanio, M. Fregonese, J. Kittel, T. Cassagne, F. Ropital, and B. Normand, "Wet hydrogen sulfide cracking of steel monitoring by acoustic emission: Discrimination of AE sources," *J Mater Sci*, vol. 45, no. 20, pp. 5534–5542, 2010, doi: 10.1007/s10853-010-4613-2.

[163] V. Smanio, M. Fregonese, J. Kittel, T. Cassagne, F. Ropital, and B. Normand, "Contribution of acoustic emission to the understanding of sulfide stress cracking of low alloy steels," *Corros Sci*, vol. 53, no. 12, pp. 3942–3949, Dec. 2011, doi: 10.1016/j.corsci.2011.07.041.

[164] M. Saeedifar, D. Zarouchas. Damage characterization of laminated composites using acoustic emission: A review. Composites Part B: Engineering, 2022, 195.

[165] J. Xu, W. Wang, Q. Han, X, Liu. Damage pattern recognition and damage evolution analysis of unidirectional CFRP tendons under tensile loading using acoustic emission technology. Composite Structures, 2020, 238.

[166] M. Shehadeh, A. Elbatran, A. Mehanna, J. Steel, R. Reuben. Evaluation of acoustic emission source location in long steel pipes for continuous and semi-continuous sources. Journal of Nondestructive Evaluation, 2019, 38 (2).

[167] M. Hamstad. Some observations on Rayleigh waves and acoustic emission in thick steel plates. J. Acoustic Emission, 2009, 27.

[168] Pearson, M.R.; Eaton, M.; Featherston, C.; Pullin, R.; Holford, K. Improved Acoustic Emission Source Location during Fatigue and Impact Events in Metallic and Composite Structures. Struct. Heal. Monit. 2017, 16, 382–399, doi:10.1177/1475921716672206.

[169] Han Yang. Development of Acoustic Emission Technology for Stress Corrosion Cracking. 2023